

Cardiac Shear Wave Elastography

Lana Beate Hendrika Keijzer

ISBN: 978-94-640-250-26

Layout & Cover: Lana B.H. Keijzer

Print: Ipskamp Printing

Copyright: © 2020 by Lana B.H. Keijzer, except for:

Chapter 2: © IEEE, 2017

Chapter 3: © IEEE, 2018

Chapter 9: © American Heart Association, Inc., 2019

All Rights Reserved. No part of this thesis may be reproduced, stored in a retrieval system of any nature, or transmitted in any form or by any means, without prior written permission of the author.

An electronic version of this dissertation is available at
<http://hdl.handle.net/1765/129604>

Cardiac Shear Wave Elastography

Cardiale shear wave elastografie

Thesis

to obtain the degree of Doctor from the
Erasmus University Rotterdam,
by command of the rector magnificus

Prof. dr. R.C.M.E. Engels

and in accordance with the decision of the Doctorate Board.

The public defence shall be held on
Wednesday the 2nd of December 2020 at 15.30 hrs

by

Lana Beate Hendrika Keijzer

born in Leiderdorp, the Netherlands.

Doctoral Committee

Promotors: Prof. dr. ir. N. de Jong
Prof. dr. ir. A.F.W. van der Steen

Other members: Prof. dr. D.J.G.M. Duncker
Prof. dr. J. van der Velden
Prof. dr. ir. C.L. de Korte

Copromotors: Dr. ir. H.J. Vos
Dr. ir. J.G. Bosch



The research described in this thesis is part of the NWO-TTW/Technologiestichting STW and Dutch Heart Foundation partnership program 'Earlier recognition of cardiovascular diseases' (DHF 2015B039; NWO-STW 14740).

The research described in this thesis has been carried out at the Department of Biomedical Engineering, Thorax Center, Erasmus University Medical Center, Rotterdam, the Netherlands.



Financial support for the printing of this thesis was kindly provided by the Erasmus University Medical Center.

Financial support by the Dutch Heart Foundation for the publication of this thesis is gratefully acknowledged.

Contents

1	Introduction	1
2	Diffuse Shear Wave Elastography.	15
3	Intra-Scan Variability of Natural Shear Wave Measurements	23
4	Reproducibility of Natural Shear Wave Measurements.	33
5	Parasternal versus Apical View in Natural Shear Wave Measurements	57
6	Wave Propagation in Temporally Relaxing Media	79
7	Natural versus Acoustic-Radiation-Force-Induced Shear Waves	95
8	Shear Waves in Relation to (Patho-)physiologic Changes	121
9	EchoPIV to Assess High Velocity Diastolic Flow Patterns.	145
10	Discussion and Conclusion	149
	References	163
	Summary	171
	Samenvatting	175
	List of Publications	179
	PhD Portfolio.	181
	Acknowledgements.	185
	About the Author	189

1

Introduction



1.1. THE CARDIAC FUNCTION

The heart circulates blood through the body via two different pathways; the pulmonary and the systemic circuit. In the pulmonary circuit, deoxygenated blood flows from the right side of the heart, to the lungs; and then returns as oxygenated blood into the left side of the heart. In the systemic circuit, oxygenated blood flows from the left side of the heart to the body's tissues, for exchange of oxygen, nutrients and waste products, and thereafter to the right side of the heart again.

Figure 1.1 gives a schematic overview of the anatomy of the heart. Due to precise timing of electrical and mechanical events, atria and ventricles contract in a rhythmic manner during the cardiac cycle, as schematically shown in Figure 1.2. The two main phases of a cardiac cycle are systole and diastole, the ventricular contraction and relaxation phase respectively. In early diastole, the ventricles are relaxed and blood flows from the atria into the ventricles. Then in late diastole, atrial contraction forces a further bolus of blood into the ventricles. Subsequently, in systole, the ventricles start to contract while their volumes remain constant (isovolumetric contraction), directly causing the closure of the tricuspid and mitral valves. The pressures in the ventricles further increase and eventually exceed the pressures in the pulmonary artery and aorta. Then, pulmonary and aortic valves open and blood is pumped out of the ventricles into the arteries. At the end of the ejection phase, the diastolic phase starts with the onset of ventricular relaxation without changing volumes (isovolumetric relaxation), and ventricular pressures decrease below artery pressures, causing the closure of the corresponding valves. After further reduction of the ventricular pressures, the tricuspid and mitral valves open and a new cardiac cycle begins with the filling of the ventricles [1].

1.2. HEART FAILURE

Heart failure (HF) is a clinical syndrome, defined by typical symptoms like breathlessness, ankle swelling and fatigue; caused by underlying cardiac dysfunction; resulting in a reduced cardiac output and/or increased intracardiac pressures at rest or during stress [2]. In other words, the heart of a HF patient cannot chronically meet the body's need for blood and oxygen, or only with abnormally high cardiac filling pressures [1]. HF is an important health care problem, due to high mortality and morbidity rates, and since healthcare costs are increasing due to the aging population [3, 4]. It currently affects 1 – 2% of the adult population in developed countries, and even more than 10% among the elderly (>70 years) [2]. Furthermore, predictions show an increase in the total number of HF patients in the United States from 2012 to 2030 with 46% to more than 8 million people, and an increase in the total HF costs with 127% to approximately \$70 billion per year [5]. Main risk factors for developing HF are (coronary) heart diseases, hypertension, diabetes mellitus, obesity and smoking [3].

HF can be caused by myocardial abnormalities leading to systolic and/or diastolic dysfunction, but also by abnormalities related to the valves, pericardium, endocardium, heart rhythm or conduction [2]. Before cardiac dysfunction turns into

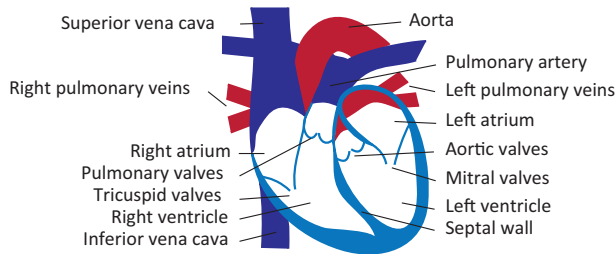


Figure 1.1: Schematic overview of the anatomy of the heart, based on [1].

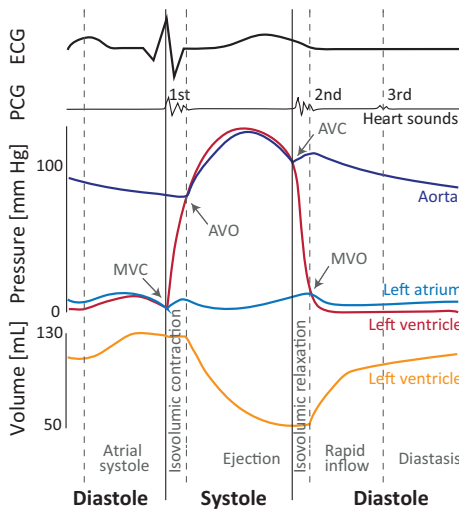


Figure 1.2: Schematic overview of the interaction between the electrocardiogram and left ventricular volumes and pressures. Abbreviations; ECG: electrocardiogram, PCG: phonocardiogram, AVC: aortic valve closure, AVO: aortic valve opening, MVC: mitral valve closure, MVO: mitral valve opening, based on [1, 7].

the clinical syndrome of heart failure, the heart has made progressive anatomical changes as a response to a chronically increased myocardial work load, reduced myocardial contractility or altered myocardial tissue composition, in order to meet with the body's demand of blood [6]. The structural and/or functional adaptation of the ventricles is called cardiac remodeling. Cardiac remodeling leads to an increase in ventricular mass (hypertrophy) and/or in an increased volume (dilatation), leading to a reduced contractility and/or increased stiffness of the myocardium. The ventricles also remodel after acute myocardial infarcts but in a different way than for chronic heart diseases [6]. This thesis will focus on heart failure as a chronic progressive disease and in particular on the left ventricle (LV) as this is currently in general most focused on for the diagnosis of heart failure.

1.3. CURRENT DIAGNOSIS OF HEART FAILURE

Left ventricular ejection fraction (LVEF) is currently the main parameter used to classify heart failure. Heart failure patients are separated into three groups; i) HF with

preserved LVEF (HFpEF, LVEF>50%), ii) HF with reduced LVEF (HFrEF, LVEF<40%), and iii) HF with mid-range LVEF (HFmrEF, LVEF: 40 – 49%) [2]. Diastolic and systolic dysfunction are typically seen as the causes of HFpEF and HFrEF respectively. However, subtly abnormal systolic function is also present in some HFpEF patients, and most HFrEF patients have also diastolic dysfunction [2, 8]. The HFmrEF group is expected to have primarily mild systolic dysfunction, with potential features of diastolic dysfunction. Although treatments have been shown to reduce morbidity and mortality in the HFrEF group, these methods are not beneficial for HFpEF patients [2, 9]. Furthermore, the diagnosis of HFpEF is more challenging than HFrEF, since the LVEF is normal and since signs and symptoms are non-specific and cannot be easily used to distinguish HF from other clinical conditions [2]. Furthermore, patients do often not show symptoms until they develop HFpEF in a late stage of the pathophysiologic process [9]. Recognizing the precursors of HFpEF at an early stage, and thus understanding the underlying causes, could potentially help in accommodating earlier and more personalized treatment.

The current clinical assessment of systolic and diastolic function relies on the echocardiographic measurement of cardiac volumes, and non-invasive Doppler measurements of blood and tissue [10–12], but not on the intrinsic mechanical properties of the myocardium [11]. For the evaluation of systolic heart function, measurements of cardiac volumes cannot give insights in the contractile forces of, or the mechanical pressures on the myocardium. The assessment of diastolic function is even more challenging. Diastolic dysfunction is generally assumed to be related to an increased myocardial stiffness of the left ventricle at end-diastole, caused by an increased passive myocardial stiffness and/or early diastolic relaxation-rate abnormalities [9, 10, 13–15]. Diastolic relaxation is an active energy-dependent process that can for example be impaired due to acute myocardial ischemia; while the passive ventricular stiffness can be increased by for example fibrosis, restrictive cardiomyopathy or left ventricular hypertrophy [1]. Invasive pressure-volume loops can be used to evaluate diastolic dysfunction; by assessing the non-linear relation between pressure and volume at end-diastole, the resistance of the left-ventricle to fill with blood is analyzed, often used as a measure of the left ventricular chamber stiffness. However, its invasive nature makes this technique less suited for patient screening purposes [9, 16]. Since noninvasive parameters used for the diagnosis of diastolic dysfunction are non-specific [2, 8, 10], a complicated algorithm is needed for diagnosis [10], leading to many undetermined situations.

The changes in cardiac volume, flow and tissue velocity that are currently measured to assess systolic and diastolic function are surrogate parameters for the myocardial function depending on loading conditions. By measuring the myocardial stiffness – an intrinsic mechanical property of the myocardium – it is assumed that the myocardial function could be assessed more directly [11]. This is especially important for the early diagnosis of diastolic dysfunction in HFpEF patients caused by an increased myocardial stiffness, where no treatments have been shown yet to be effective [2, 17]. However, such a non-invasive measure of myocardial stiffness does currently not exist.

1.4. STIFFNESS

There are multiple internal and external forces that can act on tissues; forces perpendicular to the surface of the tissue (tension and compressive), and shear forces that act parallel to the tissue. These forces apply a certain stress on the tissue (force per unit of area) causing tissue deformation, or strain (deformation per unit of length). Different terms are widely used to describe relationships between stress and strain. In general, the term elasticity refers to the ability of a material to return to its initial shape after removing the forces applied. The elastic modulus of a material mathematically describes its resistance to deformation, and the Young's and shear modulus are often used to describe the elastic modulus with respect to a longitudinal or shear force respectively [18]. Although in some fields the term stiffness is seen as the resistance of an object to deformation, depending on the material's elastic modulus, but also on the objects geometry and the loading applied; tissue stiffness often refers to the material's elastic modulus only. Since most biological materials do not have a linear stress-strain relation [18–20], instead of the Young's Modulus, the slope of a stress-strain diagram can be determined, which is called the tissue's elastic stiffness.

In cardiology, the left ventricular chamber compliance is often used to describe how easily the left ventricle can fill with blood (reciprocal of elasticity), and is often computed as the change in volume as a response to a change in pressure at end-diastole by using invasive pressure-volume loops. However, it should be noted that the chamber compliance depends not only on the intrinsic myocardial stiffness (passive myocardial stiffness and the relaxation), but also on the left ventricular chamber characteristics such as chamber size (which can be accounted for by using non-linear curve fits) and wall thickness. Thus while chamber compliance can be directly derived from pressure-volume data, theoretical models are needed to quantify (3D) stress and strain to assess myocardial stiffness [16, 20].

Although the myocardium is a complex material to be described by models, we will first discuss some mathematical definitions often used to describe different stress-strain relationships of a material. Since these definitions assume a simply linear isotropic material, we will then further discuss on the more complex application of the myocardium.

1.4.1. Physics of Stiffness

This paragraph will give a short introduction to the equations used to describe a linear isotropic elastic material under small deformation. For more information on material characterization and the derivation of the equations, see [21–23]. Hooke's law describes the linear relation between stress σ in [Pa] and strain ϵ :

$$\sigma_{ij} = c_{ijkl}\epsilon_{kl}, \quad (1.1)$$

with the indices of σ and ϵ indicating the direction of the stress/deformation and the normal of the plane on which the stress/deformation is applied respectively, and with

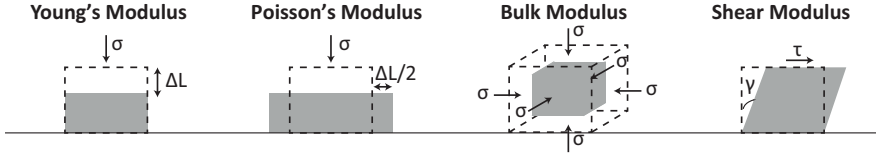


Figure 1.3: Schematic overview of the Young's, Poisson's, Bulk and Shear modulus. These engineering constants can be assessed experimentally.

c the elastic modulus tensor in [Pa]. By assuming that a material is linearly elastic under small deformation, the number of stiffness constants in the elastic modulus tensor can be reduced from 81 to only two constants, called the Lamé coefficients λ and μ . Equation 1.1 can now be simplified as follow:

$$\sigma_{ij} = \lambda e \delta_{ij} + 2\mu \epsilon_{ij}, \quad (1.2)$$

with e indicating the volume change $e = \epsilon_{11} + \epsilon_{22} + \epsilon_{33}$ and δ_{ij} indicating the Kronecker delta. The Lamé coefficients cannot be measured experimentally, but can be linked to assessable engineering constants (Figure 1.3), which will be now described briefly.

The Young's Modulus E is the resistance of a material to deform in longitudinal direction ϵ_l under a tensile stress σ_l , the relation between these variables is described as follow:

$$E = \frac{\sigma_l}{\epsilon_l} = \frac{\mu(3\lambda + 2\mu)}{(\lambda + \mu)}. \quad (1.3)$$

The Poisson's ratio ν describes how the material gets thinner (transversal strain ϵ_t) when it is stretched in the longitudinal direction:

$$\nu = -\frac{\epsilon_t}{\epsilon_l} = \frac{\lambda}{2(\lambda + \mu)}. \quad (1.4)$$

The bulk modulus κ describes the relative volume change of the material e as a consequence of a hydrostatic normal stress σ_{ii} :

$$\kappa = -\frac{\sigma_{ii}}{e} = \frac{E}{3(1 - 2\nu)} = \lambda + \frac{2}{3}\mu. \quad (1.5)$$

The compressibility of a material is the reciprocal of the bulk modulus. Soft tissues, and thus biological tissues, are often assumed to be nearly incompressible ($\lambda \gg \mu$) and thus to have an infinite bulk modulus when interpreting shear waves for elastography purposes. From Equation 1.3 - 1.5 it can be seen that this approximately results in a Poisson's ratio of $\nu = 0.5$, and a Young's modulus that is 3 times larger than the shear modulus, $E = 3\mu$ [18, 24]. Similar as for the Young's Modulus, the second Lamé coefficient μ , also known as the shear modulus, describes the resistance of a material to deform when a shear stress τ is present:

$$\mu = \frac{\tau}{\gamma} = \frac{E}{2(1 + \nu)}, \quad (1.6)$$

with γ describing the shear deformation. By rewriting Equations 1.5 and 1.6, the Lamé coefficients are expressed in the engineering constants as follow:

$$\lambda = \frac{Ev}{(1 + \nu)(1 - 2\nu)}, \quad (1.7)$$

and

$$\mu = \frac{E}{2(1 + \nu)}. \quad (1.8)$$

1.4.2. Myocardial Stiffness

The myocardium is a complex tissue that cannot be easily described by material models. First, the stress-strain relation of biological tissues is non-linear and does thus not follow Hooke's law. Non-linearity is caused by hyperelasticity [19, 25, 26] and viscoelasticity [18, 26]. Hyperelasticity means that the slope of the stress-strain curve depends on the amount of stress applied; the larger the stress the stiffer the material is. Viscoelasticity means that the deformation of the tissue depends on the rate of stress excitation; the faster the stress is applied the smaller the deformation will be. As a consequence, in the widely-used Kelvin/Voigt model, the Lamé coefficients are described by complex values with a real part that describes the elasticity and with an imaginary part that mimics the viscous behavior depending on the angular frequency of stress excitation [27, 28]. Second, the myocardium is an anisotropic material due to its complex fiber orientation [26, 29]. This means that the deformation of the tissue is not homogeneous in all directions. Therefore, the material characteristics will not only depend on the amount and rate of stress applied, but will also depend on in what direction the deformation is measured. Third, in an *in vivo* situation the stiffness of the myocardium measured depends on different components: i) the passive component representing the elastic stiffness of the isolated relaxed wall depending on the Lamé constants of the material, ii) the active component caused by muscle contraction and relaxation, and iii) the hyperelastic component caused by the pressure equilibrium in the cavities. The interaction between these components, and thus the myocardial stiffness measured, varies throughout the cardiac cycle.

1.5. ELASTOGRAPHY

Elastography techniques measure the response of a material on a mechanical stress applied, to assess the stiffness of the material. The stress can be applied with a quasi-static or with a dynamic force. In quasi-static methods, a constant stress is applied on tissue. In dynamic methods, forces that vary over time are applied, including short transient forces – called transient elastography – as well as forces oscillating with a constant frequency, called harmonic elastography [24]. The response of the material can be measured and thereafter converted into material elasticity characteristics by using a model, that is inherently related to assumptions that might be invalid for an *in vivo* situation.

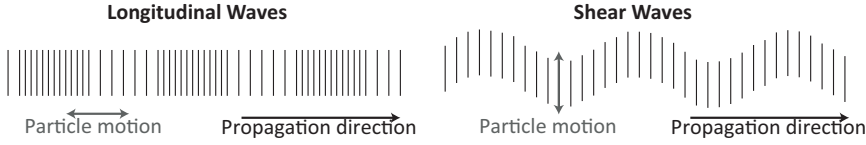


Figure 1.4: Longitudinal versus shear waves. Longitudinal waves have particle motion in the same direction as the propagation direction of the wave, while shear waves have particle motion perpendicular (transversal) to the propagation direction.

Ultrasound and Magnetic Resonance Imaging (MRI) are the two main methods used to assess the material's response in elastography measurements. Ultrasound is a safe, affordable and real-time technique that is convenient for patients and practitioners. MRI has the advantage of measuring three-dimensional motion [30], and is not restricted by the presence of gas or bone [31]. However, MRI is expensive, uncomfortable for the patient, and slow compared to ultrasound. MRI techniques are quickly developing, and several studies showed MRI as a promising technique to assess stiffness, by performing full inversion on 3D displacement wave fields [30, 32–34]. However, to track the fast phenomena such as the propagation of shear waves over time, high frame rates are required, which can currently be achieved by using ultrasound, and which will be focused on in this thesis.

1.5.1. Shear Wave Elastography

In shear wave elastography (SWE) the propagation speed of vibrations induced by a dynamic force are measured and converted into the tissue's stiffness. This paragraph will shortly introduce the relationships between propagation speeds and shear modulus in a linear isotropic bulk medium. For the derivation of the equation see [23].

Elastic waves can be categorized in longitudinal waves (P-waves; primary irrotational waves), with the vibrations in the same direction as the propagation (compressional waves), and shear waves (S-waves; secondary divergence free waves), with vibrations perpendicular to the direction of propagation (transversal waves), see Figure 1.4 for a graphical representation of these two wave types. The propagation speeds of these waves, α and β in [m/s] respectively, can be directly linked to the shear and bulk modulus of the material as follow:

$$\alpha = \sqrt{\frac{\lambda + 2\mu}{\rho}} = \sqrt{\frac{\kappa + \frac{4}{3}\mu}{\rho}}, \quad (1.9)$$

and

$$\beta = \sqrt{\frac{\mu}{\rho}}, \quad (1.10)$$

with ρ the density of the material in [kg/m³]. Since the propagation speeds of P- and S-waves are related to the bulk and/or shear modulus of the material, both types of

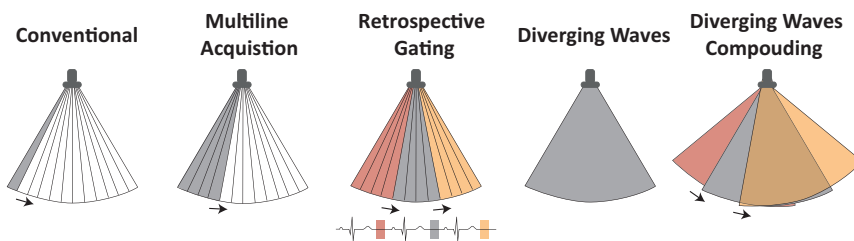


Figure 1.5: Schematic comparison of conventional focused ultrasound with several techniques that can be used to increase the frame rate, such as multiline acquisition techniques, retrospective gating, diverging waves and diverging waves compounding.

waves could in principle be used for material characterization. In practice, the propagation speed of P-waves is mainly affected by the bulk modulus κ , since this modulus is very large compared to the shear modulus μ in biological tissues (κ of $\sim 2 - 2.6$ GPa versus μ of $\sim 0.3 - 100$ kPa (based on propagation speeds in [23, 35])), while the propagation speed of S-waves only depends on the shear modulus, as shown in Equation 1.10. Furthermore, since the bulk modulus is very similar among different biological tissues compared to the shear modulus, the propagation speed of S-waves shows a larger variability among tissues than of P-waves ($\sim 0.5 - 10$ m/s versus $\sim 1400 - 1600$ m/s respectively [23, 35]). Therefore, shear waves (SWs) are expected to be more suited to assess the elastic properties of biological tissues. In SW echocardiography specifically, while the propagation speed of SWs is measured for material characterization, longitudinal ultrasonic waves are used to track the propagation of these SWs. Due to the relatively fast typical propagation speeds of SWs, ultrasound imaging needs to be applied with a high repetition rate to track these SWs when propagating through the medium. This can be done with high-frame-rate echocardiography.

1.6. HIGH-FRAME-RATE ECHOCARDIOGRAPHY

In conventional ultrasound, multiple focused beams are used to create an image (frame). These focused beams consecutively scan the region-of-interest line by line, as shown in Figure 1.5. The frame rate of ultrasonic images mainly depends on the speed of sound (typically 1540 m/s in human tissue), the imaging depth, and the number of transmissions used to create a single frame. Since multiple beams are needed for a conventional-ultrasound image, the frame rate is limited (in general 30 – 100 frames per second). However, to image fast phenomena like SWs, higher frame rates are required [36].

Frame rates can be increased by decreasing the number of transmissions needed for an individual frame, by for example limiting the region-of-interest or reducing the line density. However, this is at the cost of the field-of-view and spatial resolution respectively [37].

Multiline acquisition (MLA) techniques reconstruct multiple adjacent lines in parallel for an individual transmit beam. However, only part of the transducer's aperture is used to broaden the focused transmit beams, resulting in a lower signal-to-noise ratio (SNR) and lateral resolution. An alternative technique that maintains spatial resolution, is retrospective gating, where smaller subsectors measured in different heart cycles are combined into a single frame. Main disadvantage of this technique is that it is not applicable in patients with an instable heart rate or atrial fibrillation [37].

In plane-wave and diverging-wave imaging, a single broad beam is used to insonify the entire region-of-interest at once, typically leading to more than 1000 frames per second. The relative low contrast and spatial resolution can be improved by compounding several tilted transmissions for each frame [36–38].

1.7. CARDIAC SHEAR WAVE ELASTOGRAPHY

Several studies showed the potential of natural and active SWE techniques to assess myocardial stiffness. Figure 1.6 gives a schematic overview of the methods most often used in a cardiac setting. In natural SWE, the propagation speeds of natural vibrations are measured. These natural vibrations occur after the aortic and mitral valve closure (AVC and MVC) [39–44], often referred to as SWs. These SWs have been measured in the transversal [39, 40, 42, 43] as well as in the longitudinal [44–46] direction of the myocardium. Several studies also measured natural vibrations in the longitudinal direction after atrial contraction [47–50], but it can be argued that these vibrations cannot be classified as being SWs due to their vibrations in the longitudinal direction. In active SWE techniques, vibrations are externally induced in the myocardium. This has been done by using a mechanical shaker with a constant low frequency [51–53] (often also used in combination with MRI), but more often by using an acoustic radiation force (ARF) [54–58]. By transmitting a high-energy focused acoustic beam, an ARF in the direction of this beam is applied on the tissue, with its magnitude depending on the acoustic absorption, speed of sound in the tissue and the temporal average intensity of the acoustic beam [59]. For both natural and active SWE, the axial vibrations in the myocardium are tracked using high-frame-rate echocardiography, and the propagation speed of the SWs is measured. Since higher propagation speeds are expected for stiffer materials as shown in Equation 1.10, this results in a rather quantitative measure of tissue stiffness. As an alternative to ARF-based SWE, the magnitude of the on-axis axial displacement of the myocardium in the focus of an ARF is tracked in several studies [60–62], called ARF imaging (ARFI). This results in a more qualitative measure, as tissue displacements are expected to be inversely related to tissue stiffness (Equation 1.3) while the exact force applied is unknown. Nonetheless, recently a method has been proposed to calibrate the ARFI displacements throughout the cardiac cycle using SW propagation speed values measured in diastole [62].

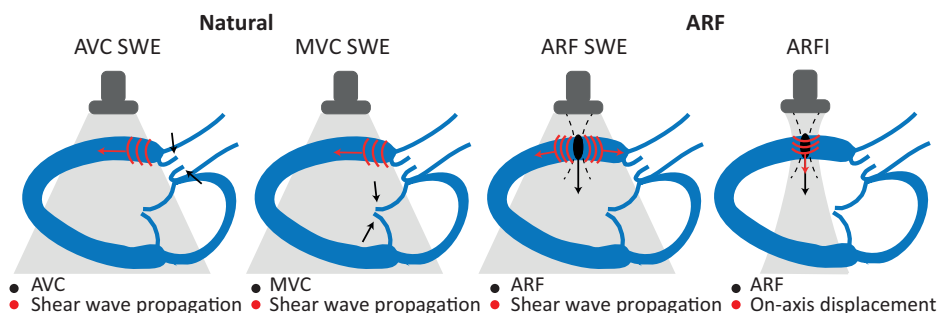


Figure 1.6: Schematic overview of the natural and ARF-based SWE and ARFI methods. In cardiac SWE techniques, the propagation speed of vibrations propagating over the myocardium is measured, as these speeds are related to the stiffness of the myocardium. In ARFI, the on-axis axial displacement of the myocardium as a response to an ARF is measured, resulting in a more qualitative measure.

The potential of natural and ARF-based SWE and ARFI has not only been shown in a research context, but also in several clinical studies. Higher propagation speeds were measured in hypertrophic cardiomyopathy patients than in healthy volunteers, using ARF-induced SWs at end-diastole [63] and natural SWs after AVC [39]. Also, higher propagation speeds were found in cardiac amyloidosis patients when analyzing natural SWs after AVC and MVC [40]. Furthermore, a correlation was found between the SW propagation speed after MVC in hypertensive heart disease patients with myocardial remodeling [41]. For the ARFI-technique, no clinical studies have been published yet. Despite the promising clinical results of both natural and ARF-based SWE, the different methods have their advantages and disadvantages. The higher tissue velocity amplitudes of natural SWs compared to ARF (~40 mm/s [64] vs ~10 mm/s [55]) likely lead to higher SNR, which forms an advantage of using these natural SWs. Furthermore, since the ultrasonic scanner does not need to induce high-energy ARF pushes, natural SW elastography could be easier implemented in current clinical practice. On the other hand, the practitioner has more freedom when using an ARF, since the SW characteristics can be adjusted by changing the ARF parameters and since an ARF can be applied at any moment in the cardiac cycle, while natural SWs only occur at the specific moments of valve closure. Nevertheless, it is challenging to induce SWs externally in a closed-chest transthoracic setting while meeting acoustic safety criteria, and to subsequently track their propagation. This is especially the case for the relatively fast-propagating small-amplitude SWs in the systole, as well as for obese patients [65]. Main advantage of ARFI is that a focused ultrasonic beam, instead of diverging waves, is used to track the on-axis displacements. This leads to higher SNR compared to SWE. Nevertheless, a feasibility rate of only 41% for ARFI applied in healthy volunteers throughout the entire cardiac cycle has been recently reported [60].

Although the potential of cardiac SWE has been shown in several studies, the development of ARF-based cardiac SWE and ARFI techniques are still at an early stage, and the interpretation of the natural SWs after valve closure remains unclear. Several factors could affect SW propagation speed measurements. First, the exact timing of valve closure within the cardiac cycle determines the instantaneous SW propagation speed measured; and it is yet unsure in what extent passive myocardial stiffness, and active contraction and relaxation is measured at the moment of valve closure. Second, also loading conditions could affect the SW propagation speeds measured, via for example hyperelasticity or the Frank-Starling mechanism. Third, since it is uncertain what wave modes are induced after valve closure, it is unknown what the exact effect is of the echocardiographic view on the SW propagation speeds assessed. Furthermore, the anisotropic fiber orientation of the IVS has been shown to affect SW measurements [55, 63, 66, 67]. Fourth, since the thickness of the IVS is small compared to the wavelengths of the SWs, wave distortion could be expected in the IVS, caused by frequency dispersion, resulting in so-called guided wave modes [28, 68–72]. Guided waves have been used to describe the SWs externally induced by an ARF [70, 73], but little is known about the exact wave modes induced after valve closure [43, 64].

1.8. THIS THESIS

The clinical aim of this thesis is to develop a non-invasive method that can directly assess myocardial stiffness, and can therefore be used for the early assessment of myocardial stiffness in people at risk of developing heart failure and for the diagnosis of underlying pathophysiologies in HFpEF patients. Our hypothesis is that SW propagation speeds are a good measure of myocardial stiffness. The objective of this thesis is to determine which factors are important for the accurate measurement and the interpretation of natural SWs after valve closure with respect to the assessment of myocardial stiffness.

1.8.1. Outline

Since diffuse natural vibrations are expected in the heart, potentially caused by breathing and flow, we study in **Chapter 2** whether a spatial-temporal correlation technique can be applied in a thin plate phantom – mimicking the myocardium – to assess the propagation speeds of such diffuse vibrations.

Chapter 3 – 6 focus on the accuracy of natural SW propagation speed measurements after valve closure. First, in **Chapter 3**, the variability of SW propagation speeds after aortic valve closure over the depth of the IVS in open-chest pigs is studied. Then, in **Chapter 4**, we assess the reproducibility of the SWs after aortic and mitral valve closure in healthy volunteers. The reproducibility with respect to different acquisitions, observers, measurement days and systems is studied. In **Chapter 5**, we compare measurements of the natural SWs after aortic valve closure in a parasternal long-axis and apical 4-chamber view in healthy volunteers. Since the

myocardial stiffness is expected to change during the propagation of the SWs after aortic valve closure (relaxation) and mitral valve closure (contraction), we performed a fundamental study on the effect of changing stiffness on wave propagation in **Chapter 6**, using a mechanical setup and finite difference simulations.

Chapter 7 – 8 focus on the comparison of natural SWs after valve closure with SWs externally induced by an ARF throughout the cardiac cycle. In **Chapter 7**, we compare these SWs within individual objects and heartbeats in open-chest pigs. In **Chapter 8**, this comparison is extended to a closed-chest situation and additionally the effect of different loading conditions on both methods is investigated.

Chapter 9 focusses on an alternative to cardiac SWE by assessing left-ventricular flow patterns with high-frame-rate echocardiography that may reveal early signs of cardiac dysfunction. This chapter shows that high-frame-rate echo-particle image velocimetry can be used to assess the high velocity diastolic blood flow patterns in 2D in a heart failure patient.

Chapter 10 discusses the overall results of this thesis and the clinical perspective and future research for cardiac SWE.

2

Diffuse Shear Wave Elastography in a Thin Plate Phantom



Lana B.H. Keijzer

Alberico Sabbadini

Johan G. Bosch

Martin D. Verweij

Antonius F.W. van der Steen

Nico de Jong

Hendrik J. Vos

Based on:

"Diffuse Shear Wave Elastography in a Thin Plate Phantom", *IEEE International Ultrasonics Symposium*, 2017 [74].

Abstract

Abnormal biomechanical properties of the myocardium, such as increased passive stiffness, prevent the heart of patients with diastolic heart failure to completely relax during diastole. Therefore, non-invasively measuring the stiffness is of importance. In this study, we used shear wave propagation speeds as a measure of stiffness of a thin plate phantom. We tested the applicability of a spatio-temporal correlation technique to determine these propagation speeds of diffuse fields in a thin plate. The obtained speeds were similar to the results found with direct shear wave measurements. We also show that propagation speeds are overestimated in non-completely diffuse wave fields with out-of-plane propagation.

2.1. INTRODUCTION

One of the most prevalent causes of death is heart failure. Left ventricular (LV) diastolic heart failure currently accounts for more than 50% of all heart failure. The abnormal biomechanical properties of the myocardium, such as increased passive stiffness, prevent the heart to completely relax during diastole [15]. Therefore, early recognition of changing passive myocardial stiffness is important to prevent further development of heart failure, e.g. by changing the patients' lifestyle.

Shear wave elastography can be used for non-invasive stiffness measurements. Different shear wave techniques have been developed, either using magnetic resonance or ultrasound imaging to detect these waves. Magnetic resonance imaging (MRI) has the advantage of making 3D images and measuring the tissue velocity in 3D, which is in particular valuable for the wave propagation in the complex heart geometry [30]. However, MRI is expensive, uncomfortable and slow.

Many studies have focused on ultrasonic shear wave elastography. Shear waves (SWs) can be generated by external sources such as drums or an acoustic radiation force (ARF), or by natural sources such as the closure of the valves [43, 44, 64]. Although the potential of ARF is shown in animal studies [54, 66, 75], the generation and detection of SWs through the human chest wall remains challenging. Only during end-diastole the myocardium is fully relaxed, which is required to measure the passive mechanical properties of the myocardium. Since valve closure is not present during this stage of the heart cycle, other sources of shear waves may be exploited.

It is expected that diffuse sources like breathing and flow noise are present during the entire heart cycle. SW propagation speeds in diffuse wave fields can be analyzed by using a spatio-temporal correlation technique. This technique has been applied to bulk omnidirectional SWs [76, 77] and surface waves. However, since the myocardium is relatively thin, Lamb wave phenomena including dispersion could be expected. Furthermore, SWs will not propagate omnidirectionally, but parallel to the surface. In this study we tested the applicability of the diffuse wave technique in a polyvinyl alcohol (PVA) thin plate phantom, and compared it to in-plane SW measurements and a mechanically measured shear modulus.

2.2. MATERIALS AND METHODS

2.2.1. Phantom

To mimic *in vivo* geometry conditions, a thin plate phantom with a thickness of around 10 mm was used. Although the myocardium mainly consists of muscle fibers arranged in different layers with changing orientation through thickness [66], the phantom was made homogeneous and isotropic for simplicity reasons. The phantom was prepared by freeze-thawing 10% polyvinyl alcohol powder, 1% silicon carbide powder (50% SiC K-800, MTN-Giethoorn, NL, 50% SiC K-400 Cats Hoogvliet, NL), 20% cooling liquid (Koelvloeistof Basic Safe, Halfords, NL) and 69% distilled water.

2.2.2. Measurement Set-up

The phantom was horizontally submerged in a water tank. IQ data was acquired with an L7-4 probe connected to a Verasonics Vantage research scanner (Verasonics, Kirkland, WA). Different sources were used to induce SWs in the phantom. First, an ultrasound transducer was used to induce direct SWs via ARF. The SWs were tracked by the same probe. Initial tests showed that anti-symmetric zero order Lamb waves were induced during ARF measurements, while mixed types (Rayleigh and Lamb) were present during measurements using contact forces to excite shear waves. To induce body forces while tapping on the phantom instead, four metal rods were glued through the entire thickness, as described by Nenadic *et al.* [71]. As a second measurement method, called rods tapping (RT), screws were used to tap on these metal rods on both sides of the phantom to create a diffuse field. To prevent a coupling effect between the rods and the bottom of the water tank, a dishcloth underneath the phantom was used as damping material. Finally, as a third method, a metal rod attached to an electromagnet functioned as mechanical push (MP) on top of the phantom.

2.2.3. Data Analysis

By using a one-lag autocorrelation technique, axial tissue velocities were obtained [44]. To reduce noise, a spatial smoothing filter was applied by convolving a Gaussian kernel with a size of 2.4 mm in axial and lateral direction with the individual frames. A 6th-order Butterworth bandpass filter from 100 – 250 Hz was applied to the IQ data in the slow-time direction.

Propagation Speeds

For the ARF measurements, the slope of a direct single wave pattern in the velocity panel was determined to obtain the propagation speed. For the RT measurements, multiple waves were coming from both sides of the probe, interacting with each other. A direct wave pattern could not be distinguished and therefore a spatial-temporal correlation technique was applied [76–79]. By correlating the temporal velocity signal of individual pixels with the signals of surrounding pixels, a cross-correlation panel for each individual pixel was obtained. By determining the slopes of the wave pattern in these correlation panels, local propagation speeds were estimated for individual pixels [79]. For this cross-correlation technique, the frequency components with highest intensity dominate. To improve the use of information in the wave field spectrum, equal weight can be given to all frequency components. This method is called phase correlation [78]. These spatial-temporal correlation techniques were also applied to MP measurements.

For the velocity panels, the axial tissue velocities of ten horizontal image lines, located in the upper region of the phantom, were averaged before further analysis of the data. When the spatial-temporal correlation technique was applied, results of ten lines were averaged after the analysis of each individual line. Subsequently, for each

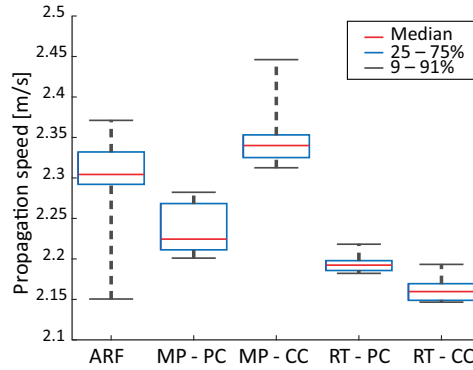


Figure 2.1: Propagation speeds obtained for the ARF, MP and RT measurements. For the ARF measurements, a Radon transform was applied directly to the velocity panels. For the other measurements, the phase- and cross-correlation panels (PC and CC) were used. Median values are based on ten measurements.

type of measurement, the median or average (depending on the underlying data distribution) of ten individual measurements was computed.

Radon transforms were used to determine the slope of the wave patterns in the velocity and correlation panels. To avoid a bias caused by the square image domain, the panels were first resampled to have an equal number of pixels in both directions. Thereafter, the Radon transform result was normalized by the Radon transform of an image of equal size with only unit values [64].

Phase Speeds

By using the 2D-Fourier spectrum of the velocity or correlation panel, and by converting the wavenumbers into phase speeds, the dispersion curves were obtained. These curves were compared with the theoretical dispersion curves of an anti-symmetric Lamb and Rayleigh wave for a plate submerged in fluid [71].

Mechanical Indentation Test

For comparison, the shear modulus of the phantom was measured mechanically via an indentation test, with an indentation rate of 0.2 mm/s and a total indentation of 2.5 mm. The results of ten measurements were averaged.

2.3. RESULTS

2.3.1. Propagation Speeds

To prevent overestimation of the propagation speeds due to misalignment [64], two rods aligned with the probe were used for the RT measurements. Propagation speeds between 2.1 and 2.4 m/s were found for a frequency band of 100 to 250 Hz, see Figure 2.1. By using the ratio between the Rayleigh wave number k_R and the shear wave number k_S ; $k_R/k_S = 1.1915$ [72], the propagation speeds were converted to a shear

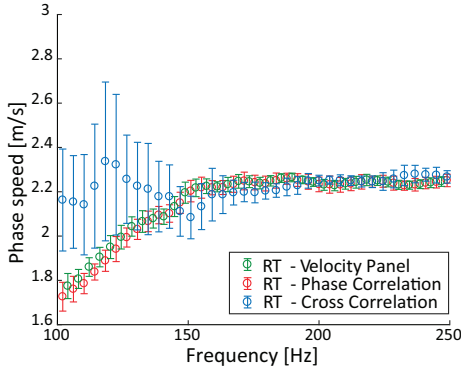


Figure 2.2: Dispersion curves obtained from the velocity, phase-correlation and cross-correlation panels for the RT measurements with two rods aligned with the probe. Median values of ten measurements with 1σ range are depicted.

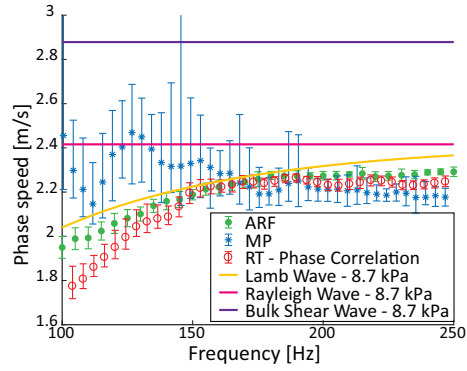


Figure 2.3: Comparison of the dispersion curves obtained from the velocity panels of the ARF and MP and the phase-correlation panel of the RT measurements. Mean values and standard deviations are shown for the ARF measurements. For the MP and RT measurements, median values of ten measurements with 1σ range are depicted.

modulus μ . Since Lamb and Rayleigh dispersion curves converge for higher frequencies, this ratio could be used by applying the following equation:

$$\mu = \rho \cdot (1.1915 \cdot c)^2, \quad (2.1)$$

with ρ the density of the phantom in $[\text{kg}/\text{m}^3]$ and c the obtained propagation speed in $[\text{m}/\text{s}]$. A value of $1050 \text{ kg}/\text{m}^3$ was used for the density of the phantom. Shear moduli of 7.9, 7.4, 8.2, 7.2 and 7.0 kPa were obtained for the ARF, MP with phase correlation, MP with cross correlation, RT with phase correlation and RT with cross correlation measurements respectively. The mechanical indentation test led to an average shear modulus of $8.7 \pm 0.2 \text{ kPa}$.

2.3.2. Phase Speeds

Dispersion curves were obtained from the phase and cross correlation panels, as well as directly from the velocity panel. The results are shown in Figure 2.2. The dispersion curves obtained from the phase correlation panel coincide with the curves obtained from the velocity panel. Cross correlation led to larger uncertainties, especially for the lower frequencies.

The dispersion curves of the ARF, MP and RT measurements are compared in Figure 2.3. The mechanically measured shear modulus of $8.7 \pm 0.2 \text{ kPa}$ was used for computing theoretical dispersion curves of Rayleigh and anti-symmetric Lamb waves in a plate submerged in fluid [72]. These theoretical dispersion curves are also shown in Figure 2.3. The dispersion curves of the ARF and RT measurements follow a theoretical anti-symmetric Lamb wave, while the curves of MP measurements show similarities with a theoretical Rayleigh wave. However, the measured phase speeds are in general lower than the theoretical speeds.

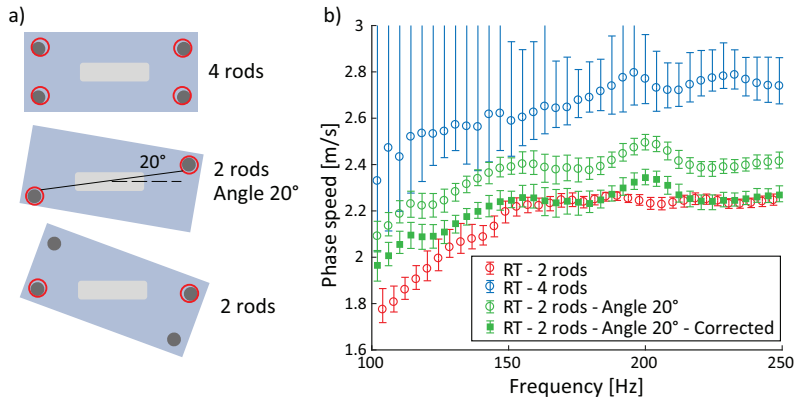


Figure 2.4: (a) Overview of the three different types of RT measurements. Two rods that were perfectly aligned with the probe, two rods that made an angle of 20° with the probe, or four rods were used. (b) Differences in dispersion curves for three different RT measurements. The measurements with an angle of 20° between the rods and probe were also corrected with a factor $\cos(20)$. Median values of ten measurements with 1σ range are depicted.

2.3.3. Out-of-Plane Propagation

To investigate the effect of an incompletely diffuse field on the measured propagation speeds, three types of RT measurements were performed. Two rods were perfectly aligned with the probe scan plane, two rods were placed under an angle of 20° with the center of the probe scan plane, and four rods were placed at the corners of the phantom, see Figure 2.4 a. The dispersion curves are depicted in Figure 2.4 b. The propagation speeds obtained for measurements with two rods under an angle with the probe, were also corrected with a factor of $\cos(\theta)$ [64].

2.4. DISCUSSION

Figure 2.1 shows similar propagation speeds for the ARF, the MP and RT measurements. This illustrates that the spatial-temporal correlation technique is applicable to Lamb waves in a slab. The propagation speeds obtained with cross correlation show a larger deviation from the ARF measurements and have larger uncertainties than the results obtained with phase correlation. All obtained propagation speeds are converted to shear moduli via Equation 2.1. These shear moduli are slightly lower than the mechanically measured shear modulus. It should be noted that the Rayleigh wave speed is needed as input for Equation 2.1, while we measured the propagation speed of a frequency band from 100 to 250 Hz. Since dispersion occurs in this frequency band, the true Rayleigh wave speeds were not obtained. Furthermore, the metal rods might have influenced the outcome of the mechanical test.

The results show, that for a diffuse field, similar dispersion curves can be obtained directly from the velocity panel and from the phase-correlation panel. Therefore, in a situation with a homogeneous sample, the spatial-temporal correlation technique can be redundant for determining phase speeds. However, for inhomogeneous media (like the myocardium) obtaining dispersion curves via a 2D Fourier spectrum becomes less accurate. The advantage of the spatial-temporal correlation technique is that more local propagation speeds are obtained since only spatial data of a few wavelengths of the selected frequency band is needed for determining propagation speeds. To obtain even more local values, instead of estimating the slope of the correlation panel, the spatial focus can be matched to a theoretical profile to estimate the propagation speed [77].

The results show overestimated propagation speeds for the measurements where the probe was not aligned with the sources of the SWs. With a completely diffuse field, this error is expected to cancel out since, for each SW, there is a SW coming from the opposite direction. However, for *in vivo* situations it will be difficult to realize a completely diffuse field. Therefore, propagation speeds will be overestimated. Compared to measurements like ARE, with inherently no out-of-plane propagation, this forms a challenge for using the spatial-temporal correlation technique, assuming diffuse fields. A potential way to deal with partly non-diffuse fields could be to make use of 3D recordings. When SWs are coming from mainly one direction, as is the case after valve closure, the direction in which the SWs are tracked is expected to influence the apparent propagation speed. Consequently, valves should be kept in the image plane, which is shown to be feasible in preliminary *in vivo* tests.

2.5. CONCLUSION

This study showed that in a plate situation with Lamb waves, a spatial-temporal correlation technique can be applied to obtain propagation speeds of diffuse fields. In addition, it is shown that for partly non-diffuse fields, out-of-plane propagation leads to overestimation. For *in vivo* measurements, it could be complicated to realize a completely diffuse field and to circumvent out-of-plane propagation. 3D recordings and / or cautious 2D scanning might be required to overcome this problem.

Acknowledgements

We thank the BioMechanical Engineering Lab at the Delft University of Technology for facilitating the mechanical indentation tests. This work is part of the STW/TTW – Dutch Heart Foundation partnership program ‘Earlier recognition of cardiovascular diseases’ with project number 14740, which is (partly) financed by the Netherlands Organization for Scientific Research (NWO).

3

Intra-Scan Variability of Natural Shear Wave Measurements



Lana B.H. Keijzer
Johan G. Bosch
Martin D. Verweij
Nico de Jong
Hendrik J. Vos

Based on:

"Intra-Scan Variability of Natural Shear Wave Measurements", *IEEE International Ultrasonics Symposium*, 2018 [80].

Abstract

Shear wave elastography can potentially be used to diagnose an increased stiffness of the myocardium of patients with diastolic heart failure. This study focusses on the shear waves induced after aortic valve closure in the interventricular septum. The propagation speed of these shear waves is expected to be related to the stiffness of the myocardium and is determined along a manually-drawn M-line over the myocardium. In this study the effect of M-line location and angle is systematically investigated. In vitro, measurements were performed using a PVA slab phantom, and in vivo using three pigs with open chest. We found large global differences in propagation speed for different M-line locations over the interventricular septum, possibly having physiological causes. To avoid these physiological effects, we averaged the propagation speed of 10 M-lines manually drawn at the endocardial side of the interventricular septum. A local median of intra-scan interquartile range of about 0.6 m/s was found.

3.1. INTRODUCTION

About 50% of all heart failure patients has a preserved ejection fraction (HFpEF) [81]. Diastolic dysfunction is expected to be an important cause of this type of heart disease, where a decreased active relaxation and/or increased passive stiffness prevent the heart to completely relax [15]. At present, there is no accurate clinical method for non-invasive stiffness measurements of the myocardium. However, early diagnosis of increased stiffness is important for preventing further development of heart diseases and could likely help in accommodating generalized and/or personalized treatment [82].

Shear waves (SWs) can potentially be used to perform noninvasive stiffness measurements of the myocardium [83], called shear wave elastography. Several studies report on using ultrasound for shear wave elastography. External sources such as a mechanical shaker or acoustic radiation force, or natural sources like the closure of the valves induce SWs in animal and human studies. This study focusses on the natural SWs induced in the interventricular septum (IVS) by the closure of the aortic valve (AVC), which thus do not require an external source. Furthermore, it was found that shear waves induced by AVC have larger amplitudes compared to the waves induced by mitral valve closure [64].

The propagation speed of SWs is linked to the shear and Young's modulus of the medium in which the SWs propagate. To determine these propagation speeds, SWs are measured along a manually-drawn line on the IVS (anatomical M-line) in long-axis parasternal high frame rate recordings. Since selecting the M-line is a manual process, we studied the influence of M-line location and angle on the measured SW propagation speed. We performed *in vitro* and *in vivo* measurements. With the *in vitro* measurements, we systematically investigated how the measured propagation speed is affected when the M-line makes an angle with the SW propagation direction. For the *in vivo* measurements, we tested the intra-scan variability in anticipation of clinical diagnostic application.

3.2. MATERIALS AND METHODS

3.2.1. Measurement Set-ups

In Vitro Measurements

For the *in vitro* measurements, we used a custom polyvinyl alcohol (PVA) slab phantom with a thickness of around 10 mm, horizontally submerged in a water tank. The phantom was prepared by freeze-thawing 10% polyvinyl alcohol powder, 1% silicon carbide powder (50% SiC K-800, MTN-Giethoorn, NL, 50% SiC K-400 Cats Hoogvliet, NL), 20% cooling liquid (Koelvloeistof Basic Safe, Halfords, NL) and 69% distilled water. We used an electromagnet to tap with a metal rod on top of the phantom to induce SWs. High frame rate images were recorded at a PRF of 1000 Hz with an L7-4 probe connected to a Vantage-256 research scanner (Verasonics, Kirkland, WA).

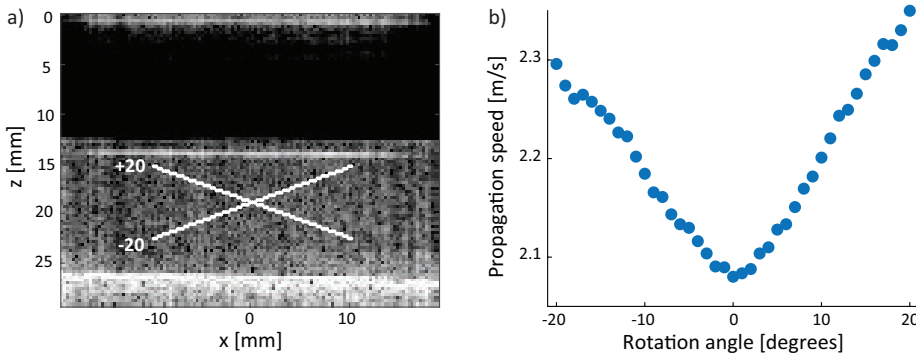


Figure 3.1: *In vitro* measurements of a slab phantom. (a) A horizontal M-line was rotated around its center from -20 to +20 degrees. (b) Propagation speeds obtained for the M-lines depicted in (a). The obtained propagation speed was found to change with rotation angle.

In Vivo Measurements

For the *in vivo* measurements, we scanned three Göttingen minipigs (age of ~ 1.5 years) with open chest that were used in a larger study cohort of diabetic animals and controls. The Erasmus MC Animal Experiments committee (DEC 109-12-22) approved the study and the experiments agreed with the NIH Guide for the Care and Use of Laboratory Animals. An intramuscular injection of Zoletil (Tiletamine/Zolazepam; 5 mg/kg) and Xylazine (2.25 mg/kg) was used for sedation. Anesthesia was thereafter induced using intravenous infusion of pentobarbital (15 mg/kg/h). During the measurements, the animals were mechanically ventilated while lying on their back after full sternotomy. To stabilize the contact between probe and heart, the pericardium stayed closed. High frame rate plane-wave images (5 MHz pulses) were recorded in long-axis parasternal view with a PRF of 1000 Hz with an L15-4 probe connected to an Aixplorer system (Supersonic Imagine, Aix-en-Provence, France).

3.2.2. Data Analysis

A one-lag autocorrelation method was applied to the analytic data to obtain axial particle velocities [44]. Propagation speeds were computed along manually-drawn M-lines. The particle velocities along an M-line for subsequent frames were combined in a velocity panel. A Radon transform was applied to these velocity panels to determine the propagation speed [64]. Before applying the Radon transform, the velocity panels were first resampled to have a square pixel size and the Radon domain was normalized [64] for higher accuracy.

In Vitro Data

To reduce noise, a Gaussian spatial smoothing filter with a kernel size of 2.4 mm in both directions was applied to the individual autocorrelation frames before

calculating the phase during the one-lag autocorrelation technique as described in [44]. When the M-line makes an angle with the wave propagation direction, it is expected that propagation speeds are overestimated due to an apparent larger wavelength, called out-of-line propagation. Therefore, to test the effect of out-of-line propagation systematically, a horizontal M-line through the middle thickness of the phantom was rotated around its center from -20 to +20 degrees, see Figure 3.1 a.

In Vivo Data

The autocorrelation frames were convolved with a spatial smoothing filter with a kernel size of 0.77 x 1.00 mm in axial and lateral direction to reduce noise. Furthermore, a fourth order Butterworth bandpass filter from 40 – 100 Hz was applied to the particle velocity data in slow-time direction. Two tests were performed on the *in vivo* data. In test 1, the effect of global M-line location and angle over the thickness of the IVS was investigated. Three straight M-lines were manually drawn over the thickness of the IVS, roughly following the curvature of the IVS. Subsequently, the M-lines were automatically rotated around their basal-ends with steps of 1 degree. In test 2, the local differences in propagation speed were investigated as follows. For every recording, 10 M-lines were drawn at the left ventricle (LV) side of the IVS to test intra-scan reproducibility. Hereby the aim was not to draw the M-lines at identical locations, but to represent variations in M-line location that could occur when different observers would repeat the analysis. We chose for the LV side in test 2 since test 1 suggested higher SNRs in the particle velocities. In test 2, different methods were used and compared to track the propagation patterns of the SWs. The maximum as well as the minimum intensity was selected in the Radon domain of the velocity panels, in order to track the maximal particle velocities away and in the direction of the probe respectively. Furthermore, the time derivative of the velocity panels was computed to obtain acceleration panels and the propagation speed was determined for these acceleration panels as well. By using acceleration panels global cardiac motion is assumed to be more suppressed [64] and the maximal and minimal particle acceleration instead of particle velocity values can be tracked. Figure 3.3. shows an example of the 10 M-lines drawn at the LV side of the IVS for one recording and shows the velocity and acceleration panel corresponding to one M-line.

3.3. RESULTS

3.3.1. *In Vitro* Results

Propagation speeds were found to increase with absolute rotation angle of the M-line, see Figure 3.1. For the horizontal M-line a propagation speed of 2.08 m/s was found, while propagation speeds of 2.30 m/s and 2.35 m/s were found for a rotation of -20 and +20 degrees respectively. Theoretically in case of a plane shear wave, a bias of $1/\cos(\theta)$ is expected. This means that for a true propagation speed of 2.08 m/s, a propagation speed of 2.21 m/s would be obtained after rotating the M-line with 20 degrees.

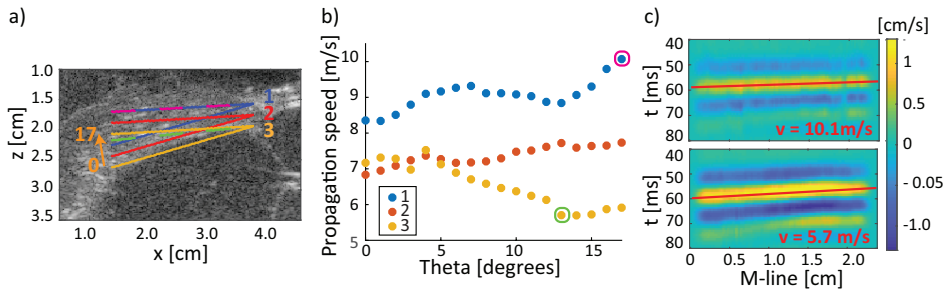


Figure 3.2: Test 1, *in vivo* measurements. (a) Overview of the M-lines drawn on the IVS for one measurement. The dashed lines depict the M-lines corresponding to the highest (pink) and lowest (green) propagation speed found. (b) Propagation speeds found for the M-lines depicted in (a) for a frequency band of 40 – 100Hz. (c) M-panels with highest and lowest propagation speeds. Positive particle velocity values correspond to axial particle motion away from the probe.

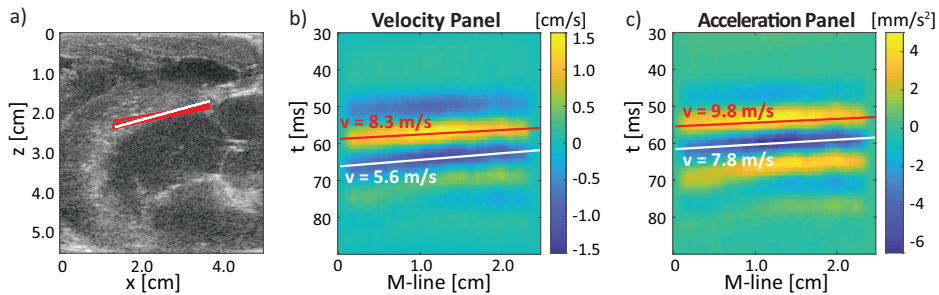


Figure 3.3: Test 2, *in vivo* measurements. For every measurement, 10 M-lines were drawn at the LV side of the IVS (a). Velocity (b) and acceleration (c) panel of the white M-line shown in (a). Different propagation speeds were obtained when selecting the maximum (red lines) or minimum (white lines) intensity in the Radon domain of both panels. Positive particle velocity values correspond to axial particle motion away from the probe.

3.3.2. In Vivo Results

In test 1, large differences were found for the different M-line locations over the thickness of the IVS. The differences in propagation speed between the M-lines varied strongly between different recordings as well. For the measurement shown in Figure 3.2, propagation speeds between 5.7 m/s and 10.1 m/s were found. In general, larger particle-velocity amplitudes, suggesting higher SNRs in the particle velocities, and lower propagation speeds were found on the LV side of the IVS. In test 2, the measured propagation speeds differed when selecting the maximum or minimum intensity in the Radon domain of the velocity and acceleration panels. Higher propagation speeds were found when tracking a rim of the SW earlier in time, see Figures 3.3 and 3.4. Median values of 6.2 m/s (inter-quartile range (IQR) 5.7 – 6.9 m/s) and 5.1 m/s (IQR 4.7 – 5.6 m/s) were found when selecting the maximum and minimum intensity respectively in the velocity panels, see Table 3.1. This difference was found to be significant ($p < 0.001$, Wilcoxon signed-rank test). Also different propagation speeds

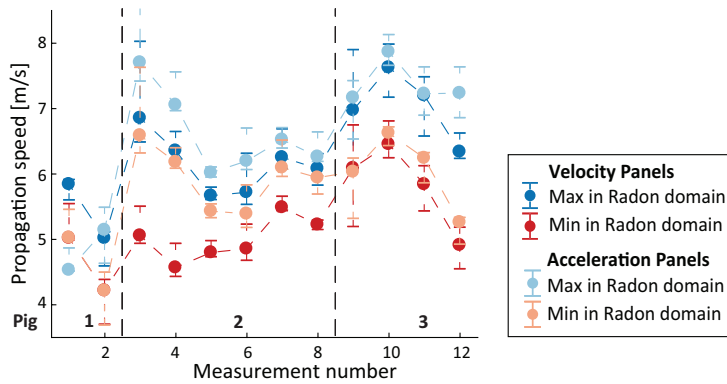


Figure 3.4: Test 2, *in vivo* measurements. Median and IQR values for the propagation speeds along 10 M-lines in each individual measurement. Particle velocity panels as well as particle acceleration panels were used to compute propagation speeds. In both panel types the maximum and minimum intensity in the Radon domain was selected.

Table 3.1: Test 2, *in vivo* measurements. Overview of the statistical characteristics of the propagation speed values obtained for the different methods used to track the propagation patterns of the SWS.

Method	Median propagation speed (IQR) [m/s]	Median of IQR (IQR) [m/s]
Velocity Panels		
Max in Radon domain	6.2 (5.7 – 6.9)	0.56 (0.41 – 0.86)
Min in Radon domain	5.1 (4.7 – 5.6)	0.56 (0.38 – 0.66)
Acceleration Panels		
Max in Radon domain	6.7 (6.0 – 7.4)	0.61 (0.40 – 0.82)
Min in Radon domain	5.8 (5.3 – 6.3)	0.46 (0.30 – 0.73)

were obtained for the maximum (median of 6.7 m/s, IQR 6.0 – 7.4 m/s) and minimum (median of 5.8 m/s, IQR 5.3 – 6.3 m/s) intensities in the acceleration panels ($p=0.0015$, Wilcoxon signed-rank test). The median of the IQRs was used as a measure of the intra-scan variability in Table 3.1. The median IQR was not found to be statistical different between the different methods used to determine the propagation speeds.

3.4. DISCUSSION

For the *in vitro* study, Figure 3.1 shows a bias in propagation speed up to 13% due to out-of-line propagation when rotating the M-line with $\theta = 20$ degrees. This bias does not completely reconcile with the expected bias of 6% in case of a perfect plane wave.

For test 1 of the *in vivo* data, the differences found in propagation speed were in multiple recordings much larger than the 13% found in the *in vitro* study. Therefore, we expect that these differences are not only caused by out-of-line propagation, but

have physiological causes. For example, the IVS is expected to be inhomogeneous and thus stiffness variations over the thickness might be present. Furthermore, SWs were found to propagate faster along the fiber orientation than perpendicular to the fiber orientation [84], and fiber orientation in the IVS might differ over the thickness, as was found for the LV free wall [66].

For test 2, the M-lines were all located at the LV side of the IVS. Therefore, the variations found in test 2 are not expected to have physiological causes, but to be caused by measurement inaccuracy. Consequently, the precision can be improved by averaging over multiple M-lines drawn at the same side of the IVS. The SWs were tracked along M-lines with a maximum length of about 2.5 cm. A SW with a center frequency of for example 70 Hz and a propagation speed of 6 m/s, has a wavelength of 8.6 cm. Therefore only a fraction of the wavelength could be tracked, causing measurement inaccuracy. This inaccuracy will increase with increasing wavelength and thus with increasing propagation speed. Whether a median IQR of about 0.6 m/s is low enough for diagnostic application should be investigated in further research. Furthermore, it should be noted that the intra-scan variability measured in this study could be different for other animals or human.

The comparison of the different methods to track the propagation pattern of the SWs shows no significant differences in intra-scan variability. Yet, a higher propagation speed was found when tracking a rim of the SW earlier in time, see Figure 3.3. Since the myocardium is relaxing during the moment of AVC, a decrease in SW propagation speed is expected over time. This change in SW propagation speed during the heart cycle was also measured in open chest sheep by using an acoustic radiation force [55]. However, this could only partly explain the measured decrease in propagation speed. Dispersion effects could be present as well. The IVS has a thickness (8 – 15 mm) smaller than the wavelength of the SWs and therefore dispersive guided waves are expected. This is supported by several authors measuring dispersion after AVC [43, 64]. By using the Radon transform, the propagation speed of a rim of the SW is measured. However, for dispersive waves, it is more accurate to measure phase speeds instead [85]. Nonetheless, dispersion analysis was not included in this study due to a limited spatial domain.

This study shows that M-line location and angle as well as the method used to determine SW propagation speeds strongly affect the results. Nonetheless, no difference in intra-scan variability was found among the different methods included. We think that for comparing different studies and for clinical diagnostic application, it is important to decide on a more standardized method.

3.5. CONCLUSIONS

This study shows that the M-line location and angle on the IVS influence the measured propagation speed of the SWs induced by AVC in open-chest pig data. In addition, it shows that results are affected by the method used to track the propagation pattern of the SWs, but that the intra-scan variability, as defined by the median inter-quartile

range, is, independent of the method. For comparing different studies and for clinical diagnostic applications, a more standardized method of shear wave tracking is needed.

Acknowledgements

We thank the Experimental Cardiology group at the Erasmus MC, Rotterdam, the Netherlands for facilitating the animal experiments. We also thank J. Bercoff, SuperSonic Imagine, for providing the Aixplorer system. This work is part of the STW/TTW – Dutch Heart Foundation partnership program 'Earlier recognition of cardiovascular diseases' with project number 14740, which is (partly) financed by the Netherlands Organization for Scientific Research (NWO).

4

Reproducibility of Natural Shear Wave Elastography Measurements



Lana B.H. Keijzer

Mihai Strachinaru

Daniel J. Bowen

Marcel L. Geleijnse

Antonius F.W. van der Steen

Johan G. Bosch

Nico de Jong

Hendrik J. Vos

Based on:

"Reproducibility of Natural Shear Wave Elastography Measurements", *Ultrasound in Medicine & Biology* **45**(12), 2019 [86].

Abstract

For the quantification of myocardial function, myocardial stiffness can potentially be measured noninvasively using shear wave elastography. Clinical diagnosis requires high precision. In 10 healthy volunteers, we studied the reproducibility of the measurement of propagation speeds of shear waves induced after aortic and mitral valve closure (AVC, MVC). Inter-scan was slightly higher but in similar ranges as intra-scan variability (AVC: 0.67 m/s (interquartile range [IQR]: 0.40 – 0.86 m/s) versus 0.38 m/s (IQR: 0.26 – 0.68 m/s), MVC: 0.61 m/s (IQR: 0.26 – 0.94 m/s) versus 0.26 m/s (IQR: 0.15 – 0.46 m/s)). For AVC, the propagation speeds obtained on different day were not statistically different ($p = 0.13$). We observed different propagation speeds between 2 systems (AVC: 3.23 – 4.25 m/s [Zonare ZS3] versus 1.82 – 4.76 m/s [Philips iE33]), $p = 0.04$). No statistical difference was observed between observers (AVC: $p = 0.35$). Our results suggest that measurement inaccuracies dominate the variabilities measured among healthy volunteers. Therefore, measurement precision can be improved by averaging over multiple heartbeats.

4.1. INTRODUCTION

In developed countries, approximately 1% – 2% of the adult population has heart failure. The prevalence is even rising to >10% among people older than 70 years [2]. Currently, geometric volumes and non-invasive Doppler measurements of tissue and blood are used for the echocardiographic evaluation of cardiac myocardial function [10, 12]. Nonetheless, these parameters that for the most part measure the effects of myocardial function are load dependent [11]. No accurate method currently exists for non-invasive cardiac stiffness measurements. Measuring the stiffness of the myocardium likely provides more direct insights in the condition of the myocardium [11], as recently shown by Villemain *et al.* (2019) [63] in a group of volunteers and hypertrophic cardiomyopathy patients using shear wave elastography measurements (SWE). To distinguish the types of diastolic and systolic dysfunctions and to accommodate more personalized treatments, non-invasive stiffness measurements could be a valuable tool.

Several studies have shown the potential of shear waves (SWs) to be used for measuring the stiffness of the myocardium non-invasively [33, 34, 39, 40, 42, 63]. The propagation speed of these SWs is expected to be linked to Young's modulus of the myocardium.

Magnetic resonance and ultrasound imaging have been used in a variety of animal and human studies to perform SWE measurements. The advantage of using magnetic resonance imaging (MRI) is that the 3D displacement field of the SWs in the complex cardiac geometry can be measured [30]. However, MRI is expensive, uncomfortable and slow. Moreover, MRI cannot be used for patients with arrhythmia because of cardiac gating. For SWE using ultrasound imaging, several studies have used external sources, such as mechanical shakers [51–53] or acoustic radiation forces (ARF) [54–57, 63, 75, 87] to induce SWs. The SWs naturally occurring after aortic valve closure (AVC) or mitral valve closure (MVC) have been investigated as well [39, 42–44, 49, 64, 88]. An advantage of exploiting the SWs induced by valve closure is that these SWs were observed to have larger tissue velocity amplitudes (>40 mm/s) [64] than the SWs induced by an external acoustical force (>10 mm/s)[55], likely leading to higher signal-to-noise ratios. However, the low frequency content of natural SWs [42, 43, 64] compared with external sources [52, 55, 56], and thus the inherently larger wavelengths form a disadvantage of natural shear wave propagation speed measurements. Because the SWs can only be tracked over the limited length of a few centimeters of the interventricular septum (IVS), smaller fractions of the wavelength can be tracked for SWs with low frequencies, causing measurement inaccuracy. In addition, for 2D natural SW propagation speed measurements, the source of the SWs is not ensured to be in the plane with the field of view, as is the case for ARF-based measurements, and therefore out-of-plane propagation could also induce measurement inaccuracy [64]. These measurement inaccuracies should be minimized for clinical diagnoses where a high precision of the SW propagation speed measurements is needed.

Other than measurement inaccuracies, SW propagation speed measurements are expected to be affected by various phenomena. First, the myocardial stiffness measured depends on the intrinsic viscoelastic material characteristics of the myocardium, independent of loading conditions. Significant different propagation speeds have been measured after AVC and MVC for pathologic stiff myocardium as in hypertrophic cardiomyopathy [39] and amyloidosis patients [40] compared with healthy volunteers. Second, the moment in the cardiac cycle will determine to what extent passive myocardial stiffness and additional myocardial contractility are measured. This is opposite to the alternative method of using ARF to induce SWs, as the ARF push can be timed throughout the cardiac cycle and hence is able to capture the myocardium in a relaxed state. The variations in myocardial stiffness during the cardiac cycle have been measured in several studies [55, 62]. However, SWs induced by valve closure only occur at two stages of the cardiac cycle, during which the heart is not completely relaxed. Therefore, natural SW propagation speed measurements most likely measure a combination of passive myocardial stiffness and contractility, potentially providing information about diastolic and systolic function, albeit that the disentangling is a challenge. Third, because of the nonlinear stress-strain relationship of biologic materials [19], the filling state of the ventricle is still expected to influence SW propagation speed measurements, even when measured at end-diastole [11]. Furthermore, contractility is also known to be affected by pre-load via the Frank-Starling mechanism. Therefore, other than measurement inaccuracies, hemodynamic variations are also expected to affect reproducibility.

For the application of clinical diagnosis, knowledge on measurement reproducibility is needed to distinguish normal and pathologic myocardial function. This study tests the reproducibility of determining the propagation speed of natural SWs induced in the IVS after AVC and MVC in healthy volunteers. Studies have shown that propagation speeds after AVC can be determined *in vivo* by using a clinical ultrasound system using conventional or adapted tissue Doppler imaging (TDI) [43, 44, 89]. Other studies have demonstrated the feasibility of measuring the SWs induced by AVC and MVC in a single recording using diverging waves [40, 42, 64]. Slope-estimator, intra-observer, inter-observer and test-retest variabilities have been recently tested for natural SWs in healthy volunteers [42]. However, we have observed that anatomic M-line location on the IVS, along which the SWs are tracked, affects the measured propagation speed in pigs, causing intra-scan variability [80]. Furthermore, other than test-retest variabilities between measurements performed on different days, variabilities between subsequently performed measurements could have been present. In addition, Santos *et al.* (2019) [42] performed SW propagation speed measurements with only one (non-clinical) echographic scanning system, but inter-system variability should be limited for clinical diagnosis. Also, hemodynamic variations could have caused variabilities in SW propagation speed measurements. When patients undergo an echocardiographic exam, they may experience various levels of psychologic and/or physiologic stress, potentially changing loading conditions and thus affecting SW propagation speed measurements.

Table 4.1: Overview of the demographic characteristics of the study population. The characteristics are averaged over all volunteers during both scanning sessions.

Characteristics	Mean ± SD *	Range
Age [y]	29.8±6.2	24 – 45
Weight [kg]	67±9.5	55 – 90
Body length [m]	1.75±0.06	1.65±1.83
Body Mass Index (weight/body length [kg/m ²])	21.9±2.3	19.4±27.5
Heartrate in rest [bpm]	62±7	50 – 73
Systolic blood pressure in rest [mmHg]	106±13	90 – 138
Diastolic blood pressure in rest [mmHg]	62±9	50 – 81
Heartrate during handgrip test [bpm]	67±8	51 – 81
Systolic blood pressure during handgrip test [mmHg]	110±10	94 – 138
Diastolic blood pressure during handgrip test [mmHg]	67±9	52 – 85

* SD = standard deviation

To the best of our knowledge, our study is the first to simultaneously report on inter-system, test-retest, inter-scan, intra-scan and inter-observer variabilities of natural SW propagation speed measurements after AVC and MVC in healthy volunteers and to report on the effect of stress causing hemodynamic variations. To test inter-system variability, we directly compared the results obtained by using a clinical system in a conventional TDI mode (Philips) with a second clinical system with a customized high frame rate (HFR) mode, using a diverging-wave pulse-inversion transmission scheme (Zonare).

4.2. MATERIALS AND METHODS

4.2.1. Study Population

The study included 10 volunteers aged 24 – 45 years, 5 males and 5 females. Table 4.1 presents an overview of the demographic characteristics of the volunteers. The study was approved by the local medical ethics committee (Erasmus MC MEC-2014-611) and all volunteers provided informed consent. The following exclusion criteria were used: a history of cardiovascular disease, cardiovascular risk factors including hypertension (cutoff value of 140/90 mmHg), being pregnant or being morbidly obese (body mass index > 40 kg/m²).

4.2.2. Data Acquisition

An overview of the study design and the tested variabilities are presented in Figure 4.1. Measurements were performed with 2 echographic scanning systems. First, a clinical system programmed by the manufacturer to have a HFR imaging mode (Zonare ZS3, P4-1 C probe, Mindray Innovation Center, San Jose, CA, USA) was used. Live B-mode images with a low frame rate (LFR) were used to position the probe.

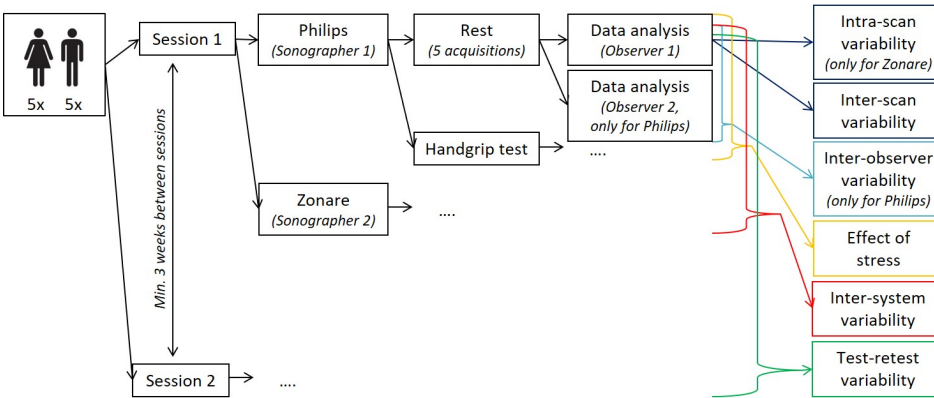


Figure 4.1: Schematic overview of the study design. The same measurements were performed during session 1 and session 2. Rest and handgrip test measurements were performed with the Zonare and the Philips system. Inter-observer variability was tested for the Philips system only, and intra-scan variability was only tested for the Zonare system.

Then a smaller box (approximately 5 x 7 cm) was selected within these LFR images for the HFR acquisition. During these recordings, the LFR images were frozen on the screen of the system and no live feedback was present. A diverging-wave pulse inversion transmission sequence was used for the HFR acquisition, and beamformed in-phase and quadrature components (IQ-based data) with a frame rate of 1000 frames/second during 1.2 s were saved for offline processing. In this way, at least a full cardiac cycle was measured for a minimum heartrate of 50 bpm. The acquisitions with this machine were carried out by a sonographer (D.J.B.). Second, acquisitions were performed by a cardiologist (M.S.) with a clinical echographic scanner in conventional TDI mode (Philips iE33, S5-1 probe, Philips, Bothell, WA, USA). To obtain maximum frame rates, a balance between opening angle and depth of TDI field was searched for, as described by Strachinaru *et al.* (2017) [89]. In this way frame rates from 490 – 570 frames/second were realized. Simultaneously a phonocardiogram (PCG) (Fukuda Denshi MA-300 HDS (V), Fukuda Denshi Co., Tokyo, Japan) was recorded, and the electrocardiographic signal was used as a trigger. All data during 2 cardiac cycles were saved in Digital Imaging and Communications in Medicine (DICOM) format for offline processing.

For every volunteer, first 5 long-axis parasternal view measurements, with intermittent probe repositioning, were performed with the Zonare system. It was ascertained that both aortic and mitral valves were in the image plane. Directly after the measurements with the Zonare system, measurements were repeated with the Philips system. Subsequently, the effect of physiologic stress causing hemodynamic variations on the SW propagation speed measurements was tested by performing handgrip tests. During the handgrip measurements, the volunteers were asked to keep a stress ball continuously squeezed with their left hand. While volunteers kept on squeezing, measurements were repeated with both machines. All measurements were performed within 30 min per volunteer. Furthermore, to investigate test-retest

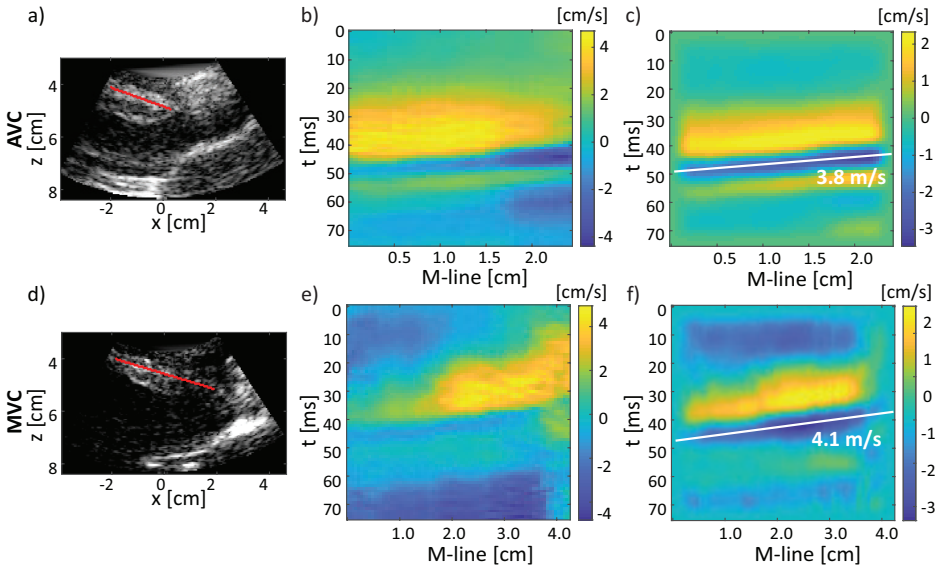


Figure 4.2: Zonare: Example of an M-line drawn at (a) AVC and (d) MVC. The corresponding M-panels are presented in (b) and (e), respectively. After applying a BPF, we applied a Radon transform to obtain the propagation velocities as presented in (c) and (f).

variability, all measurements were repeated per volunteer during a second scanning session on a separate day. The time period between the first and second session for the volunteers varied between 21 and 93 days.

4.2.3. Shear Wave Propagation Speed Analysis

The propagation speeds of the SWs induced by AVC and MVC were determined by using different methods for the Zonare and Philips system. Although one method applicable to the data of both systems could be searched for, we choose to use different methods that were more suitable for the data format of the individual systems.

Clinical System with Custom HFR Mode

Offline IQ-based data stored from the Zonare system were analyzed in Matlab R2017a (MathWorks, Natick, MA, USA). To remove high frequency TDI information that was for the most part corresponding to blood and noise, a sixth order lowpass Butterworth filter with a cut-off frequency of 250 Hz was applied to the IQ data in slowtime. Axial tissue velocities were obtained by using a one-lag autocorrelation technique [44]. To reduce the effect of speckle and noise, a Gaussian spatial smoothing filter with a size of 4 mm by 6.7° was applied to the autocorrelation frames before calculating the phase [44, 64, 89]. The moments of AVC and MVC were visible in the B-mode images. However, because the HFR box was relatively small, the aortic valves were not visible in all recordings; but, they were visible in the LFR overview images captured in the

seconds before and after the HFR recordings. Therefore, the moments of valve closure in the HFR acquisitions were determined based on the movement of the mitral valves, on the overall motion of the heart and on the derived TDI movies. For each recording, an anatomic M-line was manually drawn on the basal-mid part of the IVS at the moment of valve closure (Figure 4.2 a and d). Depending on the position of the IVS in the field of view and on the visible propagation length of the SWs, the length of the M-line varied between 1.9 – 4.1 cm (AVC) and 2.1 – 5.7 cm (MVC). Then, the axial particle velocities over the M-line were assembled in a motion panel (M-panel) for a period of 75 ms around the moment of valve closure. The SWs induced by AVC and MVC are depicted as wave patterns propagating over slowtime along the M-lines in the M-panels (Figure 4.2 b and e). The slope of these patterns represents the propagation speed of these SWs. The AVC and MVC occur during the isovolumetric relaxation and isovolumetric contraction phase, respectively, and therefore no gross motion was assumed nor seen to be present. Nonetheless, a sixth order bandpass Butterworth filter between 15 and 100 Hz was applied to the axial tissue velocities in slowtime, because the SWs were observed to be in this frequency range. Therefore, also any offset attributable to gross motion was removed. To obtain the propagation speeds of the SWs induced by the various valve closures, the slope of the patterns presented in the M-panels was determined by using a Radon transform [64, 65, 90] (Figure 4.2 c and f). Before applying the Radon transform, the M-panels were first resampled to have an equal number of pixels in space and time and then tapered in both directions. Furthermore, the Radon domain was normalized, as described by Vos *et al.* (2017) [64]. The minimum intensity, corresponding to the particle motion away from the transducer, was selected in the Radon domain to determine the propagation speed. As also reported in data regarding pigs [80], the location of the manually drawn M-line was observed to affect the results. Therefore, to test intra-scan variability for every recording, the M-lines were drawn 10 times. The location of these M-lines was chosen based on the visibility of the SW propagation. When the SW propagation was observed to be less reliable on the right and left ventricle sides of the IVS, M-lines were drawn more to the middle. Analysis of the Zonare data was done by the researcher who wrote the MATLAB analysis script (L.B.H.K.). Other than determining the moments of valves closure and drawing the M-lines, the data analysis process was fully automated. Because 10 M-lines were already drawn for every recording, inter-observer variability testing was not considered meaningful for the Zonare system.

For every volunteer 7 measurements were performed per session, leading to 140 measurements in total. SWs after AVC and MVC were tracked in 122/140 (87%) and 92/140 (66%) measurements, respectively. The main reasons to exclude recordings from the measurements were a poor B-mode quality (approximately 5% of measurements after AVC and/or MVC), or the IVS moving out of the field of view (approximately 5%). Furthermore, acquisitions with no visible propagating SWs or with propagation over only short distances (<1.8 cm [approximately 20%]) were excluded. For 1 volunteer (volunteer 8), propagating SWs after MVC could not be seen in any recording.

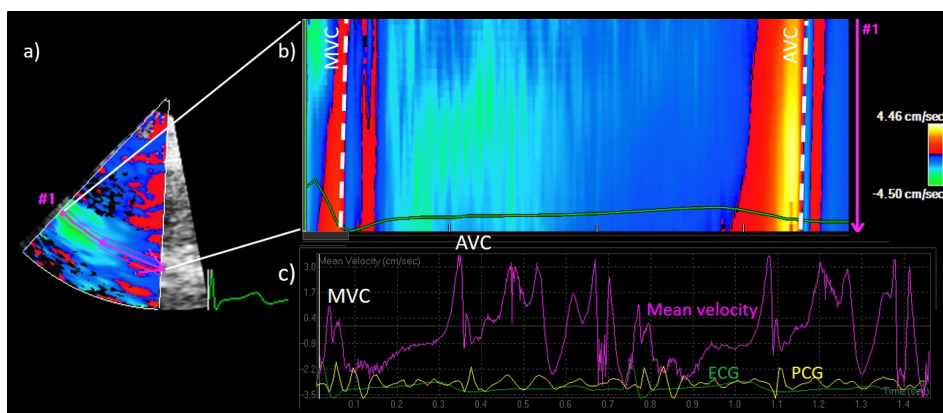


Figure 4.3: Philips: Example of a measurement where SWs were tracked after AVC and MVC. The Philips QLab8 software program shows (a) the TDI movie, (b) the M-panel and (c) the mean velocity curve.

Clinical System with Clinical HFR Mode

The Philips QLab8 software program (Bothell, WA, USA) was used for post-processing of the Philips DICOM data as described elsewhere [89]. The method is repeated here in brief. Because the depth and width of the TDI was minimized to obtain high frame rates, valves were not visible in the measurements. Therefore, the moments of valve closure were determined based on the PCG signals (onset of the heartsounds (S), S1 and S2) and the appearance of SWs in TDI (Figure 4.3). Although the moment of valve closure could not visually be determined in the B-mode images, the onset of heart sounds are well known to correspond to valve closure. Furthermore, natural SWs induced by valve closure propagate from the aortic root to the apex [39, 64], unlike electromechanical waves starting at midlevel of the IVS and propagating toward base and apex [91]. Anatomic M-lines were manually drawn over the IVS, and the length of these M-lines was defined based on the width of the TDI field of view. This length ranged between 2 and 3 cm. Subsequently, an M-panel and a mean tissue velocity curve were provided by the software (Figure 4.3). By viewing the pattern shown on the M-panel (b), the tissue velocity curve (c) and the TDI movie (a) itself, the period needed for the SW to propagate over the M-line was determined. Because data analysis was not automated and the TDI data of the entire septum could be used as a reference by viewing the TDI movies, the effect of M-line location was minimal. Therefore, only 1 M-line was drawn per recording. The transition from positive to negative TDI values of the SWs were tracked, because these were most visible to the observer. Because the SWs were tracked visually, inter-observer variability was considered as an important factor. Analysis of the Philips data was done by the same researcher who analyzed the Zonare data (L.B.H.K). To test inter-observer variability, data analysis of the Philips measurements was repeated by a cardiologist experienced with the post-processing software (M.S.), blinded to earlier values.

For the Philips system, SWs could be tracked after AVC in 365/474 (77%) and after MVC in 71/474 (15%) recorded cardiac cycles. In this study we measured the SWs after AVC and MVC in single recordings. TDI limits were chosen for the visualization of the SWs after AVC, because these had our focus for the measurements. Lower TDI limits might have been chosen when focusing on the SWs induced by MVC, because these have lower magnitudes. Therefore, the transition from positive to negative TDI values after MVC was not visible in many DICOM images, and we obtained a low feasibility for the MVC measurements compared with the MVC data with this method [39]. Furthermore, values above 10 m/s were removed because they were assumed to be non-physical, as was done by Vos *et al.* (2017) [64].

4.2.4. Statistics

Statistical analysis was done by using a statistical toolbox in MATLAB R2017a (Natick, MA, USA). Kolmogorov-Smirnov tests were used to test for normal distributions. Propagation speeds are presented as median values and interquartile ranges (IQR). To compare our results with literature values, mean and standard deviations were also reported. We observed that some volunteers were nervous when entering the scanning room. To test whether all measurements in rest could be grouped, the first and last of five rest measurements were compared. A Wilcoxon signed-rank test was applied to the median values per recording for the Zonare data and to the individual values per heart cycle for the Philips data. Also, a Bland-Altman analysis was used to depict differences (mean differences, limits of agreement [LOA] and range). A similar analysis was done to test the effect of the handgrip test and the test-retest and inter-system variability. For the Zonare data, intra-scan variability was investigated by computing the median of all IQRs of the values obtained per measurement for the 10 M-lines of all rest and stress measurements. The median value of the IQRs of the median recording values was used to measure inter-scan variability.

4.3. RESULTS

4.3.1. Hemodynamic Characteristics

Average blood pressures of 106 ± 13 mmHg (systolic) and 62 ± 9 mmHg (diastolic) were measured in rest, and average pressures of 110 ± 10 mmHg and 67 ± 9 mmHg were measured during the handgrip test. The diastolic blood pressure was statistically significantly different during the handgrip test ($p = 0.0088$) but the systolic blood pressure was not ($p = 0.077$). Also the heart rate, measured with the electrocardiogram (ECG) connected to the Philips system, was observed to increase significantly ($p < 0.01$) from 62 ± 7 bpm to 67 ± 8 bpm.

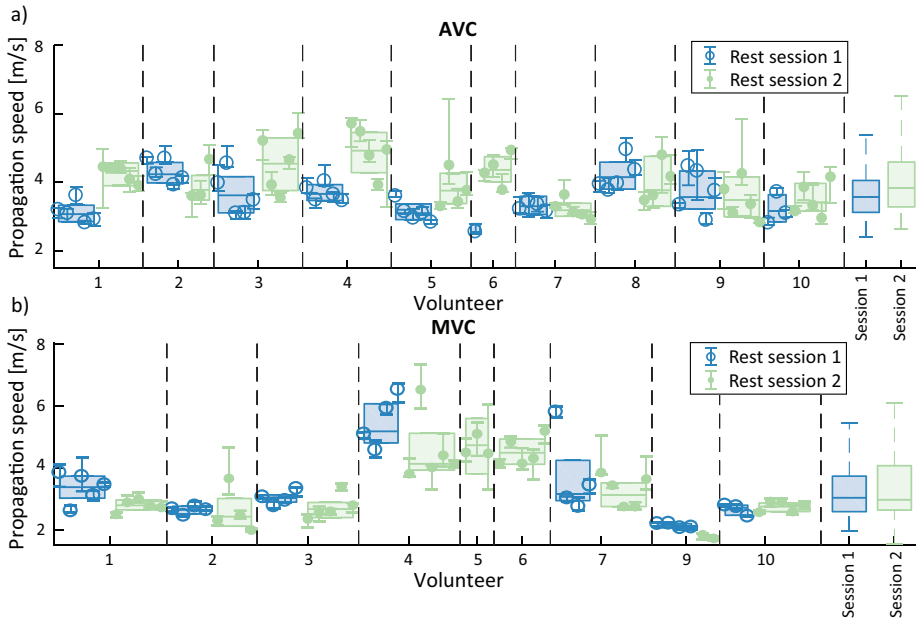


Figure 4.4: Zonare: Median values and IQRs of the measurements in rest performed for (a) the AVC and (b) the MVC. For every recording, 10 M-lines were drawn over the IVS. The IQRs depict the intra-scan variabilities. Inter-scan variabilities (median values and IQRs) per volunteer for every session are depicted in boxplots. Inter-scan variabilities were observed to be slightly higher than, but in similar ranges as, intra-scan variabilities.

4.3.2. Clinical System with Custom HFR Mode

Figure 4.4 presents the results obtained for the 10 volunteers for the AVC and MVC, respectively. The median values in rest ranged from 3.23 – 4.25 m/s for AVC and from 2.06 – 4.72 m/s for MVC. These median values were not normally distributed. Furthermore, we cannot assume that all volunteers have the same SW propagation speeds. Nevertheless, for comparison with other studies, the mean and standard deviations of these median values were computed to be 3.8 ± 0.4 m/s (AVC) and 3.4 ± 1.0 m/s (MVC). Table 4.2 presents an overview of the statistical characteristics of all measurements. For every measurement, 10 M-lines were drawn over the IVS. The IQRs per measurement presented in Figure 4.4 thus represent the intra-scan variabilities. For the AVC measurements in rest, a median value of 0.38 m/s (IQR: 0.26 – 0.68 m/s) was observed for all IQRs, for the MVC measurements in rest this was observed to be 0.26 m/s (IQR: 0.15 – 0.46 m/s). The variations in median values per recording per volunteer were used as measure for the inter-scan variability. The median IQRs of median values in rest per volunteer per session were observed to be 0.67 m/s (IQR: 0.40 – 0.86 m/s) for the AVC and 0.61 m/s (IQR: 0.26 – 0.94 m/s) for the MVC. To test whether all rest measurements could be grouped despite a possible time-dependency during the period of the exam, the medians obtained for the first

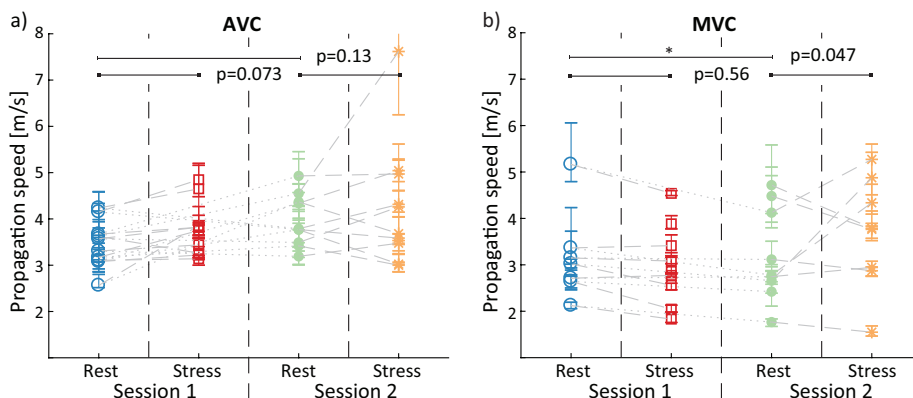


Figure 4.5: Zonare: Comparison of the median values and IQRs of the rest and stress measurements of session 1 and session 2 per volunteer for (a) AVC and (b) MVC. Test-retest differences were observed to be just significant for the MVC, but not for the AVC. No significant effect was observed for the handgrip test (rest vs. stress).

and last rest measurement per volunteer for both sessions were compared (Figure 4.6 a and d). Average differences of -0.0017 m/s (LOA: -1.22 to 1.03 m/s) (AVC) and -0.10 m/s (LOA: -1.85 to 1.64 m/s) (MVC) were observed with a Bland-Altman analysis. No statistically significant differences were observed ($p = 0.90$ for AVC and $p = 0.53$ for MVC). Therefore, we grouped all rest measurement per volunteer per session to compute the test-retest variability (Figure 4.5). Mean differences of -0.51 m/s (LOA: -2.05 to 1.02 m/s) (AVC) and 0.37 m/s (LOA: -0.35 to 1.08 m/s) (MVC) were observed for the test-retest variability of all measurements, (Figure 4.6 b and e). These differences were observed to be just significant for the MVC ($p = 0.047$) but not for the AVC ($p = 0.13$). We grouped both sessions before computing the inter-volunteer variability. The median values of the rest measurements per volunteer were observed to be in the ranges of $3.23 - 4.25$ m/s and $2.06 - 4.72$ m/s for the AVC and MVC, respectively. Subsequently, rest and handgrip measurements are compared (Figure 4.6 c and f). Average differences of -0.33 m/s (LOA: -1.94 to 1.27 m/s) for the AVC measurements and -0.072 m/s (LOA: -1.82 to 1.68 m/s) for the MVC measurements were observed. These differences were not observed to be significant ($p = 0.073$ for AVC and $p = 0.56$ for MVC) (Figure 4.5).

4.3.3. Clinical System with Clinical HFR Mode

The propagation speeds obtained from the Philips data are presented in Figure 4.7. Because the feasibility of the MVC measurements was low, no statistical tests were performed on these few MVC measurements. Therefore, only the statistics of the AVC measurements are described here. The median values in rest ranged from $1.82 - 4.76$ m/s (Table 4.2). As done for the Zonare, mean and standard deviation was computed for illustrative purposes (3.2 ± 0.9 m/s). A median value of the IQRs of the propagation speed values in rest per session per volunteer of 0.71 m/s (IQR: $0.33 -$

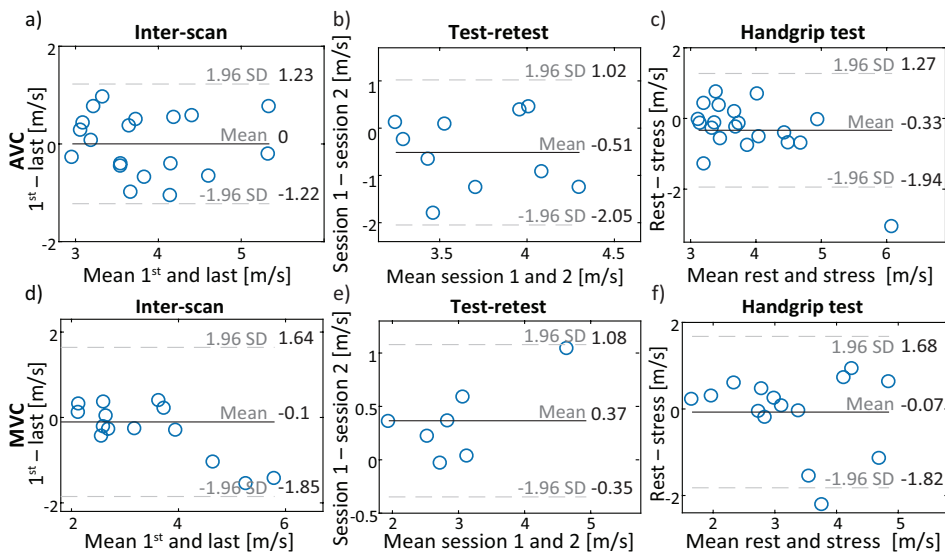


Figure 4.6: Zonare: Bland-Altman analysis of the inter-scan variability, the test-retest variability and the effect of the handgrip test for the AVC ((a), (b) and (c)) and MVC ((d), (e) and (f)). No significant differences were found between the first and last rest measurement per volunteer per session. Test-retest differences were found to be just significant for the MVC, but not for the AVC. No significant effect was found for the handgrip test.

1.07 m/s) was observed, representing the inter-scan variability. It should be noted that these values seem to be higher than the inter-scan variability values of the Zonare data, where first median values over the 10 M-lines per scan were obtained before computing inter-scan variability. As for the Zonare data, no statistically significant difference was observed between the first and last rest measurement per volunteer per session ($p = 0.15$). A Bland-Altman analysis showed a mean difference between the first and last rest measurement of -0.36 m/s (LOA: -2.29 to 1.58 m/s) (Figure 4.8 a). Therefore, all rest measurements were grouped for measuring the test-retest variability. A mean difference of -0.19 m/s (LOA of -1.59 to 1.21 m/s) was observed, which was not statistically significant ($p = 0.28$) (Figure 4.8 b). Therefore, as for the Zonare data, the measurements in session 1 and session 2 were grouped to obtain inter-volunteer variability ranges. The median rest values per volunteer were observed to be in the range of 1.82 – 4.76 m/s. Also similar to the Zonare data, the difference between rest and stress measurements was not observed to be significant ($p = 0.079$). A mean difference of -0.39 m/s (LOA: -2.22 to 1.44 m/s) was observed.

Intra-scan variability was not tested for the Philips data, because only 1 M-line curve and thus 1 propagation speed value was obtained per heart cycle with the Philips system. Instead of intra-scan variability, inter-observer variability was measured for the Philips data. The second observer computed propagation speeds per volunteer per session averaged over 3 heart cycles. These propagation speeds

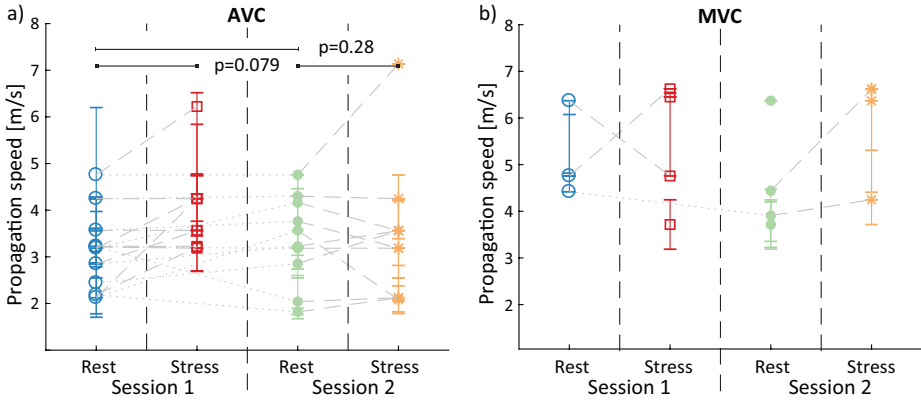


Figure 4.7: Philips: Comparison of the median values and IQRs of the rest and stress measurements of session 1 and session 2 per volunteer for (a) AVC and (b) MVC. No statistical tests were performed on the MVC measurements because of a low feasibility. For the AVC measurements, no significant effects were observed for test-retest and the handgrip test.

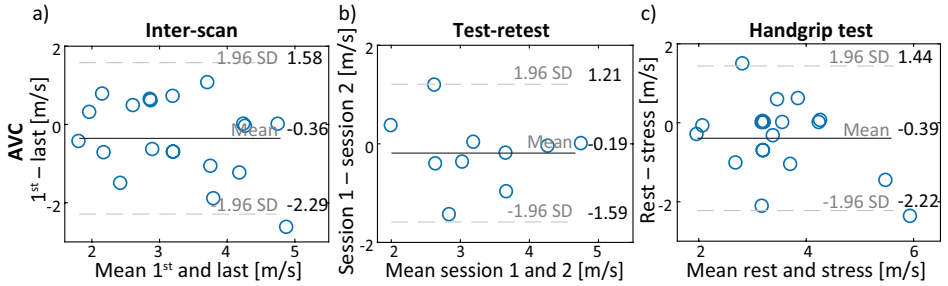


Figure 4.8: Philips: Bland-Altman analysis of the inter-scan variability (a), the test-retest variability (b) and the effect of the handgrip test (c) of the AVC measurements. No statistical tests were performed on the MVC measurements because of a low feasibility. For the AVC measurements, the first and last rest measurement per volunteer per session were not found to be statistically significantly different. Also no significant effect was found for the handgrip test.

were compared with the median rest values obtained by the first observer. An average difference of 0.11 m/s (LOA: -1.42 to 1.65 m/s) was observed (Figure 4.9), which was not observed to be significant ($p = 0.35$). The feasibility of the MVC measurements was higher for the second than for the first observer. Although the first observer obtained propagation speeds in 7 sessions, the second observer obtained values for 14 sessions. Nonetheless, for consistency, no statistical tests were performed on the MVC measurements analyzed by the second observer.

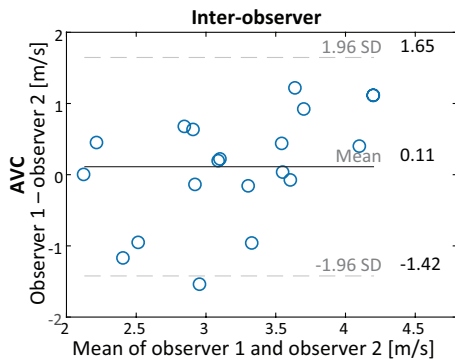


Figure 4.9: Philips: Bland-Altman analysis of the inter-observer variability for the AVC measurements per session. No statistically significant effect was found.

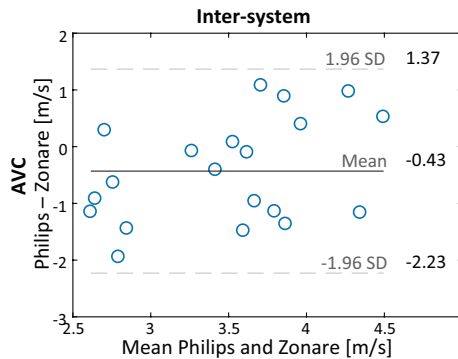


Figure 4.10: Zonare and Philips: Bland-Altman analysis of the inter-system variability for the AVC measurements per session. Statistically different propagation speeds were obtained with the different systems.

4.3.4. Comparison of the Systems

Because of the the low feasibility of the MVC measurements with the current settings on the Philips system, only the AVC measurements of the Zonare and the Philips system were compared. The difference in results obtained with the Zonare and the Philips system was observed to be statistically significant ($p = 0.044$). The Bland-Altman analysis shows a median bias of -0.43 m/s (LOA: -2.23 to 1.37 m/s), indicating that we consistently measured a lower propagation speed with the Philips system (Figure 4.10).

As suggested by others [42, 64], the difference and ratio of the propagation speeds obtained for the AVC and MVC might be of clinical relevance because of hemodynamics. Because of the low feasibility of the MVC measurements with the Philips system, these ratios and differences were only computed for the Zonare system (Figure 4.11). The median ratio and difference were observed to be 1.20 (IQR: 1.00 to 1.58) and 0.64 m/s (IQR: -0.019 to 1.50 m/s), respectively.

4.4. DISCUSSION

In this study, we tested the reproducibility of the propagation speeds of natural SWs induced by AVC and MVC in 10 healthy volunteers. For the AVC measurements, no statistically different propagation speeds were obtained on different days. Our results suggest that the variabilities of natural SW propagation speed measurements in healthy volunteers are dominated by measurement inaccuracies rather than mild hemodynamic variations. Statistically, different propagation speeds after AVC were obtained for two different systems.

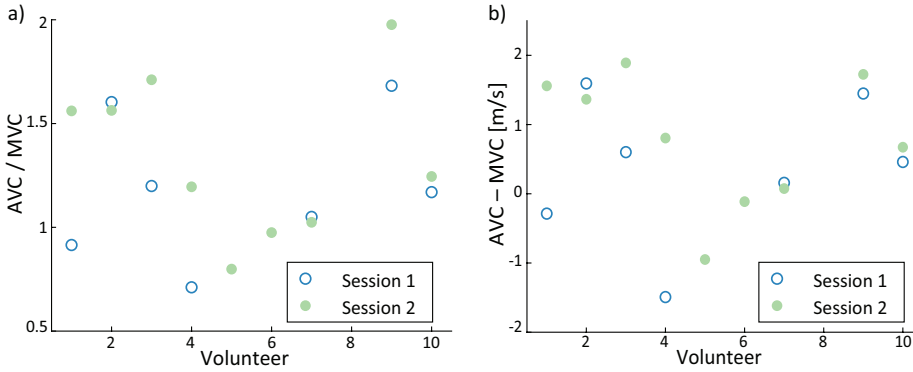


Figure 4.11: Zonare: Ratio (a) and difference (b) between propagation speeds obtained after AVC and after MVC for all volunteers. Due to the low feasibility of the MVC measurements with the Philips system, only the ratio's and differences for the Zonare system are shown.

Measurement variations can have physiologic causes or can arise because of measurement inaccuracies. Intra-scan variability is measured within individual recordings, and, therefore, physiologic causes are assumed to be non-existing. Inter-scan variabilities can also occur because of physiologic variations, and these variations are expected to be even larger when comparing different sessions. We observed inter-scan variabilities (Zonare: 0.67 m/s [IQR: 0.40 – 0.86 m/s] for AVC and 0.61 m/s [IQR: 0.26 – 0.94 m/s] for MVC) to be slightly higher than, but in similar ranges as, intra-scan variabilities (Zonare: 0.38 m/s [IQR: 0.26 – 0.68 m/s] for AVC and 0.26 m/s [IQR: 0.15 – 0.46 m/s] for MVC). Moreover, test-retest variabilities were observed to also be in similar ranges as inter-scan variabilities (Figures 4.6 and 4.8). Therefore, our results suggest that the measurement variations were dominated by several measurement inaccuracies, which are expected to have different causes. First, we observed qualitatively that contrast in the B-mode images affected the results. For recordings with a low visible contrast between tissue and blood, we experienced that positioning the M-lines on the IVS was more challenging. This was especially important for the Zonare system, where a diverging-wave transmission scheme was used, and therefore B-mode contrast was sometimes limited because of clutter. Furthermore, clutter could have affected the determination of tissue velocities. Second, the SWs could only be tracked over the limited visible length of approximately 3 cm of the IVS. An SW with a center frequency of, for example 50 Hz [42] and a propagation speed of 3.5 m/s, has a wavelength of 7.0 cm. This means that only a fraction of this wavelength can be tracked, which causes measurement inaccuracy, increasing with propagation speed.

In a uniform shear wave phantom with ARF-push-induced shear waves, Strachinaru *et al.* (2017) [89] obtained similar propagation speeds with a research scanner as with the clinical Philips system. However, for the AVC measurements, we obtained statistically different propagation speeds with the Philips system compared with the Zonare system. As the measurements with the different systems were

performed within half an hour per session, the differences are expected to be mainly attributable to the differences in data processing for the different systems. First, for the Zonare measurements, a Radon transform was used to track the maximum negative particle velocities, but for the Philips measurements, the onset of the wave, as visible from positive to negative tissue velocities, was tracked. This means that slightly different aspects of the SW pattern were tracked. In an animal model, we have observed different propagation speeds as well when tracking different rims of the SWs [80]. Second, although a frame rate of 1000 Hz was used for the Zonare, frame rates varied between 490 and 570 Hz for the Philips system, and therefore the time resolution differed by a factor of 2. This is expected to induce more uncertainties and thus more variability [89], as observed in our study (Figures 4.5 and 4.7). Third, the SWs were tracked automatically with the Radon transform for the Zonare system, and, for the Philips system, visual feedback obtained from the M-panel, the tissue velocity curve and the TDI movie was used to determine the propagation speeds. Therefore, when comparing different studies, these methodologic aspects should also be taken into account. Furthermore, the effect of using different systems and methods should be studied also for pathologic hearts in more detail.

The advantage of using the Radon transform for the Zonare system is that data analysis can be more automated. To minimize the effect of noise, we applied a lowpass filter to the IQ data in slowtime. Furthermore, a Gaussian spatial smoothing filter was applied to the autocorrelation frames. In addition, for every measurement 10 M-lines were drawn over the IVS. Moreover, we interpolated the M-panels to a panel with an equal number of pixels in space and time. We also normalized the Radon domain by dividing it by the Radon transform of a panel with an equal number of pixels with only unit values, to avoid an apparent bias [64]. To further reduce the effect of noise, the performance of using a least-squares or high resolution Radon transform [92] could be investigated in the future.

The potential hemodynamic variation attributable to psychologic stress related to the examination was estimated by comparing the first and last rest measurement within a session. No significant differences were observed. This indicates that, when patients are nervous at the beginning of a scanning session, this does not strongly affect these measurements, which is beneficial for the application of clinical diagnosis. Nonetheless, it should be noted that the number of measurements in this study was limited and thus not enough statistical power may be present to detect small differences. Therefore, to investigate the effect of larger variations in hemodynamics, a handgrip test was performed during the SW propagation speed measurements. This test is not only relevant for the different levels of physiologic stress patients may experience, but also because diastolic dysfunction patients might show normal hemodynamic characteristics in rest, but have abnormal LV diastolic pressures during exercise [10]. Although heart rate did increase significantly during the handgrip test, the propagation speeds obtained during rest and the handgrip test were not observed to be statistically different. It should be noted that for AVC we observed p values only slightly above $p = 0.05$ ($p = 0.073$ and $p = 0.079$ for Zonare and Philips, respectively). Possibly, the statistical power could be too limited to measure

significant differences. For the AVC, we did find a mean increase in propagation speed during stress of 0.33 m/s and 0.39 m/s with the Zonare and Philips system, respectively (Figures 4.6 and 4.8). Nonetheless, the differences between the measurements in rest and during the handgrip test are in the same range as the inter-scan variabilities (Figures 4.6 and 4.8). This suggests that no extra variabilities are induced because of the handgrip test. However, only low levels of stress causing small hemodynamic changes are induced by handgrip tests. Although higher levels of stress could be induced by using an exercise test, performing HFR acquisitions would be more challenging. Whether the measurement of the natural SWs induced by AVC and MVC is completely independent of loading conditions should be further investigated in a study with higher statistical power.

Several studies have reported on the propagation speed of SWs in healthy volunteers, as summarized in Table 4.3. Some studies used a long-axis parasternal view, but Brekke *et al.* (2014) [44] used a 4-chamber apical view. However, the exact effect of the imaging view on the measured propagation speed is currently unclear. The propagation speeds obtained in this study for the SWs after AVC are in the same range as the values measured in other human studies. Some studies used ARF to induce SWs during diastole in healthy volunteers. However, these values cannot be directly compared with the values obtained after closure of the valves, because the timing of the measurements is different. MVC and AVC occur around the onset of contraction and relaxation, respectively [93]. Other studies have shown stiffness variation over the cardiac cycle in animals [55, 75, 94] and human [53, 62]. Couade *et al.* (2011)[55] reported on an increase in shear modulus from approximately 5 kPa to 15 kPa in the first 50 ms after the R-peak in sheep, which corresponds to an increase in propagation speed of approximately 70%. With the Zonare system, we observed in general higher values after MVC than ARF-based studies at diastole.

Several authors have suggested that the difference and ratio of the propagation speeds obtained after AVC and MVC are potentially more clinically relevant because of hemodynamics [42, 64]. We observed a median difference of 0.60 m/s (IQR: -0.31 to 1.25 m/s) and a mean ratio of 1.21 (IQR: 0.93 – 1.46) with the Zonare system. However, these values have relatively high variability, likely caused by the combined variability of both the AVC and MVC measurements, which may reduce relevance for clinical diagnosis. Nonetheless, Santos *et al.* (2019) [42] observed a mean difference of 0.4 ± 0.6 m/s and mean ratio of 1.1 ± 0.2 , which is close to the values we obtained. Also, Petrescu *et al.* (2019) [40] observed higher mean propagation speeds for AVC than for MVC (3.48 ± 0.70 m/s vs. 3.07 ± 0.51 m/s) for healthy volunteers aged 20 – 39 years. However, for older age groups, no statistical difference was observed between the propagation speeds after AVC and MVC. In contrast, Strachinaru *et al.* (2019) [39] observed higher propagation speeds for MVC than for AVC (4.68 ± 0.66 m/s vs. 3.51 ± 0.38 m/s) in healthy volunteers. What exact clinically relevant information can be obtained from natural SW propagation speed measurements should be further investigated.

Both systems have their own advantages and disadvantages to be used for clinical diagnosis with SW propagation speed. The translation of using the clinical Philips system and its clinical data analysis package to daily clinical practice takes less time, which is a major advantage. However, the Zonare system saves IQ data rather than DICOM data, providing the possibility to apply different tracking and filter methods and to automate data analysis. Furthermore, with the Zonare system, a two times higher frame rate is obtained, theoretically corresponding to lower measurement variabilities. The higher feasibility of measuring the SWs after MVC and AVC for the Zonare system is another important advantage. In addition, the inter-volunteer range was observed to be smaller or similar, depending on the observer, for the Zonare compared with the Philips system. However, ECG and PCG could not yet be measured with the Zonare system in HFR mode. This practically means that the moment of valve closure had to be determined visually and that measurements could not be linked to a heart rate, because only one heartbeat was recorded per movie. However, we expect that ECG and PCG could be implemented in the HFR mode of the Zonare system in the future. Image quality was higher with the Philips system, and TDI data were directly shown on the Philips system. This made it easier to perform a more direct quality check of the recording than with the Zonare system. However, when performing the measurements with the Philips system, separate recordings should be made for the AVC and MVC measurements because the TDI velocity scale needs optimization for either measurement. Strachinaru *et al.* (2019) [39] showed much higher feasibilities for the MVC measurements (89% of 45 healthy volunteers) by using the same system but by performing separate recordings for measuring the SWs after AVC and MVC. For the Zonare system, AVC and MVC measurements can be performed simultaneously. As such, in this stage of developments, both systems can be used as a research bridge to further clinical translation of the technique.

For clinical diagnostic application, it is important to be able to show with a certain amount of confidence significant differences between healthy volunteers and a patient at risk. Our study suggests that measurement variabilities are dominated by measurement inaccuracies. Therefore, by averaging over multiple heartbeats, the standard error is expected to be minimized. The variabilities presented in this study can be used to estimate the minimum amount of measurements needed for clinical diagnosis, once the minimal difference in propagation speed between a patient at risk and a healthy subject are suitably investigated. Considering that data processing is done offline and that measurements can be performed subsequently, we estimate that recording up to 10 heartbeats for averaging is feasible with respect to time and effort.

The ultimate goal is to measure the increased stiffness of the myocardium. However, in this study, we only reported on linear propagation speeds. Because the typical wavelength of the SWs measured (approximately 7 cm) is large compared with the thickness of the IVS (approximately 1 cm), guided waves, rather than bulk shear waves, are expected. Guided waves show dispersion even for purely elastic media, and, thus, measured propagation speeds cannot be directly converted to shear moduli. However, the resolution in the 2D Fourier domain was restricted because of

the limited visible propagation length of the SWs, to measure dispersive effects. Xu *et al.* (2018) [95] proposed a dispersive Radon transform. However, prior knowledge on the theoretic dispersion curves of the induced modes is needed. Because the IVS is a complex structure with respect to geometry and fiber orientation, we expect that the dispersion curves of Lamb waves in plate structures are too simplistic. As such, the relationship among geometry of the myocardium, propagation speed and early diagnosis of cardiac dysfunction should be further investigated.

4.5. CONCLUSIONS

This study investigated the reproducibility of the measurement of propagation speeds of SWs naturally induced by AVC and MVC in healthy volunteers. Propagation speeds of 3.23 – 4.25 m/s (AVC) and 2.06 – 4.72 m/s (MVC) were obtained. Inter-scan variabilities were slightly higher than intra-scan variabilities. For the AVC measurements, no different propagation speeds were obtained after test-retest ($p = 0.13$). However, significantly different values were obtained with a second clinical system (1.82 – 4.76 m/s for AVC), potentially caused by differences in measurement methods. For this second system, inter-observer variability was tested and no statistical differences were observed. Based on the results of this study, measurement inaccuracies are expected to dominate measurement variations among healthy volunteers. Thus, by averaging over multiple heartbeats, precision for the application of clinical diagnosis can potentially be improved.

Acknowledgements

We thank Dr. G. McLaughlin and Dr. Y. Chen of Mindray Innovation Center (San Jose, CA, USA) for providing the Zonare system with the customized high frame rate imaging mode. This work is part of the STW/TTW – Dutch Heart Foundation partnership program 'Earlier recognition of cardiovascular diseases' with project number 14740, which is (partly) financed by the Netherlands Organization for Scientific Research (NWO).

Table 4.2: Overview of the statistical characteristics of the Zonare and Philips data

Variability Performed test		Zonare		Philips
		AVC	MVC	AVC
Intra-scan	Median of all IQRs of the values obtained per measurement for the 10 M-lines	0.38 m/s, n=136 (IQR: 0.26 – 0.68 m/s)	0.26 m/s, n=99 (IQR: 0.15 – 0.46 m/s)	-
Inter-scan	Wilcoxon signed-rank test on medians of first and last rest measurement per volunteer per session	p=0.90, n=19	p=0.53, n=16	p=0.15, n=20
	Bland-Altman: medians of first – medians of last rest measurement per volunteer per session	Mean: -0.017 m/s, n=19 (LOA: -1.22 – 1.23 m/s) (Range: -1.06 – 0.96 m/s)	Mean: -0.10 m/s, n=16 (LOA: -1.85 – 1.64ms) (Range: -1.56 – 2.36 m/s)	Mean: -0.36 m/s, n=20 (LOA: -2.29 – 1.58 m/s) (Range: -2.63 – 1.06 m/s)
Inter-scan	Median of all IQRs of (median) rest values per volunteer per session	0.67 m/s, n=19 (IQR: 0.40 – 0.86 m/s)	0.61 m/s, n=16 (IQR: 0.26 – 0.94 m/s)	0.71 m/s, n=19 (IQR: 0.33 – 1.07 m/s)
Test-retest	Wilcoxon signed-rank test on medians of all rest measurements per volunteer for Session 1 and Session 2	p=0.13, n=10	p=0.047*, n=7	p=0.28, n=10
	Bland-Altman: medians of all rest measurements per volunteer for Session 1 – for Session 2	Mean: -0.51 m/s, n=10 (LOA: -2.05 – 1.02 m/s) (Range: -1.81 – 0.45 m/s)	Mean: 0.37 m/s, n=7 (LOA: -0.35 – 1.08 m/s) (Range: -0.034 – 1.04 m/s)	Mean: -0.19 m/s, n=10 (LOA: -1.59 – 1.21 m/s) (Range: -1.44 – 1.19 m/s)

Table 4.2 continued: Overview of the statistical characteristics of the Zonare and Philips data

Variability Performed test		Zonare		Philips
		AVC	MVC	AVC
Inter-volunteer	Range of median rest values per volunteer	3.23 – 4.25 m/s, n=10	2.06 – 4.72 m/s, n=9	1.82 – 4.76 m/s, n=10
Handgrip test	Wilcoxon signed-rank test on medians of all rest and all handgrip test measurements per volunteer per session	p=0.073, n=20	p=0.56, n=15	p=0.079, n=19
	Bland-Altman: medians of all rest - medians of all handgrip test measurements per volunteer per session	Mean: -0.33 m/s, n=20 (LOA: -1.94 – 1.27 m/s) (Range: -3.07 – 0.74 m/s)	Mean: -0.0723 m/s, n=15 (LOA: -1.82 – 1.68 m/s) (Range: -2.22 – 0.93 m/s)	Mean: -0.39 m/s, n=19 (LOA: -2.22 – 1.44 m/s) (Range: -2.38 – 1.49 m/s)
	Wilcoxon signed-rank test on medians of rest measurement per volunteer per session analyzed by observer 1 and observer 2	-	-	p=0.35, n=20
	Bland-Altman: medians of all test measurements per volunteer per session for observer 1 - for observer 2	-	-	Mean: 0.11 m/s, n=20 (LOA: -1.42 – 1.65 m/s) (Range: -1.55 – 1.21 m/s)

Table 4.2 continued: Overview of the statistical characteristics of the Zonare and Philips data

		AVC
Inter-system	Wilcoxon signed-rank test on median rest values per volunteer per echographic scanner	p=0.044*, n=20
	Bland-Altman on median rest values per volunteer per echographic scanner bias + limits of agreement	Mean: -0.43 m/s, n=20 (LOA: -2.23 – 1.37 m/s) (Range: -1.95 – 1.08 m/s)
		Zonare
AVC versus MVC	Median ratio of median rest values per volunteer per session for AVC and MVC	1.20, n=16 (IQR: 1.00 – 1.58)
	Median difference of median rest values per volunteer per session for AVC and MVC	0.64 m/s, n=16 (IQR: -0.019 – 1.50 m/s)

* The p-value corresponds to a statistically significant difference (p<0.05). LOA = limit of agreement Bland-Altman analysis (± 1.96 SD).

Table 4.3: Overview of human shear wave elastography measurements described in the literature

Natural SWs				
Study	View	Subject	MVC	AVC
Kanai (2005) [43]	PLAX, IVS	HV	-	1 – 7 m/s (10 – 90 Hz)
Brekke <i>et al.</i> (2014) [44]	AP4C, IVS	HV	-	5.41 ± 1.28 m/s
Santos <i>et al.</i> (2019) [42]	PLAX, IVS	HV	3.2 ± 0.6 m/s (2.1 – 4.4 m/s)	3.5 ± 0.6 m/s (2.2 – 4.5 m/s)
Petrescu <i>et al.</i> (2019) [40]	PLAX, IVS	HV CA	3.54 ± 0.93 m/s 6.33 ± 1.63 m/s	3.75 ± 0.76 m/s 5.63 ± 1.13 m/s
Strachinaru <i>et al.</i> (2019) [39]	PLAX, IVS	HV	4.65 ± 0.77 m/s (3.25 – 6.50 m/s)	3.61 ± 0.46 m/s (3.10 – 4.66 m/s)
		HCM	6.88 ± 1.22 m/s (5.45 – 8.91 m/s)	5.13 ± 0.68 m/s (3.75 – 6.94 m/s)
Keijzer <i>et al.</i> (2019) [86]	PLAX, IVS	HV	Zonare 3.4 ± 1.0 m/s (2.06 – 4.72 m/s)	Zonare 3.8 ± 0.4 m/s (3.23 – 4.25 m/s)
			-	Philips 3.2 ± 0.9 m/s (1.82 – 4.76 m/s)
ARF based SWs				
Study	View	Subject	End-diastole	End-systole
Song <i>et al.</i> (2016) [87]	PLAX, PSAX, LVFW, IVS	HV	1.29 – 1.96 m/s	-
Villemain <i>et al.</i> (2019) [63]	PLAX, PSAX, IVS	HV	2.1 ± 1.30* m/s	-
		HCM	3.56 ± 1.71 * m/s	-

* Speed values c obtained by converting elasticity values E , using $E = \rho c^2$ with a tissue density of ρ of 1000 kg/m³). SWs = shear waves, CA = cardiac amyloidosis, HV = healthy volunteer(s), HCM = hypertrophic cardiomyopathy, PLAX = parasternal long-axis view, PSAX = parasternal short-axis view, AP4C = apical 4-chamber view, LVFW = left ventricular free wall, IVS = inter-ventricular septum.

5

Parasternal versus Apical View in Cardiac Natural Mechanical Wave Speed Measurements



Lana B.H. Keijzer

Mihai Strachinaru

Daniel J. Bowen

Annette Caenen

Antonius F.W. van der Steen

Martin D. Verweij

Nico de Jong

Johan G. Bosch

Hendrik J. Vos

Based on:

"Parasternal versus Apical View in Cardiac Natural Mechanical Wave Speed Measurements", *IEEE Transactions on Ultrasonics, Ferroelectrics, and Frequency Control* **67**(8), 2020 [96].

Abstract

Shear wave speed measurements can potentially be used to non-invasively measure myocardial stiffness in order to assess myocardial function. Several studies showed the feasibility of tracking natural mechanical waves induced by aortic valve closure in the interventricular septum, but different echocardiographic views have been used. This work systematically studied the wave propagation speeds measured in a parasternal long-axis and in an apical 4-chamber view in ten healthy volunteers. The apical and parasternal view are predominantly sensitive to longitudinal or transversal tissue motion respectively, and could therefore, theoretically, measure the speed of different wave modes. We found higher propagation speeds in apical than in parasternal view (median of 5.1 m/s vs 3.8 m/s, $p < 0.01$, $n = 9$). The results in the different views were not correlated ($r = 0.26$, $p = 0.49$), and an unexpectedly large variability among healthy volunteers was found in apical view compared to the parasternal view (3.5 – 8.7 vs 3.2 – 4.3 m/s, respectively). Complementary finite element simulations of Lamb waves in an elastic plate showed that different propagation speeds can be measured for different particle motion components when different wave modes are induced simultaneously. The in vivo results cannot be fully explained with the theory of Lamb wave modes. Nonetheless, the results suggest that the parasternal long-axis view is a more suitable candidate for clinical diagnosis due to the lower variability in wave speeds.

5.1. INTRODUCTION

Heart failure affects around 1 – 2% of all adults in developed countries, and its prevalence is even more than 10% for people aged above 70 years [2]. The clinical course of heart failure is generally regarded as a consequence of structural and/or functional cardiac changes. Currently, assessment of myocardial function primarily relies on the echocardiographic measurement of cardiac volumes, flow and tissue velocity [2, 10, 12]. However, these measurements suffer from load-dependency issues and provide a rather indirect way of evaluating myocardial function. Myocardial function could potentially be assessed more directly by evaluating cardiac stiffness [11, 14], a measure of the intrinsic cellular composition and structure of the heart muscle. At present, no non-invasive clinical routine method exists for measuring myocardial stiffness.

A highly promising tool for assessing myocardial stiffness non-invasively is ultrasound-based shear wave speed (WS) measurement [39, 40, 42, 63], in which the WS is presumably linked to the myocardial elastic properties. Shear waves (SWs) in the cardiac wall can be induced externally using a vibration device [51–53] or an acoustic radiation force (ARF) [54–57, 63, 75, 87], or can occur naturally after aortic valve closure (AVC), mitral valve closure (MVC) [39, 40, 42–44, 64, 88] and atrial contraction [47–49]. The propagation of these SWs over the myocardium can be measured using high frame rate Tissue Doppler Imaging (TDI) or Clutter Filter Wave Imaging (CFWI) [45]. This work focuses on naturally induced SWs, which has the advantages of easier implementation in current clinical echocardiographic systems [89] and higher signal-to-noise ratios compared to externally induced SWs (TDI amplitudes of ~40 mm/s [64] for natural SWs versus ~10 mm/s [55] for external SWs). More specifically, we will focus only on SWs excited after AVC in the interventricular septum (IVS), as we previously found a higher feasibility and lower inter-volunteer variability for these SWs compared to those after MVC among healthy volunteers in parasternal long-axis view [86].

Even though the feasibility of natural SW detection using TDI in humans has been demonstrated, no consensus has been achieved regarding the preferred echocardiographic view for natural SW measurements. A parasternal view was reported by some studies [39, 40, 42, 43], whereas others used an apical view [44–46]. These different views depict a different component of particle motion in TDI, since TDI is most sensitive to axial particle motion (motion along the ultrasound beam). In a parasternal long-axis view, the IVS is oriented quasi-horizontally, resulting in measurement of particle motion perpendicular to the IVS (transversal component). In an apical 4-chamber view, the IVS is oriented vertically, and therefore mainly particle motion parallel to the IVS is tracked (longitudinal component). An overview of previously reported WS in both echocardiographic views together with relevant specifications of each study is given in Table 5.1. This table shows that WS after AVC in healthy volunteers were generally higher in apical than in parasternal view. Furthermore, in general a larger inter-volunteer variability of WS between healthy volunteers was found in apical view studies. The observed differences in WS between

parasternal and apical view might be due to the different orientation of the particle motion measured in both views, but it can also have other causes, such as inter-volunteer variability [42] [86], and the use of different echocardiographic systems [86] and data analysis methods [80]. Moreover, different sonographers might select slightly different windows in a standard echocardiographic view, inducing extra variabilities. Although this manuscript focusses on AVC, the effect of different views considered in this study could also be relevant for the SWs after MVC and the longitudinal wave-pattern after atrial contraction, since these different types of natural SWs have similar spatial and temporal characteristics.

The induced wave mode determines the main component of particle motion and should thus be taken into account when selecting a sonographic view for WS measurements. As the name implies, shear WS measurements were originally developed for assessing WS of bulk SWs dominated by transversal particle motion. Our earlier studies of natural waves in the heart therefore assumed the measurement of SWs dominated by transversal particle motion, ratifying the use of a parasternal view [64] [89]. Furthermore, Kanai [43] measured in 2005 a similar WS when tracking the transversal particle motion after AVC in parasternal view and the longitudinal particle motion after AVC in apical view. Consequently a coupling between the two directions of particle motion was assumed, representing one type of wave mode. However, recent studies on natural SWs in both echocardiographic views report different WS for both views (see Table 5.1). Therefore, we hypothesized that transversal as well as longitudinal wave modes are induced by AVC simultaneously, and that a transversal mode is mainly measured in parasternal view, while a longitudinal mode is measured in apical view. To test this hypothesis, a systematic study of SWs after AVC in apical and parasternal view is needed to minimize measurement uncertainties. To the best of our knowledge, such a study has not been performed yet.

The aim of the work presented here is thus to study the propagation speed of the SWs induced by AVC measured in a parasternal long-axis view and in an apical 4-chamber view in ten healthy volunteers. In order to improve our understanding of what we are actually measuring in both echocardiographic views, we performed complementary finite element simulations of Lamb wave propagation in the IVS – approached as an elastic plate immersed in liquid – while applying different forces and therefore inducing different wave modes. Based on the WS measurements on volunteers and simulation results, we will elaborate on possible theoretical explanations of the wave phenomena measured and discuss on practical considerations. The outcomes of this study are expected to be important for determining the preferred view for robust and clinically meaningful natural WS measurements.

Table 5.1: Overview of the different human studies using the natural shear waves induced after aortic valve closure. The following abbreviations are used in the table: HV: healthy volunteer(s); CA: cardiac amyloidosis patient; WS: wave speed; AVC: aortic valve closure; HCM: hypertrophic cardiomyopathy, TDI: tissue doppler imaging, CFWI: clutter filter wave imaging.

Study	Subject	WS after AVC
Parasternal View		
Kanai, (2005) [43]	HV (n=1)	1 – 7 m/s (10 – 90 Hz)
Santos <i>et al.</i> , (2019) [42]	HV (n=30)	3.5 ± 0.6 m/s (2.2 – 4.5 m/s)
Petrescu <i>et al.</i> , (2019) [40]	HV (n=46)	3.75 ± 0.76 m/s
	CA (n=17)	5.63 ± 1.13 m/s
Strachinaru <i>et al.</i> (20019) [39]	HV (n=20)	3.61 ± 0.46 m/s (3.10 – 4.66 m/s)
	HCM (n=20)	5.13 ± 0.68 m/s (3.75 – 6.94 m/s)
		Zonare 3.8 ± 0.4 m/s (3.23 – 4.25 m/s)
Keijzer <i>et al.</i> , (2019)* [86]	HV (n=10)	Philips 3.2 ± 0.9 m/s (1.82 – 4.76 m/s)
<i>This study</i>	<i>HV (n=10)</i>	3.7 ± 0.4 m/s (3.2 – 4.3 m/s)
Apical View		
Brekke <i>et al.</i> , (2014) [44]	HV (n=10)	5.41 ± 1.28 m/s
Santos <i>et al.</i> , (2017) [46]	3D, HV (n=3)	4.2 ± 1.0 m/s (3.0 – 5.4 m/s)
Salles <i>et al.</i> , (2019) [45]	HV (n=1)	TDI 5.12 ± 0.61 m/s
		CFWI 5.37 ± 0.44 m/s
<i>This study</i>	<i>HV (n=10)</i>	5.7 ± 1.8 m/s (3.5 – 8.7 m/s)

* The same volunteers have been used as in the current study. Some measurements have been repeated in order to have a complete data set with apical and parasternal view recordings in all sessions for all volunteers.

5.2. MATERIALS AND METHODS

5.2.1. Guided Waves in the Heart Wall

Elastic waves propagating in a medium that is bound in one or two directions such as the IVS, successively reflect at these boundaries, causing conversion between longitudinal waves and SWs. For a given frequency, only specific patterns of longitudinal waves and SWs can propagate. These patterns are called guided wave modes. Each propagating mode has a specific, frequency-dependent WS, which makes these modes dispersive even in inviscid media (contrary to bulk waves). The IVS has a thickness (6 – 10 mm) smaller than the wavelength of natural SWs (~70 mm [86]), and guided waves are expected [28, 68–72].

Guided waves propagating in a plate structure can be described by symmetric (S) Lamb wave modes, anti-symmetric (A) Lamb wave modes and shear horizontal (SH) modes. Depending on the type of source, frequency, medium thickness and material properties, various wave modes might be induced [68]. We will not consider SH modes, as the particle motion of these modes is along the plate surface perpendicular to the propagation direction [68], and is therefore probably hard to detect in cardiac parasternal and apical views. The A- and S-mode guided waves are characterized by different dispersion curves, as described in [28, 68, 69]. S-modes are regularly referred to as longitudinal, and A-modes as transversal SWs, because of the dominant particle motion with respect to the propagation direction in the centerline of the medium. Nevertheless, S-modes also include transversal particle motion, and A-modes also include longitudinal particle motion [28]. The ratio of the particle motion components of a specific mode is affected by the frequency of the SW and the thickness of the medium, especially near the boundaries of the medium. We focus on the zero-order S_0 - and A_0 -modes, since higher order modes have not been detected yet in soft tissue plates [68].

Multiple studies on cardiac shear wave elastography used a theoretical Lamb wave model to improve the accuracy of tissue characterization methods, but also to extract additional information about certain material properties such as viscoelasticity. In 2005, Kanai was the first to use an A_0 -Lamb wave model to convert propagation speeds of SWs after AVC in humans into elastic and viscoelastic properties of the myocardium [43]. However, Vos *et al.* (2017) only measured mild dispersion for SWs after AVC and MVC in pigs and therefore found a poor match with A_0 -Lamb wave modes [64]. This same model was used in studies using external sources like an external shaker [51, 52, 71, 72], and ARF [70, 73]. However, it should be noted that when using an ARF source in a parasternal long-axis view, the load is directed perpendicular to the myocardium, inducing therefore mainly transversal particle motion (and thus the A_0 -mode). On the contrary, for SWs induced by AVC, a more complex particle motion pattern is probably induced at the valvular plane as a consequence of the complex interaction between the valve leaflets, the abruptly decelerating blood flow and the aortic valve annulus. Therefore, the nature of the wave modes that are induced in natural SW measurements is unknown. Note that the

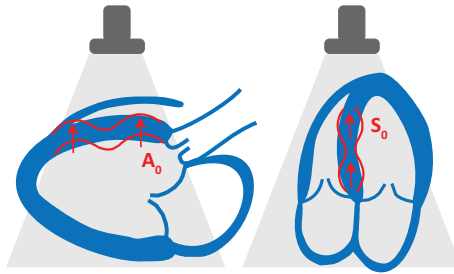


Figure 5.1: In parasternal long-axis view, mainly transversal particle motion is measured (left), while in apical 4-chamber view mainly longitudinal particle motion is measured (right) because of the angle dependency of TDI. It could be expected that if an A_0 -mode and a S_0 -mode are induced by the AVC, the A_0 -mode dominated by transversal motion is mainly measured in parasternal view, while the S_0 -mode is mainly measured in apical view.

Lamb wave model is inherently associated with various limitations, as it assumes a homogeneous isotropic (visco)elastic plate submerged in fluid, while the myocardium has a complex geometrical shape, irregular blood-tissue interfaces, and other complex material properties such as muscular anisotropy. For example, several studies have shown that fiber orientation affects WS measurements using ARF [66, 67, 97, 98]. However, natural SWs have a lower frequency content than externally induced SWs, and therefore the effect of fiber orientation on natural SWs might be different than that on ARF-induced SWs [98].

As described before, mainly longitudinal particle motion is measured in apical view, while mainly transversal particle motion is measured in parasternal view. Therefore, if both the A_0 - and S_0 -Lamb wave modes are induced by AVC, it is expected that the A_0 -mode is mainly measured in parasternal view and the S_0 -mode in apical view, as schematically shown in Figure 5.1. Nonetheless, to the best of our knowledge, the S_0 -Lamb wave mode has not been used in other studies to describe the SWs induced by AVC measured in apical view.

‘Shear wave elastography’ has become a generally accepted term for studies measuring wave propagation speeds that are presumably linked to the elasticity of the tissue. However, it should be noted that since we expect guided waves, the term ‘shear wave’ might not be appropriate from a physics viewpoint to describe all phenomena observed in this study. Therefore, we will use from this point in the manuscript, the general terms ‘(mechanical) wave’ and ‘wave propagation speed’ (WS) to refer to related wave phenomena.

5.2.2. Finite Element Simulations of Guided Waves

Since different wave modes will in general have different WS along an individual path, we performed simulations to investigate what WS can be measured when different wave modes coexist. We studied differences in transversal and longitudinal particle motion and their propagation, as well as the influence of the excitation.

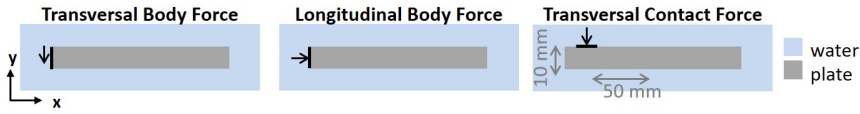


Figure 5.2: Finite Element Simulations; Overview of the different excitations used in PZFlex to simulate the wave propagation of guided waves in a plate structure submerged in water.

Model Set-up

Two-dimensional simulations of a homogeneous plate immersed in water were performed in PZFlex (Thornton Tomasetti, Inc., Cupertino, CA), a software package using the explicit Finite Element Method (FEM), to mimic guided wave propagation in plane strain conditions. The plate (10 mm x 187 mm) was modeled as an elastic material, with a bulk modulus of 22 MPa, a shear modulus of 16 kPa and a density of 1050 kg/m³. A shear modulus of 16 kPa corresponds to a shear WS of 4 m/s in an elastic bulk material, which is in the reported range of WS after AVC (see Table 5.1). To avoid reflections at the end of the plate, the length was longer than the maximum length of the IVS (~100 mm in humans) and the distance that a bulk SW has traveled within a simulation time of 30 ms. Water surrounded the plate (total size of plate and water: 30 mm x 207 mm, absorbing boundary conditions) and was modeled with a bulk modulus of 22 MPa, zero shear modulus, and density of 1000 kg/m³. To reduce simulation times, the bulk moduli used in the simulation are smaller than the actual bulk moduli of tissue and water with a factor 100 [99]. This will only have a small effect on the Poisson ratio of the medium, because the SW propagation speed c is still very small compared to the longitudinal propagation speed c_L ($c \ll c_L$) [99, 100]. Therefore, its effect on the dispersion curves is expected to be small. Quadrilateral elements were used and the element mesh size was chosen such that at least 48 elements fitted in one wavelength at 160 Hz. Mechanical waves were induced by using three different excitations: (i) a transversal body force, (ii) a longitudinal body force, and (iii) a transversal contact force, as depicted in Figure 5.2. For all excitations, a Blackman Harris driving function (pulse of 3 half-cycles) was used with a center frequency of 60 Hz (-6 dB bandwidth: 30 – 95 Hz) or 160 Hz (-6 dB bandwidth: 80 – 252 Hz) in separate simulations. To validate the simulated phase speeds with theoretical dispersion curves within a 0 – 300 Hz frequency range, the results of the simulation with the 160 Hz load was used in order to excite all frequencies within the selected range. The loading with the lower center frequency of 60 Hz resembled the frequency content of the natural waves in the IVS more realistically. Nonetheless, aim of the FEM simulations is not to mimic the *in vivo* situation as accurate as possible, but, as described before, to investigate different wave modes that coexist.

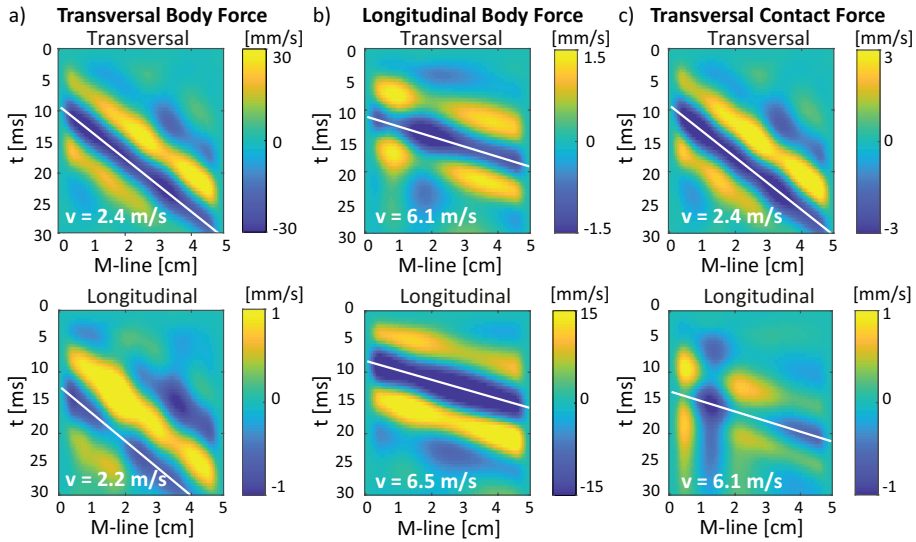


Figure 5.3: Finite Element Simulations; M-panels of transversal (top row) and longitudinal (bottom row) particle motion for a frequency band from 15 – 100 Hz obtained in a finite element simulation for different excitations on a plate submerged in water. An overview of the different excitations is given in Figure 5.2.

Data Analysis

The transversal and longitudinal particle motion, extracted along a horizontal line through the middle of the plate (50 mm length), was determined and assembled in two separate motion panels (M-panels), see the top and bottom row respectively in Figure 5.3. These M-panels depict one-dimensional particle motion as a function of space and time. To avoid a bias in the WS estimation, the axial velocities in the M-panels were first resampled to have an equal number of pixels in space and time, and were then mildly tapered along the edges of the M-panel in both directions. Moreover, a 15 – 100 Hz bandpass filter (6th-order Butterworth) was applied on the axial tissue velocity data. Subsequently, a normalized Radon transform was used to determine the WS [21].

Phase speed values c_p were obtained by first applying a 2D fast Fourier transform to the unfiltered M-panels, yielding the particle motion as function of frequency and wavenumber, and then by selecting the wavenumber k with maximum intensity in the Fourier domain for each frequency f . Subsequently, the frequency-dependent phase speed was computed by dividing the frequencies with the corresponding wavenumber ($c_p = f/k$). No bandpass filter was applied to the M-panels before computing the phase speeds. The accuracy and correctness of the numerical phase speed plots was visually verified by comparing them to the theoretical dispersion curves of A_0 - and S_0 -modes in a non-stretched inviscid plate submerged in water as described in [69].

5.2.3. Natural Wave Elastography Measurements

WS measurements in ten healthy volunteers were performed to compare the WS in a parasternal long-axis view and in an apical 4-chamber view. Details of the study population, data acquisition and analysis methods have been described previously [86] and are summarized below.

Study Population

Ten volunteers aged between 24 and 45 years were included (5 males and 5 females). The study was approved by the local medical ethics committee (Erasmus MC MEC-2014-611) and all volunteers gave informed consent.

Data Acquisition

A clinical system programmed by the manufacturer to enable a high frame rate imaging mode was used (Zonare ZS3, P4-1C probe, Mindray Innovation Center, San Jose, California). For each acquisition, an experienced sonographer first utilized a live B-mode with low frame rate (LFR) to position the probe in the correct echocardiographic view. Subsequently, high frame rate (HFR; 1000 Hz) data was recorded after selecting the correct field-of-view (FOV) on the LFR images. The beamformed IQ data of a smaller FOV (approximately 5 x 7 cm, sector width of 55°) for 1.2 s in parasternal view and of the full FOV for 2 s in apical view was saved for offline processing. During HFR recording, the live LFR B-mode was frozen. The HFR mode employed a diverging wave pulse-inversion transmission sequence for imaging, with 250 μ s in between the two consecutive pulses of each frame. Gaussian-tapered sinusoidal pulses of 7-cycles with a center frequency of 1.8 MHz were transmitted, with a mechanical index below 0.25. For every volunteer, five parasternal long-axis view HFR measurements were performed subsequently, while repositioning the probe in between the recordings. Also, one single HFR apical 4-chamber view measurement (sector width of 84°) was performed within 30 minutes after the parasternal view measurements. Depending on the heart rate of the volunteers, one or two AVC events were measured within each recording. For every volunteer, all measurements were repeated after 21 – 182 days during a second scanning session. For volunteer 1 – 4, five instead of one apical view measurements were recorded in the second scanning session to test repeatability.

Data Analysis

Data analysis was performed in Matlab R2017a (The Mathworks, Natick, MA, USA). A 250 Hz lowpass filter was applied to the IQ data in slowtime (cutoff value of 5.2 cm/s, 6th-order Butterworth), to remove high frequency TDI signal mainly arising from blood and noise. A one-lag autocorrelation technique was used to obtain axial tissue velocities [44]. Before computing the phase [44], the effect of speckle and noise was reduced with a spatial smoothing filter of 4 mm by 6.7°. The moment of AVC was determined based on the movements of the aortic and mitral valve and the overall motion of the heart in the derived TDI movies. In the frame at the moment of AVC, an

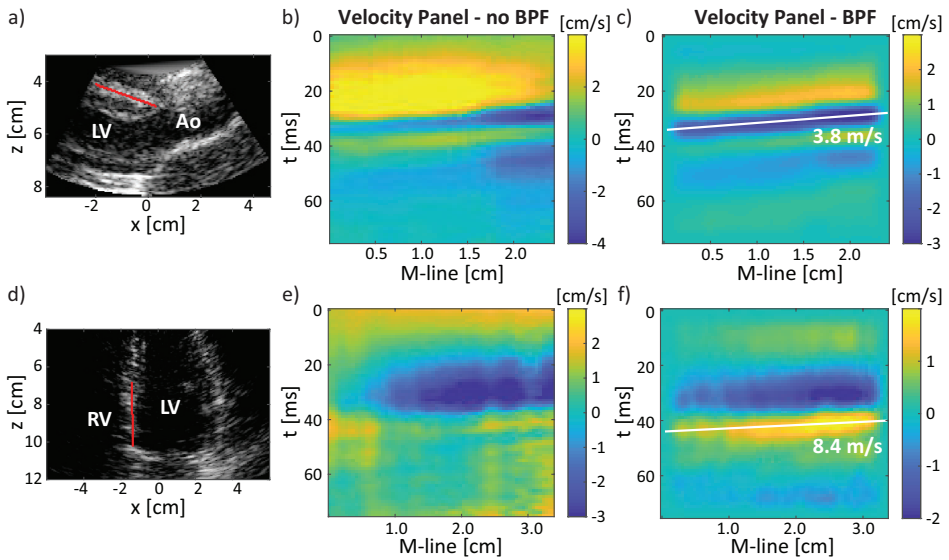


Figure 5.4: Example of an M-line drawn in a parasternal (a) and apical view (d) measurement and the corresponding velocity panels ((b) and (e)). A bandpass filter from 15 – 100 Hz was applied and a Radon transform was used to determine the propagation speeds ((c) and (f)). Abbreviations: LV: left ventricle, Ao: aorta, RV: right ventricle, BPF: bandpass filter, slowtime: time between frames.

anatomical M-line was manually drawn on the basal-mid ventricular part of the IVS, as shown in Figure 5.4 a and d for parasternal and apical view respectively. The location and length of these M-lines depended on the visibility of the wave propagation. The length of the M-lines drawn varied between 1.9 – 4.1 cm (parasternal view) and 2.5 – 5.8 cm (apical view). Since M-line location can affect the propagation speed measured [80] and since M-lines were drawn manually, variability was taken into account by drawing 10 M-lines per acquisition. M-panels showing the axial tissue velocity of an M-line over time, were used to visualize and quantify the wave propagation, see Figure 5.4 b and e. As previously described for the FEM simulations, M-panels were first resampled and mildly tapered before applying a normalized Radon transform to determine the WS. A 15 – 100 Hz bandpass filter (6th-order Butterworth) was applied on the axial tissue velocity data, since the waves after AVC were found to be in this frequency range [42]. For the parasternal view measurements, the minimum intensity corresponding to the particle motion away from the transducer was selected in the Radon domain. For the apical view measurements, the maximum intensity of the Radon transform was selected to determine WS, see Figure 5.4 c and f. These extrema were most representative for the waves in the two views as shown in the unfiltered M-panels in Figure 5.4 b and e.

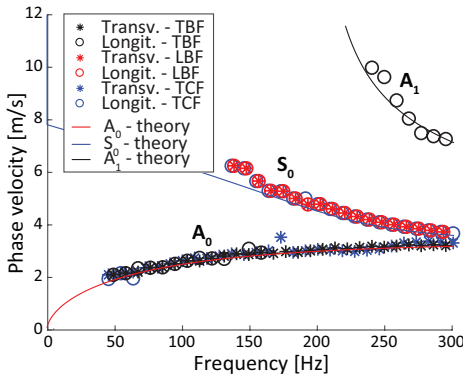


Figure 5.5: Finite Element Simulations; Phase speed plots obtained for the transversal and longitudinal particle motion of the M-panels from Figure 5.3. Different types of forces are used; a transversal body force (TBF), a longitudinal body force (LBF) and a transversal contact force (TCF). Also theoretical dispersion curves for a non-stretched inviscid plate submerged in water with a shear modulus of 16 kPa, a density of 1050 kg/m³ and a thickness of 10 mm [32] are depicted in the figure.

5.2.4. Statistics

The statistical toolbox in Matlab was used for the statistical analysis. The data were tested for being normally distributed by applying Kolmogorov-Smirnov tests. Since the data was not normally distributed, a non-parametric Wilcoxon signed-rank test was used to test whether measured differences are statistically different. A Bland-Altman analysis was performed to compare the WS for the two views by mean differences, limits of agreements (LOA) and range. Correlations were determined by computing linear correlation coefficients (Pearson) and by performing linear regressions. To compare our values with those in literature, we computed the mean and standard deviation of the median values obtained per volunteer.

5.3. RESULTS

5.3.1. Simulation Results

Figure 5.3 shows the simulation M-panels obtained for the transversal and longitudinal body force, and the transversal contact force, all with a center frequency of 160 Hz. Its resulting phase speed plots are visualized in Figure 5.5, and correspond well with the theoretical dispersion curves of the A- and S-modes for a inviscid plate submerged in water as described by [69]. For the transversal body force (Figure 5.3 a), phase speed plots of A_0 were found in the lower frequency range for both particle motion components, as can be expected from the predominantly transversal motion in such A_0 -mode. For higher frequencies, a higher order A_1 -mode was found to be dominant for longitudinal particle motion, whereas this was still the A_0 -mode for transversal particle motion. The M-panels in Figure 5.3 show similar WS for both transversal and longitudinal particle motion even though the magnitude of the transversal particle velocities was larger (ratio of 20.2 for transversal versus longitudinal motion). This indicates that a single wave mode was present. For the longitudinal body force (Figure 5.3 b), phase speed plots of S_0 were found for both particle motion components, as can be expected from the predominantly longitudinal motion in such S_0 -mode. Accordingly, similar WS were found for the

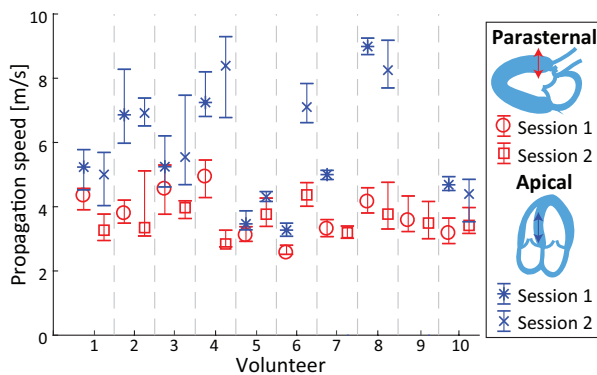


Figure 5.6: Overview of the median propagation speeds and their inter-quartile ranges obtained in parasternal and apical view.

M-panels in Figure 5.3 b, indicating the presence of one wave mode. A longitudinal body force led indeed to larger particle velocities in the longitudinal direction (ratio of 0.07 for transversal versus longitudinal motion). For the simulations of the contact force (Figure 5.3 c), a phase speed plot similar to the theoretical A_0 -mode was found for the transversal particle motion, while a phase speed plot similar to the theoretical dispersion curve of the S_0 -mode was found for the longitudinal particle motion. Hence, different WS were obtained for the M-panels in Figure 5.3 c for the longitudinal and transversal particle motion. This suggests that different wave modes are simultaneously present. In this case, the transversal particle velocities were found to be larger, but in the same order as in the longitudinal direction (ratio of 3.7 for transversal versus longitudinal motion).

When using a center frequency of 60 Hz (data not shown), similar phase speed plots were obtained. However, for the contact force, the difference in transversal and longitudinal particle velocities was found to be clearly larger (ratio of 11.7). This shows that depending on the source, different modes may be excited or the relative amplitudes of different modes may differ. Furthermore, the results show that when the particle motion in both directions is dominated by the A_0 -mode for a frequency band of 15 – 100 Hz, the particle motion is largest in transversal direction. The contrary holds for the S_0 -mode. Translating these results to cardiac valve closure, they indicate that depending on the wave modes induced by the valve closure, different WS values can be found for the transversal and longitudinal particle motion. Furthermore, the ratio of tissue motion amplitudes in both directions can be an indicator for the wave modes induced.

5.3.2. Experimental Results

Figure 5.6 shows the median WS and inter-quartile ranges (IQR) obtained for the measurements in human in parasternal and apical view. The median SWS varied between 3.2 – 4.3 m/s for parasternal view and 3.5 – 8.7 m/s for apical view. It should be noted again that the number of measurements performed in the two views differed. Furthermore, the number of heart cycles captured in a single recording

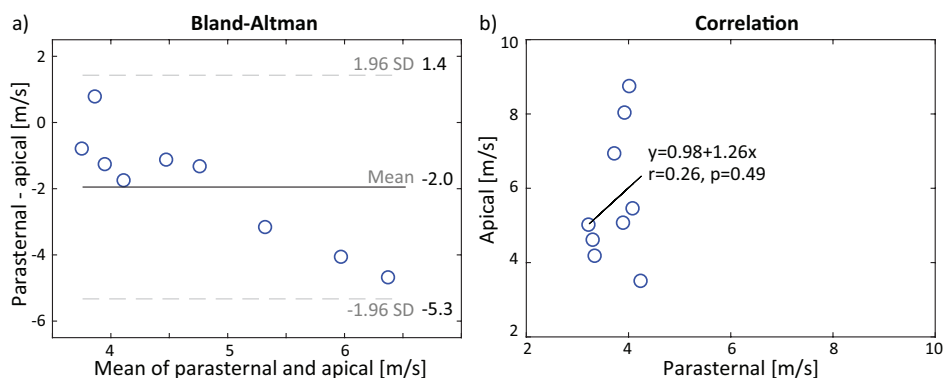


Figure 5.7: (a) Bland-Altman analysis of the median propagation speeds obtained per volunteer for the velocity panels. (b) No correlation was found between the propagation speeds obtained in apical and parasternal view.

varied depending on the heartrate of the volunteer. Moreover, recordings with a poor B-mode quality or with no visible propagating waves were excluded (13% of acquisitions). This resulted in a different total number of WS estimations for both views: $n=490$ for apical and $n=970$ for parasternal view. Propagation speeds above 10 m/s were assumed to be non-physical and were therefore excluded (apical exclusion: 14%, 68/490; parasternal exclusion: 0%, 0/970). For volunteer 9, no visible propagating wave with a speed below 10 m/s was measured in apical view.

An overview of the statistical results is shown in Table 5.2. As a first major result, for all sessions and all volunteers, we obtained higher median WS in apical than in parasternal view. A mean difference of -2.0 m/s was found (Bland-Altman analysis, LOA: -5.3 – 1.4 m/s, range: -4.7 – 0.76 m/s), see Figure 5.7 a. The differences were found to be statistically significant (Wilcoxon signed-rank test, $n=9$, $p<0.01$). We found a median for the median WS per volunteer per session of 3.8 m/s ($n=10$, range: 3.2 – 4.3 m/s) and 5.1 m/s ($n=9$, range: 3.5 – 8.7 m/s) in parasternal and apical view respectively.

As a second major result, no correlation was found between the WS in the two views ($r=0.26$, $p=0.49$), see Figure 5.7 b. Moreover, Figure 5.7 a shows that the difference in WS in general increases with the mean WS of the parasternal and apical view. Such trend in a Bland-Altman plot indicates again that the two measured variables have low correlation, as was seen with the correlation test, and/or that either has a high variance. To further investigate the differences in WS among the two views, the difference correlated to the WS in apical view ($r=-0.98$, $p<0.01$) and not to the WS in parasternal view ($r=-0.056$, $p=0.89$). When combining these statistical observations, we conclude that the differences between the two views are mainly caused by the inter-volunteer variance of the apical view measurements, and not of the parasternal view measurements. As described in the Materials and Methods section, five instead of one apical view measurements were recorded for volunteers 1 to 4 in the second scanning session. Figure 5.6 shows that the results obtained in the second session in

Table 5.2: Overview of the statistical characteristics of this study. Values denoted with an asterisk (*) are statistically significant ($p < 0.05$). Abbreviations: LOA: limits of agreement Bland-Altman analysis (± 1.96 SD), IVS: inter-ventricular septum.

Performed Test		Statistics	
Apical vs Parasternal	Wilcoxon signed-rank test on median propagation speeds per volunteer measured in apical vs parasternal view	$p = 0.0078^*$, $n = 9$	
	Bland-Altman: medians of parasternal - apical view per volunteer	Mean: -2.0 m/s LOA: -5.3 – 1.4 m/s Range: -4.7 – 0.76 m/s	
	Linear correlation of medians in apical and parasternal view	$r = 0.26$, $p = 0.49$	
	Linear correlation of differences in medians of the 2 views with the median in parasternal view	$r = -0.056$, $p = 0.89$	
	Linear correlation of differences in medians of the 2 views with the median in apical view	$r = -0.98^*$, $p < 0.01$	
		Apical View	Parasternal View
Inter-volunteer Variability	Median of median propagation speeds per volunteer	Median: 5.1 m/s, $n = 9$	Median: 3.8 m/s, $n = 10$
		IQR: 4.5 – 7.2 m/s	IQR: 3.4 – 4.0 m/s
		Range: 3.5 – 8.7 m/s	Range: 3.2 – 4.3 m/s
Test-retest Variability	Wilcoxon signed-rank test on median propagation speeds per volunteer measured in session 1 and session 2	$p = 0.31$, $n = 8$	$p = 0.43$, $n = 10$
	Bland-Altman: median propagation speeds per volunteer measured in session 1 – session 2	Mean: -0.61 m/s	Mean: 0.20 m/s
		LOA: -3.4 – 2.2 m/s Range: -3.8 – 0.74 m/s	LOA: -1.8 – 2.2 m/s Range: -1.8 – 2.1 m/s
IVS Orientation	Linear correlation of angle between M-line and axial direction and propagation speed	$r = -0.06$, $p = 0.2$	$r = 0.34^*$, $p < 0.01$

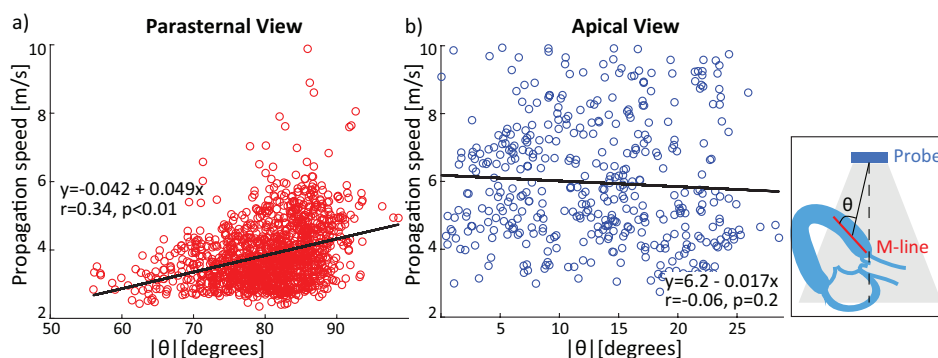


Figure 5.8: (a) A weak positive correlation was found between the propagation speed values measured in parasternal view with more horizontally aligned M-lines. (b) No correlation between propagation speed values measured in apical view and this angle was found.

5

apical view for these volunteers are within the IQR of the corresponding results in the first session. This suggests that the inter-scan variability in apical view is small compared to the intra-scan variability. Test-retest variability was tested by comparing the median values per volunteer per session. No statistically significant differences were found in apical view (Wilcoxon signed-rank test, $n=8$, $p=0.31$) and parasternal view (Wilcoxon signed-rank test, $n=10$, $p=0.43$) between the sessions. The mean differences were found to be -0.61 m/s (Bland-Altman analysis, LOA: $-3.4 - 2.2$ m/s, range: $-3.8 - 0.74$ m/s) and 0.20 m/s (Bland-Altman analysis, LOA: $-1.8 - 2.2$ m/s, range: $-1.8 - 2.1$ m/s) for the apical and parasternal view respectively.

Although the parasternal and apical views were chosen to approximate a respectively horizontal and vertical orientation of the IVS, variations in IVS angular orientation still occurred between acquisitions. This angular orientation was taken into account by manually drawing M-lines that are aligned with the orientation of the IVS. This way, the wave propagation was measured along the global orientation of the IVS. However, since the one-lag autocorrelation method is sensitive to axial tissue motion only, the tracking in the respective views could neither be attributed to purely longitudinal nor purely transversal particle motion in the IVS. By measuring the absolute angle $|\theta|$ between the M-line and ultrasound beam direction at the center of the M-line, the effect of M-line orientation with respect to the probe was tested in Figure 5.8. For the parasternal view measurements, a weak correlation between the WS and angle was found ($r=0.34$, $p<0.01$). The WS values were found to increase with increasing angle between M-line and axial directions. For the apical view measurements, no significant correlation was found ($r=-0.06$, $p=0.2$). Although this could be partly explained by the limited number of WS values obtained in apical view, also no trend in WS with respect to $|\theta|$ is visible in Figure 5.8 b.

5.4. DISCUSSION

5.4.1. General Findings

The propagation speeds of the natural mechanical waves induced after aortic valve closure measured in apical and parasternal view in ten healthy volunteers were compared in this study. This study has three main findings. First, the WS measured in apical view were found to be statistically higher than in parasternal view (median (IQR) of 5.1 m/s (4.5 – 7.2 m/s) vs 3.8 m/s (3.4 – 4.0 m/s), $p < 0.01$, $n = 9$). Although these values are in the same range as literature values (mean \pm standard deviation, parasternal: 3.7 ± 0.4 m/s, apical: 5.7 ± 1.8 m/s, see Table 5.1), they contradict the statement by Kanai (2005) that the propagation speeds measured in parasternal and apical view are similar. Second, no correlation was found between the WS measured in the two views ($r = 0.26$, $p = 0.49$). Third, an unexpectedly large inter-volunteer variability among healthy volunteers was found in apical view (3.5 – 8.7 m/s) versus parasternal view (3.2 – 4.3 m/s).

5.4.2. Relation with Lamb Waves

Our hypothesis posed in the introduction was that both A_0 - and S_0 -mode Lamb waves were excited, but that only one could be measured in each view. We measured statistically higher WS in apical than in parasternal view, which would support the hypothesis. Since one wave mode cannot have different WS along the same propagation path for the same frequency components, measuring two different WS in the two views suggests that different wave modes are measured. Furthermore, the simulations show that if one single wave mode is induced, similar WS are obtained; if different wave modes are induced simultaneously, different WS can be measured for the different particle-motion components. However, both modes would depend on the same material constants and would thus be related, but we did not find a linear correlation between the WS obtained in both views ($r = 0.26$, $p = 0.49$), suggesting that these measurements cannot be explained by a conventional Lamb wave model.

Since both A_0 - and S_0 -modes include transversal as well as longitudinal tissue motion, also a combination of different wave modes could have been measured. To what extent the different wave modes are measured in the different views could depend on the exact imaging plane, image quality, volunteer and the induced respective wave amplitudes. As an illustration, if a dominating A-wave is induced, the corresponding longitudinal tissue motion could interfere with the longitudinal tissue motion corresponding to an inferior S-wave being excited simultaneously. If the ratio of these waves differs per individual, this could have caused the variations in WS among the healthy volunteers. A smaller inter-volunteer variability was found for parasternal view (3.2 – 4.3 m/s) than for apical view (3.5 – 8.7 m/s), which could suggest that the measurements in parasternal view are less affected by the interference of different wave modes, possibly due to the presence of a dominating transversal wave mode, which might loosely be called the ‘shear wave’.

Furthermore, in additional simulations (data not shown) we found that the exact orientation of tracking direction with respect to the wave propagation direction has an effect if the amplitudes of the wave modes differ significantly. In fact, while simulating a high-amplitude A_0 and low-amplitude S_0 , the tracked propagation speed of the S_0 was strongly reduced by a minor change of rotation of the tissue. Based on these simulations one could expect lower WS in measurements with a more horizontal IVS (*cf.* Figure 5.8 a; 90 degrees indicates a horizontal M-line) if both A_0 - and S_0 -waves are induced. This is contradicted by our experimental results: we found a weak positive linear correlation between the WS and angle in parasternal view, and no correlation in apical view (see Figure 5.8). Therefore, the results of this study do not support the above hypotheses of either single or a superposition of pure Lamb waves. For this reason, we refrain from converting WS to physical quantities of myocardial stiffness in this study.

5.4.3. Apical View Measurements

In principle, other phenomena might have caused the unexpectedly large inter-volunteer variability in apical view (3.5 – 8.7 m/s) vs. parasternal view (3.2 – 4.3 m/s). A possible cause is the variability in image plane in apical view. In an apical 4-chamber view, the aortic valve – source of wave excitation – is not in the imaging plane, and possibly therefore measuring waves after AVC is more challenging. This also gives the sonographer more freedom when selecting the image plane, possibly causing extra variability. By using an apical 3-chamber view, the same plane would be imaged as in a parasternal long-axis view. However, we experienced difficulties in obtaining an acoustic window with a vertically oriented IVS in an apical 3-chamber view due to limited acoustic access for the first few volunteers and therefore decided to only record apical 4-chamber views to improve feasibility and repeatability of the acoustic window among the volunteers. Furthermore, other apical studies of the natural waves after AVC in literature also used the 4-chamber view [44, 45]. The impact of the selected apical view needs further investigation, for which a larger study population is better suited to cope with a larger fraction of unmeasurable 3-chamber views.

The used Lamb-wave model assumes a fluid-immersed elastic plate which might be too simplistic for the viscoelastic hyperelastic anisotropic IVS *in vivo* [101]. Furthermore, the apical view measurements track different tissue motion components with respect to fiber orientation. This suggests that apical WS measurements might provide additional information about the heart's mechanical properties, next to parasternal WS measurements. However, this statement should still be proven in future physiologic studies.

5.4.4. Study Limitations

The parasternal wave measurements were repeated five times per volunteer per session, whereas there was only one measurement for the apical wave recordings.

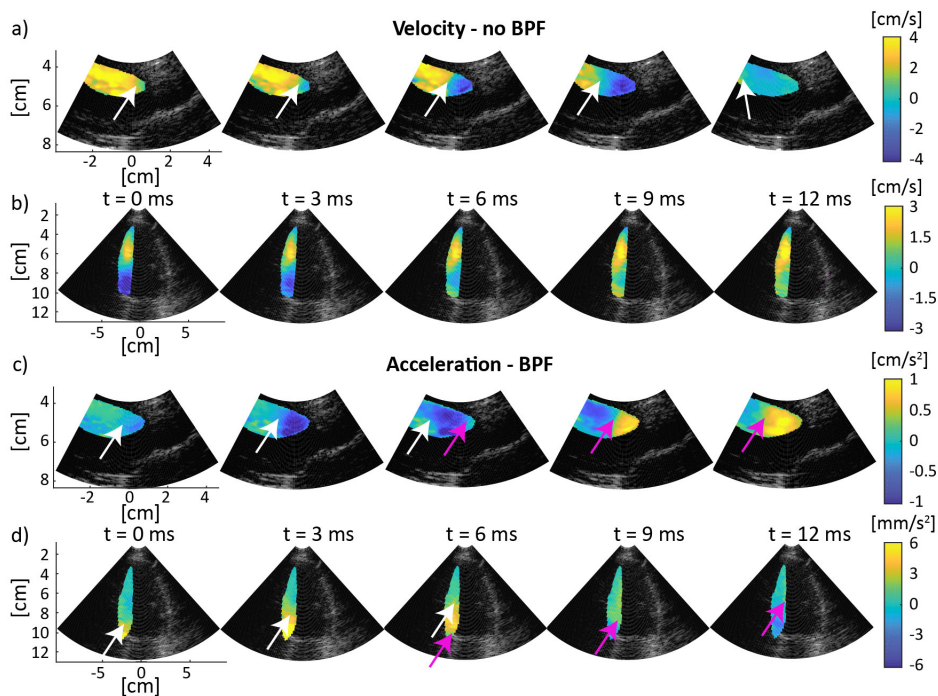


Figure 5.9: Propagation of the waves after AVC in parasternal (a, c) and apical (b, d) view. Velocity Tissue Doppler values (a, b) as well as acceleration Tissue Doppler values after applying a bandpass filter (c, d) are shown in the figure. White and pink arrows depict the propagation of the waves. No clear propagating wave is seen in apical view when using the tissue velocity values, in contrast to when using acceleration values.

Despite this limited number of apical view measurements, only one volunteer showed a remarkable disagreement in apical view for the different sessions (volunteer 6 in Figure 5.6), possibly due to the different location of the IVS in the field of view. The other volunteers showed a fair agreement between the apical sessions. Furthermore, for the first four volunteers, we also recorded five measurements in apical view in the second session. Compared to the intra-scan variability, no large inter-scan variability was found, thus validating our approach to only record one single clip in apical view for most volunteers. These observations show that the measurements in apical view are at least repeatable.

Literature [40, 42, 80] also reports the use of tissue acceleration panels instead of tissue velocity panels, which allows an easier detection of a ‘wave pattern’ propagating over the IVS (see lower two rows of Figure 5.9) as slower motion (such as cardiac rotation or translation as the heart starts to relax) is suppressed. However, when using acceleration panels in our study, different WS were obtained than when using tissue velocities, confirming observations in [89]. Additionally, we obtained more WS values above 10 m/s, which were assumed to be non-physical (apical view: 31% vs 14%; parasternal view: 1% vs 0% excluded). Therefore, we used tissue

velocities instead of tissue accelerations in the current study to investigate the differences measured in parasternal and apical view.

5.4.5. Clinical Application

For the application in clinical diagnosis, significant differences between WS estimations after AVC in healthy and diseased myocardium should be measured. First clinical studies of natural mechanical waves after AVC in parasternal view obtained higher WS values for cardiac amyloidosis and hypertrophic patients [39, 40]. To the best of our knowledge, no clinical studies using WS measurements after AVC in apical view have been published yet. This work showed a lower inter-volunteer variability in parasternal view (3.2 – 4.3 m/s in parasternal view vs 3.5 – 8.7 m/s in apical view), which is an advantage for a more robust clinical diagnosis. However, the cause of the observed high inter-volunteer variability in apical view should still be further investigated, preferably while taking an apical 4-chamber and 3-chamber view into account. 3D acquisitions with a high temporal and spatial resolution in order to measure different tissue motion components, and simultaneously measure the propagation direction would be beneficial for this purpose. Since higher WS, corresponding to larger wavelengths for the same frequency, can be tracked less accurate due to the limited IVS length and limited frame rate [89], it is an advantage for accuracy and precision to measure lower normal WS for healthy volunteers in parasternal view. Therefore, our results in combination with initial proof of clinical relevance suggest that parasternal WS measurements are currently favorable for robust clinical diagnosis. However, parasternal and apical view measurements might contain additional information about myocardial material properties, which could potentially improve current disease diagnosis. Further work should thus investigate the clinical added value of apical WS.

5.5. CONCLUSION


This study compared the propagation speeds of natural mechanical waves after AVC in apical and parasternal view in ten healthy volunteers. Significantly higher propagation speeds were obtained in apical than in parasternal view (median (IQR) of 5.1 m/s (4.5 – 7.2 m/s) vs 3.8 m/s (3.4 – 4.0 m/s), $p < 0.01$, $n = 9$). The propagation speeds in the different views were not correlated ($r = 0.26$, $p = 0.49$). Furthermore, an unexpectedly large inter-volunteer variability among healthy volunteers was found in apical view (3.5 – 8.7 vs 3.2 – 4.3 m/s in parasternal view). According to our statistics, the theory of Lamb waves alone cannot explain the differences in propagation speeds measured in the two views. However, the parasternal long-axis view seems to be preferred in future clinical diagnosis, as this view resulted in lower inter-volunteer variabilities and has been earlier shown to relate to several diseases.

Acknowledgements

The authors thank Dr. G. McLaughlin and Dr. Y. Chen of Mindray Innovation Center, San Jose, CA, USA, for providing the Zonare ZS3 system with the customized high-frame-rate imaging modes. This work is part of the STW/TTW – Dutch Heart Foundation partnership program 'Earlier recognition of cardiovascular diseases' with project number 14740, which is (partly) financed by the Netherlands Organization for Scientific Research (NWO).

6

Fundamental Modeling of Wave Propagation in Temporally Relaxing Media with Applications to Cardiac Shear Wave Elastography



Alberico Sabbadini
Lana B.H. Keijzer
Hendrik J. Vos
Nico de Jong
Martin D. Verweij

Based on:

"Fundamental Modeling of Wave Propagation in Temporally Relaxing Media with Applications to Cardiac Shear Wave Elastography", *The Journal of the Acoustical Society of America* **147**(3091), 2020 [102].

Abstract

Shear wave elastography (SWE) might allow non-invasive assessment of cardiac stiffness by relating shear wave propagation speed to material properties. However, after aortic valve closure, when natural shear waves occur in the septal wall, the stiffness of the muscle decreases significantly, and the effects of such temporal variation of medium properties on shear wave propagation have not been investigated yet. The goal of this work is to fundamentally investigate these effects. To this aim, qualitative results were first obtained experimentally using a mechanical setup, and were then combined with quantitative results from finite difference simulations. The results show that the amplitude and period of the waves increase, during propagation, proportionally to the relaxation of the medium, and that reflected waves can originate from the temporal stiffness variation. These general results, applied to literature data on cardiac stiffness throughout the heart cycle, predict as a major effect a period increase of 20% in waves propagating during a healthy diastolic phase, whereas only a 10% increase would result from the impaired relaxation of an infarcted heart. Therefore, cardiac relaxation can affect the propagation of waves used for SWE measurements and might even provide direct information on the correct relaxation of a heart.

6.1. INTRODUCTION

Cardiac diseases are a major cause of death in developed countries. Early diagnoses might help prevent the development of life-threatening conditions by detecting signs of deterioration before cardiac functionality becomes compromised. Such diagnoses may be obtained by monitoring the stiffness of the cardiac muscle, which has been observed to correlate with the health condition of the heart [20, 49, 103]. In order to monitor the material properties of the heart, however, non-invasive techniques must be employed, as invasive measurements are highly uncomfortable and potentially harmful for patients.

Shear Wave Elastography (SWE) exploits wave propagation phenomena to explore the elastic properties of a material, and it has already been proven to be a viable tool in clinical applications [104–107]. Its application to cardiac settings, however, is hindered by a challenge intrinsic to the functioning of the heart: the heart cycle.

As the heart performs its pumping function, its stiffness increases and decreases cyclically to allow for the heart chambers to fill with blood and expel it. Aortic valve closure, which provides one of the sources of waves that can be employed for cardiac SWE [40, 42, 64, 80, 89, 108], takes place at the beginning of the isovolumic relaxation of the muscle; due to the muscle relaxation, the waves generated at this time could experience a change in propagation speed of $\approx 15\%$ in just 10 ms (estimated based on the stiffness variation measured in isolated perfused rabbit hearts [109]). While SWE performed on waves naturally occurring in the heart could be more precisely called "natural" SWE, we will refer to it simply as SWE, because the phenomena involved are similar to those of shear waves from non-natural sources (e.g. acoustic radiation force pushes).

Several models are employed in literature to describe the mechanical properties of the cardiac tissue [26, 110–112], however, to the best of our knowledge, all the models employed for elastography assume the mechanical properties of the medium to be constant or, at most, slowly varying [43] in the timescales of the propagating wave. This assumption may hold true for mechanically inactive organs, yet its validity is questionable in the context of SWE measurements performed during diastolic relaxation.

In fact, the existence of measurable effects of time-varying medium properties on propagating waves has already been established in the field of electromagnetism, with theoretical descriptions of media changing smoothly or instantaneously [113–120]. These studies predict that a wave that propagates at varying speed (i.e. in a medium with temporally varying dielectric or magnetic constant) is subjected to a variation in amplitude and oscillation period; additionally, reflected waves are generated at time-discontinuities of the medium, similarly to what happens at the spatial interface of two media. Experimental studies [113, 121] confirmed the predictions regarding amplitude and frequency changes by observing magnetic waves propagating in media subjected to an externally modulated magnetic field. To the best of our knowledge, reflected waves were not observed experimentally. It remains

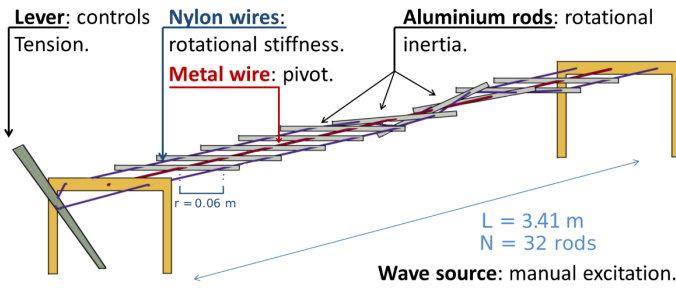


Figure 6.1: Experimental setup: the central wire (red) provides the pivot around which the bars rotate; the two nylon wires (blue) provide the restoration force to enable waves. The lever can be used to control tension in the wires.

an open question whether these effects are present also in elastic waves, and whether they should be taken into account while performing cardiac elastography.

The goal of the present study is to observe and describe the effects that a temporally varying propagation speed has on mechanical waves, in order to assess their relevance to shear wave elastography of the heart. While a live heart itself could be in principle used as a medium to perform these studies, it would be impractical, since its complicated geometry and material properties would make it hard to reliably isolate and identify the specific effects of temporal variations. For this reason, we have chosen to model a simplified setting in which speed variations represent the only complication to 1D wave propagation. We have developed an experimental setup consisting of rotating metal rods suspended by nylon wires (a wave machine), in which the tension can be controlled in real time to alter propagation speed. The rotational displacement of the rods can then travel through the setup as a 1D torsional wave with varying speed. Moreover, we developed finite difference simulations that describe these phenomena numerically. We employed the setup to obtain a first, qualitative confirmation that mechanical waves can also be affected by variations over time of medium properties. The simulation, on the other hand, allowed us to investigate quantitatively how the time-dependent effects are related to the dynamical parameters of the system, i.e. the amount of speed variation and the rate at which this happens.

We apply our findings to data on rabbit hearts [109] to predict the effects of muscle relaxation on cardiac elastography measurements, and we discuss their relevance and possible applications as a new diagnostic tool.

6.2. SETUP

6.2.1. The Wave Machine

We have built a modified Wave Machine [122] in which the speed of the wave can be controlled during propagation by means of tension variations. As shown in Figure 6.1, the setup consists of two wooden frames, placed at 3.63 m from each other, that support three wires on which 32 aluminum rods are suspended. Each rod is 60 cm long and has a 1 cm x 1 cm square cross-section. The central wire is made of steel and

runs through a hole in the midpoint of the long side of the rod, providing a pivot around which the rods can rotate freely; bolts are fixed to the central wire before and after each rod, to prevent them from translational movements. The other two wires, symmetrically placed at both sides of the steel wire, are made of nylon and can freely slide through their holes in the rods, so that stretching of these wires does not cause translation of the rods. The nylon wires provide the restoration force that opposes rotational displacements from the mutual angular position of the rods. During experiments, the amplitude of the applied perturbation had a gaussian-like shape, as this was the easiest to produce by hand. When a rotational perturbation is applied to one of the rods, it propagates along the setup through the nylon wires, effectively creating a discretized one-dimensional torsional wave. This system can be seen as a discrete approximation of the continuous case in which the distance between two consecutive rods approaches zero. For our case the propagation of the torsional wave can approximately be described by the wave equation

$$\frac{2r^2FL}{IN} \frac{\partial^2 \theta}{\partial z^2} = \frac{\partial^2 \theta}{\partial t^2}, \quad (6.1)$$

where $r = 0.060 \pm 0.001$ m is the distance between steel and nylon wires, F is the variable tension in each wire, $L = 3.410 \pm 0.005$ m is the distance between the two extremal rods, $I = 0.0049 \pm 0.0004$ kg·m² is the moment of inertia of a rod, $N = 32$ is the total number of rods and θ is their angular displacement. This yields a torsional wave speed

$$c = \sqrt{\frac{2r^2FL}{IN}}. \quad (6.2)$$

6.2.2. Tension Control

The tension in the wires could be manually controlled, during experiments, by means of a mechanical lever connected to the nylon wires: pulling the lever would result in stretching of the wires, with a consequent increase in tension. Relaxation of a muscle can be mimicked by pre-stretching the wires, then releasing the lever over a transition time τ during wave propagation; with a framerate of 60 frames per second, it was not possible to determine τ from the video recordings.

To verify the reliability of Equation 6.2, a first experiment was run with a force gauge (Force Gauge TMT-5020, OCS.tec GmbH & Co. KG, Neuching, Germany) connected to one end of the nylon wire, so as to compare the values of c derived from the equation and those measured directly. During this experimental validation, the tension read by the force gauge was $F = 13.75 \pm 0.2$ N, corresponding to a calculated speed of $c = 1.50 \pm 0.14$ m/s, a value comparable, within the experimental tolerance, with the speed measured directly from the video recordings, $c = 1.65 \pm 0.02$ m/s. While the value of speed determined from the tension measurement suffered from a relatively high experimental uncertainty, the uncertainty of the direct speed measurement depends essentially on the framerate of the recording, allowing for more precise measurements. In our experiments, therefore, the propagation speed

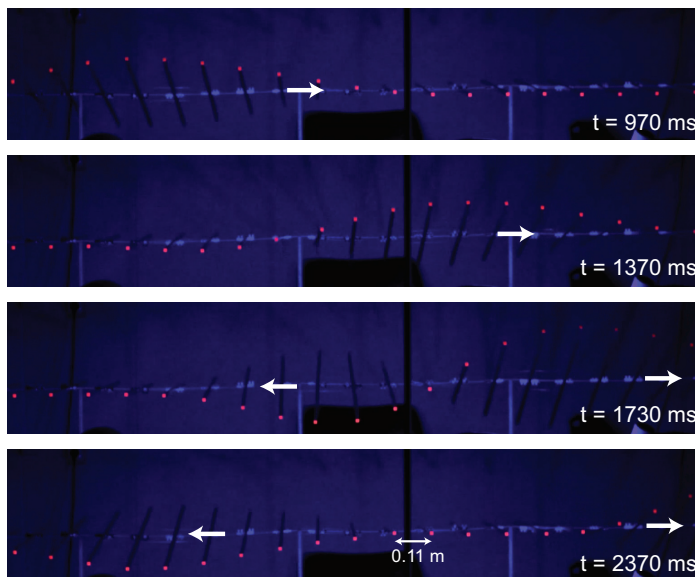


Figure 6.2: Snapshots in time of a wave propagating in the experimental setup. From $t = 1730$ ms onwards, a reflected wave can also be seen propagating backwards.

6

was measured by acquiring and analysing video-recordings of the wave. Although not necessary, the tension of the pre-stretched nylon wires could be estimated from the speed measurements via Equation 6.2: with a speed $c_1 = 3.00 \pm 0.02$ m/s, the tension was estimated to be 57.0 ± 0.1 N. With the lever in its rest position, on the other hand, the wave traveled at a measured speed of $c_2 = 1.40 \pm 0.02$ m/s, corresponding to a tension of $F = 12.4 \pm 0.1$ N.

6.2.3. Data Acquisition

A digital single lens reflex camera (Nikon D5300, Nikon Corporation, Tokyo, Japan) with framerate of 60 frames per second, facing the cross section of the rods, was used to record the propagating wave from one side, with a field of view of approximately 2 m that allowed the imaging of 18 rods in the center of the setup. In order to increase the contrast between the setup and the background, the tips of the rods were painted with an orange phosphorescent paint that reacts to ultraviolet (UV) light. We performed the experiments in a dark room illuminated only by 5 UV 60-W lamps, so that the bright orange glow of the extremities of the rods would be easily distinguishable from the background. This allowed us to isolate and track their motion in post-processing, using the software ImageJ (National Institute of Health, Bethesda, Maryland, U.S.) to isolate the motion of each individual bar, and then importing all data in Matlab (version R2016b, MathWorks, Natick, MA, U.S.A.). Frames of the recorded propagating wave are shown in Figure 6.2, while Figure 6.3 shows a single videoframe and its numerical reconstruction.

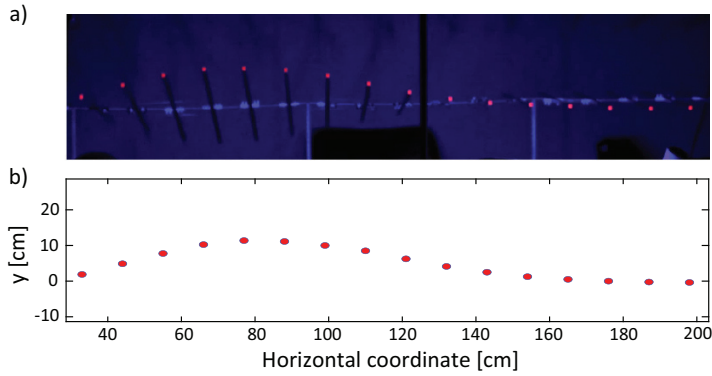


Figure 6.3: Snapshot of the wave propagating in the setup (a) and reconstructed points after image processing (b).

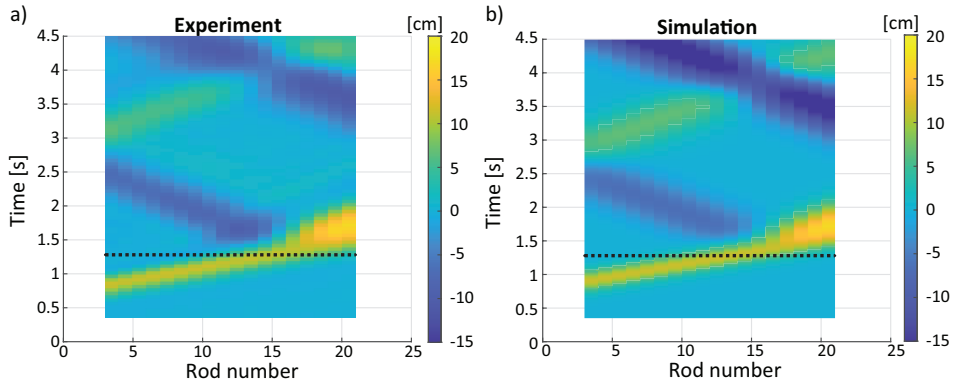


Figure 6.4: Experimental (a) and simulated (b) wave propagation in space-time. The color map represents the amplitude of the rotation of the bars: the bright yellow 'band' shows the waves with positive amplitude, the darker areas correspond to reflected waves with negative amplitude, while the brightening and the broadening in the vertical direction, starting around $t = 1.5$ s, represent the period and amplitude increase, respectively. The dotted line shows the time at which the tension in the system is suddenly dropped.

6.3. RESULTS

During the experiments, the nylon wires were first pre-stretched to the maximum tension of 57 N. A single unipolar wave pulse was then manually generated by perturbing the first metal rod, and the tension was subsequently dropped to 12.4 N by releasing the lever during propagation. In order to avoid the superposition of boundary reflections with the waves we wanted to study, the release of the lever was timed so that the waveform would always be in the center of the system when the tension dropped. The tension drop happens in a fraction of a period. Figure 6.4 shows the propagation measured during an experiment: the axes represent the time elapsed and the spatial coordinates of each rod expressed by rod number; due to the limited

field of view of the camera, the extremal rods were not imaged and therefore do not appear in the plot. The color scheme represents the amplitude of rotation of each bar, so that the bright yellow 'bands' essentially correspond to the positive forward traveling wave. At time $t \approx 1.5$ s the effects of the tension drop can be seen. A reflected wave appears as the broad band that moves backwards from right to left, with its negative amplitude represented in dark blue. In addition, broadening of the waves in the vertical (time) direction represent an increased time-period, and their increased brightness indicates a growth in amplitude.

We note a remarkable similitude with the behaviour of waves crossing the spatial discontinuity between two media, the main difference being that, in the case of a temporal discontinuity, it is wavelength that is conserved, while the period changes. In order to better understand the parallelism, let us look at a wave equation in which the wave speed depends on the spatial coordinate

$$c^2(z) \frac{\partial^2 \theta}{\partial z^2} = \frac{\partial^2 \theta}{\partial t^2}. \quad (6.3)$$

Next, we consider the current situation, in which the wave speed depends on time, giving the equation

$$c^2(t) \frac{\partial^2 \theta}{\partial z^2} = \frac{\partial^2 \theta}{\partial t^2}. \quad (6.4)$$

By defining a new parameter $s(t) = 1/c(t)$ called *slowness*, we can rewrite the equation as

$$s^2(t) \frac{\partial^2 \theta}{\partial t^2} = \frac{\partial^2 \theta}{\partial z^2}. \quad (6.5)$$

This resembles Equation 6.3, but with the roles of z and t being interchanged.

From the wave behaviour at a spatial discontinuity, it is known that the spatial period of the wave (i.e. the wavelength) varies proportionally to c , whereas its temporal period remains constant. By considering Equation 6.5 and performing the same reasoning as above, that is inverting the roles of space and time, we can expect that at a temporal discontinuity the time period will vary proportionally to s , whereas the spatial period will remain constant.

We then proceeded to implement in Matlab a 1D first order explicit Finite Difference scheme to solve Equation 6.3 numerically and simulate the behavior of the setup in different circumstances. In order to test the viability of the simulation to investigate these phenomena, we compared its results with experimental data: the parameters of the wave function, the space and the time discretizations were all chosen to match those of the experimental setup, i.e. spatial steps of 11 cm (the distance between rods) and time steps of 16 ms (the time between video-frames). The wave was simulated as a Gaussian pulse with an e^{-1} width of 0.3 s. A comparison between this function and the excursion of the third rod (the first one to be imaged in our measurements) is shown in Figure 6.5.

Figure 6.6 shows a comparison between simulation and experiment, by plotting the amplitude over time of two rods. The rods were chosen so that one would oscillate

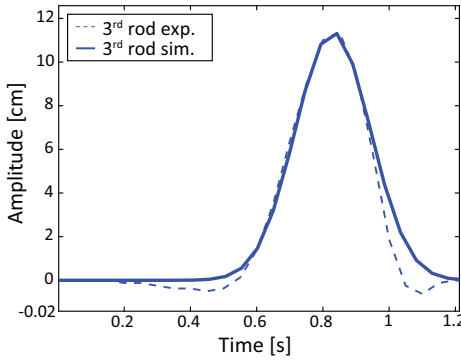


Figure 6.5: Comparison between the experimentally measured excursion of the third metal rod and the gaussian pulse used in the simulation as source of the wave.

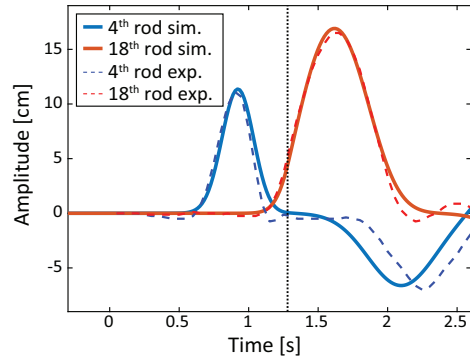


Figure 6.6: Comparison between simulation and experiment in the oscillation of two rods, reached by the wavefront respectively before and after the tension drop. The drop occurs at the time indicated by the vertical dotted line.

once before the tension lever was released, while the other would be crossed by the wave only after the sudden tension drop, which was simulated to happen in 16 ms, i.e. one time-step. The results of the simulation (solid line in Figure 6.6) are in qualitative agreement with the experiment in terms of amplitudes and period of the incident, transmitted and reflected wave around the transition phase. This validates our numerical approach. Having thus established its reliability, we continued our study by performing simulations only, in order to perform a systematic, quantitative study.

First, we ran simulations to determine the relation between the deceleration of the wave and the formation of transmitted and reflected waves. We computed the behavior of a 1-cycle, sinusoidal wave as could be generated on a 1D string. The spatial discretization was refined to a spacing of 0.01 m to increase spatial sampling of the waves, and the time discretization was shortened to steps of 0.1 ms, ensuring stability of the numerical scheme (Courant number $C_{num} \leq 0.028$) as well as correct sampling of all phenomena. Figure 6.7 shows how the amplitude and period of the transmitted and the reflected waves change as a function of c_1/c_2 , for fixed duration $\tau = 10$ ms of the deceleration. We can see that both amplitude and period increase linearly with the ratio between the initial and final propagation speed (c_1 and c_2 , respectively), in agreement with the relations $A_T/A_I = (c_2 + c_1)/2c_2$ and $A_R/A_I = (c_2 - c_1)/2c_2$ detailed in the Appendix, and the relation $T = c/\lambda$ with constant wavelength λ ; here, A represents the amplitude of the wave, T the period, and the subscripts I , R , and T represent the initial, reflected, and transmitted waves, respectively. When referring to the period of the wave before and after the tension drop, the subscripts 1 and 2 will be used, so that the two periods will be indicated by T_1 and T_2 respectively.

Furthermore, we investigated the effects of a deceleration taking place over longer spans of time, up to about twice the period of the wave. In our numerical

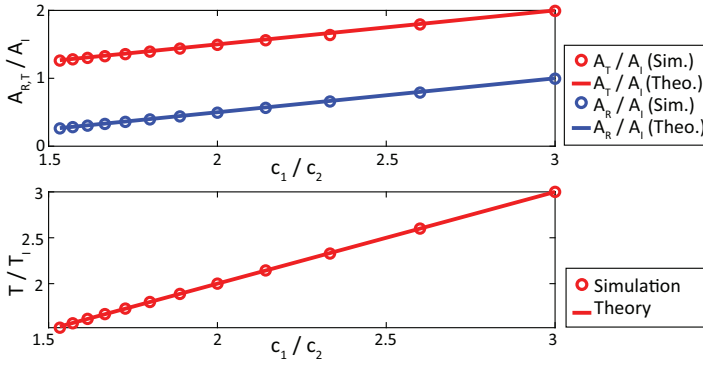


Figure 6.7: Amplitude ratios $A_{R,T}/A_I$ and period ratios T_2/T_1 as function of c_1/c_2 . Both amplitude and period can be seen to increase linearly with the decrease in speed. The blue curve shows the absolute value of the amplitude of the reflected wave, which, for a decelerating propagation, would be negative.

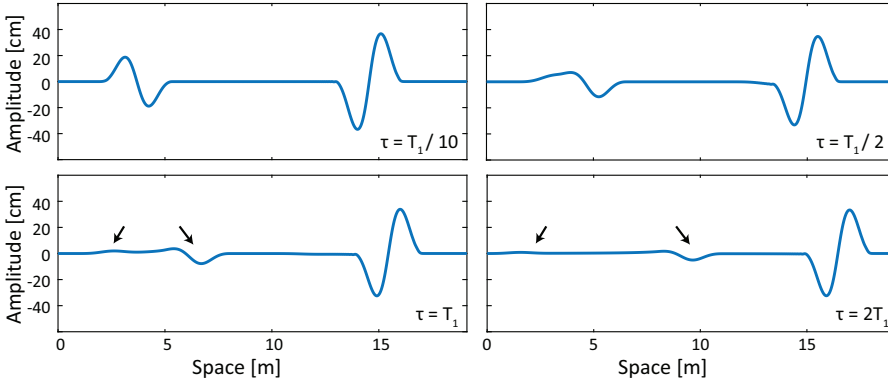


Figure 6.8: Snapshots of a wave after having propagated in a slowly relaxing medium, for different relaxation times τ . We can observe that the amplitudes decrease with increasing τ , and that a second reflected wave appears when $\tau/T_1 > 1$. The arrows point at the two reflected waves.

model, for $t < t_1$ the speed was 3 m/s; the speed then decreased linearly from 3 to 1 m/s, between t_1 and $t_2 = t_1 + \tau$, and was consequently kept at a constant value of 1 m/s for $t > t_2$. As shown in Figure 6.8, as the ratio τ/T_1 between transition time and wave period increases, the amplitude of transmitted and reflected wave decreases; the phase of the reflected wave appears to be opposite of that of the incident wave. Moreover, we can also notice that two reflected waves are actually present when $\tau/T_1 \geq 1$, whereas for shorter transition times there appears to be only one, albeit distorted, reflected wave. The variation in period of the wave does not seem to be affected by τ , as shown in Figure 6.9. Based on the results of these simulations, we conclude that reflected waves are generated at points in time when the acceleration of the wave is discontinuous; if two such points are separated by less than T_1 , two reflected waves will be generated, but they will partially overlap with each other, appearing to be a single, distorted waveform. On the other hand, if the distance in time between the two points is greater than T_1 , both distinct waveforms will be visible.

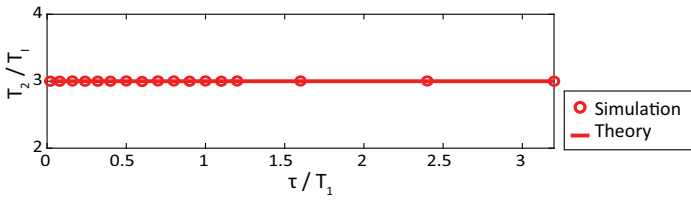


Figure 6.9: T_2/T_1 as function of deceleration time τ/T_1 . The period of the wave is unaffected by the relaxation time τ .

The results of the simulations detailed above offer an overview of the general effects that the temporal variation of a medium has on a propagating wave. In order to assess the relevance of these effects for cardiac SWE, we can input in our model realistic values of stiffness variation of the cardiac muscle to predict how the relaxation would affect a propagating shear wave. Let us first consider the diastolic phase of a heart in which the muscle isovolumic relaxation phase can be modeled by an exponential decrease in stiffness with time constant $\alpha = 50$ ms, as was measured in Langendorff perfused rabbit hearts [109]. Let us further consider that a shear wave traveling through the muscle is imaged (e.g. by means of ultrasound scanners) for a duration of $\delta = 10$ ms during this phase. Figure 6.7 and Figure 6.9 showed that the variation in period of the wave depends only on the ratio between initial and final speed, $T_2/T_1 = c_1/c_2$. The ratio itself can be easily computed knowing α and the δ , since $c_1/c_2 = e^{\delta/2\alpha}$. Considering $\alpha = 50$ ms and $\delta = 10$ ms, one could expect to observe an increase in wave period of 20%. On the other hand, an infarcted heart might have a relaxation constant $\alpha = 100$ ms [109]; under the same measuring conditions, one would then observe an increase in wave period of just 10%. Therefore, when reconstruction of the shear wave in space-time domain is possible, the broadening of the tracked shear wave in time could be used as an indirect measure of the relaxation that took place. The amplitude variation, however, being in the order of 3% and 2% for healthy and unhealthy hearts respectively, would be unlikely to be detected in realistic measurements.

6.4. DISCUSSION

Our results confirm that mechanical waves show a response to temporal variations of the medium comparable to the behavior of electromagnetic waves detailed in literature: the amplitude and the period of the traveling wave increase proportionally to the decrease in propagation speed, the wavelength is unaffected, and reflected waves can be generated at points of discontinuity in the acceleration.

Based on our numerical results, the predicted effects of cardiac relaxation are of particular interest: in fact, not only would a measured wave be affected by the relaxation of the muscle, it would actually be affected by the specific relaxation curve within the measurement. In other words, if two muscles relax at different rates, they may in principle be told apart by observing the variation in amplitude and period of waves traveling through them. The variations in period, in particular, could potentially be employed to directly help diagnoses of diastolic impairment (i.e.

reduced muscle relaxation), which is connected to diastolic heart failure. It should be noted that these results show a relation between initial and final period (or frequency), without any assumption about the initial value itself; therefore, the results are independent of the frequencies involved, and can apply to the frequency ranges typical of naturally occurring shear waves, as well as artificially induced ones.

As promising as these results may be, however, their practical implementation still presents challenges. First of all, the amplitude increase caused by diastolic relaxation is expected to be small and could be hard to measure during *in vivo* experiments, due to signal attenuation and noise. Moreover, because the relaxation of the muscle happens smoothly, there are no discontinuities to give rise to clearly observable reflected waves. Therefore, the only effect of temporal variations to be visible in clinical measurements may be the shift in wave period, and measurements with high time-resolution could be necessary to distinguish the different shifts of a healthy and a diseased heart. For example, for an initial frequency of 50 Hz, the time difference between an increase in the period by 10% and 20% is 2 ms, corresponding to a minimum imaging framerate of 500 Hz, while an initial frequency of 100 Hz would require a minimum framerate of 1000 Hz to discern the different period increases. Finally, due to the anisotropic, viscoelastic, three-dimensional nature of the heart, additional effects will compound to those produced by muscle relaxation, so that more complex models will be required in order to analyze data accurately.

Another matter to be noted is that the results presented in this study only show explicitly the effects of a wave that is generated before the relaxation begins; the relaxation of the medium takes place entirely during the propagation of the wave, and the effects are determined after the entire process has ended. However, when the closure of the aortic valve generates a wave, the cardiac muscle has already started relaxing; moreover, a SWE measurement based on such a wave would be over well before the cardiac relaxation process ended. Therefore, one could question whether the predictions formulated for real hearts can truly be trusted based solely on our numerical study. We argue that this is indeed the case: Figure 6.7 and Figure 6.9 show that the variation in period of the wave depends only on the ratio between initial and final speeds c_1/c_2 , where c_1 and c_2 correspond to the speed of the wave at the beginning and at the end of a measurement; this means that, for fixed c_1/c_2 , the variation in period will always be the same, regardless of whether the speed varies with a step function or a smooth curve. As mentioned above, the difference with our simulations, introduced by the smoothness of the diastolic relaxation, lies in the absence of reflected waves, which are generated at discontinuities. It is important to notice that, during a fixed measuring time, different relaxation curves (as could characterize healthy and diseased hearts) will result in different values of c_1/c_2 , therefore affecting the propagating wave differently.

Finally, we consider a wave produced by mitral valve closure, which may also be used to perform SWE. The mitral valve closes at the onset of systole, the contracting phase of the heart cycle, and, due to the stiffening of the muscle, waves traveling during this phase experience an increase in propagation speed. Based on our results, we expect that the amplitude and period of an accelerating wave will decrease proportionally to the increase in speed, and reflected waves will be once again generated at discontinuities in the acceleration.

From an experimental point of view, compared with other approaches proposed in literature to investigate waves in temporally varying media, the use of our setup shows several advantages. To begin with, the setup allows to observe the full phenomenon in its complexity, including not only the initial and final state of the wave, but its transition phase as well. Moreover, it can be easily built and modified so as to tailor the wave parameters (speed, amplitude) to specific needs, and the tension can be varied directly and in real time during an experiment; thanks to these features, more complex interactions (e.g. combining temporal variations with viscous behaviors) could be investigated with minor modifications of the setup.

There are a few limitations in our choice of setup as well: in particular, non-ideal matching of wires and rods, non-ideal fixed boundaries, and friction, are all factors that play a role in altering the behavior of the wave, degrading the match between experiment and idealized numerical simulation, as can be observed e.g. for the reflected wave in Figure 6.6 at times greater than 1.5 seconds. Moreover, due to the limited resolution and spatial window with which the motion of the bars can be detected by the camera, only wave amplitudes between 3 and 20 cm could be reliably detected. This meant that only a restricted parameter space could be practically investigated with the experimental setup. Nevertheless, the setup provided useful qualitative information, as well as a validation of our numerical approach; together, experiments and simulations proved to be a robust tool to investigate waves in time-dependent media.

6.5. CONCLUSIONS

We conclude that the variation over time of the stiffness of a medium, such as the beating heart, produces an inversely proportional variation in amplitude and period of a wave traveling through it. Furthermore, if the stiffness variation presented discontinuities, reflected waves would be generated. Based on the results of our numerical simulations and literature data, we predict that a healthy diastolic relaxation will affect propagating waves differently than an impaired process, producing a wave period increase twice as large as the one that might be observed in a dysfunctional organ. This difference may potentially be exploited to directly obtain information on diastolic functionality with one SWE measurement.

Acknowledgements

This work is part of the STW/TTW – Dutch Heart Foundation partnership program 'Earlier recognition of cardiovascular diseases' with project number 14740, which is (partly) financed by the Netherlands Organization for Scientific Research (NWO). Moreover, the authors would like to thank Henry den Bok, from the Delft University of Technology, and Geert Springeling, from the Erasmus MC, University Medical Center Rotterdam, for technical support with the construction of the experimental setup.

APPENDIX: REFLECTION AND TRANSMISSION COEFFICIENTS

We show here how the reflection and transmission coefficients can be calculated for a 1D transverse wave travelling on a string that undergoes an instantaneous material property variation (e.g. a decrease in tension). This situation can be considered to be the temporal equivalent of a wave travelling across the interface between two different, ideally bonded, strings. Let us assume that the instantaneous variation happens at time $t_0 = 0$, and let us consider an initial wave function $\psi_i = f_I(x - c_1 t)$ for all $t < 0$. As we have seen, after the temporal discontinuity, in the setup two waves are present, a transmitted wave $\psi_T = f_T(x - c_2 t)$ and a reflected wave $\psi_R = f_R(x + c_2 t)$. Notice that the transmitted and reflected waves travel at the same speed c_2 , with opposite signs. We can then consider two instants in time, before (B) and after (A) the discontinuity, and define two waveforms

$$\psi_B = \psi_i = f_I(x - c_1 t), \quad (6.6)$$

and

$$\psi_A = \psi_T + \psi_R = f_T(x - c_2 t) + f_R(x + c_2 t), \quad (6.7)$$

representing the deformation of the string in these two instants. Let us now make two considerations:

1. The deformation of the string has to evolve continuously from ψ_B to ψ_A at all coordinates x (a discontinuity of ψ between two consecutive instants requires movements at infinite speeds). Therefore, it follows that for all x :

$$\psi_B(x, 0) = \psi_A(x, 0) \quad (6.8)$$

$$\implies f_I(x) = f_R(x) + f_T(x).$$

2. The vertical speed of each individual particle in the string also needs to be continuous over time (a discontinuity of $\frac{\partial \psi(x, t)}{\partial t}$ in time would require infinite acceleration). We can write this condition as:

$$\left. \frac{\partial \psi_B(x, t)}{\partial t} \right|_{t=0} = \left. \frac{\partial \psi_A(x, t)}{\partial t} \right|_{t=0} \quad (6.9)$$

$$\implies -c_1 f'_I(x) = -c_2 f'_T(x) + c_2 f'_R(x).$$

Integrating the equation above and setting the integration constant to 0, we find that:

$$c_1 f_I(x) = c_2 (f_T(x) - f_R(x)). \quad (6.10)$$

We can then solve Equation 6.8 and 6.10 for f_R and f_T in terms of f_I , finding:

$$f_R(x) = \frac{c_2 - c_1}{2c_2} f_I(x), \quad (6.11)$$

$$f_T(x) = \frac{c_2 + c_1}{2c_2} f_I(x). \quad (6.12)$$

We have thus shown that the ratios of the amplitudes of initial, reflected and transmitted waves (A_I , A_R , and A_T , respectively) are equal to

$$A_R/A_I = \frac{c_2 - c_1}{2c_2}, \quad (6.13)$$

and

$$A_T/A_I = \frac{c_2 + c_1}{2c_2}. \quad (6.14)$$



A Direct Comparison of Natural and Acoustic-Radiation-Force-Induced Cardiac Mechanical Waves



Lana B.H. Keijzer*

Annette Caenen*

Jason Voorneveld

Mihai Strachinaru

Daniel J. Bowen

Jens van de Wouw

Oana Sorop

Daphne Merkus

Dirk J. Duncker

Antonius F.W. van der Steen

Nico de Jong

Johan G. Bosch

Hendrik J. Vos

**Both authors contributed equally.*

Based on:

"A Direct Comparison of Natural and Acoustic-Radiation-Force-Induced Cardiac Mechanical Waves", Accepted for publication in *Scientific Reports*, 2020. This is a post-peer-review, pre-copyedit version of an article published in Scientific Reports. The final authenticated version is available online.

Abstract

Natural and active shear wave elastography (SWE) are potential ultrasound-based techniques to non-invasively assess myocardial stiffness, which could improve current diagnosis of heart failure. This study aims to bridge the knowledge gap between both techniques and discuss their respective impacts on cardiac stiffness evaluation. We recorded the mechanical waves occurring after aortic and mitral valve closure (AVC and MVC) and those induced by acoustic radiation force throughout the cardiac cycle in four pigs after sternotomy. Natural SWE showed a higher feasibility than active SWE, which is an advantage for clinical application. Median propagation speeds of 2.5 – 4.0 m/s and 1.6 – 4.0 m/s were obtained after AVC and MVC, whereas ARF-based median speeds of 0.9 – 1.2 m/s and 2.1 – 3.8 m/s were reported for diastole and systole, respectively. The different wave characteristics on both methods, such as the frequency content, complicate the direct comparison of waves. Nevertheless, a good match was found in propagation speeds between natural and active SWE at the moment of valve closure, and the natural waves showed higher propagation speeds than in diastole. Furthermore, the results demonstrated that the natural waves occur in between diastole and systole identified with active SWE, and thus represent a myocardial stiffness in between relaxation and contraction.

7.1. INTRODUCTION

Heart failure affects 1 – 2% of the adult population in developed countries [2], and its social burden in terms of mortality, morbidity and healthcare costs is increasing due to the aging population [3, 4, 123]. Heart failure is a progressive chronic condition, typically preceded by cardiac remodeling – defined as structural and functional changes of the heart in response to altered hemodynamic loading and/or cardiac injury [6]. Current assessment of cardiac remodeling is incomplete as it relies on the ultrasonic measurement of cardiac volume, flow and tissue velocity; but not on the intrinsic mechanical properties of the heart [10]. Thus, a non-invasive technique that directly measures cardiac stiffness properties *in vivo* is highly desirable, since it could provide better understanding of the pathophysiology of heart failure. Such a direct assessment of tissue properties could be of particular value in the diagnosis of heart failure with preserved ejection fraction, in which diastolic dysfunction caused by an increase in myocardial stiffness, predominates. Furthermore, such a technique could serve as a screening tool for cardiac remodeling and be useful to stratify patients in order to accommodate personalized treatment [2].

Natural and active ultrasound-based shear wave elastography (SWE) are two promising methods that can potentially measure tissue elasticity. Natural and active SWE methods study the speed of the vibrations propagating over the myocardium, often referred to as shear waves or SWs. In theory, higher propagation speeds are expected for stiffer materials, resulting in a quantitative measure of tissue stiffness. Natural SWE analyzes the natural transverse vibrations induced in the myocardium after aortic and mitral valve closure (AVC and MVC) [39–44, 124], whereas active SWE uses a focused high-energy ultrasonic beam generating an acoustic radiation force (ARF) to induce a perturbation in the tissue of interest [54–58]. In this study, we will focus on the relationship between the natural vibrations after AVC and MVC and active SWE.

There is an increasing number of studies demonstrating the feasibility of SWE for the characterization of cardiac stiffness, of which many were performed in a research context: (i) natural SWE in *in vivo* animals [64] and *in vivo* healthy volunteers [43, 44]; and (ii) active SWE in *ex vivo* animals [84, 125, 126], *ex vivo* Langendorff-perfused animals [75, 109, 127], *in vivo* open-chest animals [51, 54, 55, 127] and *in vivo* healthy volunteers [58]. It is only very recently that various clinical studies have shown the potential of natural and active SWE to distinguish SW properties of the myocardium in different patient groups from healthy volunteers. Higher propagation speeds were measured in hypertrophic cardiomyopathy patients than in healthy volunteers, using natural SWs after AVC [39] and actively induced SWs at end-diastole [63]. Also, higher propagation speeds were found in cardiac amyloidosis patients when analyzing natural SWs after AVC and MVC [40]. Furthermore, a correlation between the SW propagation speed after MVC and myocardial remodeling in hypertensive heart disease patients was found [41].

Even though both types of SWE have shown promising results in measuring cardiac stiffness, the differences inherently related to the nature of the SWE techniques used, but also due to variations in experimental settings, complicate a direct comparison of different studies. There are two main inherent characteristics of the SWE methods that can result in differences in SW propagation speed. First, the different time of measurement in both SWE methods with respect to the relaxation/contraction state of the heart affects the measured SW propagation speed [55, 75] natural SWs after valve closure only occur at specific moments during the cardiac cycle, whereas ARF-based SWs can be induced at any time during the cardiac cycle. Second, the temporal and spatial characteristics of natural and actively induced SWs differ due to the differences in the mechanical excitation source. Typically, frequencies up to 500 Hz have been reported for active SWE [35, 128, 129], whereas this is maximally 150 Hz for natural SWE [42, 43, 64, 130]. Therefore, the measured SW propagation speed might be dissimilar due to wave velocity dispersion in the thin-walled myocardium (~10 mm). Next to these intrinsic factors, general experimental factors can also cause differences in SW propagation speed, such as the selected echocardiographic view and M-spline location and orientation within the interventricular septum (IVS) [55, 80]. For example, for ARF-induced SWs, it is known that measuring their propagation along the myocardial fiber orientation at mid-IVS (as done in a parasternal short-axis view) results in a higher SW propagation speed than measuring across the fiber orientation (as done in a parasternal long-axis view) [63]. Also, natural SWs measured in parasternal or apical view can give various SW propagation speeds due to a difference in the tracked tissue-motion component [96]. Interpretation of cardiac SWE data is thus complex, and it is unsure how these different SW measurements are related to each other and to the mechanical properties of the heart.

The term 'shear wave elastography' is generally used in literature [39, 40, 63, 64] when propagation speeds of transversal wave motion are measured to assess the material's stiffness. However, it should be noted that the term 'shear wave' does probably not describe the complex wave phenomena in the myocardium from a physics point of view. Therefore, from now on, we will use the terms 'wave' and 'wave propagation speed' throughout this manuscript to refer to the ARF-induced waves and the vibrations after valve closure.

In light of these considerations, the objective of this study is to directly compare the wave speeds in both SWE methods, within individual subjects and heartbeats. A systematic study on the effect of different experimental factors on measured wave propagation speeds as described above is outside the scope of this study. We studied the natural waves after AVC and MVC and compared these in the same echocardiographic view with actively induced waves induced throughout the cardiac cycle in four individual pigs. In this way, the potential effects of differences in experimental factors on wave propagation speeds was minimized. To make a fair comparison between the SWE methods, waves were analyzed in such ways as would have been done when using one individual SWE method. Thus, intrinsic differences in spatial and temporal characteristics of the natural and ARF-induced waves were

not circumvented. Until now, inducing and tracking ARF-induced waves throughout the cardiac cycle in a closed-chest transthoracic setting has been challenging [56, 65]. Consequently, the present study is performed in open-chest pigs in order to capture the stiffness variations throughout the cardiac cycle with active SWE. In this way, we compared the timing within the cardiac cycle and the spatial and temporal characteristics of the different SWE methods to better understand which aspects of ventricular stiffness are assessed by each method.

7.2. METHODS

7.2.1. Animals

This study included four Yorkshire x Landrace female pigs, 5 – 9 months old and weighing 85.5 – 100 kg. The study was approved by the Erasmus Medical Center Animal Experiments committee (Nrs. 17-2411-03 for animal 1 and 18-5224-01 for animal 2 – 4 [131]), and all methods were performed in accordance with relevant guidelines and regulations. Mean systolic aortic pressures of 101 mmHg, 77 mmHg and 82 mmHg were measured for pig 2, 3 and 4 respectively. These mean pressures were 76 mmHg, 33 mmHg and 57 mmHg respectively in diastole. No blood pressures were available for the first pig due to absence of such measurement in the research protocol. At time of the experiment, pigs were sedated by an intramuscular injection with a cocktail of Zoletil (tiletamine/zolazepam; 5 mg/kg; Virbac, Barneveld, the Netherlands), Sedazine (xylazine; 2.25 mg/kg; AST farma, Oudewater, the Netherlands) and atropine (2 mg; TEVA, Haarlem, the Netherlands), anesthetized with pentobarbital (9 mg/kg/h i.v.; Pharmacy Faculty of Veterinary Medicine Utrecht University, Utrecht, the Netherlands) and mechanically ventilated. Animals were positioned in a supine position to perform a sternotomy. The heart was dissected free without opening the pericardium.

7.2.2. Data Acquisition

SWE measurements were performed with a Vantage 256 ultrasound research system (Verasonics, Kirkland, United States) connected to a P4-2 probe (ATL, Bothell, Washington, United States). The probe was placed inside the animal's chest with a gel or water stand-off on the right ventricular free wall. Care was taken not to compress the stand-off material with the probe, and thus not to impose an extra pressure on the heart. Live conventional B-mode imaging (frame rate of 50 Hz) was used to find a long-axis parasternal view, with the mid-ventricular part of the IVS wall in the center of the image. The focusing depth of the push beam was then set between mid-IVS depth and endocardial border at the LV side. Live imaging was frozen when a high frame rate (HFR) SWE acquisition was performed, consisting of a natural and an active SWE sequence. Sequences were individually triggered by an analog R-peak output from an ECG module (CWE 3-leads Cardiotachometer CT-1000, Ardmore, United States). Radio frequency (RF) data were saved for offline processing.

Table 7.1: Overview of the data-acquisition and data-analysis settings for the natural and active SWE sequences. Abbreviations: SWE: shear wave elastography, RF: radio frequency, BPF: bandpass filter, IQ: in-phase and quadrature, LPF: lowpass filter, TDI: tissue Doppler imaging.

			Natural SWE	Active SWE
Data Acquisition	Wave excitation	Push frequency	-	2.0 MHz or 2.8 MHz
		Push duration	-	400 μ s
	Wave imaging	Virtual focus	-34 mm or -288 mm	
		DW imaging scheme	Progressive pulse-inversion (f_0 of 2 MHz) or 3-angle compounding (f_0 of 3 MHz)	
		Duration	1.2 s	20 ms or 28 ms at a rate of 34 Hz during 1.2 s
		Frame rate	Minimum of 2.2 kHz	Minimum of 3.5 kHz
Data Analysis	RF filter	Pulse-inversion	Butterworth 10 th -order BPF 3 – 4.5 MHz	
		Compounding	-	
	IQ filter (removal of blood motion and noise)		Butterworth 6 th -order LPF 250 Hz	-
	Tissue motion estimator		One-lag autocorrelation algorithm	
	Autocorrelated IQ filter (smoothing)		Gaussian 5.6° by 3.0 mm	Gaussian 1.9° by 1.0 mm
	TDI filter (removal of gross motion and noise)		Butterworth 6 th -order BPF 15 – 100 Hz	Butterworth 6 th -order BPF 75 – 750 Hz
	Wave speed estimator		Radon	Manual

A complete HFR SWE acquisition consisted of two consecutive sequences. During the first sequence, the natural waves were imaged for 2 s, using HFR diverging waves (DW) with a minimum frame rate of 2.2 kHz. During the second sequence, waves were induced by repeatedly applying ARF-push pulses during a period of 1.2 s, at a rate of 34 Hz. This resulted in 42 pushes per acquisition. One ARF-based SWE recording consisted of three consecutive stages: (i) HFR DW imaging as pre-push reference (4 – 20 frames), (ii) focused ARF-push beam transmission with a pulse duration of 400 μ s, and (iii) HFR DW imaging to track the wave propagation for 20 – 28 ms, at a minimum frame rate of 3.5 kHz.

Since different transmission settings have been suggested for SWE in literature [42, 58, 62, 65, 80, 132] and since there was no immediate feedback on the success of wave tracking, different settings were considered. We systematically cycled through a predefined scheme of transmission settings during the experiments, for both natural and active SWE. An overview of all data acquisition settings is given in Table 7.1. The following settings were altered throughout the acquisitions: (i) the virtual diverging-wave focus was either -34 mm or -288 mm, in which the far virtual focus theoretically resulted in a higher signal-to-noise ratio (SNR) and lower clutter levels but a reduced field-of-view width to track the wave; (ii) the tracking scheme was either a progressive pulse-inversion scheme (f_0 of 2 MHz) or a 3-angle compounding scheme (f_0 of 3 MHz); and (iii) the center frequency f_0 of the ARF-push beam was either 2.0 or 2.8 MHz. Since no superior acquisition scheme was found in terms of wave trackability, all successful SWE measurements (see section 'Feasibility of a SWE acquisition') were retained for further analysis – independent of the selected acquisition settings.

7.2.3. Data Analysis

Analytic in-phase and quadrature (IQ) data were obtained by offline beamforming the RF data using the Verasonics software (Kirkland, WA). For the pulse-inversion DW images, a 10th-order bi-directional Butterworth band-pass filter (3 – 4.5 MHz) was applied around the second harmonics of the RF data before beamforming. Post-processing of the analytic data was performed in Matlab R2019a (MathWorks, Natick, MA, USA). It is generally known that natural waves have a lower frequency content (maximal 150 Hz [42, 43, 64, 130] versus 500 Hz [35, 128, 129]) and thus larger spatial wavelength than ARF-induced waves. Therefore, different processing settings have been reported for natural and active SWE measurements in literature [42, 55, 62, 64, 86, 94, 128] (see Supplementary Table 7.1). To make a fair comparison between the SWE methods, waves were analyzed in such ways as would have been done when using one individual SWE method. An overview of the reasons for applying different processing settings for both methods is given in Supplementary Table 7.2. Taken into account the settings reported on in literature, the selected data processing settings for both SWE methods in this study are summarized in Table 7.1. A detailed explanation of the selected data analysis settings for each SWE method is given below. This table shows, for example, that a 3 times larger spatial smoothing filter and a frequency filter with 5 – 7.5 times lower cut-off frequencies were applied on the natural compared to

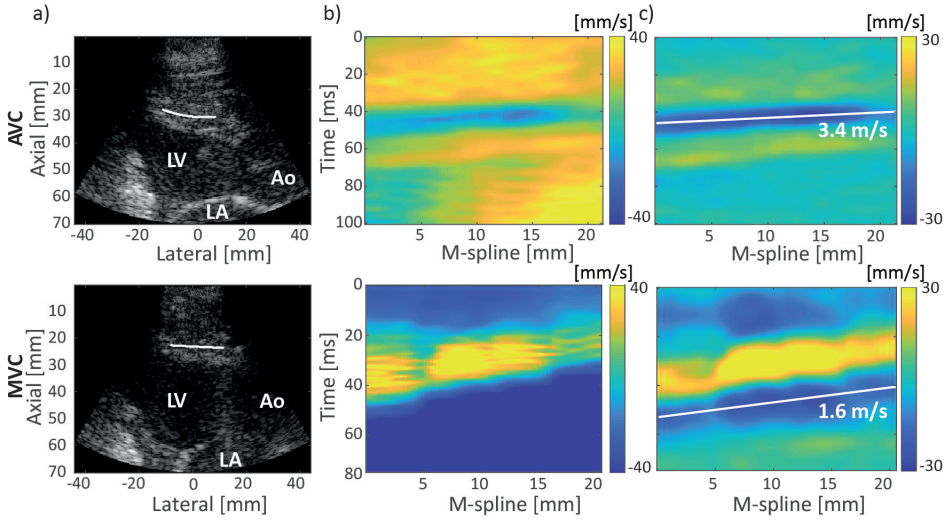


Figure 7.1: Example of a natural SWE acquisition. **(a)** B-mode at the moment of AVC and MVC, with indication of the considered M-spline. **(b)** M-panels for AVC and MVC depicting the axial tissue velocities as a function of time and space, without band-pass filtering the velocities. **(c)** Same M-panels as in **(b)**, now with a 15 – 100 Hz band-pass filter applied to the tissue velocities. The white line represents the tracked wave by using a Radon transform, with its slope corresponding to the wave speed. Abbreviations; LV: left ventricle, LA: left atrium, Ao: aorta.

the ARF-based SWE data, which is consistent with their dominant spatial and temporal wavelengths.

Natural SWE

To minimize the effect of blood motion and noise, a 6th-order bi-directional Butterworth low-pass filter (cut-off frequency of 250 Hz) was applied on the IQ data. Axial particle velocities were obtained by applying a one-lag autocorrelation technique [44], resulting in tissue Doppler imaging (TDI) data. The one-lag autocorrelation frames were smoothed using a Gaussian spatial smoothing filter of 5.6° by 3.0 mm in the polar domain, before calculating the phase. Anatomic M-mode splines (M-splines) were manually drawn on the basal/mid-ventricular part of the IVS at the moments of AVC and MVC, which were determined from B-mode and corresponding TDI image. The splines followed the curved shape of the IVS, i.e. the assumed propagation direction of the waves. Ten M-splines were drawn in total by two observers at various locations throughout the entire thickness of the IVS where waves were visible (an example for a M-spline is shown in Figure 7.1 a). Note that different propagation speeds can be obtained for separate M-splines drawn over the IVS in each acquisition, potentially caused by a changing fiber orientation over the thickness, by an inaccurate selection of the propagation direction, and by local variations in tissue stiffness, as previously shown [80]. Imprecision induced by tracking inaccuracies in determining the propagation speeds along individual

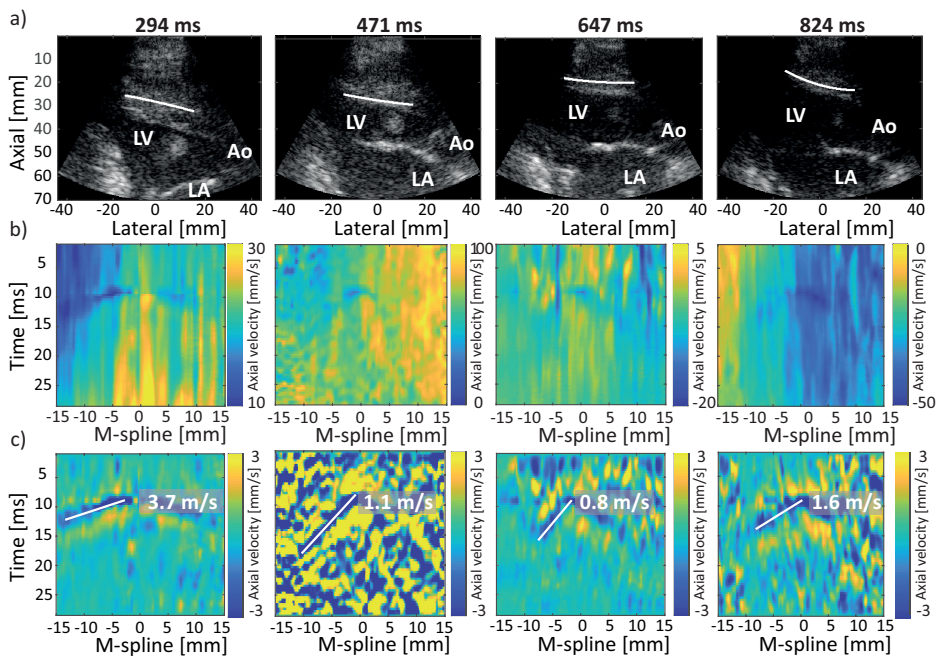


Figure 7.2: Example of an active SWE acquisition at 4 time points. **(a)** B-mode at 4 different time points across the cardiac cycle. The white spline in this B-mode represents a M-spline. **(b)** M-panels for the considered time points depicting the axial tissue velocities as a function of time and space, without band-pass filtering the velocities. **(c)** Same M-panels as in **(b)**, now with a 75 – 750 Hz band-pass filter applied to the tissue velocities. The white line represents the tracked wave, with its slope corresponding to the wave speed. Abbreviations; LV: left ventricle, LA: left atrium, Ao: aorta.

M-splines was reduced by averaging the propagation speeds obtained for the multiple M-splines drawn by two observers. This way, also the variability caused by M-spline location was included. The axial particle velocities along these M-splines were combined into M-panels, depicting tissue velocity as a function of space and time as shown in Figure 7.1 b. A 6th-order 15 – 100 Hz bi-directional Butterworth bandpass filter was applied on the TDI data to remove gross motion. In the M-panels, the waves are shown as wave patterns propagating from base to apex along the M-spline, see Figure 7.1 b and c. The propagation speeds were obtained by applying a Radon transform on the M-panels [65], which calculates the integral intensities along all possible linear wave paths in the 2D M-panel and selects the wave path corresponding to the minimum intensity. To prevent any bias, M-panels were first resampled to have an equal number of pixels in space and time, and the Radon domain was normalized [64, 86].

Active SWE

Similar to the processing of the natural SWE data, a one-lag autocorrelation technique was used to compute the axial particle velocities from the IQ data for active SWE. A

Gaussian spatial smoothing filter of 1.9° by 1.0 mm was applied to the autocorrelation frames to reduce the effect of noise. The reverberation frames that occurred after the ARF push were removed ($\sim 500 \mu\text{s}$) [128]. Subsequently, these missing frames between the reference and remaining frames were linearly interpolated to enable downstream processing. Gross motion and high frequency noise were reduced by applying a 6th-order 75 – 750 Hz bi-directional Butterworth bandpass filter to the M-panels. Similar as for the natural sequence, 5 M-splines were manually drawn by each observer for every ARF push (see Figure 7.2 a for example M-splines) to take into account inter-observer and intra-scan variability [86]. The limited SNR of the active M-panels (peak displacement values of $\sim 5 \mu\text{m}$ for active SWE [133] vs. $\sim 100 \mu\text{m}$ for natural SWE [42] [64]) did not permit a robust application of the Radon transform for wave propagation speed estimation, especially in systole where TDI amplitudes are the lowest. Therefore, each observer obtained wave propagation speeds from the slope of a manually drawn line following the negative peak TDI values in a M-panel (see Figure 7.2 b and c), propagating from the center of the probe towards the apex, as indicated in Figure 7.2 c. Performing the wave propagation speed analysis by two observers is expected to decrease the subjectivity associated with the manual wave tracking method.

7.2.4. Feasibility of a SWE Acquisition

To obtain representative diastolic and systolic wave propagation speeds without ECG recordings, a large part of the dynamic stiffness variations across the cardiac cycle needed to be captured in order to accurately define the 10% lowest and 10% highest median wave propagation speeds [62]. Therefore, a complete HFR SWE acquisition, consisting of a natural and active SWE sequence, was only included if the ARF-based waves could be tracked for more than 40% of the ARF pushes throughout the cardiac cycle by both observers. This means that SWE recordings with a significant amount of loss of probe contact during the cardiac cycle or with a low SNR for speed estimation were automatically excluded. Additionally, SWE acquisitions where the basal-mid ventricular part of the IVS was not visible, or in which the IVS was not quasi-horizontally oriented (angle with horizontal axis larger than approximately 30 degrees), were also discarded.

7.2.5. Statistics

Statistical analyses were performed using the statistical toolbox of Matlab. For natural SWE, median values and inter-quartile ranges (IQR) of the wave propagation speeds along 10 M-splines across all heart cycles within one acquisition were computed for AVC and MVC separately. A median wave propagation speed was also calculated for AVC and MVC in each pig individually. For the actively induced waves, the median and IQR of the wave propagation speeds across 10 M-splines were reported for every push in each acquisition. To obtain the median and IQR of the ARF-based wave propagation speed in systole and diastole of one animal, the time traces of individual acquisitions were first temporally matched, as ECG triggering did not properly work for the first two

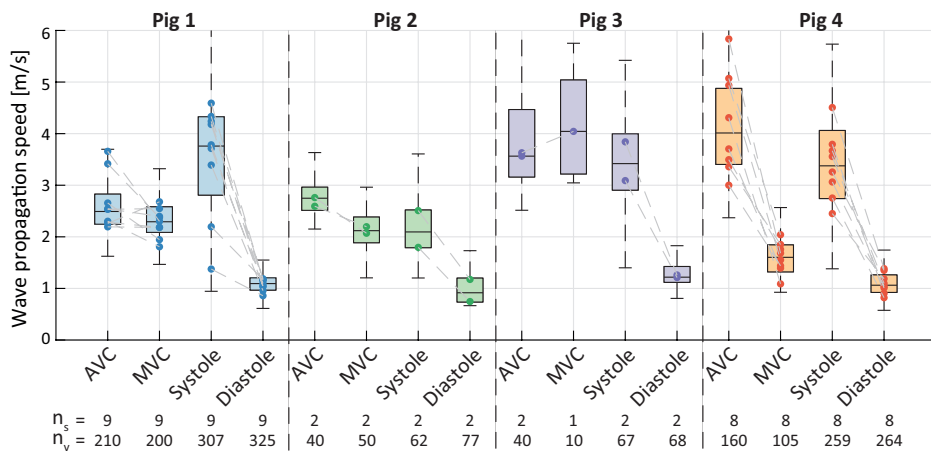


Figure 7.3: Overview of the natural and ARF-based wave propagation speeds obtained for each pig. The dots depict the median wave propagation speed of all M-splines within one sequence. The boxplots represent the variation of all wave propagation speed values across all M-splines in all sequences. The total number of successful sequences and the total number of wave speed values successfully estimated along M-splines drawn in the successful sequences are indicated by the n_s - and n_v -value at the bottom of the boxplot, respectively. Consecutive natural and active SWE sequences are connected by a dotted line. Systolic and diastolic wave speed values were computed over the 10% maximum and 10% minimum median values for each acquisition.

pigs due to signal interference in the operating room. Because ECG signals were not extracted, systolic and diastolic median wave propagation speeds were computed by selecting the 10% highest and 10% lowest median wave propagation speeds for every acquisition respectively [62]. Non-parametric two-sided Wilcoxon signed-rank tests were used to test the significance of measured differences in wave propagation speed. Correlation between wave propagation speeds was determined by computing a linear correlation coefficient (Pearson) and performing linear regression. All p-values (two-sided) smaller than 0.05 were interpreted as being significant.

7.3. RESULTS

7.3.1. Success Rate of the SWE Acquisitions

For the ARF-based SWE sequences, 32% (21 out of 65 in total) was considered successful: more than 40% of the waves throughout the cardiac cycle were tracked in these sequences. The remaining active and corresponding natural SWE data were excluded from our analysis. Figure 7.3 gives an overview of the successfully estimated propagation speeds for natural and ARF-based SWE in each pig individually. The dots in the figure depict the median values per successful sequence and the total number of successful sequences per animal is given by the n_s -value stated at the bottom of the figure. For all recorded ARF-based sequences within each pig, success rates of 36% (9/25), 14% (2/14), 13% (2/15) and 73% (8/11) were obtained respectively. Within the

corresponding natural sequences, wave propagation speeds after AVC and MVC were successfully determined in 100% (21/21) and 95% (20/21) of the sequences, respectively.

The boxplots in Figure 7.3 represent the wave propagation speed variations across all M-splines in the successful acquisitions of the individual pigs, in which the number of successful wave propagation speed values is indicated by the n_v -value mentioned at the bottom of the figure. For ARF-based SWE, diastolic wave propagation speeds were successfully determined for 90% (325/360), 96% (77/80), 85% (68/80) and 83% (264/320) of all considered M-splines for pigs 1 to 4, whereas the success rate was slightly lower in systole: 85% (307/360), 78% (62/80), 84% (67/80) and 81% (259/320). Nonetheless, median diastolic and systolic propagation speed values were obtained for all 21 successful ARF-based sequences, as indicated by the n_s -values in Figure 7.3. For natural wave propagation speed estimations, the total number of AVC and MVC events varied from 1 to 3 per sequence, depending on the heart rate of the pig. Wave propagation speeds after AVC were successfully determined in 100% (210/210), 100% (40/40), 100% (40/40) and 100% (160/160) of all M-splines for each pig. For MVC, successful wave propagation speed estimations were obtained for 100% (200/200), 100% (50/50), 33% (10/30) and 81% (105/130) of the M-splines analyzed for each pig individually. It should be stressed, that although the success rate of determining propagation speeds corresponding to individual M-splines drawn was lower for MVC than for AVC, still in 20 of the 21 sequences, median MVC propagation speed values could be obtained, as indicated by the n_s -values in Figure 7.3.

7.3.2. Natural SWE

An overview of the natural wave propagation speeds for each pig individually is illustrated in Figure 7.3; with the number of successful sequences n_s being equal to 9, 2, 2 and 8 for AVC, and 9, 2, 1 and 8 for MVC, in animal 1 – 4 respectively. For AVC, median propagation speeds of 2.5 m/s (IQR: 2.2 – 2.8 m/s), 2.7 m/s (IQR: 2.5 – 3.0 m/s), 3.6 m/s (IQR: 3.2 – 4.5 m/s) and 4.0 m/s (IQR: 3.4 – 4.9 m/s) were obtained for the pigs individually. For MVC, these values are 2.3 m/s (IQR: 2.1 – 2.6 m/s), 2.1 m/s (IQR: 1.9 – 2.4 m/s), 4.0 m/s (IQR: 3.2 – 5.0 m/s) and 1.6 m/s (IQR: 1.3 – 1.8 m/s) for each pig respectively. The median propagation speeds after AVC were found to be significantly higher than after MVC for the total set of sequences among all four animals (Wilcoxon signed-rank test, $p < 0.01$, $n_s = 20$). The ratios of the median propagation speed after AVC and MVC for each individual pig are 1.1, 1.3, 0.9 and 2.5. No statistical differences were found between the median natural wave propagation speeds obtained by the two observers (Wilcoxon signed-rank test, $p = 0.46$, $n_s = 41$), and a very strong linear correlation was found (Pearson, $r = 90$, $p < 0.01$).

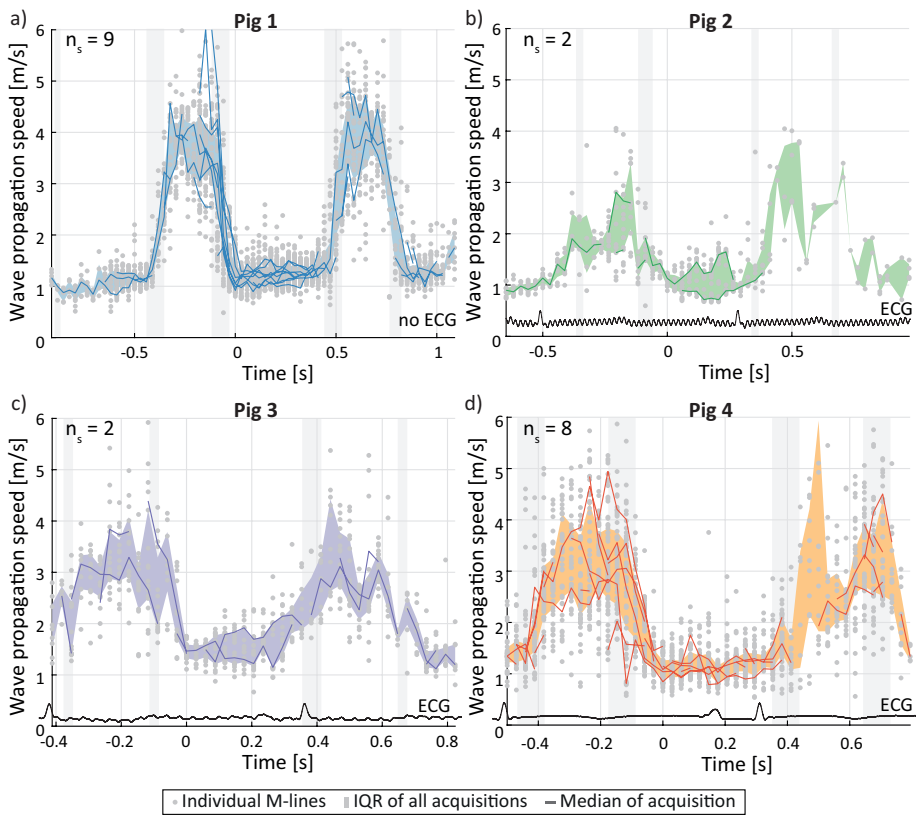


Figure 7.4: Overview of the propagation speeds obtained for the active SWE sequence. Individual sequences were aligned in time for each pig individually (panel (a) – (d) respectively), with the onset of diastole set to $t=0$ s. The dots depict the wave propagation speed values obtained with individual M-splines, while the solid lines show the median wave speeds of all M-splines within one sequence (if $n_v \geq 5$). The shaded colored areas depict the inter-quartile range of all wave speed values for all active sequences per animal. The grey shaded vertical bands depict the temporal ranges in which valve closure was observed. The total number of successful active SWE sequences is indicated by the n_s -value at the top of the figures. Representative ECG signals are also shown in this figure, but were not recorded simultaneously with the SWE acquisitions. For pig 1, no ECG data was saved due to malfunctioning of the ECG device. Note additionally that ECG triggering of the SWE acquisitions did not properly work for pig 2.

7.3.3. Active SWE

Figure 7.4 shows the propagation speeds obtained throughout the cardiac cycle for all ARF-based sequences per pig. Depending on the heart rate of the animal, one or more heart cycles were captured in the individual sequences of 1.2 s. The solid lines depict the median propagation speed values obtained for the M-splines drawn per ARF-based SWE measurement (number of successful sequences n_s is 9, 2, 2, and 8 for pigs 1 – 4 respectively). After selecting the 10% highest and 10% lowest median wave propagation speeds in each active SWE sequence (corresponding to the wave speed

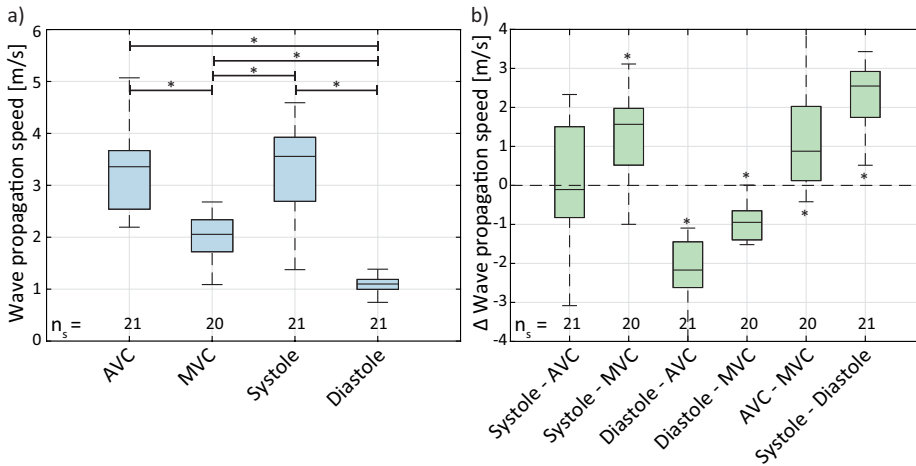


Figure 7.5: (a) Boxplots of the median wave propagation speed values obtained per acquisition for the natural and ARF-based waves. (b) The propagation speeds of the different types of waves are compared by matching the values obtained in individual sequences (for AVC vs. MVC and for systole vs. diastole) or in acquisitions (for natural vs. active SWE in consecutive heart beats). Asterisks (*) denote a significance level of $p < 0.05$ for a two-sided Wilcoxon signed-rank test. All propagation speeds were found to be significant different, except from the natural waves after AVC and the ARF-based waves in systole.

estimations of four pushes within one active SWE sequence), median systolic and diastolic values were computed per active SWE sequence, as shown in Figure 7.3. The median systolic wave propagation speeds for the selected M-splines in all acquisitions were found to be 3.8 m/s (IQR: 2.8 – 4.3 m/s), 2.1 m/s (IQR: 1.8 – 2.5 m/s), 3.4 m/s (IQR: 2.9 – 4.0 m/s) and 3.4 m/s (IQR: 2.7 – 4.1 m/s) for each pig individually. The median diastolic wave propagation speeds are 1.1 m/s (IQR: 1.0 – 1.2 m/s), 0.9 m/s (IQR: 0.7 – 1.2 m/s), 1.2 m/s (IQR: 1.1 – 1.4 m/s) and 1.1 m/s (IQR: 0.9 – 1.3 m/s) for each pig respectively. The median propagation speeds in systole were found to be significantly higher than in diastole for all acquisitions (Wilcoxon signed-rank test, $p < 0.01$, $n_s = 21$). The ratios of the median propagation speed in systole and diastole for each individual pig are 3.4, 2.3, 2.8 and 3.2. No statistical differences were found between the median systolic and diastolic wave propagation speeds obtained by the two observers (Wilcoxon signed-rank test, $p = 0.71$, $n_s = 42$), and a very strong linear correlation was found (Pearson, $r = 0.93$, $p < 0.01$).

7.3.4. Natural versus Active SWE

The median propagation speeds for the individual natural sequences are compared with the corresponding median values in systole and diastole in Figure 7.5. The propagation speeds after MVC were found to be higher than the wave speeds in diastole (Wilcoxon signed-rank test, $p < 0.01$, $n_s = 20$), and lower than in systole (Wilcoxon signed-rank test, $p < 0.01$, $n_s = 20$). The wave propagation speeds after AVC were also found to be higher than in diastole (Wilcoxon signed-rank test, $p < 0.01$,

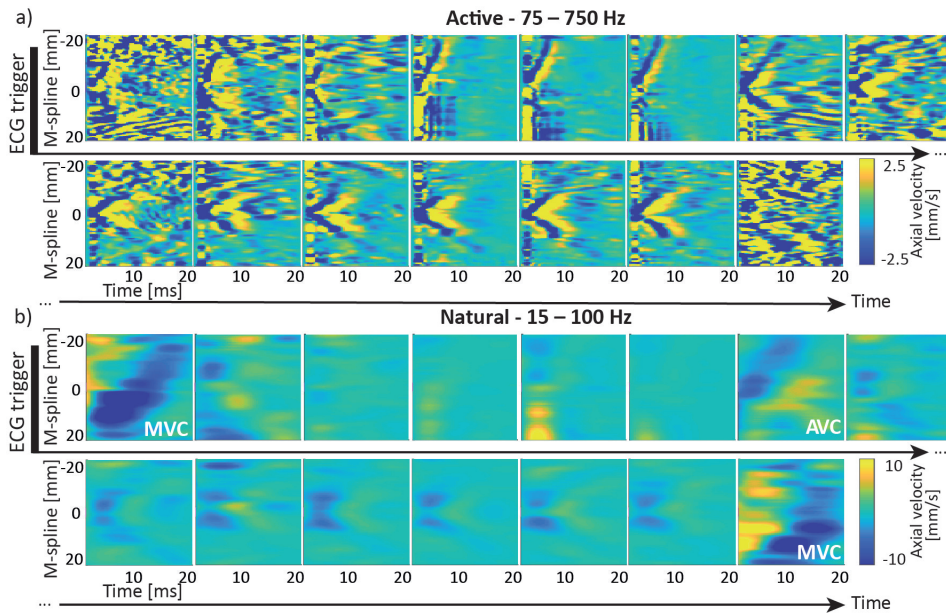


Figure 7.6: Effect of filter settings on wave visibility in M-panels of an active SWE sequence. **(a)** Various M-panels are displayed for different ARF pushes throughout the cardiac cycle, after applying a 75 – 750Hz bandpass filter to the TDI data. **(b)** The same M-panels as in **(a)** are shown after applying a 15 – 100Hz bandpass filter to the TDI Data, as done for natural SWE processing. Events of mitral and aortic valve closure (AVC and MVC) are denoted in their respective frames.

$n_s=21$), but no significant difference was found compared to systole (Wilcoxon signed-rank test, $p=0.99$, $n_s=21$). Note that especially for pig 4 propagation speeds after AVC are higher than wave propagation speeds in systole, while for the other pigs most wave propagation speed values after AVC are comparable or below systolic speeds.

7.3.5. Natural Waves in Active SWE

In most active SWE sequences, natural waves induced by AVC and MVC were also visible. To determine their propagation speeds, the same data-analysis methods were used as previously described for natural SWE. For AVC, we were able to estimate its wave propagation speed in 44% (4/9), 100% (2/2), 50% (1/2) and 100% (8/8) of the active SWE sequences for each pig, respectively. Wave speed estimation after MVC was successful in 67% (6/9), 100% (2/2), 50% (1/2) and 100% (8/8) of the active SWE sequences for each pig, respectively. For AVC, median propagation speeds of 2.5 m/s (IQR: 2.0 – 2.7 m/s), 2.8 m/s (IQR: 2.4 – 3.7 m/s), 2.0 m/s (IQR: 1.4 – 2.1 m/s) and 3.4 m/s (IQR: 2.5 – 4.1 m/s) were obtained for pigs 1 to 4 respectively. For MVC, these values are 2.1 m/s (IQR: 1.9 – 2.6 m/s), 2.4 m/s (IQR: 2.2 – 2.5 m/s), 3.4 m/s (IQR: 3.0 – 3.9 m/s) and 2.0 m/s (IQR: 1.6 – 3.1 m/s) for each pig. Despite the ARF-based waves being simultaneously present, no significant difference was found between the

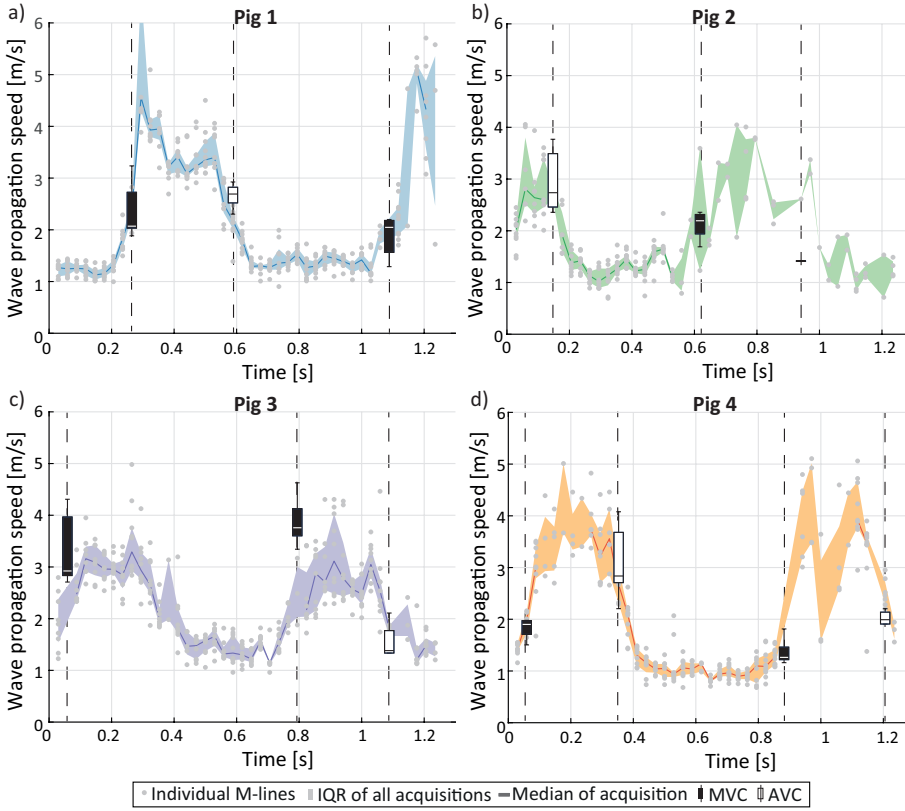


Figure 7.7: Example of an active SWE sequence for each individual pig, in which the natural waves after AVC and MVC were tracked for the same M-spline in the same sequence. The dots depict the wave speed values for individual M-splines, while the solid lines and shaded areas show the median values and inter-quartile ranges, respectively. Note that no data is shown for the first AVC event in pig 3 as waves tracking after AVC was not feasible for this specific sequence due to the limited temporal recording length.

natural wave propagation speeds in the active SWE sequences and the ones in the natural SWE sequences for AVC (Wilcoxon signed-rank test, $p=0.23$, $n_s=15$) and MVC (Wilcoxon signed-rank test, $p=0.49$, $n_s=17$).

The spatial and temporal characteristics of natural and actively induced waves are compared in Figure 7.6, visualizing M-panels obtained for an individual active SWE sequences after applying the active SWE filter settings (panel a), and after applying the natural SWE filter settings (panel b). Note that the same M-splines were used for the M-panels shown in Figure 7.6 a and b. A larger period (~ 15 ms vs. ~ 2 ms), spatial wavelength (a few cm vs. a few mm) and TDI amplitude (~ 10 mm/s vs. ~ 2.5 mm/s) was found for the natural waves than for the ARF-based waves. Figure 7.7 shows the wave propagation speed estimations of examples of active SWE sequences in each pig together with the natural wave propagation speed. Tracking natural waves

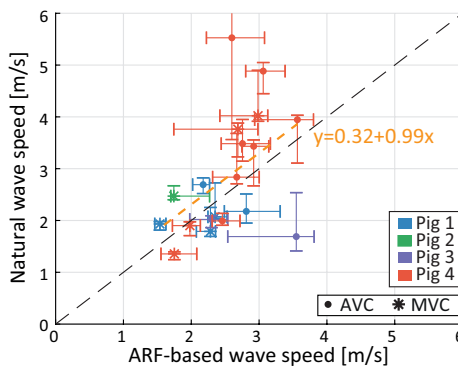


Figure 7.8: Comparison of the median propagation speed values of the natural waves within the active sequences, and the active median propagation speeds measured at the same time in the cardiac cycle as the corresponding natural wave. The orange dotted line depicts the linear regression fit of the data.

within active SWE sequences allows to compare natural and ARF-based wave propagation speed values at the same moment within the cardiac heart cycle, as shown in Figure 7.8. No statistical differences were found between the natural and ARF-based wave propagation speeds (Wilcoxon signed-rank test; AVC: $p=0.41$, $n_s=11$, MVC: $p=0.46$, $n_s=8$). Even though only a weak linear correlation was found between the natural and ARF-based wave propagation speeds (Pearson, $r=0.48$, $p=0.04$), the slope of the corresponding linear regression was found to be 0.99 ($R^2=0.23$), indicating a one-to-one relationship between natural and ARF-based wave propagation speeds (see also Figure 7.8). However, note that in this figure some propagation speeds after AVC for pig 4 are higher than the corresponding ARF-based wave speed.

7.4. DISCUSSION

Natural and active shear wave elastography (SWE) are promising non-invasive methods to potentially improve the current assessment of the mechanical properties of the heart. However, the relationship between both techniques, and which aspect of cardiac ventricular stiffness is assessed by each method remained unclear. Therefore, in this study we directly compared natural waves after aortic and mitral valve closure (AVC and MVC) with waves induced throughout the entire cardiac cycle using an acoustic radiation force (ARF), in four open-chest pigs. The results show that natural wave propagation speeds match well with the ARF-based wave speeds measured at the moment of valve closure, despite the differences in temporal and spatial characteristics of the waves. Additionally, analysis of the natural waves in the active SWE acquisitions showed that natural waves occur in between the diastolic and systolic phases identified by ARF-based wave propagation speeds, and have higher propagation speeds than in diastole. Therefore, natural SW propagation speeds not only relate to the myocardial stiffness in relaxation but also to the contractile state.

7.4.1. Natural versus Actively Induced Wave Characteristics

The excitation sources of natural and actively induced waves have different characteristics, which affect the wave properties. First, the orientation of the excitation force differs: active SWE emits a force mainly in the direction of the ultrasound beam (i.e. transversal with respect to the IVS in parasternal view) [134], whereas the exact orientation of the force for natural SWE is unknown. However, the force after AVC will probably not be purely transversally oriented because both a transversal (parasternal view) as well as a longitudinal component (apical view) of tissue motion in the IVS has been measured in an earlier study [96]. Second, the temporal and spatial characteristics of the excitation source are completely different, which might affect the spectral content of the wave [135]. In active SWE, the ARF's spatial and temporal characteristics are theoretically determined by the push settings (push duration, center frequency, etc.) and the acoustic properties of the medium [59]. Ideally, the ARF acts as a volume force with a focal extent throughout the entire IVS thickness in order to generate a wave propagating over the complete IVS. In natural SWE, the exact temporal and spatial characteristics of the wave source are unknown, but are determined by a complex interaction between the leaflet dynamics, blood pressure changes and local (back)flow dynamics. Natural waves are excited by a local force on the IVS near the valve and gradually propagate from this location to the entire IVS thickness.

Due to the different excitation sources, the natural and actively induced wave characteristics vary in terms of period, wavelength and velocity magnitude, as visualized in Figure 7.6. As natural waves have a lower frequency content than actively induced waves, earlier literature reports different TDI filter settings [42, 55, 62, 64, 86, 94, 128] depending on the wave analyzed (Supplementary Table 7.1). To make a fair comparison between the SWE methods, waves were analyzed in such ways as would have been done when studying only one SWE method. Therefore, the current filter settings of 15 – 100 Hz vs. 75 – 750 Hz were selected based on these literature reports and the observed frequency content in our SWE data. Indeed, Fourier analysis of TDI-panels of both natural and ARF-based waves showed that by applying the different filters for the different SWE methods, the relevant wave content was preserved (see Supplementary Figure 7.1). The discrepancy around the lower cut-off frequency between the Fourier spectrum of the unfiltered and filtered ARF-based wave was needed to separate the wave from low-frequency general heart motion with relatively large amplitudes, often complicating the tracking process of these waves as shown in Figure 7.2. Supplementary Figure 7.1 shows an approximated 25 dB lower signal at the upper cut-off frequency, which validates our choice of the upper cut-off frequencies. Furthermore, despite the ARF-based waves being simultaneously present, no significant difference was found between the natural wave speeds within the active SWE sequences and within the natural SWE sequences. This suggests that natural waves could be correctly separated from the ARF-induced waves, and that the ARF-induced waves that were simultaneously present with the natural waves did not cause a bias in the natural propagation speeds obtained. Assuming that antisymmetric zero-order Lamb wave modes were induced, the lower frequency

content would make natural waves theoretically more sensitive to wave dispersion [43], potentially decreasing the wave propagation speed measured. However, the smaller bandwidth of natural waves compared to actively induced waves limits frequency dispersion and consequent wave distortion. Furthermore, Urban *et al.* [98] showed using finite element simulations of impulsive and harmonic excitations that low-frequency waves are less sensitive to fiber orientation than high-frequency waves, resulting in less wave guiding along the fiber. The changing myocardial fiber orientation across cardiac thickness [29] would thus theoretically have less impact on the natural waves, resulting in less wave speed variation across the IVS thickness when neglecting other relevant factors.

This study shows higher wave propagation speeds for the waves after AVC and MVC (median speed range of 2.2 – 5.8 m/s and of 1.1 – 4.0 m/s respectively) than for the actively induced waves in diastole (median speeds between 0.7 – 1.4 m/s), as demonstrated in Figure 7.5. The ARF-based wave propagation speeds in systole (median range of 1.4 – 4.6 m/s) were found to be higher than the wave propagation speeds after MVC (median range of 1.1 – 4.0 m/s), but not statistically different from the wave speeds after AVC (median range of 2.2 – 5.8 m/s). Besides the different wave characteristics, it should be noted that – since natural and active SWE sequences were performed in consecutive heartbeats for Figure 7.3 and 7.5 – part of the wave propagation speed differences could be caused by M-spline location, cardiac natural variations (inter-beat variability), and the moment within the cardiac cycle [55, 86]. However, the second analysis, where we measured the natural and actively-induced waves simultaneously for the same M-splines, a good correspondence between natural and ARF-based wave propagation speed was found in Figures 7.7 and 7.8. This indicates that they provide equal information about the cardiac stiffness at that time instance, despite their differences in wave characteristics as described above.

The reported median wave speed values per animal for natural SWE (median of 1.6 – 4.0 m/s for MVC and 2.5 – 4.0 m/s for AVC) and active SWE (median of 0.9 – 1.2 m/s in diastole and 2.1 – 3.8 m/s in systole) are within the ranges documented in literature for the IVS in other porcine studies. For natural SWE, Vos *et al.* [64] obtained a median propagation speed of 2.2 m/s after MVC (90% interval: 0.8 – 3.2 m/s) and 4.2 m/s after AVC (90% interval: 1.4 – 6.3 m/s) in 22 closed-chest pigs. For active SWE, Hollender *et al.* [56] reported a range of median velocities between 0.89 and 2.20 m/s in diastole and 2.60 and 5.14 m/s in systole for 6 closed-chest pigs using an intracardiac probe. Although similar range of values have been reported in other animal species and even in human subjects, other species might have inherently different cardiac properties, and therefore we refrain from comparing our wave speed results with non-porcine studies.

7.4.2. Timing of Natural Waves within the Heart Cycle

Valve closure is commonly used to divide a cardiac cycle into a diastolic and systolic phase, in which AVC typically describes the end of systole or the beginning of diastole and MVC the beginning of systole or the end of diastole [136]. However, the exact

timing of the valve closure events with respect to the dynamic stiffness variation of the heart is unknown, and therefore it is uncertain in what relaxation and/or contraction state of the heart the natural wave measurements are performed. We measured higher wave propagation speeds after AVC than after MVC, as reported on by several other studies [40, 42, 64, 86], suggesting a higher myocardial stiffness at the moment of AVC than of MVC. Figure 7.7 compares natural and actively induced waves within the same heartbeat, substantiating our expectation that wave tracking after MVC occurs during the period in between diastolic and systolic speeds and wave tracking after AVC during the period in between systolic and diastolic speeds. Due to the timing of natural waves, both AVC and MVC measurements are representative for an instantaneous myocardial stiffness that does not only depend on the passive cardiac material properties but also on the loading condition and the active relaxation/contractility characteristics. This is also supported by the higher wave propagation speeds measured for natural SWE than for active SWE in diastole.

Although this study confirms that the waves after AVC and MVC occur during the phases that the heart changes contractile state (as assessed with active SWE), the exact moments within these phases could vary between test subjects and even between heartbeats. Valve closure is dictated by the pressure differences between left ventricle and atrium or aorta, and a time delay might be present between the moment of valve closure and the recording of the wave further down the septal wall along the selected M-spline[130]. For example, for pig 4 in Figure 7.7 d, lower median natural propagation speeds were measured in the second heartbeat (1.3 m/s for MVC and 2.0 m/s for AVC) than in the first (1.9 m/s for MVC and 2.8 m/s for AVC). This inter-beat variability is in line with the inter-scan variability previously reported in healthy volunteers [86] IQR of 0.26 – 0.94 m/s for MVC and 0.40 – 0.86 m/s for AVC. Furthermore, in contrast to the general findings of this study, the specific sequences in Figure 7.7 b and c (pigs 2 and 3) show lower wave propagation speed after AVC than after MVC (also visible in Figure 7.3 for pig 3). A lower propagation speed for AVC was also found by Strachinaru *et al.* [39] in 45 healthy volunteers (mean of 3.51 m/s for AVC vs. 4.68 m/s for MVC). Both observations might be related to a timing difference of valve closure between heartbeats, subjects or even species, but also to measurement inaccuracies (in wave speed estimation, echocardiographic view, and M-spline location) or to changes in the global cardiac dynamics affecting the pressure difference across the valve. These variabilities demonstrate the importance of recording multiple heartbeats to improve the accuracy [86].

7.4.3. Clinical Interpretation and Future Work

The objective of this work is to highlight the essential differences in wave characteristics (i.e. speed, wavelength, and wave magnitude) measured with natural and active SWE, and to discuss their clinical interpretation. Both SWE methods have yet demonstrated potential added value in various clinical cardiac studies [39–41, 63], however it was unsure whether the techniques assess a similar stiffness property of the heart. Systolic wave propagation speeds as well as wave speeds after AVC have

both been proposed to be potentially related to myocardial contractility [75, 137]. No statistical difference was found between the wave propagation speeds after AVC and in systole in our study. However, it should be noted that the propagation speeds after AVC (3.0 – 5.8 m/s) seem higher than in systole (2.5 – 4.5 m/s) for pig 4 in Figure 7.3. Furthermore, while pig 1 and 4 show similar systolic wave propagation speed (around 3.6 m/s in Figure 7.3), the wave speeds after AVC are different (2.5 m/s in pig 1 vs. 4.0 m/s in pig 4 in Figure 7.3). Although other studies [75, 137] showed a correlation with contractility for the propagation speeds in systole and AVC separately, the results of this study suggest that their speed magnitude is not necessarily equal. This could be caused by the different wave characteristics, the timing of the waves after AVC with respect to the functional state of the heart (as suggested by the location of the grey areas with respect to the systolic speeds shown in Figure 7.4) and measurement inaccuracies. The small sample size of this study prevents making definite claims on the link between systolic wave speed and wave speed after AVC. In literature, wave speeds in diastole are regarded as a measure for passive myocardial stiffness [57, 63]. The ARF-based wave propagation speed values in diastole were very similar for all tested subjects in this study (around 1.1 m/s in Figure 7.3). Furthermore, the variability of diastolic wave propagation speeds is much lower than for other reported natural and active metrics, which is advantageous for clinical diagnosis. On the contrary, it is unclear what the waves caused by MVC clinically represent as they do not strictly measure myocardial properties in end-diastole. Whether all findings of this study can be extrapolated to humans, needs to be investigated in future large-scale studies which apply both natural and active SWE. Clinical relevance of both natural and active SWE should be further demonstrated in the future by extending the current study with the assessment of cardiac function and stiffness via pressure-volume loops.

Both natural and active SWE have their specific advantages that might be beneficial for clinical use. Natural SWE can be easier implemented in clinical practice as no high-energy ARF pushes are needed to induce waves, setting less demanding power requirements on the scanner and posing less issues concerning acoustic safety. Furthermore, until now, the feasibility of natural SWE is in general higher than for active SWE, due to higher SNR and the absence of limiting factors for the wave excitation source to reach the IVS while meeting safety criteria (especially challenging in obese patients [65]). On the other hand, applying active SWE gives the user theoretically the freedom to control the spatial and temporal characteristics of the excitation source at any time point in the cardiac cycle. The smaller spatial wavelengths of ARF-based waves compared to natural waves (a few mm vs. a few cm) also results in more accurate ARF-based wave tracking within the limited spatial domain of the selected field-of-view (typically 3 – 4 cm). Additionally, the wave is always tracked in line with the excitation source for active SWE, whereas out-of-plane motion in natural SWE can cause wave speed estimation errors [64]. However, our study showed a low feasibility rate of 32% for ARF-based SWE in an open-chest setting. Within these successful acquisitions, wave tracking occurred successfully in 89%, 82%, 100% and 79% of all M-splines on average for diastolic waves, systolic

waves, waves after AVC and waves after MVC, respectively. Success rate of wave speed estimation after MVC is explicitly lower than that for waves after AVC, as previously reported [86]. In closed-chest settings, to the best of our knowledge, there are no feasibility studies available for ARF-based SWE throughout the cardiac cycle. However, a feasibility rate of 41% throughout the cardiac cycle has been reported in healthy volunteers for another ARF-based method called ARF imaging (ARFI) [60] – using focused pulses to track the on-axis displacement relaxation after ARF application instead of DWs to image the off-axis displacement propagation patterns as in SWE. Due to this difference in displacement tracking, ARFI has typically higher tracking SNR than SWE, explaining the higher feasibility rate. Finding a workaround for this technological limitation in ARF-based SWE remains thus an important task for the future.

7.4.4. Study Limitations

The feasibility rate of active SWE in this study was low: only 32% of all active SWE sequences fulfilled our predefined metric of success (wave visibility in more than 40% of the pushes throughout the cardiac cycle). This resulted in low sample sizes for all statistical tests. Especially the systolic phase set challenges to wave tracking due to a stiffer myocardium resulting in a decreased SNR and therefore a limited spatial window to track higher wave propagation speeds (typically around 15 mm as can be seen in Figure 7.2 and 7.6). The open-chest nature of our experiments is also partly responsible for these low success rates, even though it gave access to the dynamic changes in wave speed across the cardiac cycle. It was difficult to keep the probe in a stable position within an open thorax on a beating heart without losing probe contact, while keeping the IVS in an approximately horizontal position. Depending on the position of the heart with respect to the opening of the thorax and the ribs, this was more difficult for some pigs than for others, leading to a wide variety in success rate of the ARF acquisitions among the pigs. The low SNR for active SWE did also not permit implementation of an automatic method such as the Radon transform to estimate wave speeds. Instead, a manual method was used to get a robust estimate of wave speed, but this method is time-consuming and potentially observer dependent. Wave visibility thus played a role in wave speed estimation and therefore the chosen inclusion criterion for a complete HFR SWE acquisition was also based on wave visibility throughout the cardiac cycle by 2 observers, which is partly subjective. Technical innovations are however still ongoing to further improve SNR for ARF-based SWE measurements, such as dedicated probe development for transthoracic acquisitions or efforts for elevating acoustic output in SWE [138]. These improvements are needed for a more robust and universal method of wave tracking and a quantitative assessment of data quality for objective acquisition inclusion criteria, as well as for increasing the feasibility of transthoracic measurements. During the experiment, no ECG signal was recorded and therefore wave speed in diastole and systole were determined based on the 10% minimal and 10% maximal median wave speed values [62]. Furthermore, since no ECG signal was saved, the timing of natural waves was only compared with the speed dynamics measured with active SWE.

Due to limitations in the data acquisition system, the actively induced waves could not be tracked continuously, but were saved in blocks of 20 or 28 ms after each individual ARF push. Although the saved temporal window was large enough for actively induced wave tracking, it was more challenging to track the natural waves in these active sequences due to their longer wave period. Therefore, natural wave speeds were tracked more reliably in the individual natural SWE sequences with continuous tracking (resulting in a larger temporal window for tracking), although no statistical differences were found with the natural wave speeds in the active sequences. As a result, to make a fair comparison with optimal processing conditions for the different methods, Figure 7.3 and 7.5 show the results for natural and actively induced waves in consecutive heartbeats. The natural waves in active sequences were used to include the effect of timing of these natural waves in Figure 7.7 and 7.8.

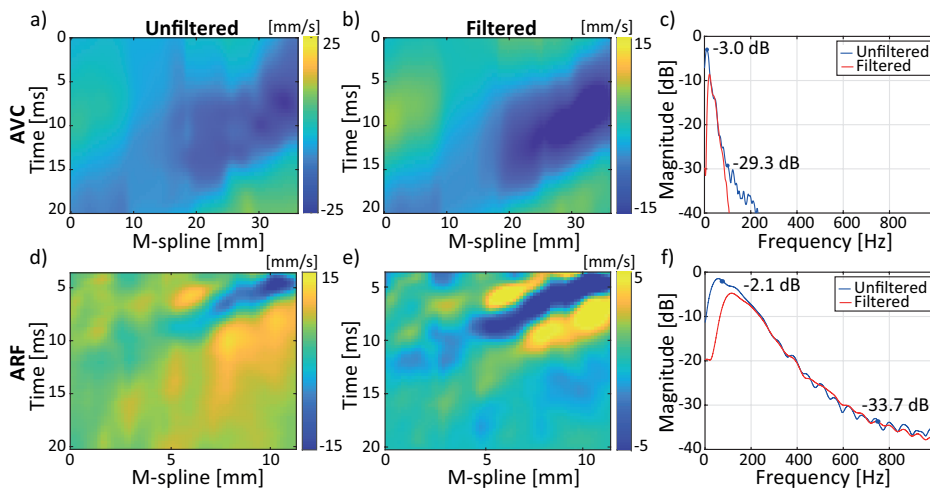
7.5. CONCLUSION

This work studied the relationship in four open-chest pigs between waves naturally occurring after aortic and mitral valve closure, and those actively induced throughout the entire cardiac cycle using an acoustic radiation force (ARF), to bridge the knowledge gap between two groups of reported shear wave elastography (SWE) studies. Despite the shorter wavelength and period of the actively induced waves, a good match in propagation speed was found for both natural and active SWE when actively induced waves were measured at the moment of valve closure. In addition, our simultaneous recordings showed that the waves after valve closures occur in between the diastolic and systolic phases identified with active SWE, and have higher propagation speeds than in diastole. This confirms that natural SWE measures a mixed state of relaxation and contraction, which might hamper easy interpretation in clinical diagnosis for diastolic and/or systolic function. On the other hand, despite the easy timing of stiffness measurements in active SWE, its feasibility was lower than natural SWE, especially in systole. Clinical validation is further needed to exploit both techniques for the assessment of diastolic and systolic function.

Acknowledgements

This work is part of the STW/TTW – Dutch Heart Foundation partnership program ‘Earlier recognition of cardiovascular diseases’ with project number 14740, which is (partly) financed by the Netherlands Organization for Scientific Research (NWO). This work was also supported by the Research Foundation Flanders (FWO) under grant 1211620N to Annette Caenen.

SUPPLEMENTARY INFORMATION



Supplementary Figure 7.1: Example of M-panels obtained for a wave after AVC (a) and for an externally induced wave using an ARF (d). Bandpass filters (6th-order Butterworth) of 15 – 100 Hz and 75 – 750 Hz were applied on the natural (b) and active (e) M-panels respectively. The Fourier spectra of the unfiltered and filtered M-panels are shown in (c) and (f). Magnitude values at the cut-off frequencies are shown.

Supplementary Table 7.1: Overview of reported processing settings in literature (this overview does not represent a complete overview of all SWE studies). Filter settings that show similarities as the settings used in our study are shown in red. Abbreviations: RF: radio frequency, IQ: in-phase and quadrature, DWI: diverging wave imaging, PIHI: pulse-inversion harmonic imaging, NR: not reported, SWE: shear wave elastography, BPF: bandpass filter, HPF: highpass filter, CFWI: clutter filter wave imaging, and LPF: lowpass filter

		SWE imaging	RF filter	IQ filter	Wave motion	Spatial smoothing	Motion Filter
Active SWE	Couade <i>et al.</i> , (2011) [55]	DWI in open- chest sheep	NR	NR	Velocity data	NR	Average wall motion subtracted
	Vejdani <i>et al.</i> , (2015) [94]	DWI in Langen- dorff perfused rabbits	Data with correlation coefficient <0.9 removed	NR	Velocity data	NR	Quadratic motion filter
	Hollender <i>et al.</i> , (2017) [62]	PIHI in <i>in vivo</i> human	NR	NR	Velocity data	NR	Butter- worth 3 rd -order BPF (75 – 750 Hz)
	Deng <i>et al.</i> , (2017) [128]	DWI: general guidelines	NR	NR	Displace- ment data	Axial averaging over depth of push field	BPF
Natural SWE	Vos <i>et al.</i> , (2017) [64]	DWI in closed- chest pigs	NR	NR	Velocity data	2.5 x 2.5 mm	Butter- worth BPF (15 – 100 Hz)
	Santos <i>et al.</i> , (2019) [42]	Multi- zone DWI in <i>in vivo</i> human	Gaussian BPF (3.5 MHz, 60% bandwidth)	NR	Acceleration data (=highpass motion filter)	2 mm x 2.4°	Moving average of 3 frames
	Keijzer <i>et al.</i> , (2019) [86]	PIHI in <i>in vivo</i> human	NR	Butter- worth LPF (250 Hz)	Velocity data	4 mm x 6.7°	Butter- worth 6 th -order BPF (15 – 100 Hz)

Supplementary Table 7.2: Overview of the reasons for applying different processing settings on the natural and active SWE sequences. Filter settings were based on settings described in literature (see Supplementary Table 7.1). Abbreviations: IQ: in-phase and quadrature, LPF: lowpass filter, SWE: shear wave elastography, and ARF: acoustic radiation force.

IQ Filter	An LPF with a cut-off value of 250 Hz was applied on the natural SWE sequence to remove data corresponding to blood motion and noise. Since ARF-induced waves have a higher frequency content, applying such filter would go hand in hand with removal of the wave motion data.
Spatial smoothing	Natural waves have larger wavelengths (as a consequence of the low frequency spectrum) than ARF-induced waves, and therefore the Gaussian smoothing filter applied on the one-lag autocorrelation frames was larger (5.6° by 3.0 mm versus 1.9° by 1.0 mm).
Motion filter	Bandpass filters were chosen such that frequency content of the specific wave type remained, while increasing the robustness of determining wave propagation speeds by filtering out low-frequency gross motion and high-frequency jitter.

8

Transthoracic Cardiac Shear Wave Elastography in Relation to (Patho-)physiologic Changes



Lana B.H. Keijzer*

Annette Caenen*

Stéphanie Bézy

Jürgen Duchenne

Marta Orlowska

Antonius F.W. van der Steen

Nico de Jong

Patrick Segers

Johan G. Bosch

Jens-Uwe Voigt

Jan D'hooge

Hendrik J. Vos

**Both authors contributed equally.*

Abstract

The clinical motivation of this thesis is the need for a non-invasive technique for the assessment of the myocardial stiffness in people at risk for developing heart failure. For this reason, shear wave elastography (SWE) techniques have been extensively studied throughout this thesis. This chapter makes a first step in studying the sensitivity of SWE to loading conditions and intrinsic myocardial characteristics. In 3 closed-chest pigs, natural shear waves induced after valve closure were studied. These shear waves were compared with shear waves externally induced throughout the cardiac cycle by using an acoustic radiation force. Loading conditions, contractility and (diastolic) myocardial stiffness were altered during the measurements. The preliminary results show correlations between shear wave propagation speeds and the intrinsic diastolic chamber stiffness, as well as with end-diastolic and end-systolic pressures.

8.1. INTRODUCTION

The clinical motivation to study shear wave elastography (SWE) throughout this thesis, is the need for a non-invasive technique for the assessment of myocardial stiffness. This is especially relevant for the early diagnosis of underlying pathophysiologies in heart failure patients with a preserved ejection fraction. Most of these patients have diastolic dysfunction, mainly caused by increased passive myocardial stiffness properties and/or by active relaxation abnormalities [9, 10, 13–15]. The current echocardiographic parameters used for the clinical diagnosis of diastolic dysfunction – such as Doppler measures and cardiac volumes – are depending on loading conditions [11], and are non-specific [2, 8, 10]. Furthermore, these parameters employed are only surrogates for altered myocardial properties (passive myocardial stiffness and/or relaxation abnormalities) in these patients. We assumed that passive myocardial stiffness, an intrinsic material characteristic of the myocardium, can be measured with SWE, and that therefore myocardial function can be assessed more directly than with the parameters currently used in clinical practice.

Stiffness can be seen as an object's resistance to deform, and thus tissue stiffness can be defined as the slope of the stress-strain diagram. Nonetheless, stress-strain relationships of biological materials are non-linear [18–20]: the slopes of the tangents of a stress-strain curve increase with stress. This practically means that even when the intrinsic stress-strain diagram of a tissue is not altered, the instantaneous myocardial stiffness measured at a specific moment in the cardiac cycle, is still depending on loading. Since shear wave (SW) propagation speeds are expected to reflect the instantaneous myocardial stiffness, these propagation speeds are also expected to be affected by loading conditions. Furthermore, in a cardiac setting, besides passive myocardial stiffness and loading conditions, also active relaxation and contraction affect the instantaneous myocardial stiffness measured.

In literature, several studies report on how propagation speeds of natural or externally-induced SWs are affected by loading conditions, as well as by changes in intrinsic material characteristics, such as contractility, relaxation and passive myocardial stiffness. In Langendorff-perfused rabbit hearts, the inotropic state was shown to have more influence than preload on the acoustic-radiation-force (ARF) based systolic SW propagation speeds [75]. Also in Langendorff-perfused rabbit hearts using ARF-based SWE, an increase in systolic SW propagation speeds with coronary perfusion pressure – used as a measure of contractility [139] – and an increase in diastolic SW propagation speeds with coronary perfusion pressure – used as a measure of cardiac compliance [94] – was found. For natural SWE, the propagation speed for the SWs after MVC were found to correlate with end-diastolic pressures in human [140]. Furthermore, an increase in propagation speed after AVC was found in healthy volunteers after administration of dobutamine and during a bicycle-exercise [137], suggesting that these SWs can be used as a measure for contractility. Different effects of ischemia on SW propagation speeds have been reported. In one open chest sheep, a short term ligation of the left anterior descending artery (LAD) of 20 minutes caused a decrease in ARF-based systolic

propagation speeds, but had no significant effect on diastolic speeds [55]. In open chest pigs, using a mechanical actuator, after long term ligation of the LAD for 1 – 3 hours and subsequent reperfusion for 1 – 2 hours, an increase in SW propagation speeds was observed in end-diastole and in systole, although the latter was not significant [52]. Also, several clinical studies suggested a correlation between SW propagation speeds and end-diastolic myocardial stiffness. However, differences in SW propagation speed could also be caused by other factors, such as wall thickness [39]. Compared to healthy volunteers, higher propagation speeds were found in amyloidosis patients for the SWs after AVC and MVC [40, 42], in patients with hypertrophic left ventricular remodeling for the SWs after MVC [41], and in hypertrophic cardiomyopathy patients for the natural SWs after valve closure [39] and for ARF-induced SWs in diastole [63]. Furthermore, the propagation speeds after MVC were found to increase with the grade of diastolic dysfunction [40], and with left ventricular remodeling [41].

SW propagation speeds are thus affected by intrinsic material characteristics, but also by the actual filling state of the ventricle, complicating the interpretation of SWE measurements [11]. Therefore, an important remaining question is whether SWE is more sensitive for changes in intrinsic myocardial stiffness than in loading. Furthermore, although ARF-based SWs and SWs after valve closure have been extensively compared in **Chapter 7**, it is unknown whether the propagation speeds of these different types of SWs are similarly affected by loading conditions. This chapter will make a first step in studying the dependence of SW propagation speeds on loading conditions and intrinsic myocardial characteristics of ARF-based SWs and SWs after valve closure. The developed high-frame-rate (HFR) SWE acquisitions for the experiments described in **Chapter 7** will be used for this purpose, while altering loading conditions, contractility and diastolic myocardial stiffness during the SWE measurements. Also, pressure-volume (PV) loops were simultaneously recorded and used as a gold standard for the function of the left ventricle (LV). Furthermore, in contrast to the previous chapter, the echocardiographic acquisitions were performed in a transthoracic setting, which is especially challenging for the ARF-induced SWs in systole with relatively low amplitudes, but is also an important next step towards the direction of clinical application.

8.2. METHODS

8.2.1. Animal Preparation and Instrumentation

Three pigs (York x Landrace) were included in this study, weighing 38, 29.6 and 32.6 kg, respectively. The second pig was a female, while the other two animals were males. The Ethical Committee for Animal Experiments of KULeuven approved the study (P041/2019). The experiments started with sedation (Zoletil 100: 8 mg/kg and Xylazine 2%: 2.5 mg/kg), analgesia (Ultiva 2 mg: 0.3 µg/kg/min) and anesthesia (Diprivan 2%: 10 mg/kg/h, and the animals were mechanically ventilated. The pigs were placed in an approximately supine position, but with the pig slightly turned to its

right side. A PV-loop catheter (Millar Ventri-Cath 510, ADInstruments) was inserted into the LV via the right carotid artery. Furthermore, two balloon catheters were used (PTS25, Braun Interventional Systems): one was placed into the descending aorta via either the carotid artery or femoralis for changing afterload, and the other was inserted into the vena cava inferior through the femoral vein for changing preload. To induce a myocardial infarction, an introducer sheath (7F) was placed into the left carotid artery, the ascending aorta and the ostium of the left main coronary artery. A guided wire was subsequently advanced through the guiding catheter into the left anterior descending artery (LAD) distal from the first diagonal, in order to place a coronary angioplasty balloon catheter. During SWE and PV-loop recordings, mechanical ventilation was stopped to mimic breath hold in end-expiration.

8.2.2. Alterations of Hemodynamics, Contractility and Compliance

Loading (preload and afterload), contractility and the intrinsic (diastolic) myocardial stiffness were altered during separate measurements (called 'conditions' in this chapter). Their effect on SW propagation speeds was studied by comparing the SWE measurement of the induced conditions with that of the baseline measurements. A chronological overview of the different conditions tested and measurements performed is given in Table 8.1.

Hemodynamics

First, baseline SWE and simultaneous PV-loop measurements were performed before and after placing the different catheters (BL1 and BL2 in Table 8.1). Second, preload was reduced (PR in Table 8.1) by slowly inflating the catheter balloon in the vena cava inferior with 3 – 4 ml, until a steady state was observed in the PV-loop recordings. Third, afterload was increased (AI in Table 8.1) by inflating the catheter balloon in the aorta with 3 – 5 ml until again a steady state was observed in the PV-loop recordings, such that a rise in end-systolic blood pressures could be observed. For both preload and afterload changes, the amount of balloon inflation was optimized for each pig, such that a change in end-systolic pressure of at least 30 mmHg was observed. Fourth, preload was increased (PI in Table 8.1) by intravenous administration of 500 ml of saline, and then within 20 minutes hereafter the acquisitions were performed. SWE and PV-loop acquisitions were simultaneously performed during the PR, AI and PI conditions. For the assessment of contractility and diastolic chamber compliance, new PV-loops were subsequently acquired while reducing preload (PI PR in Table 8.1). Due to time constraints, and since an extra balloon catheter would have been needed to acquire such PV-loops during PR, PV-loop based contractility and compliance were not assessed during PR and AI.

Dobutamine

SWE and PV-loop measurements were performed simultaneously after intravenous administration of dobutamine ($\pm 10 \mu\text{g/kg/min}$) to investigate the effect of increased inotropy and thus contractility (DOB in Table 8.1). Since high heart rates complicate

Table 8.1: Chronological overview of the different conditions tested and measurements performed. All SWE and PV measurements were performed in threefold. If both SWE and PV measurements are indicated in the table for a specific condition, this means that they were performed simultaneously. Abbreviations: SWE: shear wave elastography, PV: pressure-volume loop, ✓: measurement performed.

Abbreviation	Condition	Method	SWE	PV
BL1	Baseline before catheters	-	✓	✓
BL2	Baseline after catheters	-	✓	✓
PR	Preload reduction	Inflating catheter balloon in vena cava inferior with 3 – 4 ml	✓	✓
AI	Afterload increase	Inflating catheter balloon in aorta with 3 – 5 ml	✓	✓
PI	Preload increase	Administrating 500 ml saline intravenously	✓	✓
PI PR	Preload reduction	Inflating catheter balloon in vena cava inferior with 3 – 4 ml during PI		✓
DOB	Intropy increase through dobutamine administration	Administrating dobutamine ($\pm 10 \mu\text{g/kg/min}$) intravenously	✓	✓
DOB PR	Preload reduction	Inflating catheter balloon in vena cava inferior with 3 – 4 ml during DOB		✓
BL3	Baseline	-	✓	✓
BL3 PR	Preload reduction	Inflating catheter balloon in vena cava inferior with 3 – 4 ml		✓
MI	Myocardial infarction	Inflating coronary angioplasty balloon catheter for 60 – 90 minutes	✓	✓
MI PR	Preload reduction	Inflating catheter balloon in vena cava inferior with 3 – 4 ml during MI		✓
REP	Reperfusion	Deflating coronary angioplasty balloon catheter and wait for 40 minutes	✓	✓
REP PR	Preload reduction after reperfusion	Inflating catheter balloon in vena cava inferior with 3 – 4 ml during REP	✓	✓

the performance of SWE acquisitions, the dobutamine dose was optimized per pig to obtain heart rates in the range of 100 – 150 bpm. Afterwards, the preload was reduced and PV-loops were recorded in order to characterize the function of the LV in a dobutamine state (DOB PR in Table 8.1). Dobutamine administration was then stopped and a waiting time of at least 15 minutes was included to let the heart rate decrease again to approximately the same rate as before dobutamine infusion.

Myocardial Infarction

New simultaneous baseline SWE and PV-loop measurements (BL3 in Table 8.1) were performed before the infarction, followed by only PV-loop acquisitions during preload reduction for the assessment of contractility and the intrinsic (diastolic) myocardial stiffness (BL3 PR in Table 8.1). A myocardial infarction was subsequently induced by inflating a coronary angioplasty balloon catheter in the LAD to occlude the artery for 60 – 90 minutes. Then within 10 minutes, SWE and PV-loop measurements were simultaneously performed (MI in Table 8.1), whereafter the balloon was deflated. For the first pig, next to LAD occlusion, also some fat was used to occlude the first septal branch of the LAD. In this way, a more uniform ischemia across the IVS should be created, also affecting the basal part of the IVS. However, this process was not repeated for the other pigs, since it was time consuming and since edema also developed over the entire septum after reperfusion even when only the distal LAD was occluded. Preload was subsequently reduced for PV-loop registration (MI PR Table 8.1). Then, the balloon was deflated followed by 40 minutes of reperfusion, and baseline (REP in Table 8.1) and preload-reduction (REP PR in Table 8.1) measurements were performed to acquire SWE and PV-loop data.

8.2.3. Data Acquisition

A full description of the high frame rate (HFR) SWE data acquisition is given in **Chapter 7**. A P4-2 probe (ATL, Bothell, Washington, United States) or a P4-2V probe (Verasonics, Kirkland, United States) connected to a Vantage 256 ultrasound research system (Verasonics, Kirkland, United States) was used to perform HFR SWE measurements. An HFR SWE acquisition consisted of two consecutive sequences: a natural and an active SWE sequence. Each sequence was triggered by the R-peak of the electrocardiogram (ECG, CWE 3-leads Cardiotachometer CT-1000, Ardmore, United States). The natural SWE sequence tracked the SWs after valve closure during 1.5 s; while the active sequence induced 52 SWs with a repetition rate of 34 Hz during 1.5 s by using an ARF.

The natural sequence used diverging waves (DWs) with a virtual focus of -34 mm for SW tracking. The active sequences consisted of three stages: (i) acquiring 20 DW reference frames, (ii) generating a focused ARF-push beam (push duration of 800 μ s and center frequency of 2 MHz), and (iii) tracking SW propagation during 28 ms using DWs (virtual focus of -288 or -100 mm). A progressive pulse-inversion transmission scheme (center frequency of 2 MHz) was implemented for both sequences to improve image quality for tracking SWs using DWs [65]. Depending on the depth of the field

of view, frame rates varied between 6159 Hz and 8774 Hz. For offline processing, the radio frequency (RF) data of the natural and active sequence were saved.

ECG traces were simultaneously measured with the SWE acquisitions. A trigger-out signal from the Vantage 256 system at the start of each sequence, together with the ECG signal using the Multi-Channel Software (TiePie Handyscope HS3, TiePie engineering, Sneek, the Netherlands), was recorded. In this way, ECG data was synchronized with the SWE measurements. During each HFR SWE acquisition, PV-loops of the LV were also recorded (MPVS ULTRA, LabChart 6, ADInstruments) and saved for offline post processing. PV-loop registration is accompanied with a separate ECG recording (Powerlab, ADInstruments), which was used to match the PV and SWE data in time. For every condition tested, 3 HFR SWE and 3 simultaneous PV-loop acquisitions were performed. Furthermore, conventional echocardiographic B-modes were recorded with a Vivid E95 system (GE Vingmed, Ultrasound, Horten, Norway) for the calibration of the LV volumes of the PV data. When only PV-loops were acquired during preload reduction, this was also repeated for 3 times.

8.2.4. Data Analysis

SWE

A 10th-order bi-directional Butterworth band-pass filter from 3 MHz to 5 MHz (around the second harmonic at 4 MHz) was applied to the RF data before performing offline beamforming using the Verasonics software (Kirkland, United States). Post-processing was performed in Matlab R2019a (Mathworks, Natick, MA, USA). Since data analysis of the SWE data was done in a similar way as described in **Chapter 7**, we would like to refer to this chapter for the description of the methods used to obtain propagation speeds in the natural and active sequences. Due to the lower frequency content of the natural compared to the ARF-induced SWs, different smoothing and frequency filters were applied (e.g. Butterworth 6th-order bandpass filter of 15 – 100 Hz versus 75 – 750 Hz on the tissue Doppler data of the natural and ARF-induced SWs respectively). Analogous to **Chapter 7**, all SWs were analyzed by two observers, who each manually selected 5 M-splines over the IVS for each SW. In this way, variabilities induced by M-spline locations as well as by tracking inaccuracies were included [80]. Furthermore, due to a limited signal-to-noise ratio for the ARF-induced SWs, propagation speeds were obtained manually instead of using a Radon transform as was done for the natural SWs.

The SWs after valve closure were also tracked in the active sequences, by performing the same data-analysis methods as used for the natural sequences. However, compared to **Chapter 7**, data analysis was further improved. The active sequences consisted of 52 separate recordings of 28 ms, with periods of approximately 1.4 ms in between (ARF-repetition rate of 34 Hz). Natural SWs have larger wavelengths than ARF-based SWs and could thus (partially) propagate in between active recordings. Therefore, for a more accurate tracking of the natural SWs, tissue velocity data of 5 individual recordings (of 28 ms each) around the moment of valve

closure were merged by linearly interpolating the tissue Doppler data in between the recordings, to obtain continuous data during 147 ms.

PV-loop Parameters

End-diastolic and end-systolic LV volumes were measured using the Teichholz method [141] on conventional parasternal long-axis echocardiographic B-modes recorded with a Vivid E95 ultrasound system for each condition. These volumes were then used to calibrate the volumetric data signals recorded with the conductance catheter. Different hemodynamic parameters were derived from the PV data, to quantify the induced changes in loading, contractility and LV chamber compliance.

To study the effect of hyperelasticity, the end-diastolic and end-systolic pressure (*EDP* and *ESP*) were determined as the pressure at the foot of the pressure pulse ($dP/dt > 0$) [16], and at $(dP/dt)_{\min} - 20$ ms [142], respectively. These parameters were derived from the heart cycles in the PV recordings of which its ECG signal correlated best to that of the HFR SWE data. This procedure was repeated for every condition.

The preload recruitable stroke work relationship (*PRSW*) was used as a measure of contractility. The *PRSW* was defined as the slope of the linear relation between stroke work (*SWK*) and end-diastolic volume (*EDV*) [143]

$$SWK = PRSW \cdot EDV + b, \quad (8.1)$$

with *SWK* in [mmHg·ml], the slope *PRSW* in [mmHg], *EDV* in [ml], and *b* a constant in [mmHg·ml]. In acquisitions with preload reduction, the *SWK* of different subsequent heart cycles was plotted against the *EDV*. Then, a linear least square fitting procedure was used to fit Equation 8.1 to the data, and to obtain the *PRSW*. A bisquare weighting function was used to obtain a more robust fit by giving less weight to outliers.

To describe the passive filling curve for the LV, which is assumed to correlate with the passive material properties of the myocardium, the end-diastolic pressure-volume relationship (EDPVR) was assessed. An exponential model [16] was fit to the (*EDV*, *EDP*)-points of the PV-loops obtained during preload reduction, in a non-linear least squares fashion. The following exponential model was considered:

$$P = c \cdot \exp(\beta V) + d, \quad (8.2)$$

with *P* the pressure in [mmHg], *c* and *d* constants in [mmHg], and *V* the volume in [ml]. We used two parameters derived from the EDPVR. The first parameter assessed is β in $[ml^{-1}]$, which has been used by many researchers to index diastolic chamber properties [16]. The second parameter is dP/dV in [mmHg/ml]. This parameter represents the classic definition of chamber stiffness [16], i.e. the relative change in pressure and volume of the LV, which is described by the slope of a tangent to the non-linear EDPVR at a specific volume. The parameter dP/dV was determined at a mean end-diastolic LV volume among all conditions in all animals (i.e. at 72.6 ml), such that the effect of hyperelasticity was minimized.

8.2.5. Feasibility

Natural SWE sequences in which a clear trackable SW pattern in the tissue velocity data was visible around AVC and/or MVC, were included. Active sequences in which SWS were visible in at least 20% of the ARF pushes were included. This threshold was lower than the one used in **Chapter 7** (40%), since we experienced it to be more difficult to externally induce SWs in a transthoracic setting and wanted to minimize the number of acquisitions excluded. Since both inclusion criteria can be rather subjective, we only included natural and ARF-based SW recordings for which at least 2 propagation speeds (corresponding to successful SW tracking in 2 distinct TDI panels and thus 2 M-splines) per observer were obtained. Furthermore, a total of at least 20 propagation speed values (successful SW tracking in 20 TDI panels) per pig per condition were required for all AVC or MVC events or for all pushes in systole or diastole respectively, to include a specific condition.

8.2.6. Statistics

Statistical analyses were performed using the statistical toolbox of Matlab. For every SW, propagation speeds along 10 M-splines drawn by two observers were obtained to include intra-scan and inter-observer variability [80]. The three acquisitions corresponding to a specific condition were grouped, and median values and inter-quartile ranges (IQR) of all M-splines in all acquisitions of a specific condition were computed for AVC, MVC, systole and diastole. To select the ARF-pushes corresponding to systole and diastole, the 10% highest and lowest median SW propagation speeds of a specific condition were computed [62], respectively. Non-parametric two-sided Wilcoxon signed-rank tests were used to compare different groups of SW propagation speeds. P-values (two-sided) smaller than 0.05 were considered to be significant.

The median and IQR of the PV-loop parameters were computed per condition per animal. Due to the limited number of acquisitions, a multivariate analysis could not be performed to study the effect of loading, contractility and PV-derived end-diastolic stiffness on SW propagation speeds. Therefore, individual correlations between SW propagation speeds and PV-loop parameters were investigated. Correlations were tested by performing linear regressions and computing the Pearson (linear) correlation coefficients. When p-values (two-sided) smaller than 0.05 were obtained, correlations were interpreted as being significant. Correlation values (R) were classified as follows: moderate for $0.4 \leq R < 0.6$, strong for $0.6 \leq R < 0.8$, and very strong for $0.8 \leq R < 1$. To study the effect of loading, correlations of SW speed with EDP and ESP were investigated for the BL, PR, AI and PI conditions. In these conditions, the effects of changes in contractility, relaxation and the passive characteristics of the myocardium were assumed to be negligible. To study the effect of contractility, SW speeds were correlated with $PRSW$ for the DOB, MI and REP acquisitions, since these conditions are expected to affect contractility and thus $PRSW$. SW speed correlations with the intrinsic diastolic myocardial stiffness, and thus with β and dP/dV , were studied for the MI and REP acquisitions, as the intrinsic diastolic passive myocardial

Table 8.2: Overview of the feasibility of tracking the SWs after AVC and MVC and the ARF-based SWs. The numbers represent the acquisitions in which SWs were tracked. Abbreviations: AVC: aortic valve closure, MVC: mitral valve closure, ARF: acoustic radiation force.

	Pig 1	Pig 2	Pig 3
AVC	75% (15/20)	90% (28/31)	97% (30/31)
MVC	30% (6/20)	68% (21/31)	35% (11/31)
ARF	55% (11/20)	71% (22/31)	74% (23/31)

stiffness is expected to change in these conditions.

8.3. RESULTS

8.3.1. Feasibility

For the natural SWE sequences, a higher feasibility was obtained for the SWs after AVC than after MVC. SWs were tracked in 75% – 97 % of the acquisitions of the individual pigs after AVC; and in 30% – 68% after MVC. An overview is given in Table 8.2. Conditions for which less than 20 SW propagation speed values were obtained per pig, were excluded. Hereafter, we did not have AVC propagation speeds values for conditions BL1, PR, DOB, REP and REP PR in pig 1; and for condition AI in pig 2. For MVC, the missing values were obtained in conditions PR, AI and MI for all pigs; PI, DOB, REP for pig 1 and 2; and BL1, BL3, and REP PR for pig 1. Due to the many missing values for the SWs after MVC, resulting in too many excluded conditions, the results will not be further presented in this chapter.

For the active sequences, SWs were tracked in 55% (11/20), 67% (22/31), and 74% (23/31) of the acquisitions, respectively for the different pigs. For pig 2 and 3, all HFR SWE acquisitions were recorded by placing the probe on the right side of the chest, while for pig 1 SWE acquisitions were taken from the right and left side of the chest. Afterwards, the SWE acquisitions from the left were excluded for consistency reasons. No successful active acquisitions were taken for BL1, PR, DOB, and REP PR in pig 1; REP PR in pig 2; and DOB and REP in pig 3.

8.3.2. PV-loop Measurements

Figure 8.1 gives an overview of the PV-loop parameters obtained for the different conditions tested. Due to the limited number of pigs, no statistical tests could be applied on the PV-loop parameters.

Figure 8.1 a and b give an overview of the *EDP* and *ESP* obtained for the different conditions. We will especially focus on the conditions PR, AI and PI, as these were included to assess the effect of hyperelasticity. *EDP* and *ESP* were in general lower for PR (mean decrease of 9.8 mmHg and of 47 mmHg respectively) and higher for AI (mean increase of 3.4 mmHg and of 21 mmHg respectively) compared to BL2. Less consistent differences were observed for PI compared to BL2 (differences of -3.4

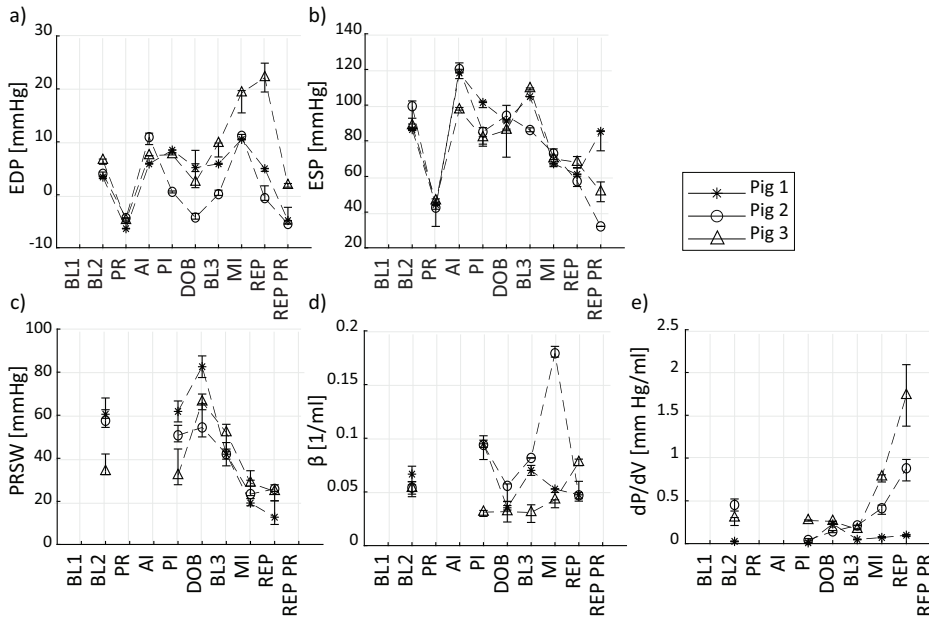


Figure 8.1: Overview of the PV-loop parameters obtained for the different conditions tested in this study. *EDP* and *ESP* are shown in (a) and (b). Preload recruitable stroke work (*PRSW*), a measure for the contractility is shown in (c). The parameters β and dP/dV , used as measures for diastolic chamber stiffness, are shown in (d) and (e) respectively. Errorbars depict median values and the corresponding interquartile ranges. Abbreviations: *EDP*: end-diastolic pressure, *ESP*: end-systolic pressure, *PRSW*: preload recruitable stroke work, BL: baseline, PR: preload reduction, AI: afterload increase, PI: preload increase, DOB: dobutamine, MI: myocardial infarction, REP: reperfusion, REP PR: reperfusion preload reduction.

– 5.1 mmHg and –14 – 15 mmHg for *EDP* and *ESP* respectively). The *EDP* changes in the other conditions were approximately consistent across all pigs, except for REP. The *ESP* also altered consistently in all pigs for the other conditions, except for BL3 and REP PR.

Figure 8.1 c gives an overview of *PRSW*, used as a measure of contractility, obtained for the different conditions. PI had a negligible effect on the *PRSW* for all pigs. The condition DOB was included in the protocol to test the effect of contractility, and a general increase of *PRSW* was found compared to BL2 (mean increase of 17 mmHg). *PRSW* was found to decrease after MI (mean decrease of 22 mmHg) and even further for REP (mean decrease of 24 mmHg) compared to BL3.

Figure 8.1 d and e give an overview of the β and dP/dV parameters, that both are used to assess the diastolic LV chamber stiffness. MI and REP were the two conditions in the protocol that deliberately altered the diastolic stiffness. A large increase in β was observed after MI in pig 2 (increase of 0.10 ml^{-1}) compared to BL3, and the β after REP was only found to be higher than BL3 in pig 3. dP/dV was found to increase among all pigs after MI (mean increase of 0.3 mmHg/ml) and even further for REP (mean increase

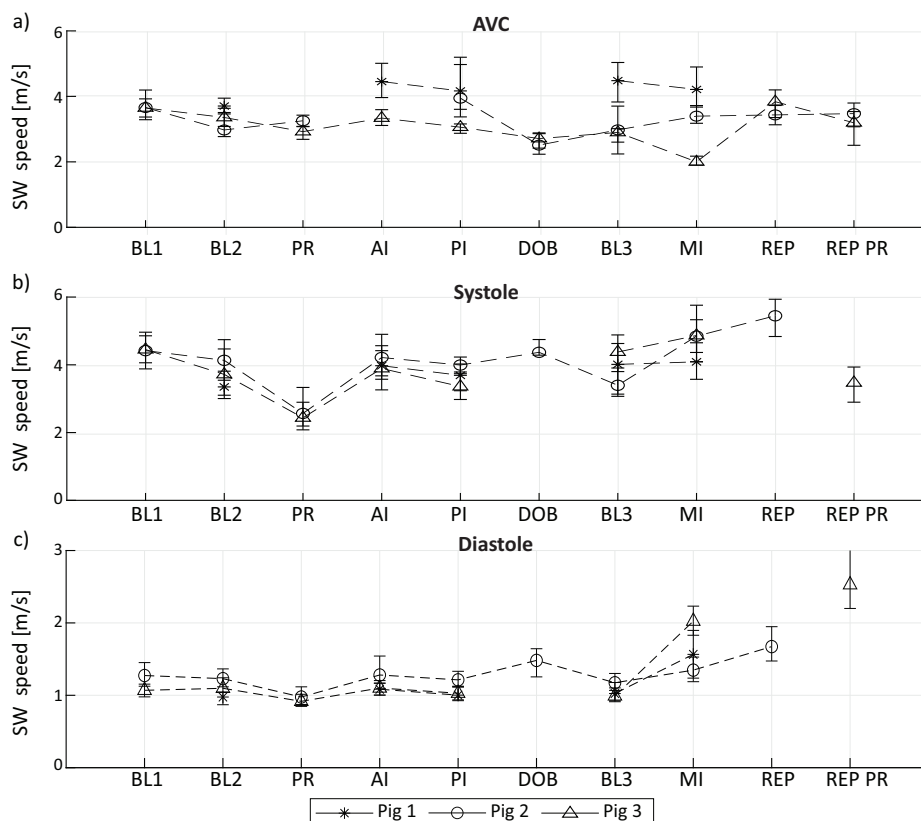


Figure 8.2: Overview of the propagation speeds obtained after (a) AVC, and the ARF-based SW propagation speeds in (b) systole and (c) diastole for the different conditions tested in this study. Errorbars depict median values and the corresponding inter-quartile ranges. Abbreviations: AVC: aortic valve closure, BL: baseline, PR: preload reduction, AI: afterload increase, PI: preload increase, DOB: dobutamine, MI: myocardial infarction, REP: reperfusion, REP PR: reperfusion preload reduction.

of 0.8 mmHg/ml) compared to BL3. The conditions PI and DOB showed negligible effects in terms of chamber stiffness based on dP/dV , whereas larger, but inconsistent, changes were measured based on parameter β .

8.3.3. SWE Acquisitions

An overview of the propagation speed values after AVC, in systole and in diastole, obtained for the different conditions in the three pigs is given in Figure 8.2. When using all median propagation speed values per condition per pig, the propagation speeds after AVC were found to be borderline significantly lower than in systole (Wilcoxon signed-rank test, $n=22$, $p=0.05$), and significantly higher than in diastole (Wilcoxon signed-rank test, $n=22$, $p<0.01$).

Since only three pigs were included in this study, the changes in SW propagation speeds could not be statistically tested. Nonetheless, especially for the ARF-based speeds in systole and diastole, a good agreement between the changes in SW propagation speeds across the animals was visually observed. In general, SW propagation speeds decreased after placing the catheters (mean decrease from BL1 to BL2 of 0.5 m/s for AVC, of 0.5 m/s for systole and of 0.01 m/s for diastole). To make fair comparisons, the different conditions tested were only compared with baseline measurements performed after placing the catheters (BL2 and BL3).

For both active and natural SWE, SW propagation speeds first generally decreased for PR (mean decrease of 1.4 m/s, 0.2 m/s and 0.08 m/s for systole, diastole and AVC respectively), then increased for AI (mean increase of 0.3 m/s, 0.05 m/s and 0.4 m/s for systole, diastole and AVC respectively compared to BL2), and then decreased again for PI (mean differences of -0.05 m/s, -0.02 m/s and +0.4 m/s for systole, diastole and AVC respectively compared to BL2).

Although an increase in systolic and diastolic propagation speeds was observed for DOB in pig 2 (mean increase of 0.2 m/s and 0.3 m/s respectively for systole and diastole), the corresponding propagation speeds after AVC decreased compared to BL2 (mean decrease of 0.5 m/s). Furthermore, while the ARF-based propagation speeds show an increase for MI (mean increase of 0.7 m/s and 0.6 m/s respectively for systole and diastole compared to BL3) and REP (mean increase of 2.1 m/s and 0.5 m/s respectively for systole and diastole compared to BL3), a decrease in AVC-based propagation speeds for MI was observed in pig 1 and 3 (decrease of 0.3 m/s and 0.9 m/s respectively) and a general increase for REP (mean increase of 0.4 m/s). This shows that correlation between natural and ARF-based SW propagation speeds are not trivial. To illustrate, the median ARF-based propagation speeds of pig 3 obtained for BL3 and MI, together with the AVC-based speeds in the same cardiac cycles for the same M-splines, are shown in Figure 8.3. The figure shows a clear increase in diastolic propagation speeds after ligation of the LAD for 90 minutes, a small increase in systolic speeds, and a decrease in the propagation speeds after AVC. For REP PR, ARF-based propagation speeds were obtained only in pig 3: while a decrease in systolic speeds was measured (decrease of 0.9 m/s), the diastolic propagation speeds and the SW propagation speeds after AVC were found to increase (increase of 1.5 m/s and 0.3 m/s respectively for diastole and AVC compared to BL3).

8.3.4. SWE versus PV-loop Parameters

For clinical application, an important question is whether SW propagation speeds are more depending on intrinsic material characteristics of the myocardium than on loading conditions. To make a first step into the direction of answering this question, we visualized potential correlations of SW propagation speeds with *EDP* and *ESP* in Figure 8.4 (effect of hyperelasticity), and with *PRSW* (effect of contractility) and LV chamber compliance parameters in Figure 8.5.

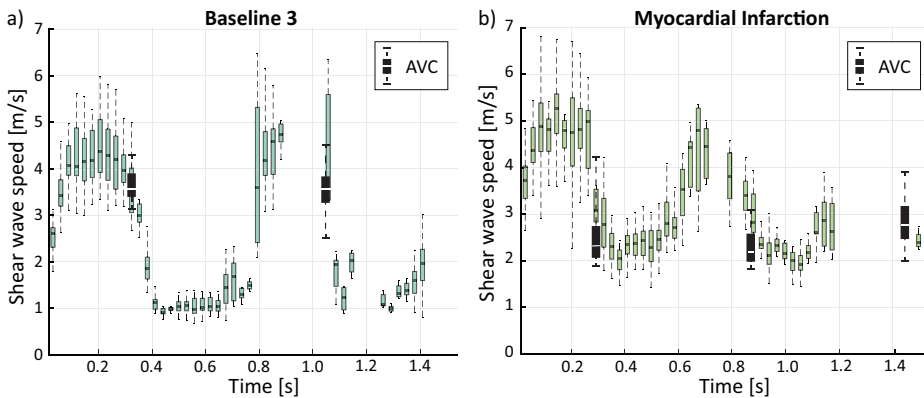


Figure 8.3: Propagation speeds obtained throughout the cardiac cycle for ARF-induced SWs together with the SWs obtained after AVC within the same heartbeats for the same M-splines, before (a) and after (b) ligation of the LAD for 90 minutes in order to induce a myocardial infarction. Boxplots are over all M-splines obtained for three consecutive acquisitions for the individual plots. Although an increase in diastolic propagation speed can clearly be observed, the SWs after AVC seem to decrease after ligation. Abbreviation: AVC: aortic valve closure.

First, Figure 8.4 plots AVC-based, systolic and diastolic SW propagation speeds as a function of *EDP* and *ESP* for conditions BL2, PR, AI and PI, in which any effect on contractility and chamber stiffness is assumed to be negligible. It should be noted that the effects of hyperelasticity and the Frank-Starling mechanism on myocardial stiffness could not be separated in systole and after AVC, while in diastole the effect of the Frank-Starling mechanism is expected to be minimized. All propagation speeds were visually observed to increase with increasing *EDP* and *ESP*, and significant correlations were found for all propagation speeds except for the propagation speeds after AVC with *EDP*. A very strong correlation was found between the ARF-based propagation speeds in systole and *ESP* (Pearson correlation coefficient $R=0.91$, $p<0.01$).

Second, correlations with *PRSW*, and thus with contractility, were studied in Figure 8.5 a, d and g for conditions BL2, DOB, BL3, MI and REP. Negative correlations were visually observed between all SW propagation speeds and *PRSW*, which were found to be statistically significant for the ARF-based speeds (Pearson correlation coefficient systole: $R=-0.50$, $p=0.019$, and diastole: $R=-0.58$, $p<0.01$). While in general a decrease in *PRSW* was measured for MI and REP (as expected), higher propagation speeds were found for these conditions compared to BL3 (see also Figure 8.1 and 8.2).

Third, correlations with the LV chamber stiffness in diastole were studied in Figure 8.5 b, c, e, f, h and i for BL3, MI and REP. Correlations with β were studied in Figure 8.5 b, e and h, but no significant correlations were found with any SW quantity. As an alternative to β , correlations with dP/dV were studied in Figure 8.5 c, f and i. Strong positive correlations were found between dP/dV and the ARF-based SW propagation speeds (Pearson correlation coefficient systole: $R=0.81$, $p<0.01$, and diastole: $R=0.76$, $p<0.01$), but not with the SW propagation speeds after AVC.

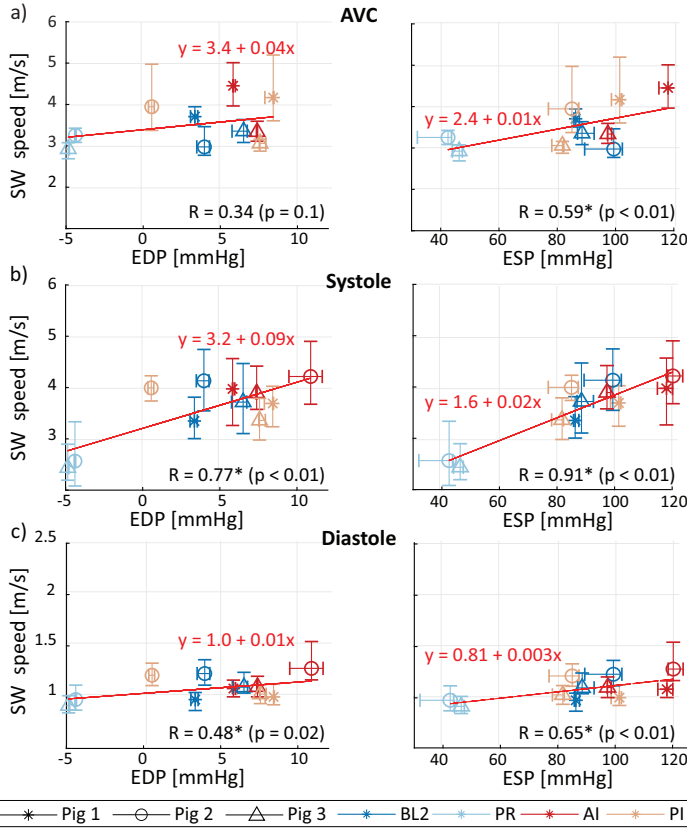


Figure 8.4: Hyperelasticity: Overview of the correlations between the propagation speeds after (a) AVC, and the ARF-based propagation speeds in (b) systole and in (c) diastole with EDP and ESP. Errorbars depict median values and the corresponding inter-quartile ranges. Correlations were tested by performing linear regressions (red lines) and computing the Pearson (linear) correlation coefficients (R-values). Asterisks (*) denote a significance level of $p < 0.05$. Abbreviations: AVC: aortic valve closure, ARF: acoustic radiation force, SW: shear wave, EDP: end-diastolic pressure, ESP: end-systolic pressure.

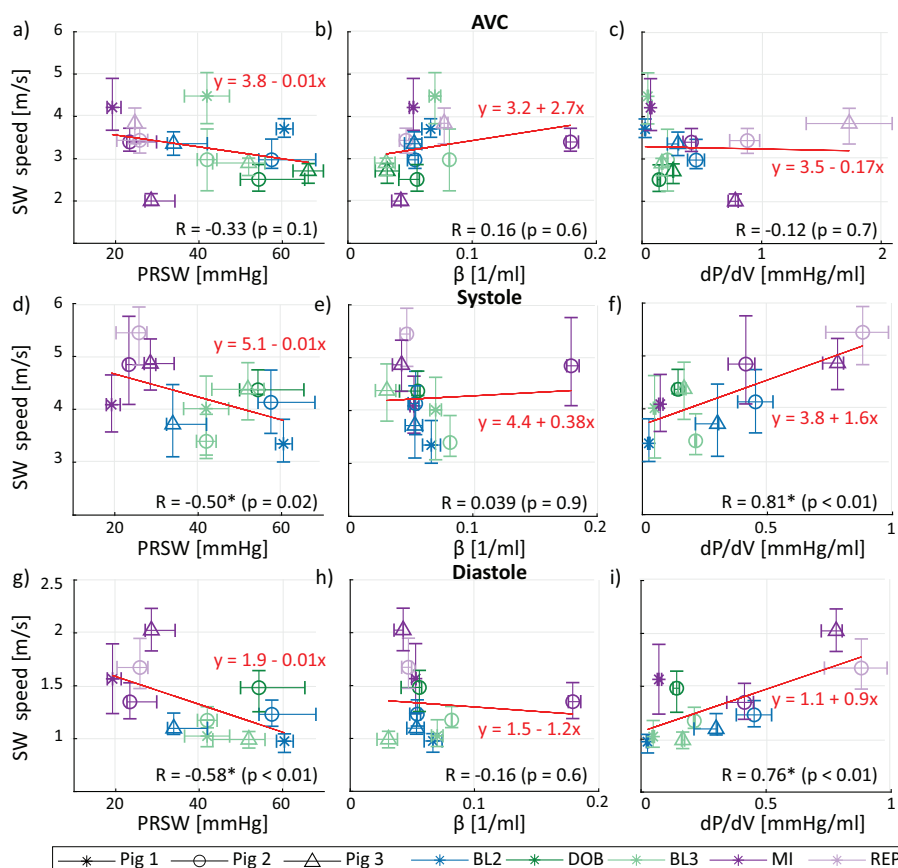


Figure 8.5: LV contractility and chamber stiffness: Overview of the correlations between the propagation speeds after AVC (upper panels), and the ARF-based propagation speeds in systole (middle panels) and in diastole (lower panels), with PRSW, β and dP/dV . Errorbars depict median values and the corresponding inter-quartile ranges. Correlations were tested by performing linear regressions (red lines) and computing the Pearson (linear) correlation coefficients (R-values). Asterisks (*) denote a significance level of $p < 0.05$. Abbreviations: AVC: aortic valve closure, ARF: acoustic radiation force, SW: shear wave, PRSW: preload recruitable stroke work.

8.4. DISCUSSION AND CONCLUSION

This chapter studies how shear wave (SW) propagation speeds are affected by changes in loading conditions and intrinsic characteristics of the myocardium, such as contractility and diastolic chamber compliance. In three pigs, SWs induced by an acoustic radiation force (ARF) and after valve closure were tracked while altering preload or afterload, administering dobutamine (DOB) intravenously, or inducing a myocardial infarction (MI) followed by reperfusion (REP). Some clear observations are made, but since only three pigs were included in this study, no definite conclusions can be drawn.

8.4.1. Hyperelasticity

The ARF-based propagation speeds in diastole and systole were observed to increase with end-diastolic and end-systolic pressures (*EDP* and *ESP*), and the SW speeds after aortic valve closure (AVC) with *ESP*. These correlations are probably caused by material hyperelasticity and the Frank-Starling mechanism. The results support other studies reporting on a preload dependency for SWs externally induced with a mechanical actuator in diastole in open chest pigs using a viscoelastic material model [52], and for ARF-based SWs in Langendorff-perfused rat hearts [75]. The latter study saw a significant increase only in systolic speeds with preload (by using systolic pressures), but this is potentially due to a smaller pressure range compared to our study (pressure range of 14.8 mmHg and 52.7 mmHg vs. 25.9 mmHg and 87.4 mmHg in this chapter, in diastole and systole respectively). Our results also show stronger correlations with *EDP* and *ESP* for the ARF-based speeds in systole than in diastole, potentially due to the minimized effect of the Frank-Starling mechanism in diastole, and since diastole occurs at a flatter part of the stress-strain relationship.

8.4.2. Contractility and Chamber Compliance

Several effects of the induced ischemia were observed in the SWE and PV-loop data. For the ARF-induced SWs, in general higher propagation speeds were measured after MI and REP. Although a lower preload-recrutable stroke work (*PRSW*) – parameter used for contractility – was observed in these conditions, the β parameter – used for diastolic chamber compliance – did not increase in all animals. On the other hand, dP/dV did increase for all animals from baseline to MI to REP, indicating that the intrinsic diastolic myocardial stiffness was increased in these conditions compared to baseline. The unexpected results of the parameter β could be explained by several causes, such as i) β is depending on the other parameters used to fit the pressure-volume relation in Equation 8.2; ii) the fitting outcome is depending on the ranges included, and thus hyperelasticity could explain the differences in β among the animals; and iii) β is only a single parameter used to describe pressure-volume relations, while the first derivative of this relation is expected to better represent chamber stiffness. However, it should also be noted that although the effect of hyperelasticity is minimized in the dP/dV values (since these values were determined

at a fixed end-diastolic LV volume), pressures still varied during BL3, MI and REP SWE acquisitions (see Figure 8.1). Furthermore, although the values obtained for $PRSW$ and dP/dV show the expected effects of ischemia – a reduced contractility and an increased LV chamber stiffness – it should be noted that the PV-loop parameters represent the functioning of the entire LV and is thus rather a global measure, whereas the MI was only locally induced and SW propagation speeds were only locally tracked.

The higher propagation speeds measured for MI and REP and the strong correlations found between the ARF-based speeds and dP/dV suggest that SWE can be used as a measure of the intrinsic diastolic myocardial stiffness. The observations made in this chapter are in agreement with previous findings. An increased diastolic stiffness was also measured with ARF-based SWE in open-chest sheep after a ligation of the LAD for 120 minutes [57]. Furthermore, increased diastolic and (non-significantly) increased systolic speeds were also observed for SWs generated with an mechanical actuator in open chest pigs after LAD ligation for 1 – 3 hours and LAD reperfusion for 1 – 2 hours [52]. However, our systolic SW speed results are not in agreement with the decreased ARF-based systolic speed measured after a short-term ligation of 20 minutes in open-chest sheep [55]. The different results in literature suggest that different effects of ischemia on SW propagation speeds can be expected depending on the duration of the ischemia, since the process of changes induced by MI is dynamic. Furthermore, the effect of ischemia might be animal / species dependent.

The decrease in $PRSW$ measured for MI and REP suggests a decrease in contractility. Although a decrease in contractility is expected to result in lower propagation speeds, we observed the opposite in our dataset. This can possibly be explained by the fact that an increased diastolic chamber stiffness has a larger effect on the SW propagation speeds than a decreased contractility. Different studies suggest that ARF-based systolic [75, 139] as well as SW propagation speeds after AVC [137] are correlated with contractility. However, due to the limited number of successful DOB acquisitions and since ischemia also affected the diastolic chamber compliance, we could not do a multi-variate analysis in order to estimate the isolated effect of contractility on SW propagation speeds.

8.4.3. Natural versus ARF-based SWE

The SW propagation speeds after AVC were found to be higher than the ARF-based speeds in diastole ($p < 0.01$) (as also found in an open-chest setting in **Chapter 7**) and to be lower than the ARF-based systolic speeds ($p = 0.05$). Thus, the results of this study support the suggestion made in **Chapter 7** that with SWs after valve closure, a mixed state in between contraction and relaxation is measured.

In pig 3, we observed an increase in systolic and diastolic propagation speeds for MI and REP, but for MI a decrease in propagation speeds after AVC was also measured (Figure 8.3). This is an unexpected result, since the natural and ARF-based propagation speeds are expected to be correlated. It is furthermore notable that this

decrease in propagation speed for AVC after MI was consistently measured in the natural SWE acquisitions as well as for the natural SWs in the active acquisitions. A potential explanation could be that the timing of the AVC with respect to the dynamic myocardial stiffness, is affected by MI in this specific animal. Although timing of AVC was measured within the active SWE sequences, it could not be accurately measured with respect to a ground-truth for the dynamic myocardial stiffness, due to a lack of a fixed reference among the different acquisitions.

The ARF-based SW propagation speeds were observed to be more consistent among the different animals than the SW speeds after valve closure, which is a potential advantage for clinical application. Natural SWs have relatively large wavelengths and thus only a small part of the wavelength could be tracked, resulting in less accurate results. Furthermore, the natural SWs were less distinguishable from the general heart motion than the high frequency ARF-induced SWs. Since gross motion of the heart was affected by the different conditions, not only different propagation speeds but also different tissue motion patterns were visible, complicating the comparison among animals and conditions.

8.4.4. Shear Waves after Mitral Valve Closure

Representative wave propagation patterns after AVC are shown in Figure 8.6 a, whereas panels b and c demonstrate wave patterns after MVC. The results of the SWs after MVC were not included in this chapter for several reasons. First, the apparent propagation speed in the tissue velocity panels was often observed to be non-linear. An example of this non-linear pattern is shown in Figure 8.6 b: an apparent lower propagation speed was observed nearby the basal part compared to the mid-ventricular/apical part of the IVS in most acquisitions among all pigs. The cause of this discrepancy in propagation speed is yet unknown. Although MVC occurs around the onset of contraction, and thus an increase in propagation speed can be expected, this cannot explain a sudden change in propagation speed as was observed. Local differences in fiber orientation or propagation direction could also have caused this phenomenon, which needs further study.

Second, in many MVC tissue-velocity panels a dominating transition from positive to negative tissue motion was observed (see Figure 8.6 b and c), which could also correspond to more general low frequency motion of the heart instead of to SW-related vibrations (although expected to be a slower phenomenon). Since no high-frequency ‘wave-like’ pattern was visible, tracking this phenomenon with the Radon transform was more difficult. By using tissue acceleration data, the transition from positive to negative tissue motion becomes more apparent, as visible in the right panel of Figure 8.6 c. The wave could therefore be tracked easier, as done by several other promising studies [40–42]. Therefore, we compared the results for tissue velocity and tissue acceleration data after AVC and MVC for all conditions in pig 3. Especially the feasibility for MVC increased for tissue acceleration data (acceleration vs tissue: total number of M-splines: 499 vs 560 for AVC, and 272 vs 186 for MVC; total number of conditions: 9 vs 10 for AVC and 6 vs 4 for MVC). Furthermore, significant

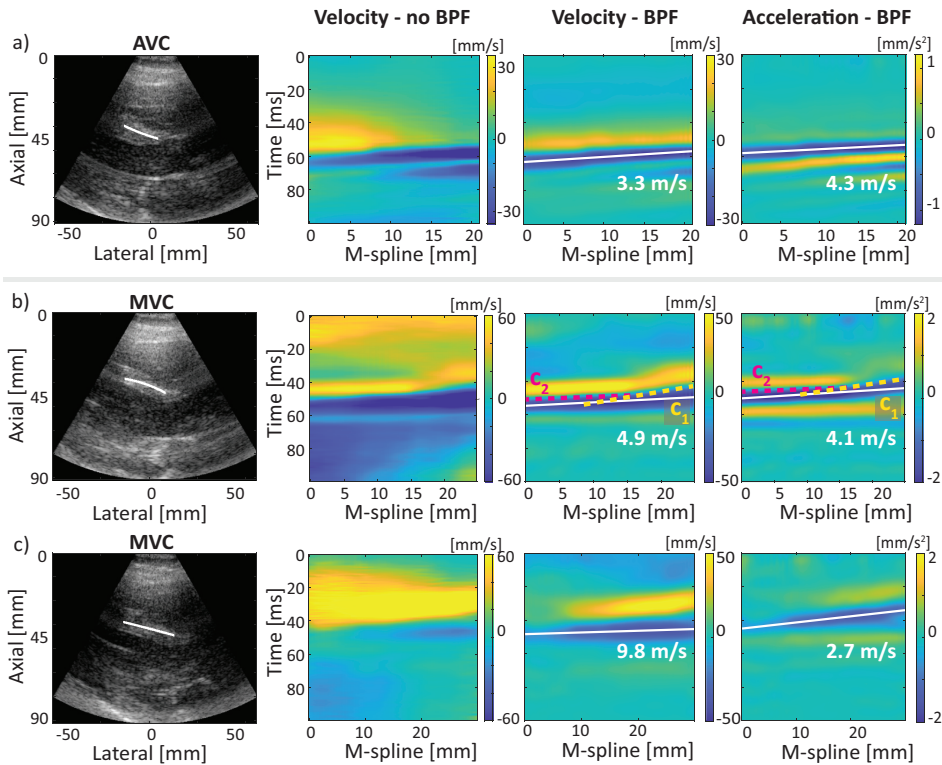


Figure 8.6: Example of tissue velocity and tissue acceleration panels obtained after AVC (a) and MVC (b and c). For the SWs after MVC, lower propagation speeds were observed on the basal part compared to the mid-apical part ($c_1 < c_2$) of the IVS (b). Furthermore, often mainly a transition from positive to negative tissue velocity was observed (c) instead of a distinct 'wave-like' patterns as for AVC. Abbreviations: AVC: aortic valve closure, MVC: mitral valve closure, BPF: bandpass filter.

higher propagation speeds were obtained for the SWs after AVC when using tissue acceleration data instead of tissue velocity data (Wilcoxon signed-rank test: $p < 0.01$, $n = 9$; Pearson correlation coefficient: $r = 0.87$, $p < 0.01$). These differences can possibly be explained by dispersion, since dispersion effects might be present as described in **Chapter 1**, and since higher frequencies are amplified when using acceleration data. Also in **Chapter 3**, we showed different propagation speeds after AVC for tissue velocity versus tissue acceleration data in open-chest pigs and for different rims in time [80]. Therefore, the discrepancy in SW speeds measured in this chapter, could also be caused by the fact that different aspects of the complex tissue motion are tracked. Thus, the results obtained for the tissue velocity data of ARF-induced SWs and the SWs after AVC, could not be directly compared with tissue acceleration data after MVC. Furthermore, for consistency throughout this thesis, this chapter focused on the results of tissue velocity data. Since tissue velocity data resulted in a low feasibility for the SWs after MVC, MVC data was excluded.

8.4.5. Limitations and Future Work

This chapter describes the preliminary results of 3 pigs, without drawing any definite conclusions. Measurements were however performed in 8 pigs in total, whereof ARF-induced SWs could not be observed in 5 animals (success rate of 37.5%). The main reason for this low feasibility rate is probably the sub-optimal transthoracic image quality that was observed in these animals, which is especially crucial for the small magnitude of tissue displacements induced by ARF. However, the feasibility rate is only slightly lower than the 41% that has been previously reported for healthy volunteers using ARF imaging [60]. Furthermore, the feasibility rate was found to slightly improve when using a newer P4-2V probe (Verasonics, Kirkland, United States) instead of the P4-2 probe (ATL, Bothell, Washington, United States): the success rate increased from 1 out of 4 animals to 2 out of 4 animals). In addition, the success of inducing SWs with an ARF seemed to strongly depend on the IVS location and orientation in combination with the ARF-push depth, and we were not able to find an optimal combination in all animals.

Intra-scan, inter-observer and inter-scan variabilities were dealt with by drawing 5 M-splines by 2 observers each for every individual SW, and by performing 3 acquisitions for every condition. The variabilities measured are depicted by the errorbars in the figures. For the SWs after AVC, the IQRs of all SW propagation speed values per condition per animal were found to be in the range of 0.3 – 1.6 m/s. This range was found to be 0.5 – 1.7 m/s and 0.2 – 0.8 m/s for the SWs in systole and diastole respectively. It should be noted that these variabilities are in the same range as the mean differences in SW propagation speeds for individual conditions compared to baseline (0.01 – 2.1 m/s), as described in ‘Results – SWE acquisitions’. Furthermore, due to the limited data, this study on the effect of the different conditions on SW propagation speeds has a low statistical power. Consequently, differences in SW propagation speeds could not be statistically tested. Therefore, the research described in this chapter will be extended with more animals. Extending the current results will hopefully provide more insights in how SW propagation speeds depend on loading conditions, contractility and LV chamber stiffness on a group level instead of the individual level.

During the *in vivo* experiments, the effects of different mechanisms on the myocardial stiffness and thus on the SW propagation speeds could not be fully separated. First, although dobutamine is expected to affect contractility, also heart rate is increased, potentially resulting in an incomplete relaxation in diastole. Heart rate could also have induced a large inter-beat variability in the measurements after reperfusion, since arrhythmia was observed in all pigs. Second, while increasing preload, the effects of hyperelasticity and the Frank-Starling mechanism cannot be distinguished at the moment of AVC and in systole. Third, we observed a decrease in contractility and an increase in LV chamber stiffness after ischemia, of which the net effect on the SW propagation speeds measured is expected to depend on the moment in the cardiac cycle at which the measurements are performed. Fourth, after reperfusion, the thickness of the IVS was observed to increase. Since chamber

compliance does not only depend on the intrinsic myocardial stiffness, but also on LV chamber characteristics such as wall thickness, these effects could not be isolated.

8.4.6. Clinical Relevance

This chapter describes one of the first studies in which ARF-based SWs were induced throughout the entire cardiac cycle in a transthoracic setting. Villemain *et al.* showed that ARF-based SWE is also feasible in human in diastole, and that SW propagation speeds increase with age and are significantly higher in hypertrophic cardiomyopathy patients than in healthy volunteers [63]. In this chapter, a first step in investigating the effect of loading conditions and intrinsic myocardial characteristics on the SW propagation speeds of ARF-based SWs and SWs after valve closure was made. The preliminary results suggest that the propagation speeds in diastole, systole and after AVC are affected by LV chamber stiffness, as well as by hyperelasticity. Furthermore, the results suggest that the effect of chamber compliance changes ($\Delta 1.05$ m/s, Figure 8.5 i) dominates the effect of loading changes ($\Delta 0.36$ m/s, Figure 8.4 c) on diastolic SW propagation speeds. For the application of early clinical diagnosis, it should be further investigated whether the technique is sensitive enough to make a distinction between increased SW propagation speeds due to hyperelasticity, and thus instant LV pressures, and due to pathological intrinsic material characteristics, such as passive material characteristics and active relaxation and contraction. To answer this question, a multivariate analysis should be performed in the future by including realistic ranges of pressures, diastolic stiffness and contractility.

Acknowledgements

We would like to thank the animal facilities of KU Leuven for accommodating the animal experiments. In particular, Patricia Holemans, Matthew Amoni, Sebastian Ingelaere, Keir McCutcheon and Alexis Puvrez for helping us in performing the experiments. This work is part of the STW/TTW – Dutch Heart Foundation partnership program 'Earlier recognition of cardiovascular diseases' with project number 14740, which is (partly) financed by the Netherlands Organization for Scientific Research (NWO). Annette Caenen was supported by a grant of the Research Foundation Flanders (FWO) (1211620N). Stéphanie Bézy was supported by a grant of the Research Foundation-Flanders (FWO) (G092318N).

9

High-Frame-Rate Echo-Particle Image Velocimetry Can Measure the High Velocity Diastolic Flow Patterns



Jason Voorneveld

Lana B.H. Keijzer

Mihai Strachinaru

Daniel J. Bowen

Jeffrey S.L. Goei

Folkert J. ten Cate

Antonius F.W. van der Steen

Nico de Jong

Hendrik J. Vos

Annemien E. van der Bosch

Johan G. Bosch

Based on:

"High-Frame-Rate Echo-Particle Image Velocimetry Can Measure the High-Velocity Diastolic Flow Patterns", *Circulation: Cardiovascular Imaging* **12**(4), 2019 [144].

9.1. INTRODUCTION

Left ventricular (LV) flow patterns have been studied as potential early stage markers of cardiac dysfunction [145]. A relatively new method of measuring LV flow patterns, named echo-particle image velocimetry (echoPIV), tracks the motion of ultrasound contrast agent (UCA) microbubbles in the blood using echocardiography. However, the low frame rates (50 – 70 Hz) permitted by the current generation of clinical ultrasound scanners causes velocity magnitudes to be severely underestimated during filling and ejection (<40 cm/s at 50 Hz) [146]. High-frame-rate (HFR) echocardiography, using diverging-wave transmission schemes, has allowed for frame rates of up to 100 times faster than conventional line-scanning echocardiography. The image quality improvements when using HFR contrast enhanced ultrasound over conventional contrast enhanced ultrasound have recently been described [147]. Still, measurement of the high energy and high velocity trans-mitral jet has yet to be demonstrated in humans. We have shown previously, in an *in vitro* LV phantom study, that HFR echoPIV can accurately measure the high energy diastolic flow patterns [148]. In this work we demonstrate that this holds true in a patient with heart failure.

9.2. METHODS

A patient (19, female, 1.65 m, 66 kg) with dilated cardiomyopathy and DDD-ICD was admitted for decompensatio cordis. Apical 3-chamber views were obtained using both a clinical scanner (EPIQ 7 with X5-1 probe, Philips Healthcare, Best, the Netherlands), and a research scanner (Vantage 256, Verasonics, Kirkland, WA) with a P4-1 probe (ATL). Pulsed-wave (PW) Doppler measurements were obtained, using the clinical scanner, in the region of the mitral valve tips. UCA (SonoVue®, Bracco Imaging SpA, Milan, Italy) was then continuously infused at 0.6 ml/min (VueJect BR-INF 100, Bracco Imaging) and its arrival in the LV was verified with the clinical scanner. The research scanner was then used to obtain HFR contrast enhanced ultrasound acquisitions using a 2-angle (-7° , 7°) diverging wave sequence with 2-pulse contrast scheme (pulse inversion, mechanical index $\sim 0.06 - 0.01$) at a pulse repetition frequency of 4900 Hz, resulting in an imaging frame rate of 1225 Hz. EchoPIV analysis was performed in the polar domain, using custom PIV software that used correlation compounding on ensembles of 5 frames for each angle 4. The final vector-grid resolution was 1.25° by 1.25 mm. HFR echoPIV magnitudes were validated by comparing the mean temporal velocity profile to the PW Doppler spectrum captured in the same location. This study was approved by Erasmus Medical Center's medical ethics committee (NL63755.078.18).

9.3. RESULTS

The velocities measured with HFR echoPIV agreed well with the PW Doppler spectrum (Figure 9.1 a), with peak velocities up to 80 cm/s measured in this patient. This is the first demonstration of echoPIV measuring the high velocities present in the trans-mitral jet in adults. The high temporal resolution also permits study of the flow patterns in greater detail (**Supplementary Video**). For example, the large, central clockwise vortex was observed pinching off the trans-mitral jet before migrating apically (Figure 9.1 b – d: ★). Smaller, more transient vortices were also observed, such as the counter-clockwise vortex between the jet and the free-wall (Figure 9.1 b: †).

9.4. CONCLUSION

We have demonstrated in a patient with heart failure that high-frame-rate echoPIV can measure the, previously unobtainable, high velocity flow patterns in 2D. This development has potential to become a useful tool in the study of intra-ventricular blood flow and its relation with ventricular function.

Acknowledgements

This study was supported by ZonMW (Innovative Medical Devices Initiative program [project Heart Failure and 4D Flow, number 104003001]), the Hague, the Netherlands.

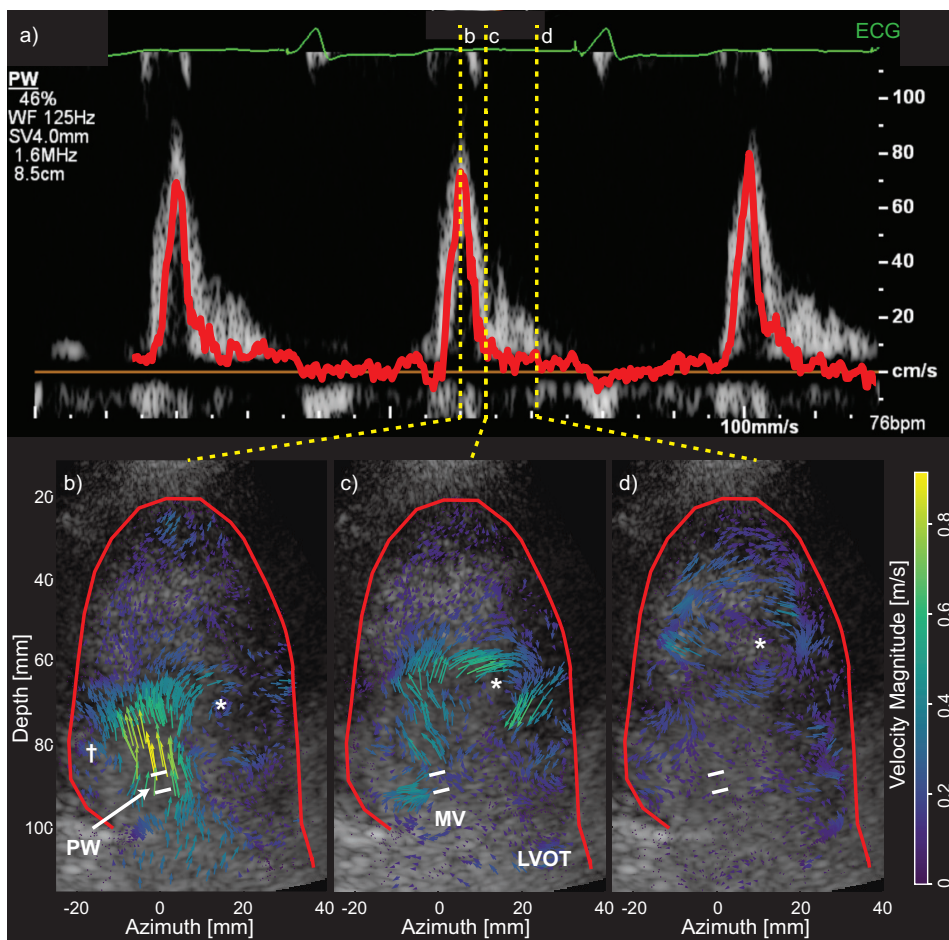


Figure 9.1: (a) Mean echoPIV velocity (red) overlaid on Pulsed-wave Doppler spectrogram obtained in the mitral valve region (see PW in (b)). (b – d) Velocity map visualization during diastolic filling (temporal locations marked in (a)), showing the high velocity trans-mitral jet entering the ventricle (b) and central clockwise vortex that starts basally and migrates apically (c – d). Supplementary Video included online. MV = Mitral valve, LVOT = left ventricular outflow tract. *Large, persistent clockwise vortex that pinches-off the jet and migrates apically. † Small, transient counter-clockwise vortex constrained by free-wall.

10

Discussion and Conclusion



The clinical aim of the work in this thesis is the development of a non-invasive method to directly assess myocardial stiffness. This is important for the early assessment of myocardial stiffness in people at risk of developing heart failure and for the diagnosis of underlying pathophysiologies in patients with heart failure with a preserved ejection fraction (HFpEF). This thesis focusses in particular on the accurate measurement and interpretation of natural shear waves (SWs) after aortic and mitral valve closure (AVC and MVC).

10.1. ACCURACY OF NATURAL SHEAR WAVES

For the application of clinical diagnosis, it is important that differences between healthy individuals and people with an increased myocardial stiffness can be distinguished at an early stage of the disease process. The results in **Chapter 4** suggest that, for healthy volunteers with only mild hemodynamic variations, variability in assessment of SW propagation speeds after valve closure is dominated by measurement inaccuracies. Therefore, the standard error can be reduced by averaging over multiple heartbeats. A mean standard deviation of 0.60 m/s was found for the SW measurements after AVC, which we will use to estimate the minimum amount of measurements needed for clinical diagnosis.

In literature, higher natural SW propagation speeds are reported for hypertrophic cardiomyopathy patients [39] and for cardiac amyloidosis patients [40] compared to healthy volunteers. Mean differences of 1.49 m/s and 1.88 m/s for the SWs after AVC, and of 2.23 m/s and 2.79 m/s for the SWs after MVC were reported, respectively. Furthermore, an increase in SW propagation speed was measured between age groups of 20 – 39 years and 60 – 80 years (mean differences of 1.02 m/s and 1.26 m/s for AVC and MVC respectively) [40]. These increases in SW speeds are presumably caused by the natural aging process of progressive stiffening of the myocardium. Assuming that minimal differences of 0.5 m/s should be measured for the early clinical diagnosis of an increased myocardial stiffness, minimally 6 measurements are estimated to be needed for a confidence level of 95%. For this estimation, we used the following equation; $\mu_{patient} - \mu_{healthy} > 2\sigma/\sqrt{n}$, hereby assuming a similar normal distribution of measurement inaccuracies among healthy volunteers and patients. Although many assumptions have been made for this calculation, it illustrates that in the order of 10 heartbeats are needed for a presumably clinically relevant value. Thus, the *first main finding* is that for the application of early diagnosis of an increased myocardial stiffness, precision should be improved by averaging over multiple heartbeats. Averaging over about 10 heart cycles is nowadays not often done in clinical practice. However, assuming that measurements are performed subsequently, and that data processing is done offline and will be automated in the future, we think that such number of measurements is feasible with respect to time and effort.

10.1.1. Apical versus Parasternal View

Since the interventricular septum (IVS) is relatively thin compared to the wavelength of natural SWs, guided wave modes might be expected. These guided wave modes are characterized by different dispersion curves, and a dominating transversal or longitudinal particle motion. Furthermore, depending on the echocardiographic view, mainly transversal or longitudinal vibrations with respect to the IVS are measured. Since it is unknown what wave modes are induced after valve closure, and thus which echocardiographic view should be used, this was studied in **Chapter 5**. We show in healthy volunteers that higher propagation speeds are obtained in an apical four-chamber view (median of 5.1 m/s (IQR: 4.5 – 7.2 m/s)) than in a parasternal long-axis view (median of 3.8 m/s (IQR 3.4 – 4.0 m/s)) after AVC; and that the propagation speeds in these two views are not correlated. The results cannot be explained by our hypothesis that symmetric and anti-symmetric Lamb waves are induced after AVC, and that a single or a superposition of different modes is measured in a specific echocardiographic view. Therefore, we refrain from converting SW propagation speeds into myocardial stiffness values. Nonetheless, for clinical application this conversion into myocardial stiffness might not be necessary when normal and pathological ranges of SW propagation speeds are known for specific age groups, types of SWs and left ventricular (LV) geometries.

The differences in propagation speeds measured in the two views could not only represent different types of SWs, but also measurement inconsistencies. First, it should be noted that slightly different planes are imaged in an apical four-chamber and in a parasternal long-axis view, and that the aortic valves are not in the imaging plane of an apical four-chamber view. The latter makes it possibly more challenging to measure the SWs after AVC and gives the sonographer more freedom to select the image plane. This could lead to out-of-plane propagation (as shown in a phantom in **Chapter 3**), potentially explaining the unexpectedly large inter-volunteer range in apical view (3.5 – 8.7 m/s versus 3.2 – 4.3 m/s). The effect of out-of-plane propagation could be further investigated in future studies by using an apical three-chamber view, in which the same plane is imaged as in a parasternal long-axis view. Also, more insights could be obtained by performing 3-dimensional acquisitions in which different tissue motion components as well as the propagation direction can be measured simultaneously. First steps in this direction have been recently made for the vibrations after atrial kick [149–151]. Second, different tissue motion components with respect to the fiber orientation of the myocardium are measured, which could mean that different tissue properties are assessed in the different views. For example, also Villemain *et al.* (2019) showed that myocardial elastic properties are anisotropic, by measuring different propagation in long-axis and short-axis views for shear waves externally induced by an acoustic radiation force (ARF).

First clinical studies show the potential of the SWs after AVC in parasternal view [39–41, 63], while to the best of our knowledge no clinical studies have been published yet in apical view. Furthermore, since SWs with smaller wavelengths can be tracked more accurately and precise over the limited length of the IVS, the lower median

propagation speeds in parasternal view are, next to the lower inter-volunteer variabilities, advantageous for a more robust clinical diagnosis. Thus, the *second main finding* is that the parasternal view is currently preferred for the clinical diagnostic application. However, both views might contain additional information about myocardial stiffness, and further studies on the potential clinical added value of apical view SWE measurements are needed. In current clinical practice, echocardiographic measurements in both views are already used for the evaluation of LV diastolic function [10]. Thus, performing measurements in either of the two views is feasible. Nonetheless, the clinical relevance of apical SWE measurements remains currently unknown.

10.1.2. Intra-Scan Variability

In **Chapter 3**, we show that the location of the propagation path on the IVS along which a SW after AVC is tracked, affects the propagation speed measured in open-chest pigs. The LV (endocardial) side of the IVS showed in general higher SW amplitudes – suggesting higher signal-to-noise ratios (SNRs) –, and lower propagation speeds than the right-ventricular (epicardial) side. The propagation speed variations measured along different paths *in vivo* were larger than the variations measured in a phantom where the measurement direction was deliberately misaligned with the propagation. Therefore, the differences over the IVS are probably not only caused by measurement inaccuracies but are also expected to have physiological causes, such as a changing fiber orientation over its thickness and small local stiffness variations. Since larger amplitudes were found in these pigs on the endocardial side, 10 propagation paths were then selected at this side of the IVS within each acquisition, resulting in a median inter-quartile range of 0.6 m/s. Hereby the aim was not to select identical paths, but to represent variations in propagation path when different observers would repeat the analysis. Since propagation paths were selected at one side of the IVS, variabilities are expected to be mainly caused by measurement inaccuracies. Therefore, the precision of individual acquisitions can be improved by averaging over multiple propagation paths. This is especially important since an IQR of 0.6 m/s is similar as the previously assumed minimal difference of 0.5 m/s that should distinguish between a healthy person and a person with an increased myocardial stiffness. Therefore, for all studies in this thesis described after **Chapter 3**, as well as for the estimation of minimal number of heartbeats made at the beginning of this discussion, we averaged over 10 propagation paths per SW. The *third main finding* of this thesis is thus that besides averaging over multiple heartbeats, intra-scan variabilities should be included by averaging over several propagation paths within each acquisition. Averaging over multiple propagation paths is currently not done by other SWE studies described in literature. Currently, we manually select multiple propagation paths and this requires thus extra time and effort. However, we think that the selection of several propagation paths could be automated in the future and is required to obtain sufficient precision for clinical diagnosis.

10.1.3. Method to Determine Propagation Speeds

Different aspects of SW tissue motion have been evaluated in literature to determine the natural SW propagation speeds. SWs are represented by specific patterns of positive and negative tissue motion propagating over time. However, tissue motion at the moment of valve closure is complex and it is not trivial to completely distinguish SW motion from other general motion of the heart and noise. Therefore, it is uncertain what the best method is to track SW propagation speeds. Throughout this thesis, we used the Radon transform. Integral intensities along all possible linear paths are compared and the path corresponding to the maximum or minimum intensity is selected, to determine propagation speeds of positive or negative tissue motion amplitudes respectively (called rims). In **Chapter 3**, we tracked different rims of the SWs after AVC in open-chest pigs by using tissue velocity and tissue acceleration data, and obtained lower propagation speeds for rims later in time. Furthermore, we obtained in general higher propagation speeds for tissue acceleration than for tissue velocity data for the SWs after AVC in healthy volunteers (**Chapter 5**) and in pigs (**Chapter 8**) (rim tracked of acceleration data was earlier in time than of velocity data).

These differences in propagation speeds can be induced by different factors. First, since the myocardium is relaxing or contracting at the moment of AVC and MVC respectively, different speeds might represent a change in stiffness over time. Kanai (2005) measured rapidly decreasing phase speeds in healthy volunteers after AVC and suggested that this was caused by myocardial relaxation [43]. Also Couade *et al.* (2011) measured a decrease in shear modulus around the AVC from 25 kPa to 20 kPa in approximately 25 ms in open chest sheep [55], corresponding to a decrease in propagation speed from 5 m/s to 4.47 m/s. For a time difference of approximately 5 ms between two rims (see Figure 3 in **Chapter 3**), this effect would result in a decrease of 0.11 m/s. Thus, relaxation could partly explain the differences in propagation speeds obtained for different rims. Second, by taking the derivative of tissue velocity data to obtain acceleration values, higher frequencies are amplified, which could affect the propagation speed measured due to dispersion. Nonetheless, it should be noted that it is uncertain to what extent the SWs after valve closure are dispersive due to contradicting observations reported on in literature [43, 64]. Third, by using tissue velocity or tissue acceleration data, different aspects of the complex wave pattern in the tissue motion data around valve closure are tracked. And the complex tissue motion at the moments of valve closure make the comparison of different studies, tracking different tissue motion components, more complicated. However, in **Chapter 8**, we could easier track the SWs after MVC by using acceleration panels, since a more distinct pattern became visible. Furthermore, clinical studies tracking acceleration data or the transition from positive to negative tissue velocity data after MVC, show a correlation between propagation speed and myocardial stiffness, [39, 41, 42].

Thus, the *fourth main finding* is that different propagation speeds can be measured when tracking different aspects of the tissue motion patterns, or when using tissue velocity versus tissue acceleration data. Therefore, SW propagation speed values obtained using different methods cannot be compared directly. Thus, for clinical application there is a need for a more universal and robust method to determine SW propagation speeds. Although we only used a Radon transform to determine the propagation speed of the natural SWs in this thesis, it should be noted that also different propagation speeds might be obtained for the same dataset when using other methods, such as correlation-based methods [42, 152].

10.1.4. Feasibility

In healthy volunteers in **Chapter 4**, the feasibility of performing natural SW measurements was found to be higher after AVC than after MVC (Zonare: 87% versus 66%; Philips: 77% versus 15% of all cardiac cycles). Also, in transthoracic pig measurements in **Chapter 8**, we experienced problems with tracking the SWs after MVC. Although a transition from positive to negative tissue velocity data was present in most acquisitions, a clear distinct SW pattern could not always be observed. The feasibility for these SWs after MVC was found to increase for tissue acceleration data, while the feasibility for the SWs after AVC was less affected. Other studies using tissue acceleration data, show only slightly larger feasibility rates for AVC than for MVC in healthy volunteers, but in similar ranges (AVC versus MVC: 100% versus 90% [42], 94% versus 84% [40] of all volunteers). Also when manually tracking the transition from positive to negative tissue velocity data, similar feasibility ranges were obtained in healthy volunteers (AVC versus MVC: 93% versus 89% of all volunteers), but the feasibility rate for MVC decreased more than for AVC in hypertrophic cardiomyopathy patients (AVC versus MVC: 88% versus 56% of all patients) [39]. Reason for the generally lower feasibility of tracking SWs after MVC could be that the SW source – the mitral root – is not directly connected to the IVS, and therefore vibrations induced by MVC have to be transferred via the aortic root first. This could result in a relatively lower SW amplitude for the SWs after MVC. Although using the tissue acceleration data seems to increase the feasibility for MVC, it should be noted once more that not the same tissue motion component is tracked as when using tissue velocity data, illustrating the need for a more universal method. For the application of clinical diagnosis, we think that the feasibility rates for the natural SWs of about 90% among subjects in literature and of about 60 – 90% among all cardiac cycles found in this thesis are sufficient, taking into account that multiple heart cycles are consequently recorded for each individual.

10.2. INTERPRETATION OF NATURAL SHEAR WAVES

10.2.1. Timing with Respect to the Cardiac Cycle

The clinical aim of this thesis is to develop a non-invasive method to measure an increased myocardial stiffness in patients with diastolic dysfunction. However, the stiffness of the myocardium changes throughout the cardiac cycle due to an interaction between the passive myocardial stiffness, myocardial contraction and relaxation, and the blood pressure in the LV. Therefore, SW measurements would ideally be performed in diastasis to minimize the effect of contraction on the myocardial stiffness measured. However, the natural SWs after valve closure only occur at two specific moments of the cardiac cycle. At these valve closure moments, the heart has already started to relax or contract, and the exact timing with respect to the stiffness dynamics of the heart is unknown. Therefore, we compare the ARF-based SW propagation speeds measured throughout the cardiac cycle, with the SW propagation speeds after AVC and MVC. We did this in open- and closed-chest pigs respectively in **Chapter 7 and 8**. Similar propagation speeds were found for natural and ARF-induced SWs simultaneously measured along the same propagation path in **Chapter 7**. This suggests that both types of SWs assess the same tissue characteristic at the moment of valve closure, despite the different SW and SW-source characteristics. **Chapter 7 and 8** show that AVC and MVC take place at moments in between the occurrence of the lowest (diastolic) and highest (systolic) ARF-based speeds, and that the propagation speeds after AVC and MVC are higher than of the slowest ARF-induced SWs in diastole. This suggests that the natural SWs are not only a measure of diastolic myocardial stiffness, but also of contractility. Furthermore, higher propagation speeds are measured after AVC than after MVC in **Chapter 4 and 7**, as was also found in several other studies [40, 42, 64] (but not in [39]). This indicates that AVC is more depending on contractility than MVC. In addition, the propagation speeds after AVC were not significantly different from the ARF-based systolic speeds in **Chapter 7** – although this could be caused by low statistical power –, and only just significantly lower in **Chapter 8**. These small differences in propagation speeds after AVC and in systole support the correlation found in other studies between contractility and the propagation speeds in systole [75, 139] or after AVC [137]. Thus, the *fifth main finding* of this thesis is that the SWs after valve closure represent two states between relaxation and contraction. This practically means that natural SWs could be used to assess diastolic as well as systolic function. However, it is yet unknown how to separate abnormalities in relaxation, contraction, passive myocardial stiffness and/or hemodynamic loading.

The different ratios for individual pigs between the propagation speeds after AVC and in systole in **Chapter 7**, and the inter-beat and inter-scan variability measured for the natural SWs throughout this thesis, could not be only caused by measurement inaccuracies. Potentially, also differences in timing of the corresponding valve closure have caused these variabilities. Surely, the timing of SW with respect to the cardiac cycle determines in what extent myocardial relaxation and/or contraction is assessed. As an illustration, in **Chapter 8**, we saw as an interesting result in one of the pigs an

increase in ARF-based systolic and diastolic propagation speeds, but a decrease in the propagation speeds after AVC. The cause of this observation remains unknown, due to a lack of ground truth for the myocardial stiffness curve throughout the cardiac cycle and since we had no means to accurately measure the timing of the valve closure within this curve. In future studies, it would be interesting to study the effect of valve-closure timing on propagation speeds and to relate this timing to the electrical activation (depolarization) of the septal region.

10.2.2. Loading Conditions

In **Chapter 4**, we found no significant effect of a mild stress test (handgrip) on the propagation speeds measured after AVC and MVC in healthy volunteers. There was a slight mean increase in propagation speed measured after AVC (0.33 m/s and 0.39 m/s for Zonare and Philips respectively) which was in the same range as the intra-scan variabilities measured (AVC Zonare: median IQR of 0.38 m/s (IQR: 0.26 – 0.68 m/s). Although this was statistically not significant, it should be noted that the corresponding p values were only slightly above $p=0.05$ ($p=0.073$ and $p=0.079$ for Zonare and Philips respectively). Furthermore, although no significant differences were measured between observers, the effect of the handgrip test was found to be significant for the 2nd observer of the Philips data ($p=0.01$) [153], suggesting a weak effect. Also, Bézy *et al.* (2019) found a significant increase in propagation speeds after AVC by performing a bicycle-exercise test in healthy volunteers [137]. Furthermore, the propagation speeds after MVC were found to correlate with end-diastolic pressures in humans by Werner *et al.* (2020) [140]. Thus, although no significant effect of a mild stress test was found in **Chapter 4**, the propagation speeds measured after valve closure can be affected by larger hemodynamic changes, which was studied in transthoracic pig experiments in **Chapter 8**. This chapter shows a correlation between ARF-based SW propagation speeds and the intrinsic myocardial diastolic stiffness, but also with end-diastolic and end-systolic pressures. The preliminary results in this chapter suggest that SW propagation speeds are not only depending on intrinsic myocardial characteristics, such as the passive myocardial stiffness, relaxation and contraction, but also on hemodynamic loading. Therefore, before clinical application, it should be further investigated whether difference in SW propagation speeds measured are caused by intrinsic characteristics, such as passive myocardial stiffness and active relaxation and contraction, or by loading conditions. This could be studied by performing a multivariate analysis, including realistic ranges of pressures and of intrinsic characteristics.

10.2.3. Temporally Relaxing or Contracting Myocardium

Since AVC and MVC occur when the myocardium is relaxing or contracting respectively, the effect of a temporal change in stiffness on wave propagation is fundamentally studied in **Chapter 6**. This chapter shows that for a relaxing medium, the amplitude and period of the wave increase proportionally over time, and that a reflected wave can develop at moments where the acceleration is discontinued.

However, since relaxation is assumed to happen smoothly *in vivo*, no reflected waves are expected. The changes in wave amplitude and period could in theory be used to measure relaxation and/or contraction abnormalities. Assuming an isotropic one-dimensional medium, it is estimated that for a normal relaxing heart, an increase in wave period of 20% and an increase in wave amplitude of 3% can be expected over 10 ms. For an infarcted heart, increases of 10% and 2% were estimated respectively. However, throughout the *in vivo* studies in this thesis, we did not observe an increase in amplitude for the SWs after AVC. This is probably since the estimated effect is small, and since SW attenuation causes the wave amplitude to decrease. Also, we could not observe systematic changes in wave period *in vivo*, potentially due to interference with additional effects related to the anisotropic viscoelastic three-dimensional nature of the heart. However, although we did not observe an increase in SW amplitude and period over time *in vivo*, we did see that propagation speeds were not always constant over space and time (e.g. MVC in **Chapter 8**), and that different propagation speeds were obtained for different rims in time (**Chapter 3, 5 and 8**). This can potentially be partly caused by temporal changes in stiffness. As an alternative to changes in wave amplitude and period, propagation speeds of SWs externally induced throughout the cardiac cycle could potentially be used to assess relaxation and/or contraction abnormalities. For example, the relaxation time constant in isolated rabbit hearts has been assessed using ARF-based propagation speeds and displacements by Vejdani-Jahromi *et al.* [109, 154].

10.3. ALTERNATIVES TO NATURAL SHEAR WAVES

This thesis focuses on natural SWs and compares these SWs with SWs externally induced with an ARF in **Chapter 7 and 8**. However, as discussed in the introduction of this thesis, also other SW-based alternatives are used in the cardiac application, such as the natural vibrations after atrial kick and ARF imaging (ARFI).

10.3.1. Atrial Kick

Besides the natural SWs after valve closure, also natural longitudinal motion patterns after atrial contraction have been assessed by several studies in the apical view [47–50]. Main advantage of using the motion pattern after atrial kick compared to the SWs after valve closure is that atrial contraction occurs in late diastole when the myocardium is presumed to be in a relaxed state. This may provide the possibility to better assess the passive myocardial stiffness. Furthermore, the advantage of using natural vibrations (atrial kick and valve closure) compared to externally-induced vibrations is that the implementation in current clinical practice is expected to be easier, since ultrasonic scanners do not need to be able to induce high-energy pulses. The propagation speed of the vibrations after atrial contraction have been shown to increase with preload and myocardial stiffness in pigs [49], and to be higher in patients with severe mitral regurgitation and aortic stenosis [48] and in patients with amyloidosis [50]. However, the non-linear propagation measured in HCM patients

(possibly due to the maximal longitudinal distension of the collagen network) [47] make the interpretation of these waves more difficult. Furthermore, due to the purely longitudinal stretch motion, these motion patterns cannot be purely SWs, and thus future research is required for the conversion of propagation speeds into stiffness values. However, these motion patterns could potentially still give more information on the diastolic function of the LV.

Thus, assessing the vibrations after atrial kick is promising, since vibrations can be measured in late diastole and since the implementation in current clinical practice is easier than for ARF. Although the vibrations after atrial kick cannot be measured in the parasternal long-axis view, as preferably used for the SWs after valve closure, it would be interesting to further investigate the clinical relevance of both types of natural vibrations within individual studies.

10.3.2. ARF-based Methods

Although ARF-based SWs have been used in **Chapter 7 and 8**, mainly to improve our understanding of natural SWs, these ARF-based SWs can also be used as a stand-alone SWE technique. Besides the advantage of timing within the cardiac cycle as discussed before, ARF-based SWs have some other advantages compared to natural SWs. First, by changing the parameters of the ARF, SW characteristics can be adapted, while the complex phenomenon inducing the SWs after valve closure is fixed. We observed a more complex SW pattern in the tissue motion data after valve closure than for ARF-based SWs, making the interpretation more difficult. Second, the higher frequency content of ARF-based SWs, inherently related to smaller wavelengths, makes it easier to accurately track these ARF-based SWs over the limited length of the IVS. On the other hand, lower frequencies were found to be less affected by fiber orientation [98]. Third, since the ARF-based SWs are induced and tracked by the same ultrasonic probe, out-of-plane propagation is less of a problem than for the SWs after valve closure. In **Chapter 7 and 8**, we observed lower variabilities for the ARF-based SWs in diastole compared to the SWs after AVC and MVC, which is an advantage for the application of clinical diagnosis. Fourth, fiber orientation can be measured by inducing SWs in a short- and long-axis view [55, 63, 66, 67]. In this way, different elasticity constants can be assessed, and furthermore lower fractional anisotropy was found in HCM patients compared to healthy subjects [63].

Having said all that, disadvantages of using an ARF are the low tissue motion amplitudes (10 mm/s [55] vs 40 mm/s [64] for ARF and valve closure respectively), and the challenge to induce SWs in a closed-chest transthoracic setting while meeting acoustic safety criteria. This is especially challenging for the low-amplitude fast propagating SWs in systole, and for obese patients. Nonetheless, it should also be further investigated whether natural SWs are present in a wide range of patients. For example, natural SWs may not be present in patients with strong regurgitation, and thus with poor valve closures. However, the feasibility rates of SWs after valve closure of about 60 – 90% among all cardiac cycles in healthy volunteers in **Chapter 4** are promising.

A related but different technique is ARF imaging (ARFI). Instead of tracking SW propagation, ARFI measures the on-axis axial displacement in the focus of the ARF by using focused ultrasonic beams, improving the signal-to-noise ratio. This enables the measurement of a parameter for tissue stiffness in both systole and diastole in a transthoracic setting. The tissue displacements measured are expected to be inversely related to tissue stiffness. However, since it is unknown what absolute force is applied, only relative tissue stiffness changes in time and space can be measured. Furthermore, it should be noted that this method assumes that the applied force stays constant between measurements within an individual sequence. But the fiber orientation changes due to normal cardiac motion, as visible by alternating backscatter strength on images, and these changes might lead to variations in absorption. Therefore, the ARF magnitude might change throughout the cardiac cycle. To obtain a more quantitative measure of tissue stiffness throughout the cardiac cycle, Hollender *et al.* (2017) recently proposed a method to calibrate the ARFI displacements with the propagation speeds measured with ARF SWE in diastole [62]. Within the constraints described above, this study is promising, since it shows that by combining ARF SWE and ARFI, the instantaneous myocardial stiffness can be assessed throughout the entire cardiac cycle in a transthoracic setting while meeting safety criteria.

Thus, since ARF-based methods can be applied at any moment of the cardiac cycle, these methods are very promising as a distinction can be made between myocardial relaxation and contraction. Nonetheless, further innovations are needed to improve the SNR of these ARF-based methods to increase the transthoracic feasibility.

10.4. CLINICAL PERSPECTIVE

The main motivation to study SWs in this thesis was the assumption that more intrinsic mechanical properties of the myocardium can be assessed with SWE than with the echocardiographic parameters currently used for the assessment of diastolic and systolic function. Different studies suggest that the SW propagation speeds are correlated to the inotropic state of the heart [42, 139, 153], as well as to diastolic myocardial stiffness. This was tested by inducing ischemia [52, 57, 109], or by comparing healthy volunteers with patient groups with an assumed increased myocardial stiffness [39–42, 63]. Nonetheless, **Chapter 8** shows that SW propagation speeds also depend on loading, which supports the results of ARF-based studies in Langendorff-perfused rabbit [155] and rat hearts [75]. Whether SW propagation speeds depend more on the intrinsic mechanical properties than on normal varying loading conditions *in vivo*, will be further investigated by including more subjects in the study described in **Chapter 8**.

This thesis illustrates that the conversion from SW propagation speeds after valve closure into intrinsic myocardial stiffness values is complex. The type of SWs induced, and thus the corresponding dispersion curve, are ambiguous (**Chapter 5**); SW propagation speeds theoretically depend on geometries such as wall thickness [39];

the SWs after valve closure are measured at time points representing a mixed state of contraction and relaxation (**Chapter 7**); SW propagation speeds are depending on loading conditions (**Chapter 8**); in contrast to invasive pressure-volume loops, SWs are assessed locally on the IVS and thus might not be representative for the entire heart; and also the complex anisotropic material properties of the myocardium make the conversion to stiffness values challenging. However, for clinical application, conversion to stiffness values might not be necessary, as long as dependence of SW propagation speeds on these factors described above is known. Nonetheless, when measuring propagation speeds of SWs after valve closure or in diastole, still no distinction can be made between the contribution of passive myocardial stiffness and relaxation abnormalities. This is in contrast to invasive pressure-volume curves and echocardiographic indices of mitral inflow velocities, surrogate parameters of the myocardial stiffness, that can be used to distinguish relaxation and passive properties [156]. Thus, natural SWs can first be used to detect whether HFpEF is caused by an increased myocardial stiffness, or by non-myocardial causes of HFpEF [13]. Thereafter, when an increased myocardial stiffness is measured, ARF-based propagation speeds throughout the cardiac cycle are probably required to distinguish the contributions of passive myocardial stiffness and relaxation.

In **Chapter 9**, we focused on the assessment of the high velocity diastolic LV flow patterns using high-frame-rate echocardiography, as an alternative to cardiac SWE to measure early signs of cardiac dysfunction. By using ultrasound contrast agent microbubbles, echo-particle image velocimetry (echoPIV) obtained diastolic blood-flow velocities with similar accuracies as pulsed-wave Doppler. Since SWE and echoPIV both require a high frame rate system, both techniques could potentially be combined for the assessment of cardiac function. Performing echoPIV measurements next to SWE, could potentially give more insights in how myocardial stiffness affects flow velocities. However, the relevance for clinical diagnosis, as well as the feasibility and accuracy – especially in obese patients –, should be further investigated.

10.5. FUTURE STUDIES

Besides the remaining questions discussed throughout this discussion, other aspects should be investigated in future studies before SWE methods can be used for the clinical application of early diagnosis.

First, it is important that in an early stage of the disease process, a distinction can be made between an increase in propagation speed due to pathological reasons [39–41, 63] and due to aging [40, 63]. At the beginning of this discussion, we made an estimation of the minimal number of heart cycles needed. However, many assumptions were made for this estimation. Therefore, it would be interesting to perform a longitudinal study including people at risk for developing heart failure. Such study could give more insights in whether pathological effects can be distinguished from the natural variations within a specific age group. Furthermore, as an extension of **Chapter 8**, the effect of the progression of an induced myocardial disease on the SW propagation could be studied over time in animal studies.

Second, although first steps are made in **Chapter 8**, studies in human and including more subjects are needed to investigate to what extent SW propagation speeds are affected by intrinsic tissue characteristics and by hemodynamic variations.

Third, it is important to investigate the feasibility of the different SWE methods for a wide variety of patients. Although inducing external SWs transthoracically might be challenging, especially in obese patients; natural SWs might not be present in patients with severe abnormal valve closures, which should be further investigated. Furthermore, atrial fibrillation might hamper the accurate measurement of natural SWs in many individuals at risk for developing heart failure. For clinical diagnostics, it is important that the technique is reliable in most patients, and therefore that the feasibility of natural and ARF-induced SWE methods will be increased.

10.6. CONCLUSIONS

The clinical aim of this thesis was the development of a non-invasive method to directly assess myocardial stiffness. This is relevant for the assessment of myocardial stiffening in people at risk for developing heart failure and potentially for the diagnosis of underlying pathophysiologies in patients with HFpEF. The focus of this thesis was the accurate measurement and interpretation of natural SWs after valve closure, using novel high frame rate ultrasound imaging techniques. This thesis shows that natural SWs represent a mixed state of passive myocardial stiffness, relaxation, contraction and loading. Therefore, although SWs can potentially be used to detect an increased myocardial stiffness, it is likely that a combination with other techniques is required to further distinguish the contributions of passive myocardial stiffness, relaxation and contraction.

References

- [1] L. S. Lilly, "Pathophysiology of Heart Disease", *Wolters Kluwer*, 2016.
- [2] P. Ponikowski, A. A. Voors, S. D. Anker, *et al.*, "2016 ESC Guidelines for the diagnosis and treatment of acute and chronic heart failure", *European Heart Journal*, vol. 37, no. 27, 2016.
- [3] E. J. Benjamin, P. Muntner, A. Alonso, *et al.*, "Heart Disease And Stroke Statistics-2019 Update: A Report From The American Heart Association", *Circulation*, vol. 139, no. 10, 2019.
- [4] S. Stewart, K. MacIntyre, S. Capewell, *et al.*, "Heart failure and the aging population: an increasing burden in the 21st century?", *Heart*, vol. 89, no. 1, 2003.
- [5] P. A. Heidenreich, F. Chair, N. M. Albert, *et al.*, "Forecasting the Impact of Heart Failure in the United States: A Policy Statement From the American Heart Association", *Circulation: Heart Failure*, vol. 6, no. 3, 2013.
- [6] O. Gjesdal, D. A. Bluemke, and J. A. Lima, "Cardiac remodeling at the population level-risk factors, screening, and outcomes", *Nature Reviews Cardiology*, vol. 8, no. 12, 2011.
- [7] E. L. Boulpaep, "The heart as a pump", in *Medical Physiology*, 2012.
- [8] M. R. Zile, "Heart failure with preserved ejection fraction: Is this diastolic heart failure?", *Journal of the American College of Cardiology*, vol. 41, no. 9, 2003.
- [9] G. D. Plitt, J. T. Spring, M. J. Moulton, *et al.*, "Mechanisms, diagnosis, and treatment of heart failure with preserved ejection fraction and diastolic dysfunction", *Expert Review Cardiovascular Therapy*, vol. 16, no. 8, 2018.
- [10] S. F. Nagueh, O. A. Smiseth, C. P. Appleton, *et al.*, "Recommendations for the evaluation of left ventricular diastolic function by echocardiography: an update from the american society of echocardiography and the european association of cardiovascular imaging", *Journal of the American Society of Echocardiography*, vol. 29, no. 4, 2016.
- [11] J. U. Voigt, "Direct Stiffness Measurements by Echocardiography. Does the Search for the Holy Grail Come to an End?", *JACC: Cardiovascular Imaging*, vol. 12, no. 7, 2019.
- [12] R. M. Lang, L. P. Badano, M. A. Victor, *et al.*, "Recommendations for cardiac chamber quantification by echocardiography in adults: An update from the American Society of Echocardiography and the European Association of Cardiovascular Imaging", *European Heart Journal - Cardiovascular Imaging*, vol. 16, no. 3, 2015.
- [13] W. H. Gaasch, "Deliberations on Diastolic Heart Failure", *The American Journal of Cardiology*, vol. 119, no. 1, 2017.
- [14] D. A. Kass, J. G. Bronzwaer, and W. J. Paulus, "What mechanisms underlie diastolic dysfunction in heart failure?", *Circulation Research*, vol. 94, no. 12, 2004.
- [15] M. R. Zile, C. F. Baicu, and W. H. Gaasch, "Diastolic Heart Failure - Abnormalities in Active Relaxation and Passive Stiffness of the Left Ventricle", *New England Journal of Medicine*, vol. 350, no. 19, 2004.
- [16] D. Burkhoff, I. Mirsky, and H. Suga, "Assessment of systolic and diastolic ventricular properties via pressure-volume analysis: a guide for clinical, translational, and basic researchers", *American Journal of Physiology - Heart and Circulatory Physiology*, vol. 289, no. 2, 2005.
- [17] M. Senni, W. J. Paulus, A. Gavazzi, *et al.*, "New strategies for heart failure with preserved ejection fraction: The importance of targeted therapies for heart failure phenotypes", *European Heart Journal*, vol. 35, no. 40, 2014.
- [18] R. G. Wells, "Tissue mechanics and fibrosis", *Biochimica et Biophysica Acta*, vol. 1832, no. 7, 2013.
- [19] I. Mirsky and W. W. Parmley, "Assessment of passive elastic stiffness for isolated heart muscle and the intact heart", *Circulation Research*, vol. 33, no. 2, 1973.
- [20] W. H. Gaasch, H. J. Levine, M. A. Quinones, *et al.*, "Left ventricular compliance: Mechanisms and clinical implications", *The American Journal of Cardiology*, vol. 38, no. 5, 1976.
- [21] F. P. Beer, E. R. Johnston, J. T. DeWolf, *et al.*, "Mechanics of materials", *McGraw-Hill Education*, 2001.
- [22] W. M. Lai, D. Rubin, and E. Krempf, "Introduction to Continuum Mechanics", *Butterworth Heinemann*, 1993.

- [23] L. Vasconcelos, J. L. Gennisson, and I. Nenadic, "Continuum Mechanics Tensor Calculus and Solutions to Wave Equations", in *Ultrasound Elastography for Biomedical Applications and Medicine*, 2019.
- [24] J. L. Gennisson, T. Defieux, M. Fink, *et al.*, "Ultrasound elastography: Principles and techniques", *Diagnostic and Interventional Imaging*, vol. 94, no. 5, 2013.
- [25] S. M. Haddad and A. Samani, "A novel micro-to-macro approach for cardiac tissue mechanics", *Computer Methods in Biomechanics and Biomedical Engineering*, vol. 20, no. 2, 2017.
- [26] G. A. Holzapfel and R. W. Ogden, "Constitutive modelling of passive myocardium: A structurally based framework for material characterization", *Philosophical Transactions of the Royal Society A*, vol. 367, no. 1902, 2009.
- [27] J.-L. Gennisson, "Rheological Model-based Methods for Estimating Tissue Viscoelasticity", in *Ultrasound Elastography for Biomedical Applications and Medicine*, 2019.
- [28] J. L. Rose, "Waves in Plates", in *Ultrasonic Waves in Solid Media*, 1999.
- [29] H. Lombaert, J. M. Peyrat, P. Croisille, *et al.*, "Human atlas of the cardiac fiber architecture: Study on a healthy population", *IEEE Transactions on Medical Imaging*, vol. 31, no. 7, 2012.
- [30] A. Arani, K. L. Glaser, S. P. Arunachalam, *et al.*, "In Vivo, High-Frequency Three-Dimensional Cardiac MR Elastography: Feasibility in Normal Volunteers", *Magnetic Resonance in Medicine*, vol. 77, no. 1, 2017.
- [31] P. N. Wells and H. D. Liang, "Medical ultrasound: Imaging of soft tissue strain and elasticity", *Journal of the Royal Society Interface*, vol. 8, no. 64, 2011.
- [32] A. Manduca, T. Rossman, D. Lake, *et al.*, "Waveguide effects and implications for cardiac magnetic resonance elastography: A finite element study", *NMR in Biomedicine*, vol. in press, 2018.
- [33] P. A. Wassenaar, C. N. Eleswarpu, S. A. Schroeder, *et al.*, "Measuring Age-Dependent Myocardial Stiffness across the Cardiac Cycle using MR Elastography: A Reproducibility Study", *Magnetic Resonance in Medicine*, vol. 75, no. 4, 2016.
- [34] A. Arani, S. P. Arunachalam, I. C. Y. Chang, *et al.*, "Cardiac MR Elastography for Quantitative Assessment of Elevated Myocardial Stiffness in Cardiac Amyloidosis", *Journal of Magnetic Resonance Imaging*, vol. 46, no. 5, 2017.
- [35] A. P. Sarvazyan, M. W. Urban, and J. F. Greenleaf, "Acoustic waves in medical imaging and diagnostics", *Ultrasound in Medicine and Biology*, vol. 39, no. 7, 2013.
- [36] M. Tanter and M. Fink, "Ultrafast imaging in biomedical ultrasound", *IEEE Transactions on Ultrasonics, Ferroelectrics, and Frequency Control*, vol. 61, no. 1, 2014.
- [37] M. Cikes, L. Tong, G. R. Sutherland, *et al.*, "Ultrafast cardiac ultrasound imaging: Technical principles, applications, and clinical benefits", *JACC: Cardiovascular Imaging*, vol. 7, no. 8, 2014.
- [38] C. Papadacci, M. Pernot, M. Couade, *et al.*, "High-contrast ultrafast imaging of the heart", *IEEE Transactions on Ultrasonics, Ferroelectrics, and Frequency Control*, vol. 61, no. 2, 2014.
- [39] M. Strachinaru, J. G. Bosch, L. van Gils, *et al.*, "Naturally occurring shear waves in healthy volunteers and hypertrophic cardiomyopathy patients", *Ultrasound in Medicine and Biology*, vol. 45, no. 8, 2019.
- [40] A. Petrescu, P. Santos, M. Orłowska, *et al.*, "Velocities of naturally occurring myocardial shear waves increase with age and in cardiac amyloidosis", *JACC: Cardiovascular Imaging*, vol. 12, no. 12, 2019.
- [41] M. Cvijic, S. Bézy, A. Petrescu, *et al.*, "Interplay of cardiac remodelling and myocardial stiffness in hypertensive heart disease: a shear wave imaging study using high-frame rate echocardiography", *European Heart Journal - Cardiovascular Imaging*, vol. 21, no. 6, 2019.
- [42] P. Santos, A. Petrescu, J. Pedrosa, *et al.*, "Natural shear wave imaging in the human heart: normal values, feasibility and reproducibility", *IEEE Transactions on Ultrasonics, Ferroelectrics and Frequency Control*, vol. 66, no. 3, 2019.
- [43] H. Kanai, "Propagation of spontaneously actuated pulsive vibration in human heart wall and in vivo viscoelasticity estimation", *IEEE Transactions on Ultrasonics, Ferroelectrics and Frequency Control*, vol. 52, no. 11, 2005.
- [44] B. Brekke, L. C. L. Nilsen, J. Lund, *et al.*, "Ultra-high frame rate tissue doppler imaging", *Ultrasound in Medicine and Biology*, vol. 40, no. 1, 2014.
- [45] S. Salles, L. Løvstakken, S. A. Aase, *et al.*, "Clutter Filter Wave Imaging", *IEEE Transactions on Ultrasonics, Ferroelectrics and Frequency Control*, vol. 66, no. 9, 2019.

- [46] P. Santos, L. Løvstakken, E. Samset, *et al.*, "Volumetric imaging of fast mechanical waves in the heart using a clinical ultrasound system: A feasibility study", *IEEE International Ultrasonics Symposium*, 2017.
- [47] M. Strachinaru, M. Geleijnse, N. de Jong, *et al.*, "Myocardial stretch post-atrial contraction in healthy volunteers and hypertrophic cardiomyopathy patients", *Ultrasound in Medicine and Biology*, vol. 45, no. 8, 2019.
- [48] C. Pislaru, M. M. Alashry, J. J. Thaden, *et al.*, "Intrinsic wave propagation of myocardial stretch, a new tool to evaluate myocardial stiffness: a pilot study in patients with aortic stenosis and mitral regurgitation", *Journal of the American Society of Echocardiography*, vol. 30, no. 11, 2017.
- [49] C. Pislaru, P. A. Pellikka, and S. V. Pislaru, "Wave propagation of myocardial stretch: correlation with myocardial stiffness", *Basic Research in Cardiology*, vol. 109, no. 6, 2014.
- [50] C. Pislaru, F. Ionescu, M. Alashry, *et al.*, "Myocardial stiffness by intrinsic cardiac elastography in patients with amyloidosis: comparison with chamber stiffness and global longitudinal strain", *Journal of the American Society of Echocardiography*, vol. 32, no. 8, 2019.
- [51] M. W. Urban, C. Pislaru, I. Z. Nenadic, *et al.*, "Measurement of viscoelastic properties of in vivo swine myocardium using Lamb wave dispersion ultrasound vibrometry (LDUV)", *IEEE Trans Med Imaging*, vol. 32, no. 2, 2013.
- [52] C. Pislaru, M. W. Urban, S. V. Pislaru, *et al.*, "Viscoelastic properties of normal and infarcted myocardium measured by a multifrequency shear wave method: comparison with pressure-segment length method", *Ultrasound in Medicine and Biology*, vol. 40, no. 8, 2014.
- [53] H. Tzschätzsch, T. Elgeti, K. Rettig, *et al.*, "In vivo time harmonic elastography of the human heart", *Ultrasound in Medicine and Biology*, vol. 38, no. 2, 2012.
- [54] R. R. Bouchard, S. J. Hsu, P. D. Wolf, *et al.*, "In vivo cardiac, acoustic-radiation-force-driven, shear wave velocimetry", *Ultrasonic Imaging*, vol. 31, no. 3, 2009.
- [55] M. Couade, M. Pernot, E. Messas, *et al.*, "In vivo quantitative mapping of myocardial stiffening and transmural anisotropy during the cardiac cycle", *IEEE Transactions on Medical Imaging*, vol. 30, no. 2, 2011.
- [56] P. J. Hollender, P. D. Wolf, R. Goswami, *et al.*, "Intracardiac echocardiography measurement of dynamic myocardial stiffness with shear wave velocimetry", *Ultrasound in Medicine and Biology*, vol. 38, no. 7, 2012.
- [57] M. Pernot, W. N. Lee, A. Bel, *et al.*, "Shear wave imaging of passive diastolic myocardial stiffness: stunned versus infarcted myocardium", *JACC: Cardiovascular Imaging*, vol. 9, no. 9, 2016.
- [58] P. Song, X. Bi, D. C. Mellema, *et al.*, "Pediatric cardiac shear wave elastography for quantitative assessment of myocardial stiffness: a pilot study in healthy controls", *Ultrasound in Medicine and Biology*, vol. 42, no. 8, 2016.
- [59] M. L. Palmeri and K. R. Nightingale, "Acoustic radiation force-based elasticity imaging methods", *Interface Focus*, vol. 1, no. 4, 2011.
- [60] V. Kakkad, M. LeFevre, P. Hollender, *et al.*, "Non-invasive Measurement of Dynamic Myocardial Stiffness Using Acoustic Radiation Force Impulse Imaging", *Ultrasound in Medicine and Biology*, vol. 45, no. 5, 2019.
- [61] P. Hollender, D. Bradway, P. Wolf, *et al.*, "Intracardiac Acoustic Radiation Force Impulse (ARFI) and Shear Wave Imaging in Pigs with Focal Infarctions", *Bone*, vol. 60, no. 8, 2013.
- [62] P. Hollender, V. Kakkad, and G. Trahey, "Calibration of ARFI displacements using diastolic shear wave speeds for estimating systolic elasticity", in *IEEE International Ultrasonics Symposium*, 2017.
- [63] O. Villemain, M. Correia, E. Mousseaux, *et al.*, "Myocardial stiffness evaluation using noninvasive shear wave imaging in healthy and hypertrophic cardiomyopathic adults", *JACC: Cardiovascular Imaging*, vol. 12, no. 7, 2019.
- [64] H. J. Vos, B. M. van Dalen, I. Heinonen, *et al.*, "Cardiac Shear Wave Velocity Detection in the Porcine Heart", *Ultrasound in Medicine and Biology*, vol. 43, no. 4, 2017.
- [65] P. Song, H. Zhao, M. W. Urban, *et al.*, "Improved shear wave motion detection using pulse-inversion harmonic imaging with a phased array transducer", *IEEE Transactions on Medical Imaging*, vol. 32, no. 12, 2013.
- [66] W. N. Lee, M. Pernot, M. Couade, *et al.*, "Mapping Myocardial Fiber Orientation Using Echocardiography-Based Shear Wave Imaging", *IEEE Transactions on Medical Imaging*, vol. 31, no. 3, 2012.
- [67] M. Wang, B. Byram, M. Palmeri, *et al.*, "Imaging transverse isotropic properties of muscle by monitoring acoustic radiation force induced shear waves using a 2-D matrix ultrasound array", *IEEE Transactions on Medical Imaging*, vol. 32, no. 9, 2013.

- [68] J. Brum, "Transverse Wave Propagation in Bounded Media", in *Ultrasound Elastography for Biomedical Applications and Medicine*, 2019.
- [69] G. Y. Li, Q. He, R. Mangan, *et al.*, "Guided waves in pre-stressed hyperelastic plates and tubes: Application to the ultrasound elastography of thin-walled soft materials", *Journal of the Mechanics and Physics of Solids*, vol. 102, 2017.
- [70] I. Z. Nenadic, M. W. Urban, C. Pislaru, *et al.*, "In Vivo Open- and Closed-chest Measurements of Left-Ventricular Myocardial Viscoelasticity using Lamb wave Dispersion Ultrasound Vibrometry (LDUV): A Feasibility Study", *Biomedical Physics & Engineering Express*, vol. 4, no. 4, 2018.
- [71] I. Z. Nenadic, M. W. Urban, S. Aristizabal, *et al.*, "On Lamb and Rayleigh Wave Convergence in Viscoelastic Tissues", *Physics in Medicine and Biology*, vol. 56, no. 20, 2011.
- [72] I. Z. Nenadic, M. W. Urban, M. Bernal, *et al.*, "Phase velocities and attenuations of shear, Lamb, and Rayleigh waves in plate-like tissues submerged in a fluid (L)", *Journal of the Acoustical Society of America*, vol. 130, no. 6, 2011.
- [73] A. Caenen, M. Pernot, I. Kinn Ekroll, *et al.*, "Effect of Ultrafast Imaging on Shear Wave Visualization and Characterization: An Experimental and Computational Study in a Pediatric Ventricular Model", *Applied Sciences*, vol. 7, no. 8, 2017.
- [74] L. B. H. Keijzer, A. Sabbadini, J. G. Bosch, *et al.*, "Diffuse Shear Wave Elastography in a Thin Plate Phantom", *IEEE International Ultrasonics Symposium*, 2017.
- [75] M. Pernot, M. Couade, P. Mateo, *et al.*, "Real-time assessment of myocardial contractility using shear wave imaging", *Journal of the American College of Cardiology*, vol. 58, no. 1, 2011.
- [76] J. Brum, S. Catheline, N. Benech, *et al.*, "Quantitative Shear Elasticity Imaging From a Complex Elastic Wavefield in Soft Solids With Application to Passive Elastography", *IEEE Transactions on Ultrasonics, Ferroelectrics, and Frequency Control*, vol. 62, no. 4, 2015.
- [77] K. J. Parker, J. Ormachea, F. Zvietcovich, *et al.*, "Reverberant shear wave fields and estimation of tissue properties", *Physics in Medicine and Biology*, vol. 62, no. 3, 2017.
- [78] N. Benech, S. Catheline, J. Brum, *et al.*, "1-D Elasticity Assessment in Soft Solids from Shear Wave Correlation: The Time-Reversal Approach", *IEEE Transactions on Ultrasonics, Ferroelectrics, and Frequency Control*, vol. 56, no. 11, 2009.
- [79] T. Gallot, S. Catheline, P. Roux, *et al.*, "Passive Elastography: Shear-Wave Tomography From Physiological-Noise Correlation in Soft Tissues", *IEEE Transactions on Ultrasonics, Ferroelectrics, and Frequency Control*, vol. 58, no. 6, 2011.
- [80] L. B. H. Keijzer, J. G. Bosch, M. D. Verweij, *et al.*, "Intra-scan variability of natural shear wave measurements", in *IEEE International Ultrasonics Symposium*, 2018.
- [81] T. T. E. Owan, D. O. Hodge, R. M. Herges, *et al.*, "Trends in prevalence and outcome of heart failure with preserved ejection fraction.", *The New England Journal of Medicine*, vol. 355, no. 3, 2006.
- [82] W. J. Paulus, C. Tschöpe, J. E. Sanderson, *et al.*, "How to diagnose diastolic heart failure: A consensus statement on the diagnosis of heart failure with normal left ventricular ejection fraction by the Heart Failure and Echocardiography Associations of the European Society of Cardiology", *European Heart Journal*, vol. 28, no. 20, 2007.
- [83] O. Villemain, M. Correia, D. Khraiche, *et al.*, "Myocardial Stiffness Assessment Using Shear Wave Imaging in Pediatric Hypertrophic Cardiomyopathy", *JACC: Cardiovascular Imaging*, vol. 11, no. 5, 2018.
- [84] M. W. Urban, B. Qiang, P. Song, *et al.*, "Investigation of the effects of myocardial anisotropy for shear wave elastography using acoustic radiation force and harmonic vibration", *IEEE International Ultrasonics Symposium*, 2015.
- [85] E. Maksuti, E. Widman, D. Larsson, *et al.*, "Arterial Stiffness Estimation by Shear Wave Elastography: Validation in Phantoms with Mechanical Testing", *Ultrasound in Medicine and Biology*, vol. 42, no. 1, 2016.
- [86] L. B. H. Keijzer, M. Strachinaru, D. J. Bowen, *et al.*, "Reproducibility of natural shear wave elastography measurements", *Ultrasound in Medicine and Biology*, vol. 45, no. 12, 2019.
- [87] P. Song, X. Bi, D. C. Mellema, *et al.*, "Quantitative Assessment of Left Ventricular Diastolic Stiffness Using Cardiac Shear Wave Elastography", *Journal of Ultrasound in Medicine*, vol. 35, no. 7, 2016.
- [88] M. Pernot, K. Fujikura, S. D. Fung-Kee-Fung, *et al.*, "ECG-gated, Mechanical and Electromechanical Wave Imaging of Cardiovascular Tissues In Vivo", *Ultrasound in Medicine and Biology*, vol. 33, no. 7, 2007.
- [89] M. Strachinaru, J. G. Bosch, B. M. van Dalen, *et al.*, "Cardiac shear wave elastography using a clinical ultrasound system", *Ultrasound in Medicine and Biology*, vol. 43, no. 8, 2017.

- [90] N. C. Rouze, M. H. Wang, M. L. Palmeri, *et al.*, "Robust Estimation of Time-of-Flight Shear Wave Speed Using a Radon Sum Transformation", *IEEE Transactions on Ultrasonics, Ferroelectrics and Frequency Control*, vol. 57, no. 12, 2010.
- [91] J. Provost, W.-N. Lee, K. Fujikura, *et al.*, "Imaging the electromechanical activity of the heart in vivo", *Proceedings of the National Academy of Sciences*, vol. 108, no. 21, 2011.
- [92] J. R. Thorson and J. F. Claerbout, "Velocity-stack and slant-stack stochastic inversion", *Geophysics*, vol. 50, no. 12, 1985.
- [93] E. W. Remme, E. Lyseggen, T. Helle-Valle, *et al.*, "Mechanisms of preejection and postejection velocity spikes in left ventricular myocardium: interaction between wall deformation and valve events.", *Circulation*, vol. 118, no. 4, 2008.
- [94] M. Vejdani-jahromi, M. Nagle, G. E. Trahey, *et al.*, "Ultrasound Shear Wave Elasticity Imaging Quantifies Coronary Perfusion Pressure Effect on Cardiac Compliance", *IEEE Transactions on Medical Imaging*, vol. 34, no. 2, 2015.
- [95] K. Xu, P. Laugier, and J.-G. Minonzio, "Dispersive Radon transform", *Journal of the Acoustical Society of America*, vol. 143, no. 5, 2018.
- [96] L. B. H. Keijzer, M. Strachinaru, D. J. Bowen, *et al.*, "Parasternal versus Apical View in Cardiac Natural Mechanical Wave Speed Measurements", *IEEE Transactions on Ultrasonics, Ferroelectrics, and Frequency Control*, vol. 67, no. 8, 2020.
- [97] A. Caenen, L. Mertens, M. Pernot, *et al.*, "An in silico framework to analyze the anisotropic shear wave mechanics in cardiac shear wave elastography", *Physics in Medicine and Biology*, vol. 63, no. 7, 2018.
- [98] M. W. Urban, B. Qiang, P. Song, *et al.*, "Investigation of the effects of myocardial anisotropy for shear wave elastography using acoustic radiation force and harmonic vibration", *Physics in Medicine and Biology*, vol. 61, no. 1, 2016.
- [99] I. Pelivanov, L. Gao, J. Pitre, *et al.*, "Does group velocity always reflect elastic modulus in shear wave elastography?", *Journal of Biomedical Optics*, vol. 24, no. 07, 2019.
- [100] M. L. Palmeri, B. Qiang, S. Chen, *et al.*, "Guidelines for finite-element modeling of acoustic radiation force-induced shear wave propagation in tissue-mimicking media", *IEEE Transactions on Ultrasonics, Ferroelectrics, and Frequency Control*, vol. 64, no. 1, 2017.
- [101] N. C. Rouze, M. H. Wang, M. L. Palmeri, *et al.*, "Finite element modeling of impulsive excitation and shear wave propagation in an incompressible, transversely isotropic medium", *Journal of Biomechanics*, vol. 46, no. 16, 2013.
- [102] A. Sabbadini, L. B. H. Keijzer, H. J. Vos, *et al.*, "Fundamental modeling of wave propagation in temporally relaxing media with applications to cardiac shear wave elastography", *The Journal of the Acoustical Society of America*, vol. 147, no. 3091, 2020.
- [103] R. R. Chaturvedi, T. Herron, R. Simmons, *et al.*, "Passive stiffness of myocardium from congenital heart disease and implications for diastole", *Circulation*, vol. 121, no. 8, 2010.
- [104] Y. K. Mariappan, K. J. Glaser, and R. L. Ehman, "Magnetic resonance elastography: A review", *Clinical Anatomy*, vol. 23, no. 5, 2010.
- [105] J. F. Deprez, E. Brusseau, J. Fromageau, *et al.*, "On the potential of ultrasound elastography for pressure ulcer early detection", *Medical Physics*, vol. 38, no. 4, 2011.
- [106] M. Dhyani, A. Anvari, and A. E. Samir, "Ultrasound elastography: liver", *Abdominal Imaging*, vol. 40, no. 4, 2015.
- [107] L. Sang, X. M. Wang, D. Y. Xu, *et al.*, "Accuracy of shear wave elastography for the diagnosis of prostate cancer: A meta-analysis", *Scientific Reports*, vol. 7, no. 1, 2017.
- [108] H. Kanai, "Propagation of Vibration Caused by Electrical Excitation in the Normal Human Heart", *Ultrasound in Medicine and Biology*, vol. 35, no. 6, 2009.
- [109] M. Vejdani-Jahromi, J. Freedom, Y.-J. Kim, *et al.*, "Assessment of diastolic function using ultrasound elastography", *Ultrasound in Medicine and Biology*, vol. 44, no. 3, 2018.
- [110] T. C. Gasser and C. Forsell, "The numerical implementation of invariant-based viscoelastic formulations at finite strains. An anisotropic model for the passive myocardium", *Computer Methods in Applied Mechanics and Engineering*, vol. 200, no. 49-52, 2011.
- [111] T. S. Eriksson, A. J. Prassl, G. Plank, *et al.*, "Influence of myocardial fiber/sheet orientations on left ventricular mechanical contraction", *Mathematics and Mechanics of Solids*, vol. 18, no. 6, 2013.

- [112] O. Gültekin, G. Sommer, and G. A. Holzapfel, "An orthotropic viscoelastic model for the passive myocardium: continuum basis and numerical treatment", *Computer Methods in Biomechanics and Biomedical Engineering*, vol. 19, no. 15, 2016.
- [113] B. Auld and J. H. Collins, "Signal processing in a nonperiodically time-varying magnetoelastic medium", *Proceedings of the IEEE*, vol. 56, no. 3, 1968.
- [114] S. Rezende and F. Morgenthaler, "Magnetoelastic Waves in Time-Varying Magnetic Fields. I. Theory", *Journal of Applied Physics*, vol. 40, no. 2, 1969.
- [115] L. B. Felsen and G. M. Whitman, "Wave Propagation in Time-Varying Media", *IEEE Transactions on Antennas and Propagation*, vol. 18, no. 2, 1970.
- [116] R. L. Fante, "Transmission of Electromagnetic Waves into Time-Varying Media", *IEEE Transactions on Antennas and Propagation*, vol. 19, no. 3, 1971.
- [117] F. V. Fedotov, A. G. Nerukh, T. M. Benson, *et al.*, "Investigation of Electromagnetic Field in a Layer With Time-Varying Medium by Volterra Integral Equation Method", *Journal of Lightwave Technology*, vol. 21, no. 1, 2003.
- [118] C. Bing-Kang, Z. Ying, and G. Ben-Qing, "Solution of Electromagnetic Wave in Time-Varying Media in Two-Dimensional Space", *Chinese Physics Letters*, vol. 23, no. 3, 2006.
- [119] A. Nerukh, T. Remayeva, and N. Sakhnenko, "Evolution of Waves Induced by Time Change of Medium Permittivity in a Sphere", *AIP Conference Proceedings*, vol. 1176, no. 1, 2009.
- [120] A. G. Hayrapetyan, J. B. Götte, K. K. Grigoryan, *et al.*, "Electromagnetic wave propagation in spatially homogeneous yet smoothly time-varying dielectric media", *Journal of Quantitative Spectroscopy and Radiative Transfer*, vol. 178, 2016.
- [121] V. Preobrazhenskii and Y. K. Fetisov, "Magnetostatic waves in a time-dependent medium", *Soviet Physics Journal*, vol. 31, no. 11, 1988.
- [122] J. Shive and R. Webe, *Similarities in Physics*. 1982.
- [123] E. Wilkins, L. Wilson, K. Wickramasinghe, *et al.*, "European cardiovascular disease statistics 2017 edition", *European Heart Network*, 2017.
- [124] L. B. H. Keijzer, J. Voorneveld, D. J. Bowen, *et al.*, "A comparison of natural and acoustic radiation force induced shear wave propagation speed measurements in open-chest pigs", *IEEE International Ultrasonics Symposium*, 2019.
- [125] A. Caenen, A. Thabit, M. Pernot, *et al.*, "The effect of stretching on transmural shear wave anisotropy in cardiac shear wave elastography: An ex vivo and in silico study", *IEEE International Ultrasonics Symposium*, 2017.
- [126] I. Z. Nenadic, M. W. Urban, S. A. Mitchell, *et al.*, "Lamb wave dispersion ultrasound vibrometry (LDUV) method for quantifying mechanical properties of viscoelastic solids", *Physics in Medicine and Biology*, vol. 56, no. 7, 2011.
- [127] W.-N. Lee, B. Larrat, M. Pernot, *et al.*, "Ultrasound elastic tensor imaging: comparison with MR diffusion tensor imaging in the myocardium.", *Physics in Medicine and Biology*, vol. 57, no. 16, 2012.
- [128] Y. Deng, N. C. Rouze, M. L. Palmeri, *et al.*, "Ultrasonic shear wave elasticity imaging sequencing and data processing using a verasonics research scanner", *IEEE Transactions on Ultrasonics, Ferroelectrics, and Frequency Control*, vol. 64, no. 1, 2017.
- [129] T. Deffieux, G. Montaldo, M. Tanter, *et al.*, "Shear wave spectroscopy for in vivo quantification of human soft tissues visco-elasticity", *IEEE Transactions on Medical Imaging*, vol. 28, no. 3, 2009.
- [130] M. Pernot and O. Villemain, "In the heart of stiffness", *JACC: Cardiovascular Imaging*, vol. 12, no. 12, 2019.
- [131] J. van de Wouw, O. Sorop, R. W. A. van Drie, *et al.*, "Perturbations in myocardial perfusion and oxygen balance in swine with multiple risk factors: a novel model of ischemia and no obstructive coronary artery disease.", *Basic Research in Cardiology*, vol. 115, no. 2, 2020.
- [132] G. Montaldo, M. Tanter, J. Bercoff, *et al.*, "Coherent plane-wave compounding for very high frame rate ultrasonography and transient elastography", *IEEE Transactions on Ultrasonics, Ferroelectrics, and Frequency Control*, vol. 56, no. 3, 2009.
- [133] P. Song, M. W. Urban, S. Chen, *et al.*, "In vivo transthoracic measurement of end-diastolic left ventricular stiffness with ultrasound shear wave elastography: A pilot study", *IEEE International Ultrasonics Symposium*, 2014.
- [134] M. L. Palmeri, A. C. Sharma, R. R. Bouchard, *et al.*, "A finite-element method model of soft tissue response to impulsive acoustic radiation force", *IEEE Transactions on Ultrasonics, Ferroelectrics, and Frequency Control*, vol. 52, no. 10, 2005.

- [135] M. L. Palmeri, Y. Deng, N. C. Rouze, *et al.*, “Dependence of shear wave spectral content on acoustic radiation force excitation duration and spatial beamwidth”, *IEEE International Ultrasonics Symposium*, 2014.
- [136] R. O. Mada, P. Lysyansky, A. M. Daraban, *et al.*, “How to define end-diastole and end-systole? Impact of timing on strain measurements”, *JACC: Cardiovascular Imaging*, vol. 8, no. 2, 2015.
- [137] S. Bézy, M. Cvijic, A. Petrescu, *et al.*, “Shear wave propagation velocity after aortic valve closure could be a novel parameter for myocardial contractility”, *Abstract EuroEcho*, 2019.
- [138] Y. Deng, M. L. Palmeri, N. C. Rouze, *et al.*, “Evaluating the benefit of elevated acoustic output in harmonic motion estimation in ultrasonic shear wave elasticity imaging (SWEL)”, *Ultrasound in Medicine and Biology*, vol. 44, no. 2, 2018.
- [139] M. Vejdani-Jahromi, J. Freedman, M. Nagle, *et al.*, “Quantifying Myocardial Contractility Changes Using Ultrasound-Based Shear Wave Elastography”, *Journal of the American Society of Echocardiography*, vol. 30, no. 1, 2017.
- [140] A. E. Werner, S. Bézy, M. Orlowska, *et al.*, “Shear Wave Elastography: Can we estimate diastolic filling pressures?”, *Abstract European Society of Cardiology Congress*, 2020.
- [141] L. E. Teichholz, T. Kreulen, M. V. Herman, *et al.*, “Problems in echocardiographic volume determinations: Echocardiographic-angiographic correlations in the presence or absence of asynergy”, *The American Journal of Cardiology*, vol. 37, no. 1, 1976.
- [142] J. D’hooge, O. Turschner, C. Dommke, *et al.*, “The relationship between regional integrated backscatter levels and regional strain in normal, acutely ischemic, and reperfused myocardium”, *International Workshop on Functional Imaging and Modeling of the Heart*, 2003.
- [143] D. D. Glower, J. A. Spratt, N. D. Snow, *et al.*, “Linearity of the Frank-Starling relationship in the intact heart: The concept of preload recruitable stroke work”, *Circulation*, vol. 71, no. 5, 1985.
- [144] J. Voorneveld, L. B. H. Keijzer, M. Strachinaru, *et al.*, “High-Frame-Rate Echo-Particle Image Velocimetry Can Measure the High-Velocity Diastolic Flow Patterns”, *Circulation: Cardiovascular Imaging*, vol. 12, no. 4, 2019.
- [145] P. P. Sengupta, G. Pedrizzetti, P. J. Kilner, *et al.*, “Emerging trends in CV flow visualization”, *JACC: Cardiovascular Imaging*, vol. 5, no. 3, 2012.
- [146] C. Prinz, R. Faludi, A. Walker, *et al.*, “Can echocardiographic particle image velocimetry correctly detect motion patterns as they occur in blood inside heart chambers? A validation study using moving phantoms.”, *Cardiovascular Ultrasound*, vol. 10, no. 1, 2012.
- [147] M. E. Toulemonde, R. Corbett, V. Papadopoulou, *et al.*, “High Frame-Rate Contrast Echocardiography: In-Human Demonstration”, *JACC: Cardiovascular Imaging*, vol. 11, no. 6, 2018.
- [148] J. Voorneveld, A. Muralidharan, T. Hope, *et al.*, “High Frame Rate Ultrasound Particle Image Velocimetry for Estimating High Velocity Flow Patterns in the Left Ventricle”, *IEEE Transactions on Ultrasonics, Ferroelectrics, and Frequency Control*, vol. 65, no. 12, 2018.
- [149] S. Salles, V. Perrot, B. Nicolas, *et al.*, “Natural mechanical wave detection using ultrafast ultrasound and velocity Clutter Filter Wave Imaging”, *hot Topics in IMaging (TOPIM)*, 2019.
- [150] S. Salles, L. Løvstakken, T. Espeland, *et al.*, “3D mechanical wave trajectory mapping in the left ventricle using Clutter Filter Wave Imaging.”, *IEEE International Ultrasonics Symposium*, 2019.
- [151] K. F. Kvåle, S. Salles, L. C. N. Lervik, *et al.*, “Detection of Tissue Fibrosis using Natural Mechanical Wave Velocity Estimation: Feasibility Study”, *Ultrasound in Medicine and Biology*, vol. 00, no. 00, 2020.
- [152] H. J. Vos, B. M. Van Dalen, J. G. Bosch, *et al.*, “Myocardial passive shear wave detection”, *IEEE International Ultrasonics Symposium*, 2015.
- [153] M. Strachinaru, L. Keijzer, D. Bowen, *et al.*, “Light exercise may induce an increase in the propagation velocity of naturally occurring shear waves”, *Abstract EuroEcho*, 2019.
- [154] M. Vejdani-jahromi, M. Nagle, Y. Jiang, *et al.*, “A Comparison of Acoustic Radiation Force Derived Indices of Cardiac Function in the Langendorff Perfused Rabbit Heart”, *IEEE Transactions on Ultrasonics, Ferroelectrics and Frequency Control*, no. 3, 2016.
- [155] M. Vejdani-Jahromi, J. Freedman, G. E. Trahey, *et al.*, “Measuring intraventricular pressure using ultrasound elastography”, *Journal of Ultrasound in Medicine*, vol. 38, no. 5, 2018.
- [156] A. F. Leite-Moreira, “Current perspectives in diastolic dysfunction and diastolic heart failure”, *Heart*, vol. 92, no. 5, 2006.

Summary

The clinical motivation for performing the work in this thesis is to develop a non-invasive method that can directly measure myocardial stiffness, as described in **Chapter 1**. This is relevant for the early evaluation of myocardial stiffness in people at risk for developing heart failure, as well as for the detection of underlying pathophysiologies in heart failure patients with a preserved ejection fraction. This thesis focusses in particular on the accurate measurement and interpretation of natural shear waves (SWs) after aortic and mitral valve closure (AVC and MVC).

In **Chapter 2**, a spatio-temporal correlation technique was used to assess propagation speeds of a diffuse field in a thin-plate phantom. Similar propagation speeds were obtained compared to the direct in-plane assessment of SWs propagating in one direction. Nonetheless, the spatio-temporal correlation technique was shown to overestimate propagation speeds for incompletely diffuse wave fields. Although diffuse natural vibrations caused by breathing and flow noise might be expected in the heart, we could not observe them *in vivo*.

Chapter 3 & 4 focus on the accurate measurement of SW propagation speed after valve closure. In **Chapter 3**, we show in open-chest pigs that SW propagation speeds after AVC are strongly affected by the manually selected propagation path on the interventricular septum. The differences in propagation speed potentially reflect physiologic differences. However, when selecting multiple propagation paths on the left ventricular side of the septum, still large intra-scan variations were measured, potentially caused by measurement inaccuracies. Therefore, the standard error can be reduced by averaging over multiple propagation paths within individual acquisitions. In this way, measurement inaccuracies as well as physiologic variabilities due to different M-spline locations are dealt with. This is important for clinical diagnosis, since an increased myocardial stiffness should be identified at an early stage of the disease process. This chapter also shows higher propagation speeds when tracking aspects of the SW tissue motion earlier in time (median increase of maximal 31% was measured), which illustrates the general need of a more standardized method for SW tracking.

In **Chapter 4**, we extended our research on intra-scan variabilities to a more general reproducibility study of the SWs after AVC and MVC in healthy volunteers. Inter-scan variabilities were found to be only slightly higher than intra-scan variabilities, and test-retest variabilities were also found to be in the same range as inter-scan variabilities. To study the effect of larger hemodynamic variations, the effect of a mild handgrip test was studied. However, no statistical effect was observed. This suggests that the variabilities measured among healthy volunteers with only mild hemodynamic variabilities, are dominated by measurement inaccuracies rather than

by physiological causes. Therefore, precision for clinical diagnosis can be further improved by averaging over several heartbeats. Furthermore, in this chapter, significantly higher propagation speeds were obtained after AVC for a clinical system with a custom high-frame-rate mode compared to a clinical system with a clinical high-frame-rate mode. This distinction in propagation speeds is probably caused by differences in data processing. Thus **Chapter 3 & 4** both illustrate that the method used affects the SW propagation speed measured. Therefore, for clinical application a universal and robust method is needed.

It is currently unknown what types of wave modes are induced after valve closure, and thus which echocardiographic view is preferred for measuring these SWs. Therefore, in **Chapter 5**, we compared SW propagation speed measurements after AVC in a parasternal long-axis view with measurements in an apical four-chamber view in healthy volunteers. Finite element simulations of Lamb waves in an elastic plate show that different propagation speeds can be measured for the longitudinal and transversal particle-motion components when multiple Lamb waves are induced simultaneously. Since the apical view is predominantly sensitive to longitudinal particle motion and the parasternal view for transversal motion, the simultaneous presence of multiple wave modes could explain measuring a view-dependent propagation speed. Indeed, we obtained higher propagation speeds in apical than in parasternal view (median of 5.1 m/s vs. 3.8 m/s), but these propagation speeds in the two views did not correlate. Furthermore, an unexpectedly large range of values among healthy volunteers was found in the apical view compared to the parasternal view (3.5 – 8.7 m/s vs. 3.2 – 4.3 m/s). Therefore, these results cannot be explained by our hypothesis of symmetric and anti-symmetric Lamb waves being simultaneously induced after AVC, or by a superposition of different wave modes measured within an individual echocardiographic view. Nonetheless, due to the presence of promising clinical studies in the parasternal view only, due to the lower median propagation speed – corresponding to smaller wavelengths that can be tracked more accurately –, and due to the lower inter-volunteer variability in parasternal view found in this chapter, the parasternal view is currently preferred for the clinical application. However, since apical view measurements might contain additional information on myocardial characteristics, future studies are desired.

In **Chapter 6**, the effect of a temporally changing stiffness on wave propagation was fundamentally studied, since it is expected that the myocardium is relaxing or contracting at the moments of valve closure. We showed that the amplitude and period of a wave increase over time proportionally with the relaxation of the medium. Furthermore, a reflected wave can be induced at the moments of discontinuity in acceleration. However, this latter effect is not expected nor observed *in vivo*, since relaxation happens smoothly. The increase in wave amplitude and period depends on the relaxation rate of the myocardium, and could therefore theoretically be used to diagnose relaxation and/or contraction abnormalities. However, the expected effects are small and we could not observe them *in vivo*.

In **Chapter 7 & 8**, the SW propagation speeds after AVC and MVC were compared with SWs induced with an acoustic radiation force (ARF) throughout the entire cardiac cycle. This was done in an open- and closed- chest pig setting, respectively in two chapters. In **Chapter 7**, despite the different SW and SW-source characteristics of the two methods, similar propagation speeds were found for the simultaneous natural and ARF-induced SWs, when tracked along the same propagation path. Furthermore, we show that the natural SWs occur at moments in between the prevalence of the highest and lowest ARF-based speeds, corresponding to systole and diastole respectively. Also, the propagation speeds after valve closure were found to be statistically higher than the ARF-based speeds in diastole. Thus, the results suggest that with natural shear wave elastography a myocardial stiffness in between relaxation and contraction is measured.

In **Chapter 8**, in closed-chest pigs, we performed similar measurements as in the previous chapter, while altering preload and afterload, administering dobutamine intravenously and inducing a myocardial infarction. The preliminary results show that SW propagation speeds not only depend on intrinsic myocardial characteristics, but also on hemodynamic loading.

As an alternative to cardiac shear wave elastography for the early diagnosis of cardiac dysfunction, we studied echo-particle image velocimetry (echoPIV) in **Chapter 9**. The high-velocity diastolic left-ventricular flow patterns were measured in a heart failure patient, by tracking ultrasound contrast agent microbubbles. 2D high-velocity flow patterns were obtained. Furthermore, the trans-mitral jet measured with echoPIV was very similar to the pulsed wave Doppler velocities.

Chapter 10 connects the results obtained throughout the other chapters, and discusses on the interpretation, clinical relevance and future perspectives of this thesis.

Samenvatting

De klinische motivatie van dit proefschrift is het ontwikkelen van een niet-invasieve techniek die de stijfheid van het myocard direct kan meten, zoals beschreven in **Hoofdstuk 1**. Dit is met name relevant voor het vroegtijdig detecteren van een toegenomen myocard stijfheid in mensen met een risico op hartfalen, en ook voor het bepalen van onderliggende pathofysiologieën in patiënten met hartfalen met een behouden ejectiefraction. Dit proefschrift focust specifiek op het accuraat meten en interpreteren van de natuurlijke *shear waves* (SWs) die ontstaan na het sluiten van de aortaklep en mitraalklep (AVC en MVC).

In **Hoofdstuk 2**, hebben we een spatiële en temporele correlatie techniek gebruikt om propagatiesnelheden te meten van SWs die in verschillende richtingen propageren in een dunne plaat fantoom. Vergelijkbare propagatiesnelheden waren gemeten vergeleken met de directe meting van SWs die slechts propageren in één richting. Desalniettemin, de correlatie techniek overschatte propagatiesnelheden wanneer de SWs niet compleet in alle richtingen propageerden. Hoewel diffuse natuurlijke vibraties, ontstaan door ademhaling en bloedstroming, verwacht werden in het hart, hebben we deze niet kunnen observeren *in vivo*.

Hoofdstuk 3 & 4 behandelen het accuraat meten van SW propagatiesnelheden na klepsluiting. In **Hoofdstuk 3** laten we zien in varkens met een open borstkast dat de SW propagatie snelheden na AVC sterk beïnvloed worden door het handmatig geselecteerde propagatiepad over het interventriculaire septum. De gemeten verschillen in propagatiesnelheden hebben waarschijnlijk fysiologische oorzaken. Echter, wanneer alleen propagatiepaden op de linkerkamer zijde van het septum werden geselecteerd, werden nog steeds grote intra-scan variaties gemeten. Deze variaties zijn mogelijk veroorzaakt door meetonzekerheden, en daarom kan de standaardfout gereduceerd worden door te middelen over verschillende propagatiepaden binnen individuele metingen. Op deze manier wordt er rekening gehouden met meetonnauwkeurigheden en met fysiologische variaties. Dit is belangrijk voor klinische diagnose, zodat een toegenomen myocard stijfheid kan worden gedetecteerd in een vroeg stadium van het ziekteproces. Dit hoofdstuk laat bovendien zien dat wanneer een deel van de SW-beweging in het weefsel wordt geselecteerd, dat sneller na klepsluiting plaatsvindt, hogere propagatiesnelheden worden gemeten (mediaan toename van maximaal 31% was gemeten). Dit laat zien dat er een meer gestandaardiseerde methode nodig is voor het meten van SWs.

In **Hoofdstuk 4** hebben we onze studie naar intra-scan variaties uitgebreid naar een meer algemene herhaalbaarheidsstudie van de SWs na AVC en MVC in gezonde vrijwilligers. De gemeten inter-scan variaties waren slechts iets hoger dan de intra-scan variaties, en de test-retest variaties waren ook in hetzelfde bereik als de

inter-scan variaties. Een milde handgriptest was gebruikt om de effecten van grotere hemodynamische variaties te onderzoeken. We hebben echter geen significant effect gemeten. Dit suggereert dat de variaties gemeten binnen gezonde vrijwilligers met alleen milde hemodynamische variaties, worden gedomineerd door meetonnauwkeurigheden in plaats van door fysiologische oorzaken. Daarom kan de precisie voor klinische diagnose verbeterd worden door te middelen over verschillende hartslagen. Bovendien zijn er in dit hoofdstuk significant hogere snelheden gemeten na AVC met een klinisch systeem met een op maat gemaakte hoge-beeldsnelheid modus vergeleken met een klinisch systeem met een klinische modus. De afwijkende propagatiesnelheden zijn waarschijnlijk veroorzaakt door verschillen in de dataverwerking. Kortom, **Hoofdstuk 3 & 4** laten beide zien dat de gebruikte methode invloed heeft op de gemeten SW propagatiesnelheden. Daarom is een universele en robuuste methode gewenst voor klinische toepassing.

Het is momenteel niet bekend welke type golven worden geïnduceerd na klepsluiting, en dus welk echocardiografisch beeld het meest geschikt zou zijn voor het meten van deze SWs. Daarom hebben we in **Hoofdstuk 5** de SW propagatiesnelheden na AVC in een parasternale lange-as opname vergeleken met metingen in een apicale vier-kamer opname in gezonde vrijwilligers. Numerieke simulaties van Lamb golven in een elastische plaat laten zien dat verschillende propagatiesnelheden gemeten kunnen worden voor de longitudinale en transversale componenten van de deeltjes beweging, wanneer meerdere Lamb golven tegelijkertijd geïnduceerd zijn. Omdat de apicale weergave met name gevoelig is voor longitudinale en de parasternale weergave voor transversale bewegingen, kan dit dus ook leiden tot het meten van verschillende propagatiesnelheden in beide echocardiografische weergaves. We verkregen inderdaad hogere snelheden in de apicale vergeleken met de parasternale opnames (mediaan van 5.1 m/s vs. 3.8 m/s), maar deze propagatiesnelheden waren niet aan elkaar gecorreleerd. Bovendien werd een onverwacht groot bereik van waardes tussen gezonde vrijwilligers gemeten in de apicale vergeleken met de parasternale opnames (3.5 – 8.7 m/s vs. 3.2 – 4.3 m/s). Daarom kunnen deze resultaten niet verklaard worden op basis van onze hypothese dat symmetrische en antisymmetrische Lamb golven tegelijkertijd geïnduceerd worden na AVC, of dat een superpositie van verschillende golfmodi wordt gemeten in een individuele echocardiografische opname. Desalniettemin, omdat er alleen veelbelovende klinische studies in parasternale beelden gerapporteerd zijn, en omdat we een lagere mediaan propagatiesnelheid – overeenkomend met kleinere golflengtes die nauwkeuriger gemeten kunnen worden – en een lagere variabiliteit tussen vrijwilligers hebben gemeten voor de parasternale weergave in dit hoofdstuk, wordt momenteel voor mogelijke klinische toepassing de voorkeur gegeven aan parasternale opnames. Echter, studies in de toekomst moeten aantonen of apicale opnames misschien extra informatie kunnen geven over de eigenschappen van het myocard.

In **Hoofdstuk 6** wordt het effect van een veranderende stijfheid in tijd op golfpropagatie fundamenteel onderzocht. Immers, op het moment van klepsluiting is het myocard waarschijnlijk aan het ontspannen of samentrekken. We laten zien dat

de amplitude en periode van een golf proportioneel toenemen met het ontspannen van het medium in tijd. Bovendien kan er een gereflecteerde golf ontstaan op een moment van discontinuïteit in acceleratie. Echter, dit laatste effect wordt niet verwacht en is niet geobserveerd *in vivo*, omdat relaxatie geleidelijk plaatsvindt. De toename in golfamplitude en periode hangt af van de relaxatiesnelheid van het myocard, en kan daarom theoretisch gebruikt worden voor de diagnose van abnormale relaxatie en/of contractie. Echter, deze effecten zijn waarschijnlijk klein en hebben we niet kunnen observeren *in vivo*.

In **Hoofdstuk 7 & 8** zijn de SW propagatiesnelheden na AVC en MVC vergeleken met SWs die extern geïnduceerd zijn met behulp van een akoestische stralingsdruk (ARF) tijdens de gehele hartcyclus. Dit is gedaan in varkens met respectievelijk een open en een gesloten borstkast in de twee hoofdstukken. In **Hoofdstuk 7** hebben we, ondanks de verschillen in SW en SW-bron eigenschappen, vergelijkbare propagatiesnelheden gemeten voor de natuurlijke en ARF-gebaseerde SWs op het moment van klepsluiting langs hetzelfde propagatiepad. Bovendien laten we zien dat de natuurlijke SWs plaatsvinden op momenten tussen de hoogste en laagste ARF-gebaseerde propagatiesnelheden, die corresponderen met systole en diastole respectievelijk. De propagatiesnelheden na klepsluiting waren ook statistisch hoger dan de ARF-gebaseerde snelheden in diastole. Kortom, de resultaten suggereren dat natuurlijke SWS corresponderen met een myocardstijfheid met een waarde tussen die van relaxatie en contractie in.

In **Hoofdstuk 8**, in varkens met een gesloten borstkast, hebben we vergelijkbare experimenten uitgevoerd als in het vorige hoofdstuk. Hierbij hebben we vullingsdrukken gevarieerd, dobutamine intraveneus toegediend, en een infarct geïnduceerd in het myocard. De voorlopige resultaten laten zien dat SW propagatiesnelheden niet alleen afhankelijk zijn van intrinsieke myocardeigenschappen, maar ook van hemodynamische belasting.

We onderzochten *echo-particle image velocimetry* (echoPIV), een alternatief voor het gebruik van *shear wave* elastografie voor het vroegtijdig diagnosticeren van cardiale dysfunctie, in **Hoofdstuk 9**. De bloedstromingspatronen met hoge diastolische snelheden in de linkerkamer waren gemeten in een patient met hartfalen, met behulp van ultrageluid in combinatie met ultrageluid *contrast-agent* microbellen. 2D bloedstromingspatronen met hoge snelheden waren gemeten. Bovendien, vergelijkbare snelheden voor de trans-mitrale stroming was gemeten met echoPIV als met reguliere klinische *pulsed wave* Doppler.

Hoofdstuk 10 verbindt de resultaten van de verschillende hoofdstukken in dit proefschrift, en bespreekt hoe de resultaten moeten worden geïnterpreteerd, alsook de klinische relevantie en perspectieven voor de toekomst.

List of Publications

PEER-REVIEWED PAPERS

L.B.H. Keijzer^{*}, A. Caenen^{*}, J. Voorneveld, M. Strachinaru, D.J. Bowen, J. van der Wouw, O. Sorop, D. Merkus, D.J. Duncker, A.F.W. van der Steen, N. de Jong, J.G. Bosch, H.J. Vos, *A Direct Comparison of Natural and Acoustic-Radiation-Force-Induced Cardiac Mechanical Waves*, Accepted for publication in Scientific Reports, 2020, ^{*}Both authors contributed equally

A. Sabbadini, **L.B.H. Keijzer**, H.J. Vos, N. de Jong, M.D. Verweij, *Fundamental Modeling of Wave Propagation in Temporally Relaxing Media with Applications to Cardiac Shear Wave Elastography*, The Journal of the Acoustical Society of America **147**(3091), 2020

L.B.H. Keijzer, M. Strachinaru, D.J. Bowen, A. Caenen, A.F.W. van der Steen, M.D. Verweij, N. de Jong, J.G. Bosch, H.J. Vos, *Parasternal versus Apical View in Cardiac Natural Mechanical Wave Speed Measurements*, IEEE Transactions on Ultrasonics Ferroelectrics and Frequency Control **67**(8), 2020

L.B.H. Keijzer, M. Strachinaru, D.J. Bowen, M.L. Geleijnse, A.F.W. van der Steen, J.G. Bosch, N. de Jong, H.J. Vos, *Reproducibility of Natural Shear Wave Elastography Measurements*, Ultrasound in Medicine and Biology **45**(12), 2019

J. Voorneveld, **L.B.H. Keijzer**, M. Strachinaru, D.J. Bowen, J.S.L. Goei, F. ten Cate, A.F.W. van der Steen, N. de Jong, H.J. Vos, A.E. van den Bosch, J.G. Bosch, *High-Frame-Rate Echo-Particle Image Velocimetry Can Measure the High-Velocity Diastolic Flow Patterns*, Circulation: Cardiovascular Images **12**(4), 2019

MANUSCRIPTS IN PREPARATION

A. Caenen^{*}, **L.B.H. Keijzer**^{*}, S. Bézy, J. Düchenne, M. Orlowska, A.F.W. van der Steen, N. de Jong, P. Segers, J.G. Bosch, J-U. Voigt, J. D'hooge, H.J. Vos, *Transthoracic Cardiac Shear Wave Elastography in Relation to (Patho-)physiologic Changes*, In preparation, ^{*}Both authors contributed equally

A. Sabbadini, A. Caenen, **L.B.H. Keijzer**, P. van Neer, N. de Jong, H.J. Vos, M. Verweij, *Tapering of the Interventricular Septum Can Effect Ultrasound Shear Wave Elastography: an In Vitro and In Silico Study*, In preparation

CONFERENCE PROCEEDINGS PAPERS

L.B.H. Keijzer, J. Voorneveld, D.J. Bowen, M. Strachinaru, A.F.W. van der Steen, N. de Jong, J.G. Bosch, H.J. Vos, A. Caenen, *A Comparison of Natural and Acoustic Radiation Force Induced Shear Wave Propagation Speed Measurements in Open-chest Pigs*, IEEE International Ultrasonics Symposium, 2019

A.J. Kortenbout, **L.B.H. Keijzer**, N. de Jong, J.G. Bosch, H.J. Vos, *Direction-Independent Bulk Shear Wave Speed in 3D*, IEEE International Ultrasonics Symposium, 2019

L.B.H. Keijzer, J.G. Bosch, M.D. Verweij, N. de Jong, H.J. Vos, *Intra-Scan Variability of Natural Shear Wave Measurements*, IEEE International Ultrasonics Symposium, 2018

L.B.H. Keijzer, M. Langendijk, N. Stigter, C.H.M. van Deurzen, C. Verhoef, W. van Lankeren, L.B. Koppert, K.W.A. van Dongen, *Measurement of the Speed of Sound, Attenuation and Mass Density of Fresh Breast Tissue*, International Workshop on Medical Ultrasound Tomography, 2017

L.B.H. Keijzer, A. Sabbadini, J.G. Bosch, M.D. Verweij, A.F.W. van der Steen, N. de Jong, H.J. Vos, *Diffuse Shear Wave Elastography in a Thin Plate Phantom*, IEEE International Ultrasonics Symposium, 2017

PhD Portfolio

International Conferences	Year	ECTS
European Symposium on Ultrasound Contrast Imaging – Rotterdam, the Netherlands	2017	0.6
IEEE International Ultrasonics Symposium – Washington DC, USA (poster presentation)	2017	1.4
European Symposium on Ultrasound Contrast Imaging – Rotterdam, the Netherlands	2018	0.6
International Tissue Elasticity Conference – Avignon, France (oral presentation, 2nd price)	2018	2.2
IEEE International Ultrasonics Symposium – Kobe, Japan (oral and poster presentation)	2018	2.4
Meeting on Myocardial Function Imaging – Leuven, Belgium	2019	0.6
Artimino – Nijmegen, the Netherlands (oral presentation)	2019	1.9
IEEE International Ultrasonics Symposium – Glasgow, Scotland (2 oral presentations)	2019	2.9
Meeting on Myocardial Function Imaging – Leuven, Belgium (invited oral presentation)	2020	1.6

Courses	Year	ECTS
Molmed: Basic Introduction Course on SPSS	2017	1
Basic Training and Intensive Course Sonography	2017	0.9
COEUR: Cardiovascular Imaging and Diagnostics	2017	1
Cardiac function and adaptation – Papendal, the Netherlands	2017	2
Ultrafast Ultrasound Imaging: Basic Principles and Applications – Washington DC, USA	2017	0.15
Elasticity Imaging: Methods and Applications – Washington DC, USA	2017	0.15
Scientific Integrity	2018	0.3
COEUR: Heart Failure Research	2018	0.5
Motion Estimation Algorithms in Ultrasound Imaging: Principles and Hands-On Development – Kobe, Japan	2018	0.15
Biomedical English Writing and Communication	2018/2019	3.0
Artificial Intelligence in Ultrasound Imaging – Glasgow, Scotland	2019	0.15
Molmed: The translational imaging workshop by AMIE: from mouse to man	2019	1.3

Research Symposia and Seminars	Year	ECTS
Young @ Heart day: Strategic Alliances, Netherlands Heart Institute – Utrecht, the Netherlands	2017	0.3
COEUR: Discoveries in Atrial Fibrillation Pathophysiology: Implications for AF Therapy	2017	0.4
COEUR: MRI-based Assessment of Biomechanical Stress and Atherosclerosis in Carotid Arteries	2017	0.4
Dutch Society of Medical Ultrasound Spring Meeting – Delft, the Netherlands	2017	0.15
Earlier Recognition of Cardiovascular Disease Hartstichting and NWO – Utrecht, the Netherlands	2017	0.3
Young @ Heart day: Mobility, Netherlands Heart Institute – Utrecht, the Netherlands	2017	0.3
Netherlands Heart Institute Conference – Utrecht, the Netherlands	2017	0.6
COEUR PhD Day	2017/2019	0.6
Erasmus PhD Day	2017–2019	0.9
Young @ Heart day: Diversity, Netherlands Heart Institute – Utrecht, the Netherlands	2018	0.3
Dutch Society of Medical Ultrasound Autumn Meeting – Eindhoven, the Netherlands (oral presentation)	2018	1.15
Medical Imaging Symposium for PhD Students – Rotterdam, the Netherlands	2018	0.3
2 nd Translational Research Meeting Netherlands Heart Institute – Utrecht, the Netherlands (poster presentation)	2018	1.1
Earlier Recognition of Cardiovascular Disease Update Meeting Hartstichting and NWO – Utrecht, the Netherlands	2019	0.3
7 th Dutch Biomedical Engineering Conference – Egmond aan Zee, the Netherlands (poster presentation)	2019	1.1
Young @ Heart day: How to Conquer the World with your PhD?, Netherlands Heart Institute – Utrecht, the Netherlands	2019	0.3
Networked Sciences Symposium – Rotterdam, the Netherlands	2019	0.2
Total		33.5

Acknowledgements

I would not have been able to write this thesis without the support of many others. I truly enjoyed the many collaborations during my PhD adventure; it is what taught me the most on a scientific, and more importantly, on a personal level. Furthermore, performing experiments and obtaining results is more fun when shared with others.

Rik, uiteraard begin ik dit dankwoord bij jou. Ik wil je graag bedanken voor alles wat je mij hebt geleerd. Jij stond altijd klaar om resultaten te bespreken en om te helpen, zelfs wanneer dat betekende dat jij in mijn plaats experimenten moest uitvoeren in Leuven. Ik wil je danken voor het meedenken, maar ook omdat je mij hebt vrijgelaten om mijn eigen weg te bepalen. Ik en mijn ietwat kritische karakter hebben het jou niet altijd even makkelijk gemaakt, maar met jou was alles bespreekbaar, ook wanneer we het ergens niet over eens waren. Bedankt voor je support, zonder jouw enthousiasme en optimisme was ik niet zo ver gekomen. Ik had dit PhD avontuur voor geen goud willen missen!

Hans, jouw frisse blik op onderzoeksresultaten heeft mij vaak een stap vooruit geholpen. Bedankt dat jouw deur altijd openstond, zodat ik even binnen kon lopen voor wat snelle input. Ik wil je in het bijzonder bedanken voor jouw mentale ondersteuning, dit had je echt niet beter kunnen doen.

Ton, wat ben jij toch een goed opperhoofd van de BME familie. De atmosfeer van de afdeling heb ik als uniek ervaren; mensen met ongelooflijk verschillende achtergronden kunnen zichzelf zijn en ontwikkelen, en iedereen staat tegelijkertijd klaar om elkaar te helpen zonder enige vorm van concurrentie. Ik ben blij dat ik hier aan deel heb mogen nemen. Jij realiseert je als geen ander dat een luisterend oor soms al genoeg is om zelf keuzes te maken in de laatste cruciale fase van een PhD avontuur. Bedankt voor alles!

Nico, bedankt dat jij mij de kans hebt geboden om dit PhD avontuur aan te gaan, en voor je begeleiding als promotor de afgelopen jaren. **Nico** en **Martin**, al in 2013 deed ik mijn Bachelor afstudeerproject bij jullie in Delft. Daarna kwam ik terug op de afdeling in 2015 voor mijn Master afstudeerproject onder begeleiding van **Koen**. Bedankt dat jullie mij enthousiast hebben gemaakt over onderzoek binnen een medische setting. Zonder deze ervaring was ik waarschijnlijk nooit in een ziekenhuis terecht gekomen.

Annette, wij hebben veel samengewerkt en wat waren we toch een goed team! Onze ietwat eigenwijze karakters zorgden er soms voor dat we zinnen wel 20 keer herschreven, maar we wisten in ieder geval zeker dat wanneer we iets indienden, er goed over was nagedacht. Ik denk dat wij echt hebben laten zien dat je samen meer bereikt dan alleen; met gebundelde krachten wisten we zelfs mijn auto een helling op te duwen! We hebben vele hoogte- en dieptepunten meegemaakt, en ik ben blij dat we deze samen hebben kunnen beleven. Het moment dat we voor het eerst actieve shear waves zagen *in vivo* zal ik niet snel meer vergeten!

Jason, I am glad we finally came out of our trees and started talking to each other (Yes, I was not the only person hidden in a tree!). Thank you for everything you taught me. I am glad that we could do the PHRASE patient study together. Thank you for covering me when I almost fainted during one of our experiments. Your complaints about random subjects taught me that the grass is not always greener on the other side of my computer screen.

Mihai and **Dan**, you showed the importance of a steady hand and performed many measurements described throughout this thesis. Thank you, without your sonographic expertise, my measurements would have been meaningless. **Mihai**, I totally benefitted from the fact that you already had a lot of experience with shear wave elastography before I even started. Discussing my results with you helped me to think from a more clinical, and thus more relevant, perspective. **Annemien**, ik bewonder je volhardendheid om projecten van de grond te brengen, en ik ben blij dat ik heb kunnen deelnemen aan de patienten studie PHRASE. **Bas**, bedankt dat je altijd zo snel reageerde op mijn emails wanneer ik weer eens hulp nodig had bij de klinische interpretatie van het project.

To all members of my **Doctoral Committee**, thank you for taking the time to read my dissertation. To all members of the **User Committee**, you helped us to look at our results from another perspective and in performing more relevant research.

Glen McLaughlin and **Yuling Chen** from Mindray, thank you a lot for providing the Zonare system with the customized high frame rate imaging mode. Thanks to your help, I could more easily collect and analyze the data for my volunteer studies.

The collaboration with the KU Leuven was a great and unique experience within my PhD adventure. **Prof. Jan D'hooge** and **Prof. Jens-Uwe Voigt**, thank you for giving me the opportunity to participate in your interesting and extensive pig experiments. Through these experiments, we were able to make an important step in the interpretation of shear waves. I really enjoyed collaborating with you and people from your lab, you have a great team! **Stéphanie**, ontzettend knap hoe jij de experimenten runt in alle aspecten. Bedankt voor alle extra moeite en tijd die je erin hebt gestoken om ons mee te laten doen. Het is zeker bewonderingswaardig hoe jij vaak met een beetje extra kracht op de probe toch nog ergens een acceptabel beeld vandaan wist te toveren. **Marta**, thank you for performing one of our experiments. Most people need months to master the Verasonics, but with a little bit of help you managed to learn the basics in a few hours! **Jürgen**, **Patrica** and all others who helped during the experiments, thank you very much for your help, without your expertise we would not

have been able to perform these experiments. Thank you for the great time, I enjoyed working with you all.

I would also like to thank the people from the Experimental Cardiology department for letting us participate in their pig experiments. **Prof. Dirk J. Duncker, Oana, Maaïke, Jens, Daphne en Ruben**, wat hebben jullie het ons ongelooflijk makkelijk gemaakt. We hoefden slechts de gang over te steken en stonden vaak alweer binnen 1 uur buiten de operatiekamer. Zonder jullie hadden we dit nooit voor elkaar gekregen.

To the entire Biomedical Engineering department, thank you for the great time over the past 4 years. It was a pleasure to get to know all of you. I enjoyed the many discussions and conversations in the lab, but also all fun activities outside working hours. Special thanks to everyone with whom I had a great time with during the different conferences, it brought me a lifetime of memories.

Robert, bedankt voor je helpende hand en technische support, maar veel belangrijker, voor alle flauwe grapjes die jij altijd met zoveel enthousiasme weet te vertellen. Ruben zal je tools missen en waarschijnlijk ook het advies dat jij mij altijd wist te geven wanneer ik een verjaardagscadeau moest kopen! **Frits**, bedankt voor het meedenken. **Gerard**, bedankt voor alle ICT gerelateerde support. **Sharon**, bedankt dat je altijd het overzicht hield, en voor het oplossen van allerlei problemen. De support van jullie allen maakt het leven van een PhD student op onze afdeling een stuk gemakkelijker.

My office mates, **Jorinde** and **Gonzalo**, thank you for teaching me how to play chess, for the Friday treats and for listening to my thoughts. I am sorry for talking to myself and for my poorly developed singing skills. **Kirby**, thank you for the great conversations, for all your help in mastering the English language, and for supporting me on my first trip to Leuven. **Sophinese**, thank you for celebrating my first paper by surprising me with a cake including sparkles, and for taking care of me during my first conference in Washington D.C. **Mirjam**, wij keken elke dag uit naar jouw thee pauze rond 4 uur waarin je altijd wat gezelligheid kwam brengen in ons kantoor. **Eline**, het blijft bewonderingswaardig hoe jij over elk willekeurig onderwerp een gesprek weet te voeren. Onze eerste ontmoeting in de bus onderweg naar het labuitje in Den Bosch, en het moment dat wij hoog in een boom zaten en er geen weg terug meer was, zal ik niet snel vergeten. **Inés, Eline, Mirjam en Astrid**, ik heb genoten van onze (online) theebransjes binnen de 'Final Countdown' groep, wat heb ik gelachen! **Alberico**, thank you for your company within the EFFECTS project. We approach research in completely different ways, but I think it was good for both of us to see that there are many roads that lead to Rome. Also to all other PhD students, it was a pleasure to be part of such a supportive group, and my PhD adventure would not have been the same without you!

Inés, de afgelopen tien jaar hebben we samen de onderzoekswereld mogen ontdekken. Het is moeilijk voor te stellen dat er een moment komt, dat wij elkaar niet meer elke dag zullen zien. Hoewel we nooit inhoudelijk hebben samengewerkt, konden we altijd bij elkaar langsgaan voor advies of gezelligheid. Ik ben dankbaar dat

we onze avonturen met elkaar hebben kunnen delen en ik heb genoten van onze vele koffie momentjes samen met Bas in het Erasmus MC. **Bas**, bedankt voor je luisterend oor, en natuurlijk voor de doos met chocola die je mij opstuurde op de dag dat ik mijn proefschrift inleverde! Het is jammer dat we naast onze 'Master is vet onmogelijk' club, nooit een club 'Hoe overleef ik mijn PhD?' hebben opgericht. **Joep, Liesbeth, Inés en Bas**, ik ben blij dat, ondanks dat we nu allemaal Delft hebben verlaten, onze 'Master was eigenlijk redelijk doenbaar' club deze afstand toch weet te overbruggen. Ik hoop wel dat de tweedeling tussen 'academia' en 'industry' snel wordt opgeheven, zodat ik nooit meer zal verliezen van 'team industry'!

Daniëlle, wij werden vriendinnen toen we zo'n 13 jaar oud waren, en kijk ons beide nu eens! Het is altijd ontzettend fijn om elkaar bij te praten en ik bewonder de manier waarop jij het leven aanpakt!

Mijn schoonfamilie, **Dick, Zilpa, Sam, Anneloes, Michael en Katie**, bedankt dat jullie mij de afgelopen 10 jaar hebben verwelkomd in jullie familie. Bedankt voor de support en gezelligheid!

Lieve **Papa en Mama**, bedankt dat jullie er altijd voor mij zijn. Wat hebben jullie het mij altijd ongelooflijk makkelijk gemaakt. Jullie onvoorwaardelijke steun en liefde, heb ik en zal ik altijd voelen. Ik zal jullie deur blijven plat lopen. Mijn grote zussen, **Ava en Nina**, wij zijn alle drie een totaal andere kant op gegaan, en tegelijkertijd zullen jullie altijd naast mij staan. Jullie hebben laten zien hoe ontzettend groot de wereld is, en jullie hebben mij geleerd om te vechten voor je dromen. Ik ben blij dat jullie mijn zussen zijn. Lieve **Ruben**, jij bent mijn grootste steunpilaar en zal altijd zeggen: 'Ga ervoor, als iemand het kan, dan ben jij het!' Ik geniet van onze road-trips op zoek naar wilde koeien en kometen, van onze vakanties in de mini tent, en van onze vele projecten (die ik vaak bedenk en jij dan mag uitvoeren). Ik kijk uit naar de vele avonturen die wij nog samen mogen beleven. Lieve **Papa, Mama, Ava, Nina en Ruben**, bedankt voor de thuisbasis, jullie zijn voor mij het allerbelangrijkst.

About the Author

Lana Beate Hendrika Keijzer was born on May 24th, 1992 and grew up in Alphen aan den Rijn, the Netherlands. In 2010, she graduated from pre-university education (Gymnasium) at the Groene Hart Lyceum (Alphen aan den Rijn, the Netherlands). Then, she received a Bachelors and Masters degree in Applied Physics at the Delft University of Technology (Delft, the Netherlands), in 2013 and 2015 respectively. During her Masters, she specialized in medical and acoustical waveform imaging, and focused on measuring the speed of sound and attenuation of breast tissue during her thesis at the Department of Imaging Physics at the Delft University of Technology, in collaboration with the department of Surgical Oncology at the Erasmus University Medical Center (Rotterdam, the Netherlands). Hereafter, she also graduated from her Masters in Management of Technology in 2016, at the Delft University of Technology.



In 2016, she joined the Biomedical Engineering Department of the Thorax center at the Erasmus University Medical Center (Rotterdam, the Netherlands), where she started her PhD project about cardiac shear wave elastography. This project focusses on non-invasive shear wave elastography techniques for the assessment of myocardial stiffness in heart failure patients. She was involved in many *in silico*, *in vitro* and *in vivo* (animals, volunteers and patients) experiments, and focused on the physical interpretation and clinical relevance of shear waves.